AURORA AND ASSOCIATED VLF PHENOMENA

by

DESMOND D. DUTHIE

Submitted in partial fulfillment of the requirements for the degree of Doctor of Philosophy in the Department of Physics, University of Natal.

Durban, July, 1978

To my Parents

ABSTRACT

Observations have been made at Sanae (gm. lat. -63,71°) on occurring auroral forms, (diffuse and pulsating aurora), and simultaneous occurring VLF phenomena, (whistlers and auroral hiss). Two studies are presented in this thesis.

(a) A comparison of the positions of auroral forms and the positions of field lines, along which whistlers propagate, is made and it is found that:

(i) Diffuse aurora occurs on closed field lines and indirect evidence shows that this is also the case for pulsating aurora.

(ii) For two periods of data the separation of diffuse aurora from the plasmapause ranges from < 0,9 L to < 0,2 L but during a third period, the diffuse aurora lies, at least partially, within the plasmasphere.

(b) An investigation into the association between pulsating aurora and pulsating auroral hiss is made and it is shown that:

(i) A common identical pulsation period of 0,75 s and high coherency exists between the light intensity of an auroral patch and the intensity of the associated pulsating auroral hiss. This suggests a wave-particle interaction as a common modulation mechanism.

(ii) Cyclotron instability (gyroresonance) or Cerenkov radiation mechanisms occurring in the equatorial plane do not account for the time delays, typically between 0,90 s and 0,157 s, found to be present between the two phenomena, where the incident auroral electrons,

responsible for the auroral patch light intensity, are observed to arrive *before* the auroral hiss emissions.

The results of the analysis in (a) are reported in The Journal of Atmospheric and Terrestrial Physics, 39, 1429, 1977.

ACKNOWLEDGEMENTS

The author wishes to express his sincere thanks to the following persons and organization:

Professor M.W.J. Scourfield, who initiated the projects and provided inspiration and enthusiasm when most needed.

Messrs. R.J. Taylor, D.W. Kennard, W.G. Sanford, W.J. de Beer, E.E. Higginson and E.J.S. Tait who provided excellent advice in the electronic and technical needs of this thesis.

The South African Department of Transport and C.S.I.R. for logistic and financial support.

Professor L. Nattrass without whose analysis system and advice one half of this thesis would not have been completed.

Dr. Arthur Hughes and Mr. Mike Barker for advice and direction.

Mrs. E. Serfontein and Mrs. F. Fletcher for typing and encouragement.

The Library staff for their constant assistance.

Misses C. Duthie and K. Kohler for proofreading.

Dave and Judy Boynton for helping with the diagrams and giving moral support.

The Physics fifth floor for their fine company and sense of humour.

CONTENTS

CHAPTER THREE: (Continued)

CHAPTER THREE: (Continued)

CHAPTER FOUR: INSTRUMENTATION

CHAPTER FIVE: THE SPATIAL RELATIONSHIP BETWEEN AURORAL FORMS AND CLOSED MAGNETIC FIELD LINES

CHAPTER SIX: POWER SPECTRA, CORRELATION AND COHERENCY OF PULSATING AURORAL PATCHES AND SIMUTANEOUSLY OBSERVED VLF HISS

CHAPTER ONE

INTRODUCTION

1.1 Perspective

Long recognised as contributing significantly to knowledge of the sun-earth environment are high latitude polar observations. Attention was focused on the Arctic regions when international scientific cooperation brought about the First and Second Polar years of 1832-33 and 1932-33 respectively. A much broader international research programme, the International Geophysical Year of 1957-58, concentrated on scientific research in the Antarctic. At present, Antarctic research is being carried out at about 30 scientific stations manned by ten countries. The International Magnetospheric Study planned for 1976-78, has as its chief objective coordinated international observations from groundbased facilities, balloons, aircraft, rockets and spacecraft, leading to a quantitative understanding of the dynamic processes operating on plasmas in the geomagnetic field.

1.2 Sanae, Antarctica

Sanae, the main South African Antarctic station, is located near the optimum position for the observation of plasmapause-associated events directly overhead. The field observations of very low frequency (VLF) phenomena and aurora for this thesis were made at this station, which is a member of the 'L = 4 chain of stations'.

The L = 4 chain includes:

Kerguelen	L = 3,70
Siple	L = 3,89
Sanae	L = 3,98
Halley Bay	L = 4,22
General Belgrano	L = 4,61

A map showing the position of these stations is given in Figure 1.1, and a summary of the coordinates and other data for Sanae, relevant to this thesis, is given in Table 1.1.

1.3 Scope of the present work

This thesis is divided into two portions. The first deals with the analysis and interpretation of simultaneous observations of whistlers and auroral forms, and the second portion is an investigation into the simultaneous occurrence of pulsating aurora and pulsating auroral hiss.

A broad review of magnetospheric processes and morphology, and detailed reviews of the plasmapause, auroral oval, hiss and pulsating aurora are given in order to provide a background for the interpretation of the data analysed in this thesis. The Video Analyser, an instrument used in the analysis of the auroral data, is described in detail. Data from three nights of simultaneously observed aurora, as imaged by a TV system, and whistlers are analysed, and a comparison of the positions of auroral forms and field lines along which the observed whistlers propagated, is made. Diffuse aurora is found to occur on closed field lines and indirect evidence shows that this is also the case for pulsating aurora. For two periods of data the separation of diffuse aurora from the plasmapause ranges from $< 0,9$ L to $< 0,2$ L but during a third period diffuse aurora lies, at least partially, within the plasmasphere. Further, there is presented an investigation into the association between pulsating aurora and pulsating auroral hiss. The common identical

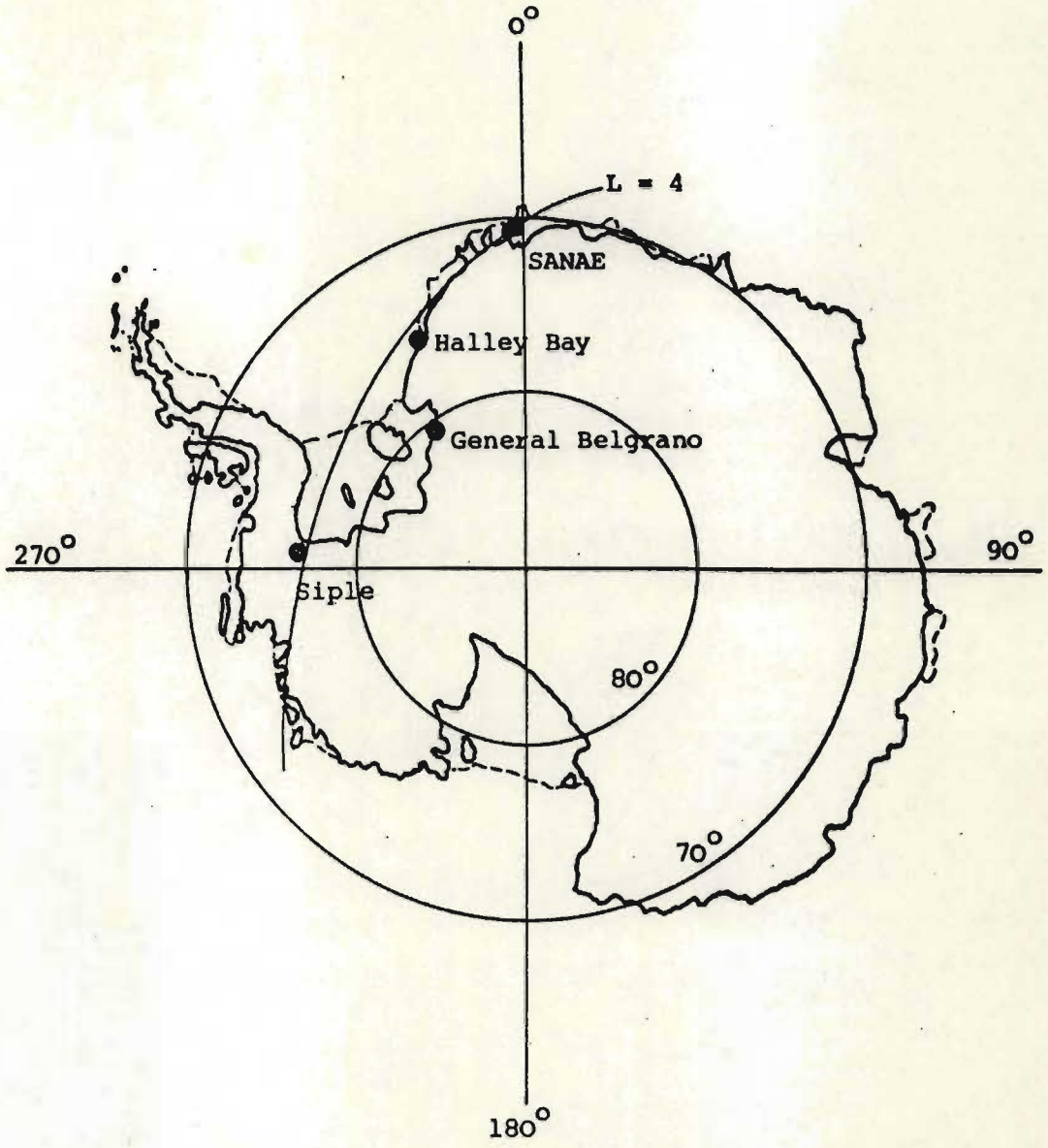

Figure 1.1 Sketch map of Antarctica showing the location of the L = 4 chain of stations

SANAE		
Geographic Co-ordinates:	Lat	-70,30
	Long East	357,65
Geomagnetic Co-ordinates:	Lat	-63,71
	Long East	44,53
Geom. Conjugate Geog. Co-ord:	Lat	53,42
	Long East	316,54

L - value	3,98
Invariant Latitude	59,90
Geocentric Dip	-62,56
Altitude (Metres)	53

World Data Centre A for Solar and Terrestrial Physics Report UAG 38 - December, 1974.

Table 1.1 Data for SANAE

pulsation period of 0,75 s and high coherency between the two phenomena suggest a wave-particle interaction as a modulation mechanism. Time delays, typically between 0,090 s and 0,157 s where the auroral electrons responsible for the auroral patch light intensity, are observed to arrive before the auroral hiss emissions at the point of observation, are not explained by a cyclotron instability (gyroresonance) or Cerenkov radiation mechanisms occurring in the equatorial plane.

CHAPTER TWO

THE MAGNETOSPHERE

2.1 INTRODUCTION

The magnetosphere may be described as that region of space surrounding the earth where physical processes are dominated by the geomagnetic field. The ionosphere is customarily set as the lower limit and is usually treated separately. Plasmas of solar and terrestrial origin fill the magnetosphere. The former streaming through interplanetary space can enter the magnetosphere, while the latter diffuses upwards from the ionosphere at polar latitudes. The geomagnetic field dominates the magnetospheric plasmas and is the determining factor in its behaviour.

The role played by the magnetosphere in the earth's environment is a protective and significant one. It shields earth from high levels of interplanetary radiation but supports belts of trapped radiation particles. Radio communications may be disrupted for days by magnetospheric processes which on the other hand help to maintain the winter polar ionosphere. The understanding of the physical processes involved in the magnetosphere is still in an early stage although much progress has been made in determining the general topology of the magnetosphere during the last fifteen years.

Regions of the magnetosphere project along field lines onto the ionosphere below. Thus the upper atmosphere may be regarded as a fixed viewing screen on which processes occuring further out in the magnetosphere may be monitored as the earth rotates underneath. Continuous ground-based observations can therefore form a valuable complement to *in situ* satellite observations which are of a low frequency synoptic nature.

Because various regions of the magnetosphere and the physical processes occurring therein are interdependant, it is impossible to study any magnetospheric phenomenon in isolation. Thus a broad review of magnetospheric processes is appropriate and this is presented as a background for later sections of this thesis.

2.2 INTERACTION BETWEEN THE SOLAR WIND AND THE MAGNETOSPHERE

An interplanetary magnetic field is carried by plasma of solar origin streaming outwards from the sun. This plasma stream, the solar wind (PARKER, 1958), undergoes perturbations analogous to gusts. Solar wind velocity exceeds both the thermal and Alfvén velocities so that a shock front is established in front of the obstacle, such as the geomagnetic field.

2.2.1 Models of the magnetosphere

Consider the superposition of a homogeneous interplanetary magnetic field on the geomagnetic dipole. Two cases are possible.

The case where the interplanetary field is directed northwards leads to the situation illustrated in Figure 2.1(a) where the magnetosphere is closed. No flux linkage occurs between the geomagnetic and the interplanetary magnetic fields. A southward directed interplanetary field gives rise to an open magnetosphere in which high latitude flux linkage takes place between the superimposed fields (Figure 2.1(b)). Satellite observations near the earth's orbit show that the average direction of the interplanetary magnetic field is in the ecliptic plane 45° tangent to the earth's orbit. However, there are large temporal and spatial variations and the instantaneous magnetic field can have many directions, (FALTHAMMAR, 1973).

Various open and closed models of the magnetosphere have been

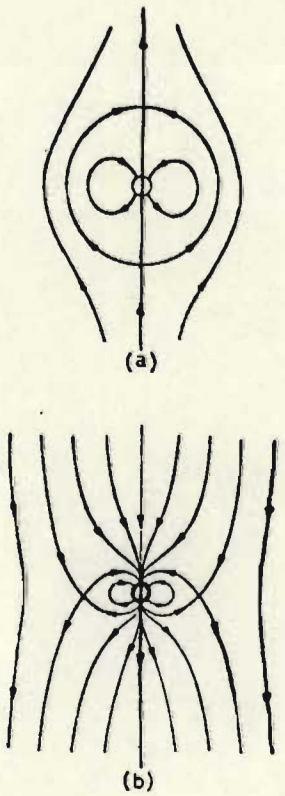

Figure 2.1(a) Superposition of a N-directed interplanetary magnetic field on the geomagnetic dipole results in a closed magnetosphere
(b) Superposition of a S-directed interplanetary magnetic field on the geomagnetic dipole results in a magnetosphere open at high latitudes
(BLOCK, 1972)

proposed but, as PAULIKAS (1974) pointed out, it should be borne in mind that these models are abstractions meant to illustrate and illuminate limiting, extreme cases of topology. AXFORD and HINES (1961) and MICHEL and DESSLER (1965) proposed closed models, (Figures 2.2(a) and (b)), which require that plasmas from the solar wind diffuse across the field lines into the magnetospheric tail from where they propagate towards the polar cap. Open models such as those proposed by MORFELL and QUENBY (1971) and VAN ALLEN *et al* (1971), (Figures 2.3(a) and (b)), provide direct entry for the solar wind plasmas into the magnetosphere along magnetic field lines between the geomagnetic tail region and the interplanetary magnetic field. A different temporal development is thus expected to be exhibited by solar plasma gaining entry by diffusion into a closed magnetosphere than that exhibited by plasma entering the open magnetosphere. Comparisons of the closed and open models, on the basis of the behaviour of particle fluxes over the polar caps, have been presented in the literature. VAN ALLEN *et al* (1971) concluded from an energetic solar particle event that the composite evidence favoured an open magnetosphere. It was pointed out by RUSSELL (1975) that the open model provided explanations for the observed control of magnetospheric current systems by the interplanetary magnetic field, and it also explained all the phases of the magnetospheric substorms. The closed model, however, seems to be a good representation of the magnetosphere during quiet steady state solar conditions. Perhaps the real state of the magnetosphere is that it is partly closed and partly open.

2.3 CONFIGURATION OF THE MAGNETOSPHERE

A noon-midnight meridian section of the magnetosphere is given in Figure 2.4. The solar wind, which is super-Alfvénic forms a shock front where the presence of the geomagnetic dipole causes a transition to sub-Alfvénic, subsonic flow. Behind the bow shock is a turbulent

(a)

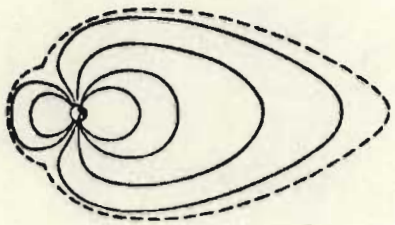

(b)

Figure 2.2 Closed models proposed for the magnetosphere.
(a) is after AXFORD and HINES (1961)
(b) is after MICHEL and DESSLER (1965)

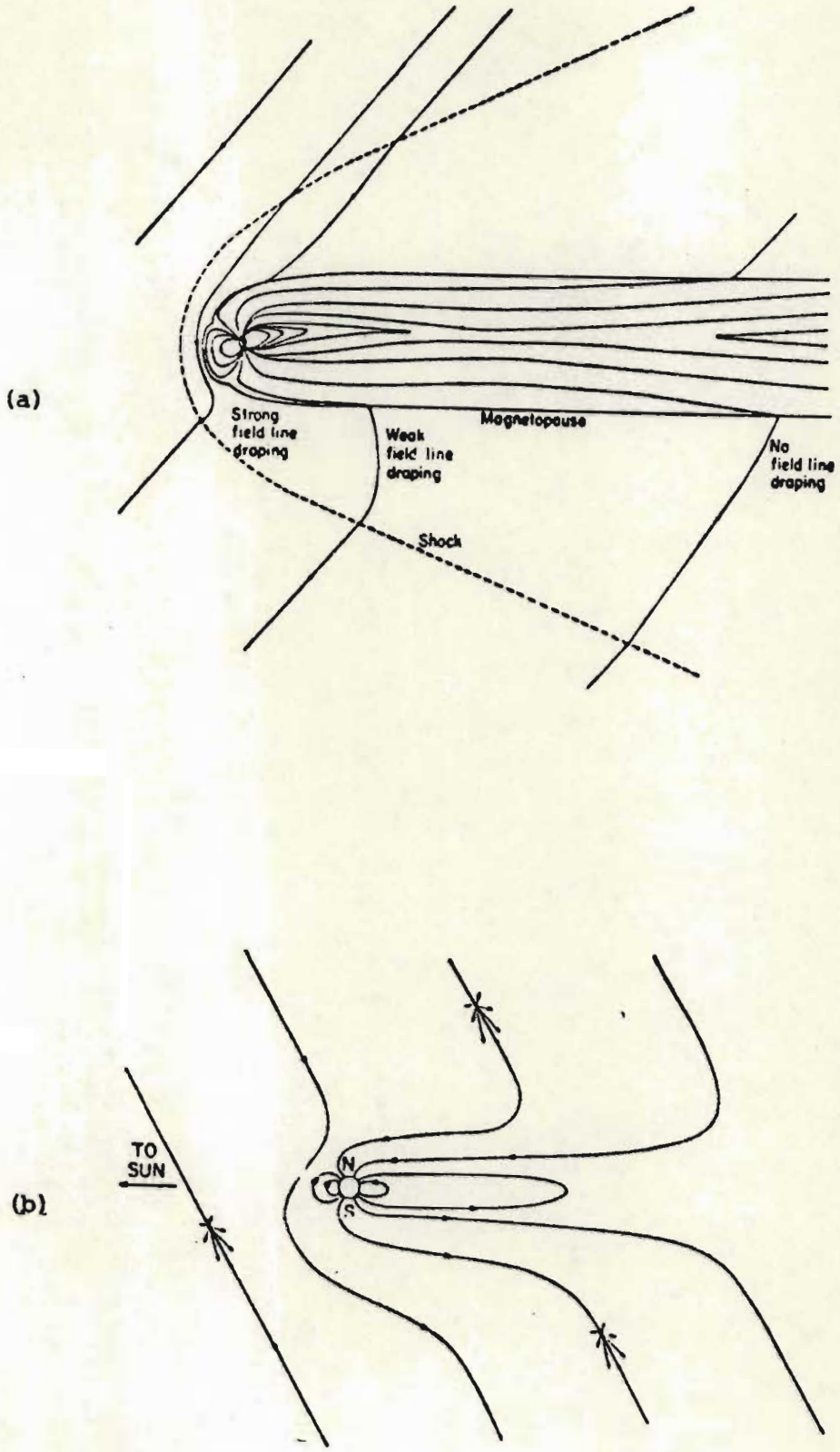

Figure 2.3 Open models proposed for the magnetosphere.
(a) is after MORFILL and QUENBY (1971)
(b) is after VAN ALLEN et al (1971)

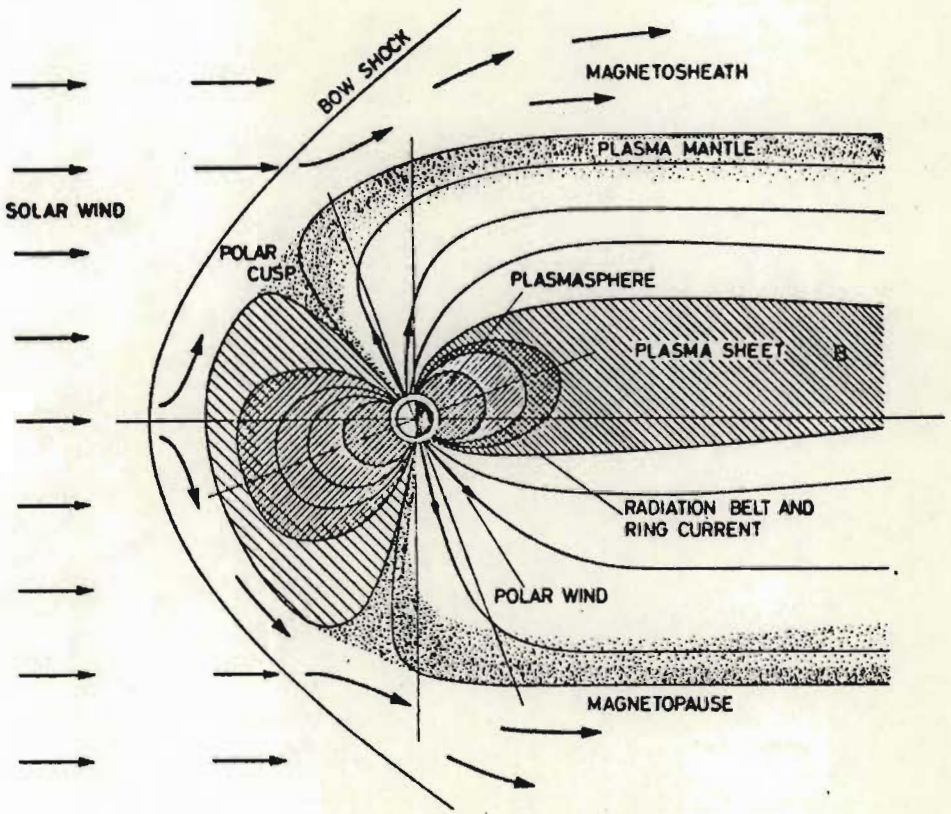

Figure 2.4 Noon-midnight meridian cross-section of the magnetosphere (ROSENBAUER et al, 1975)

region, the magnetosheath, which envelops the magnetosphere on the dayside and along the flanks. The magnetopause or demarcation between the geomagnetic field and the interplanetary magnetic field, is a well determined boundary of the magnetosphere on the dayside. Where the interplanetary magnetic field and geomagnetic field merge along the flanks the magnetopause is more diffuse. The geometric dimensions of the magnetosphere, as determined from satellite measurements, is given in Table 2.1. R_E is the unit of length and is the earth's radius, approximately 6400 km. An indication of the senstivity of the magnetosphere to changing solar conditions, is given by variations, percentage wise, in parentheses.

2.3.1 Magnetospheric current systems

Extensive current systems resulting from the plasma flow within the magnetosphere modify the geomagnetic dipole field to produce the magnetic field configuration of Figure 2.4. The lack of well determined details prevent the complete understanding of all the currents responsible for this configuration but four main current systems (ROEDERER, 1974) may be distinguished as illustrated in Figure 2.5.

Dayside magnetopause currents make up a system which varies greatly with time in response to the changing interplanetary magnetic fields just beyond the magnetopause. The sharp confinement of the magnetosphere is due to these currents which flow tangentially along the magnetopause in all directions. There is, however, an average flow directed from dawn to dusk on the dayside near the equatorial plane. The return circuit is though to be along the flanks, closing over the lobes.

The neutral sheet current divides the magnetotail into two lobes of oppositely directed magnetic fields as shown in Figure 2.5. The

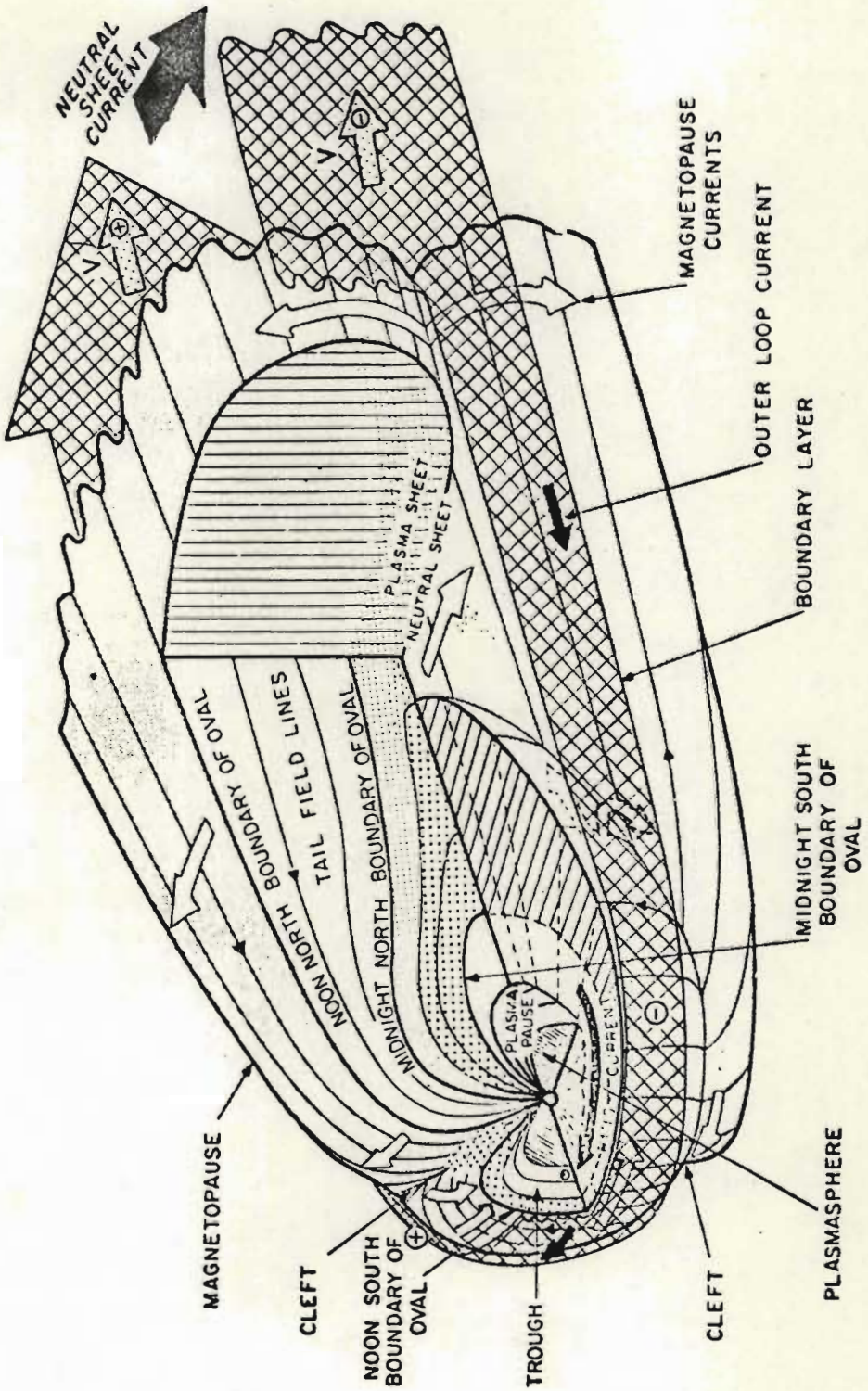

Figure 2.5 Magnetospheric current systems shown on a cutaway model (HEIKKILA, 1972)

Distance to magnetopause subsolar point	10 (6-15) R_E
Distance to shock front	14 (10-20) R_E
Length of magnetotail	1 000 R_E
Distance to magnetopause at dawn and dusk meridians	16 R_E
N-S thickness of tail at 20 R_E	40 R_E
E-W thickness of tail at 20 R_E	50 R_E
Distance to centre of ring current	4-7 R_E
Distance to plasmapause	4 (3-8) R_E
Plasma sheet inner boundary at midnight	5-10 R_E
Thickness of plasma mantle	$\geq$ 4 R_E

Table 2.1 Magnetospheric geometric data, from BLOCK (1973) and ROSENBAUER et al (1975)

direction of this current is dawn-to-dusk which is sustained by drifting plasma sheet particles, closing on the north and south tail lobes.

The ring current is a third current system and flows from east to west around the earth. It is centred on the magnetic equator at a radius of 4-7 R_E. Sustained by low energy particles trapped in the geomagnetic field, this current causes the geomagnetic field to be compressed inside the ring current and inflated outside it.

Left are the currents which make up the fourth current system which include the ionospheric currents (the auroral and equatorial electrojets), currents flowing along the polar cusp field lines in both directions, and telluric currents induced in the earth's crust by magnetospheric processes.

2.3.2 Electric fields of the magnetosphere

Indirect techniques such as the study of energetic particle motions and convection of natural plasmas, have, until recently, been relied upon as measuring methods of the magnetospheric electric fields. Satellite probes confirm in general the existence of relatively weak electric fields of the order of mVm^{-1} as measured by the above techniques.

There are distinct correlations between some features exhibited by the electric field and the interplanetary magnetic field. It has been found that different types of detailed variations in the distribution of electric field intensities over the polar cap region correlate closely with select directions of the interplanetary magnetic field, (HEPPNER, 1972). ROEDERER (1974) pointed out that the interplanetary

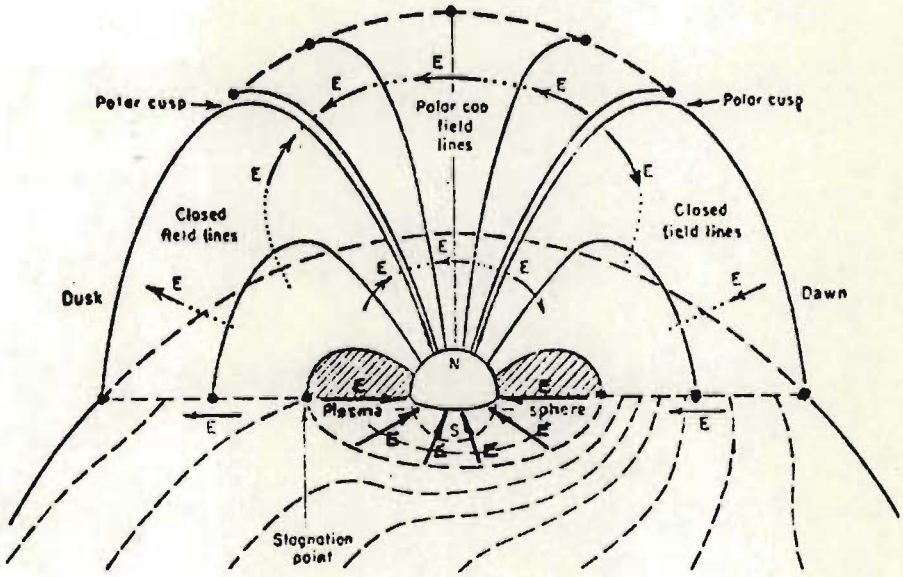

Figure 2.6 Electric fields of the magnetosphere with respect to an external observer situated in the N-lobe of the magnetotail
(adapted from ROEDERER, 1974)

field could represent the external 'driving mechanisim' of the magnetospheric electric field. However,there is almost certainly a secondary steady-state source for the electric field possibly in a viscous interaction between the magnetopause and the solar wind.

The configuration of the twilight meridian of the electric field with respect to an external observer is shown in Figure 2.6. There are three main distinct regions. The plasmasphere is a region where the electric field is directed radially inwards accounting for the corotation of plasma with the earth. The second region, the dawn-to-dusk electric field, is a zone where closed field lines outside the plasmasphere carry an electric field and the field is directed equatorwards on the dawn side and polewards on the dusk side. The third region is that of the polar cap with an electric field across open magnetic field lines. The direction is dawn-to-dusk as shown in Figure 2.6. Because of the high conductivity along field lines in the magnetosphere, the electric field is everywhere perpendicular to the magnetic field.

The noon-midnight meridian presents a less regular and more complex situation. Multiple field reversals have been detected and the midnight region shows electric field variations extremely sensitive to magnetospheric conditions.

Figure 2.7 shows typical plasma convection paths in the equatorial plane (KAVANAGH *et al*). All magnetic field lines passing through a given convection curve define an equipotential surface. The plasmapause defines a sharp boundary between closed and open convection paths at a position between 3 R_E and 7 R_E around the earth. The convection results in a general sunward movement of plasma from the magnetotail along open paths and a corotational flow around the earth along the closed equipotentials.

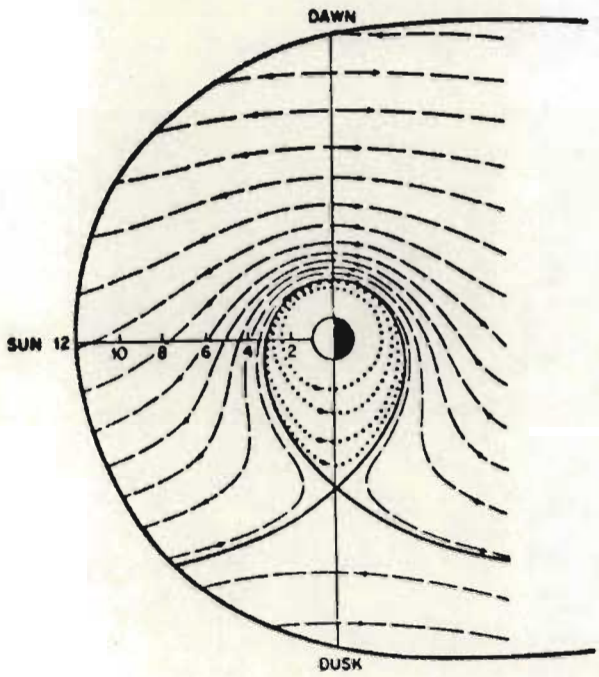

Figure 2.7 The equatorial flow paths within the magnetosphere of magnetic tubes of force containing thermal plasma. The dashed lines indicate convectional flow, the dotted lines corotational flow
(CHAPPELL, 1972)

2.4 PLASMA POPULATIONS IN THE MAGNETOSPHERE

Within the magnetosphere charged particles are to be found in three main regions with electron energies varying from the thermal range (eV) up to several MeV. Proton energies extend to several hundred MeV. Although there is a general spread of lower energy particles throughout the magnetosphere, certain natural limiting boundaries can be defined.

The high energy population is concentrated in the radiation belts, a doughnut shaped zone symmetrical about the equatorial plane. A second zone is the plasmasphere which constitutes a near-earth doughnut shaped reservoir of thermal electrons and protons subject to the corotational convection pattern discussed earlier and illustrated in Figure 2.7. The plasmasphere exhibits a drop in particle density at its boundaries, termed the plasmapause. Densities within the plasmasphere are of the order of 10^8 eℓ $\bar{m}^3$ (10^2 eℓ $c\bar{m}^3$) and just beyond the plasmapause they fall to 10^6 eℓ m^{-3}(1 eℓ cm^{-3}). The plasmasphere and plasmapause are subject to a detailed discussion in Chapter Three of this thesis.

2.4.1 The plasma sheet

The third main reservoir of plasma is the plasma sheet, depicted in Figure 2.4 as the region marked B. It surrounds the earth on the night side and fills the distant magnetospheric tail separating the N and S lobes. It is a region of hot plasma where the energy density remains approximately constant in quiet magnetospheric conditions, (HONES *et al*, 1971). Plasma sheet characteristics at 18 R_E are well documented with the aid of Vela satellites. Particle density is 10^5 to 10^6 particles m^{-3}. Electron energies range from 100 - 500 eV and protons from 1 - 5 KeV. BAME *et al* (1967) found that the plasma sheet stretches across the tail from the dawn-to-dusk flanks with a thickness in the midnight meridian at 17 R_E

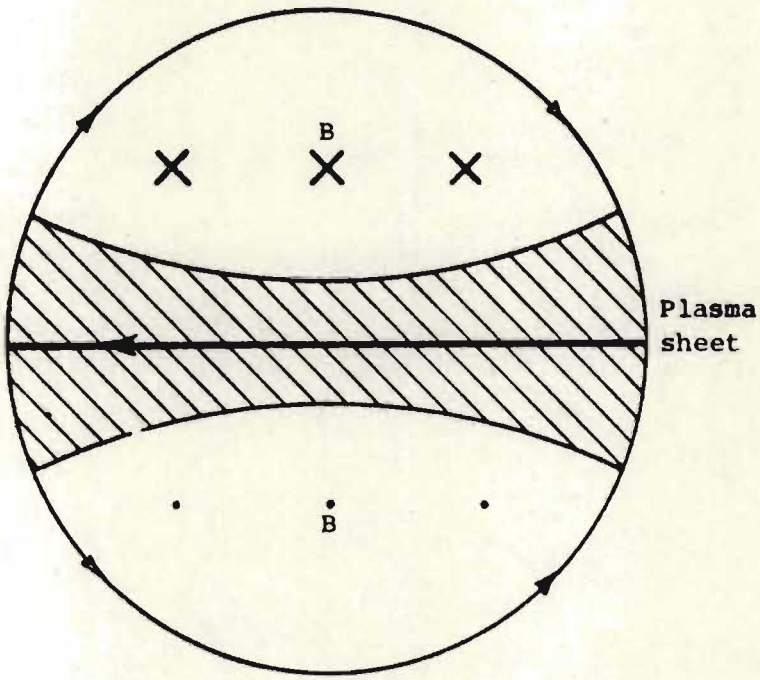

Figure 2.8 Schematic dawn-to-dusk cross-section of the magnetotail at about 18 R_E looking earthwards

of 4 - 6 R_E. At the flanks the thickness is increased by a factor of two as shown in a cross-sectional view of the magnetotail looking towards the earth, Figure 2.8. BAME *et al* (1967) also found the plasma sheet to be frequently in motion either by 'flapping' or by pulsations as the thickness varied.

During the development of magnetospheric substorms, which are the manifestations of stored magnetic energy suddenly released in the form of particle energy, a plasma decrease in the magnetotail at 18 R_E was detected by HONES *et al* (1967). HONES *et al* (1971) noted evidence that thinning of the plasma sheet could be a direct consequence of a southward turning of the interplanetary magnetic field. AUBREY and (McPHERRON(1971) investigated the relationship between the configuration of the magnetotail, substorm activity, and changes in solar wind parameters. From a broad coverage of satellite data, they concluded that a change from a N-directed interplanetary magnetic field to S-directed one caused a thinning of the plasma sheet. The change back to N-directed field caused the plasma sheet only in the outer magnetosphere to thicken. They concluded a substorm expansion phase was necessary to expand the plasma sheet in the inner magnetosphere.

The average plasma sheet configuration near 60 R_E was observed by MENG and MIHALOV (1972) and the shape was found to be similar to that at 18 R_E. The plasma sheet thickness at 60 R_E, however, was found by RICH *et al* (1973) to be half that at 18 R_E, and energy density to be down by a factor of five.

A schematic representation of the average plasma distribution in the equatorial plane was presented by ATKINSON (1971), and is reproduced in Figure 2.9. There is a well defined tongue of plasma flowing sunwards around the evening flank towards noon. The inner edge of the plasma sheet is well separated from the boundary of the plasmasphere in the

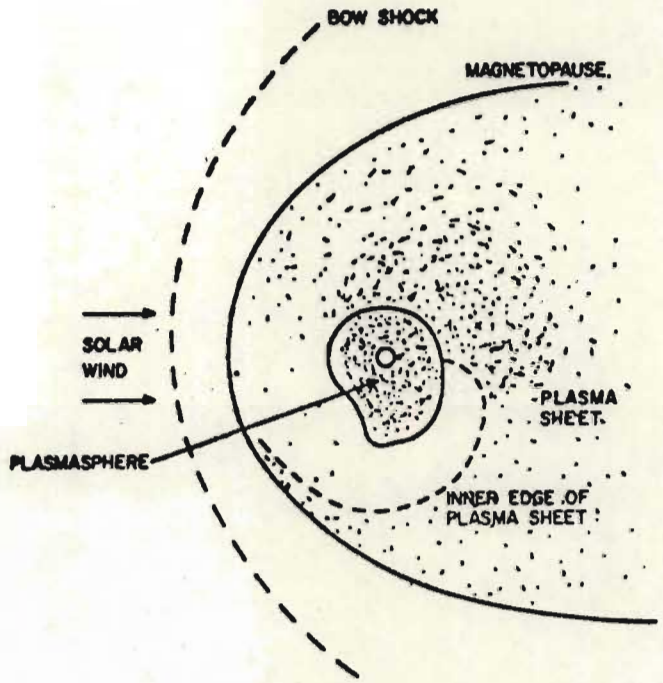

Figure 2.9 Schematic representation of the average plasma distribution in the equatorial plane. Note the morning-evening asymmetry of the plasma sheet and the tongue extending into the afternoon sector

(BURROWS and McDIARMID, 1972)

evening sector. CHASE (1969) presented evidence that the plasma sheet is the source of auroral electrons, in a comparison of high resolution energy measurements of particles precipitating in the auroral zones and particle energies in the magnetotail. The boundaries of the plasma sheet are important in determining the latitude limits of auroral precipitation. BURROWS and McDIARMID (1972) point out that the properties of the inner edge of the plasma sheet are very variable.

FRANK (1971) discusses the relationship of the plasma sheet, ring current, trapping boundary and plasmapause near the magnetic equator and local midnight. His findings are summarised in Figure 2.10. The earthward edge of the plasma sheet is located in the post-midnight sector such that its inner boundary is coincident with the plasmapause position. These two features are usually separated by 1 - 3 R_E by the electron trough in the pre-midnight sector. During polar magnetic substorms the electron trough region disappears and the structure in the pre-midnight sector becomes similar to that of the post-midnight sector. The earthward edge of the plasma sheet was defined by FRANK (1971) to be the region where there is an exponential decrease of electron energy density with decreasing L-value.

2.4.2 The origin of the plasma sheet

Several hypotheses on the origin of the plasma sheet have been presented. EASTWOOD (1973) advanced a *current sheet acceleration hypothesis* involving polar wind particles as the source of the plasma sheet. The *reconnection hypothesis* of AXFORD (1967, 1969), the *cusp entry hypothesis* of FRANK (1971) and HILL and DESSLER (1971), and the *magnetopause diffusion hypothesis* of AXFORD (1970), involve the penetration of solar wind particles into the magnetotail to form the plasma sheet. HILL (1974) evaluated the importance of the various hypotheses on the basis that a complete theory for the formation of the plasma sheet must be consistent with the following constraints:

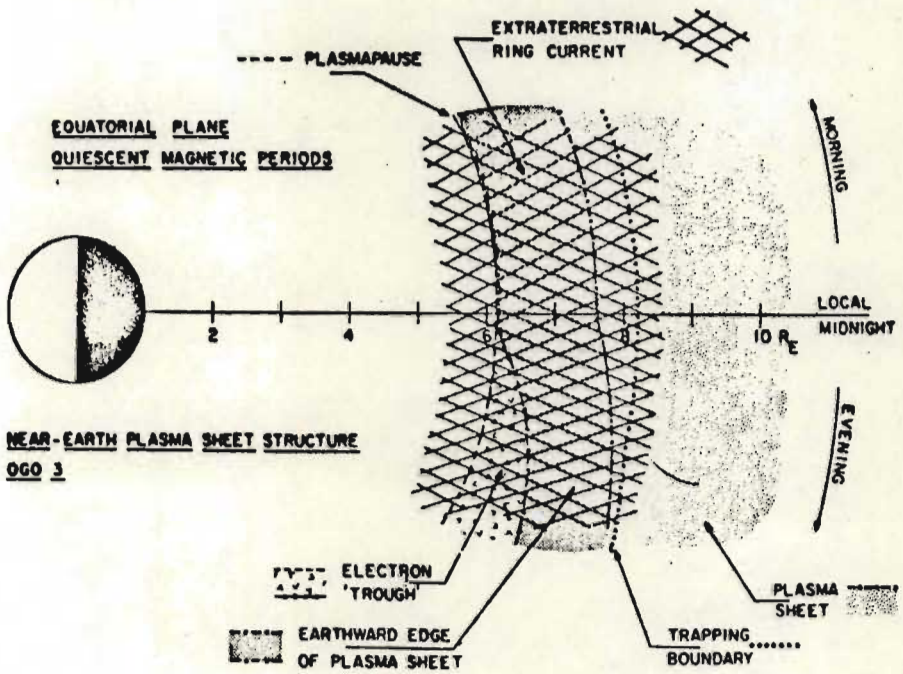

Figure 2.10 Graphic summary of the structure of the near-earth plasma sheet in the post and pre-midnight sectors of the magnetosphere in the equatorial plane during periods of relative magnetic quiescence

(FRANK, 1971)

(i) A small fraction (10^{-3}) of the incident solar wind flux is captured.

(ii) Injected particles are accelerated by a factor of 10.

(iii) The injection mechanism is highly selective in energy and/or pitch angle.

(iv) The plasma sheet has no gross dawn-to-dusk assymetry.

(v) The plasma sheet is probably threaded by closed field lines during quiet times.

He concluded that diffusion at the dayside magnetopause (especially in the cusp) is the primary mechanism for injection of solar wind particles to form the plasma sheet, and that the polar wind contribution is insignificant. Static magnetic field drifts determine the plasma/magnetic configuration of the tail. The cross-tail electric field generated by magnetopause diffusion and magnetic field lines merging in the tail results in adiabatic acceleration and thus determines the energy distribution in the plasma sheet.

AKASOFU (1974) discussed briefly the merging of the geomagnetic field lines with the interplanetary magnetic field on the dayside. Figure 2.11 shows a schematic diagram of the merging process and subsequent convection of the merged field lines to the tail. Reconnection in the magnetotail traps solar wind plasma in the plasma sheet as can be seen in the diagram. The association of the plasma sheet with diffuse and discrete auroras is discussed separately in the auroral sections of Chapter Three.

2.5 MAGNETOSPHERIC SUBSTORMS

RODERER (1974) pointed out that a substorm is the single most important perturbation event in the magnetosphere. Accumulated magnetic energy in the tail is suddenly released and dissipated in the form of

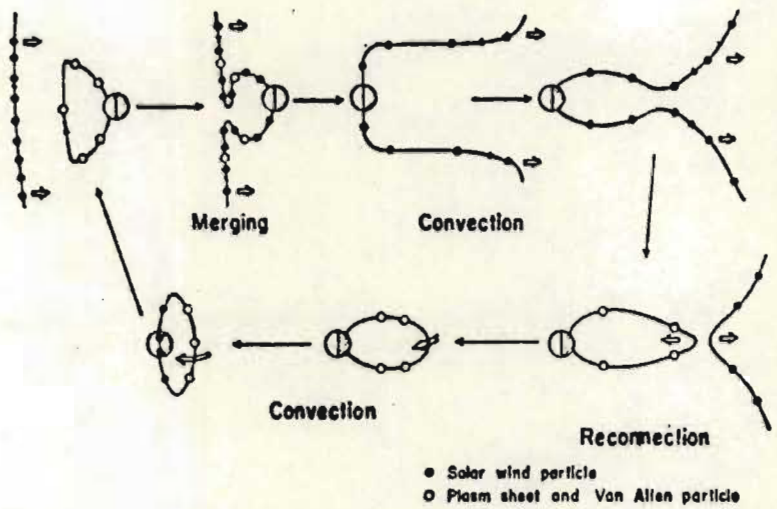

Figure 2.11 Schematic diagram showing merging with the interplanetary field in the midday sector of the magnetosphere, and reconnection in the magnetotail (AKASOFU, 1974)

particle energy. LUI *et al* (1975) investigated the response of the plasma sheet at ∿ 18 R_E to sudden southward turnings of the interplanetary magnetic field. They concluded that the onset of a substorm is associated with a large decrease of pressure in the magnetotail, the so-called thinning of the plasma sheet. However, they found that the sudden southward turning of the interplanetary magnetic field alone does not significantly reduce plasma pressure in the plasma sheet.

2.5.1 The phases of a substorm

ROEDERER (1974) summarised the course of a substorm which proceeds in several phases:

(i) *A growth phase* features a gradual compression of the dayside magnetosphere, a lowering of the dayside cusp latitudes and an increase of the area and magnetic flux encompassed by the polar caps. The magnetic field intensity in the tail increases and the plasma sheet thins, as a result of a transfer of magnetic flux tubes from the dayside magnetosphere to the tail. The resultant accumulating magnetic energy in the tail may be dissipated continuously, but a certain not well established point may be reached where the expansive phase may be triggered by an event such as the southward turning of the interplanetary magnetic field.

(ii) *The expansive phase* includes many effects observable on the ground. The neutral sheet starts collapsing possibly because its current system is redirected along magnetic field lines. The plasma sheet begins to thicken again and the polar electrojet starts flowing in the ionosphere of the auroral zones. It seems that the dawn-to-dusk electric field in the distant magnetosphere becomes enhanced, resulting in the energisation of plasma sheet particles which are precipitated during auroral displays, or injected into the radiation belts.

(iii) *The recovery phase* sets in while the plasma sheet and magnetic field gradually attain a quiet time configuration. It appears, though, that the magnetosphere never fully attains a quiet time configuration, but is always in a state of recovery between substorms. These substorms may occur as isolated events as far apart as several days or they may happen in rapid sequence as often as several an hour.

CHAPTER THREE

WHISTLERS, AURORA AND VLF HISS.

DIAGNOSTIC AIDS IN THE STUDY OF MAGNETOSPHERIC DYNAMICS.

3.1 INTRODUCTION

The plasmasheet and the plasmasphere constitute two important reservoirs of magnetospheric plasma. A relationship between the inner boundary of the plasmasheet and the boundary of the plasmasphere, i.e. the plasmapause, has been indicated by measurements made by satellites. Simultaneous ground-based observations of the plasmapause by means of whistlers, and the inner boundary of the plasmasheet as indicated by diffuse aurora, provides a valuable complement to the satellite work.

Another study that has been the subject of intense research, both experimental and theoretical, is the investigation into the processes by which auroral particles are precipitated into the ionosphere. A modulation of intensity is often found to be superimposed on the gross features of a precipitation event and an integral part of the search for the precipitation process has revolved around trying to locate the source of the modulation. An investigation into simultaneously occurring phenomena such as pulsating aurora and VLF hiss, which are both believed to be manifestations of the modulation processes of precipitating particles, can help locate the source of modulation and also clarify what processes are involved.

This chapter is a review of whistlers, aurora (particularly diffuse and pulsating aurora), and VLF hiss. Emphasis has been given to these aspects which are of particular importance for the work to be described later in this thesis.

3.2 WHISTLERS AND THE PLASMASPHERE

The earth is surrounded by a region of dense thermal plasma of terrestrial origin trapped in near corotation. This region, the plasmasphere, is one where electron densities are of the order of 10^8 to 10^9 el m^{-3}. A magnetic field aligned surface, the plasmapause, separates the plasmasphere from a sparsely populated outer region, the plasma trough, where densities of 10^6 to 10^7 el m^{-3} may be expected. STOREY (1953) and HELLIWELL *et al* (1956) pioneered the use of whistling atmospherics as a means of studying the electron density of the plasmasphere. GRINGAUZ (1963) discovered the plasmapause from satellite observations and CARPENTER (1963) presented a classic paper showing whistler evidence for the plasmapause.

3.2.1 Whistlers

Whistlers are bursts of very low frequency (VLF) electromagnetic energy, which may be received on wide band audio amplifiers. They consist of gliding tones smoothly varying in frequency over a range from 30 kHz at maximum to a minimum of 300 Hz. A typical whistler lasts for one or two seconds and has a maximum amplitude at between 4 and 5 kHz. Usually generated by lightning discharges, whistlers resulting from nuclear explosions have been detected. A lightning stroke is the source of a wide spectrum of electromagnetic energy as an impulse in which all the frequency components present are generated simultaneously. Such impulses cause the typical atmospherics of short wave radio communication, but also present is energy in the VLF or audio spectrum.

Some of the energy is able to propagate around the earth in the earth-ionosphere waveguide, so that it may be received at a distant ground station as a weak, slightly delayed impulse. This is shown in Figure 3.1 where the idealised spectra of the impulses at source point A and conjugate point B are arrowed on the frequency-time insets, or spectrograms.

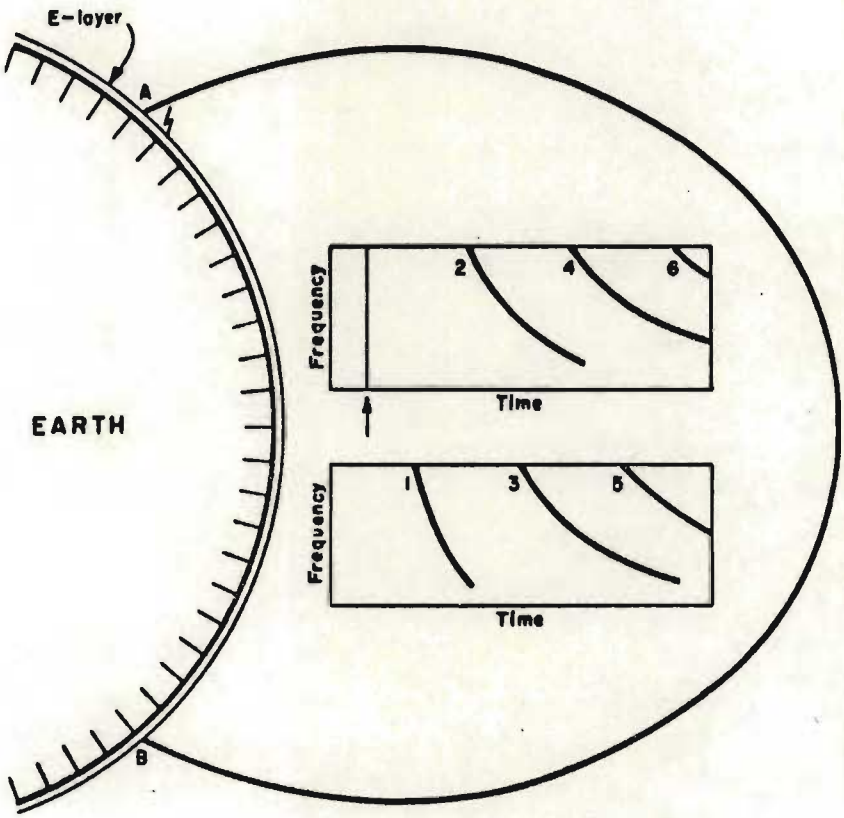

Figure 3.1 Field line path followed by a ducted whistler originating at A. Inset diagrams show idealised spectra of whistler echo trains at conjugate points A and B

(HELLIWELL, 1965)

Part of the VLF energy penetrates the ionosphere somewhere in the vicinity of the discharge. Field-aligned enhancements of ionisation provide ducts along which the energy propagates in the whistler mode to the conjugate point (SMITH, 1961). Part of the energy can leak out of the ionosphere where it is recorded on a spectrogram at Station B as whistler 1 in Figure 3.1. If some of the energy is reflected back along the duct it may be recorded at A as a two-hop whistler, 2. In this manner whistler echo trains e.g. 1,3,5... or 2,4,6.... in the diagram may result from a single discharge, the signal becoming more dispersed with each traverse.

The VLF radio waves characteristic of whistlers, propagate along field aligned ducts with a group velocity V_g given by

$$V_g = \frac{2C\, f^{\frac{1}{2}}\, (f_H - f)^{3/2}}{f_H\, f_o} \qquad (1)$$

where C = velocity of light in vacuum

f = wave frequency

f_H = gyrofrequency

f_o = plasma frequency = $9\sqrt{N}$ when f_o is given in kHz

N = electron density in el cm^{-3}.

The maximum value of V_g occurs for $f = f_H/4$ and V_g becomes zero for $f = 0$ and $f = f_H$. However, SMITH (1961) showed that the upper cut-off frequency for whistler propagation is approximately $f_H/2$, determined by trapping conditions of whistler energy in ducts.

HELLIWELL (1965) gave a detailed theory of whistlers. The difference in time between the originating lightning discharge in one hemisphere and the reception of a given frequency in the opposite hemisphere is referred to as the propagation delay t(f). It is obtained

by integrating $^1/V_g$ along the duct:

$$t(f) = \int_{path} (^1/V_g) \cdot ds. \qquad (2)$$

$$t(f) = {}^1/2C \int_{path} \frac{f_o \, f_H}{f^{\frac{1}{2}} \, (f_H - f)^{\frac{3}{2}}} \cdot ds. \qquad (3)$$

The dependence of the group velocity on the wave frequency leads to the dispersion of the impulsive originating signal into the pure gliding tones characteristic of well defined whistlers.

Several ducts may be 'illuminated' by a single lightning discharge to produce a multi-component whistler group as in Figure 3.2, which is a spectrogram of a whistler recorded at SANAE. As shown in Figure 3.2, a typical multi-component whistler group contains high latitude components with noses, and lower latitude components without noses. Either the noses of the lower latitude components lie above the whistler cut-off frequency $f_H/2$ or they fall out of the spectrogram range. As expected from expression (3) the noses show a smooth fall-off in frequency f_n with a smooth increase in propagation delay t_n. As the propagation paths become longer as for higher latitude ducts, so f_n falls as f_H falls in association with weakening magnetic field strengths. Evaluation of the whistler integral (3) requires the specification of an electron density distribution model and a magnetic field model. These will be discussed in 3.2.3.

3.2.2 Information obtained from Whistlers

The minimum magnetic field strength and the electron density distribution along a whistler duct determine the shape of the characteristic whistler spectrogram. A well-defined component provides information such as the radial distance at which its path of propagation

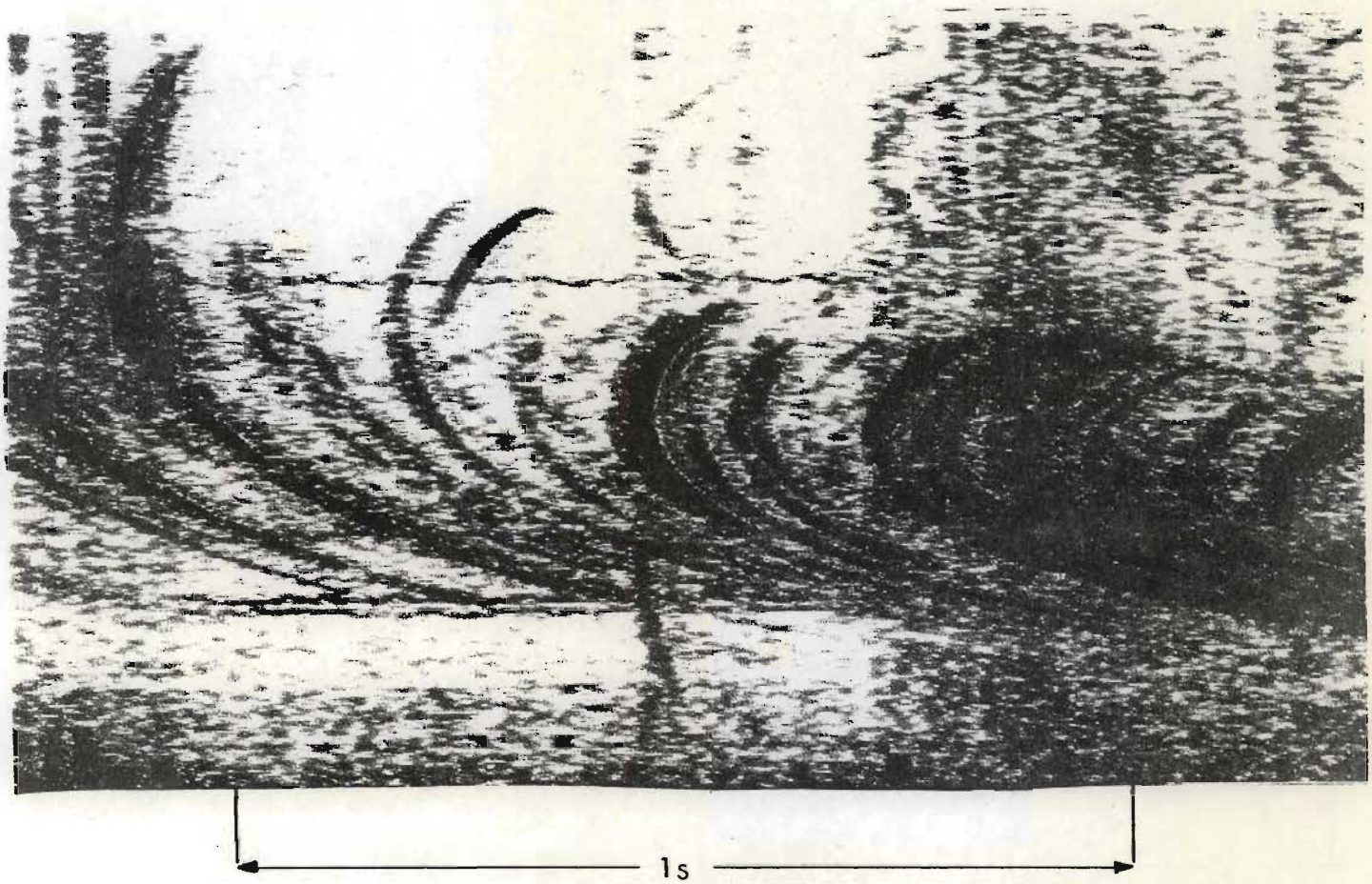

Figure 3.2 Spectrogram of a typical multicomponent whistler recorded at SANAE

intersects the equatorial plane, and the equatorial electron density encountered. The minimum electron cyclotron frequency, a function of minimum magnetic field intensity, determines the component's nose frequency, (if a nose is present). The dispersion and delay of the component are determined by the electron density distribution along the path, and its length. The propagation delay is proportional to the square root of the density weighted inversely as the square root of the magnetic field. Thus the high electron densities occurring over a short distance in the ionosphere,where the magnetic field is strong, make only a small contribution to the propagation time.

The whistler properties most readily obtained from a spectrogram such as that shown in Figure 3.2 are nose frequencies (where noses are present), and propagation delays of the noses if the position of the initiating impulse, or causative sferic can be found. As can be seen from the background of atmospherics in Figure 3.2 the identification of the initiating sferic,if it is indeed recorded, may be difficult. CARPENTER (1959) outlined a number of methods to determine the initiating sferic from spectrograms. Frequently both the initiating sferic and the nose are absent. Curve fitting techniques for deducing the initiating sferic position and the nose frequency were presented by RYCROFT and MATHUR (1973) and HO and BERNARD (1973), based on the whistler group delay fitting formulae of DOWDEN and ALLCOCK (1971) and BERNARD (1973) respectively.

A full discussion of these methods is beyond the scope of this thesis and the reader is referred to WOODS (1974) and WALKER and DEANE (1974) for critical reviews of methods of whistler analysis.

3.2.3 Electron density distribution models

In the evaluation of the whistler integral of Section 3.2.1 it is customary to assume a model for the distribution of electrons along the ducts. ANGERAMI and CARPENTER (1966) made a study with the object of finding models in accord with the experimental data then available. They pointed out that the results were insensitive to the model chosen in the case of equatorial profiles within the plasmasphere, but that the investigation of the distribution of ionization near the plasmapause required choice of the correct model. It was concluded that within the plasmasphere a diffusive equilibrium model is appropriate and that beyond the plasmapause a collisionless model with electron density inversely proportional to R_E^{-4} should be used.

PARKS (1972) provided a review of methods of determining plasmaspheric parameters from nose whistlers. He derived formulae for the calculation of whistler paths in terms of L-value, equatorial electron density, electron density at 1000 km altitude, and total electron content of a flux tube. He presented four diffusive equilibrium models (allowing for different temperature and ion composition values), a collisionless model and a hybrid model.

3.2.4 The effect of the ring current on whistler propagation

The earth's magnetic field may be approximated by that of a centred dipole in the evaluation of the whistler integral relationship (Section 3.2.1) for magnetically quiet periods. There is, however, a departure from dipolar conditions during geomagnetic storms, due to an enhanced ring current in the equatorial plane. Charged particles are injected deep into the magnetosphere near the equatorial plane where they become trapped and drift around the earth as a ring current. FRANK (1967) found that the protons in the 3-50 KeV range predominantly contributed to the energy density of the ring current. During the main

phase of a substorm the ring current is situated at between 3 and 4 R_E and is an order of magnitude more energetic than the quiet time ring current situated at 6 to 7 R_E.

SPREITER and BRIGGS (1962) considered the effect of the ring current on whistler propagation, and in a theoretical study they showed that the dispersion and time delay of high latitude whistlers would be increased by an enhanced ring current. SAGREDO and BULLOUGH (1972) found that both the nose frequency and the nose propagation delay of a whistler component, change with changing ring current. They found further, that the relationship between the whistler nose frequency, the equatorial distance of its path of propagation, and the geomagnetic latitude at which the field line is anchored, is altered by ring current distortion of the magnetic field. Four cases equivalent to four different values of magnetic depression, D_{ST}, ranging from -25 nT for the first case to -128 nT for the fourth case, were considered at the earth's magnetic equator. Reproduced in Figure 3.3 are graphs showing nose frequency versus equatorial distance for the dipolar field case and for the four levels of ring current distortion. The curves are for the winter night ionosphere. The top graph shows the case of the diffusive equilibrium model of electron distribution along a duct and the bottom graph applies to the collisionless model. It may be seen from Figure 3.3 that the effect of ring current distortion is maximum at about 4,5 R_E. The required correction for ring current distortion corresponding to an observed value of D_{ST}, may be read off the appropriate curve of Figure 3.3.

MATHUR *et al* (1972) discussed the ring current effect on electron density profiles derived from plasmapause whistlers. They concluded that the effect is significant beyond the plasmapause, noticeable at the plasmapause, and insignificant inside the plasmasphere. They pointed out that when the ring current is taken into account, the electron density

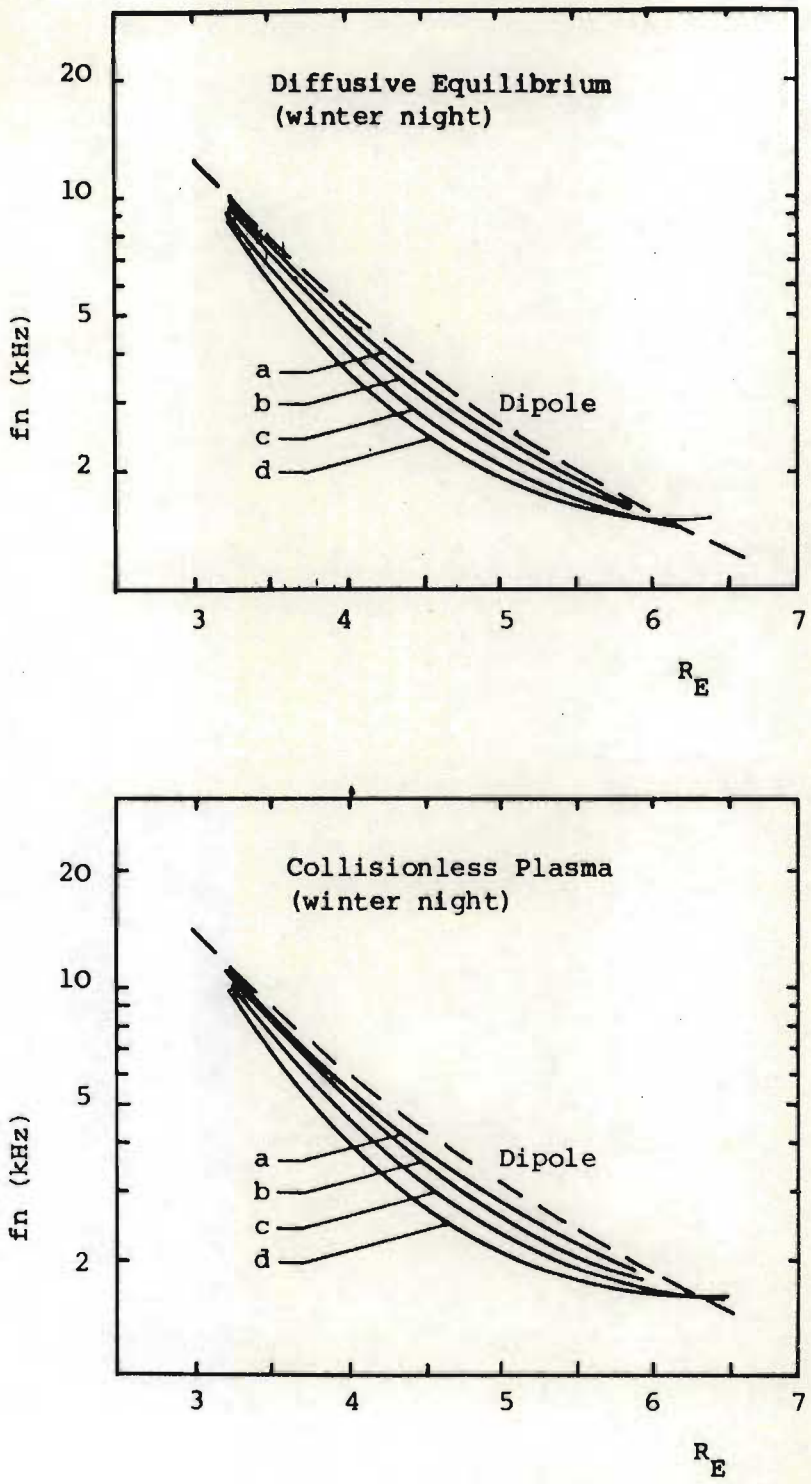

Figure 3.3 Graphs of whistler nose frequency vs equatorial distance for 'dipolar' whistlers (----) and 'ring current' whistlers (——). a,b,c,d represent the four cases where D_{ST} = -25 nT to D_{ST} = -128 nT

(SAGREDO and BULLOUGH, 1972)

change at the plasmapause is increased. As corroborated by satellite measurements, this makes the plasmapause even more pronounced during storms.

The foregoing discussion may be summarised by repeating that, during geomagnetically disturbed times whistler results for propagation path and electron density in the equatorial plane must be corrected for the departure from geomagnetic dipole conditions. The maximum correction to propagation path applies to paths in the vicinity of 4,5 R_E. Electron density corrections are negligible within the plasmasphere but significant beyond the plasmapause.

3.2.5 Morphology of the plasmasphere and plasmapause

It was believed prior to the early 1960's that the ionization density in the magnetosphere fell off relatively smoothly with increasing radial distance from the earth. In 1962 a report appeared describing satellite measurements which detected a boundary to the 'ionized gas envelope of the earth' (GRINGAUZ, 1963). Knee whistler evidence (CARPENTER, 1962) indicates two separate regions in the near-earth magnetosphere. The inner region, or plasmasphere, contains high density thermal plasma. It is separated from the outer region or plasma trough, where densities are from one to two orders of magnitude lower, by a magnetic field aligned density gradient, the plasmapause. In quiet conditions the gradient is less steep (the density difference appears over about 0,8 R_E) than in conditions of high activity where the extent of the plasmapause may be 0,1 R_E as shown in Figure 3.4.

Whistler evidence (CARPENTER, 1966) and satellite measurements (CHAPPELL, 1972) have established the plasmapause as a permanent feature of the magnetosphere, with day-to-day repeatability. It forms a doughnut shape shell which encircles the earth and is symmetrical with respect to

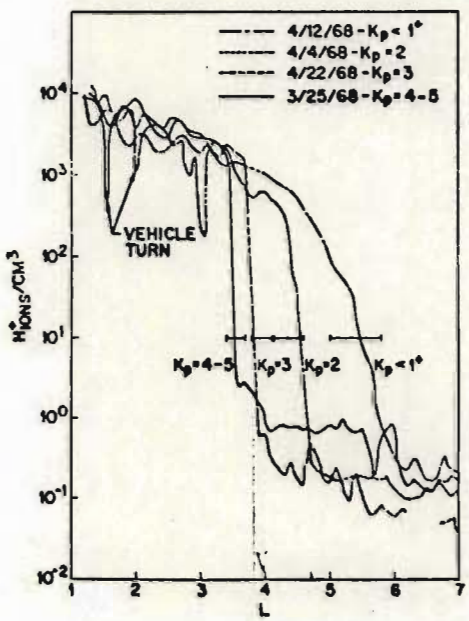

Figure 3.4 A composite graph showing the reaction of the plasmasphere in the nightside region to changes in the level of magnetic activity as measured by OGO 5. The plasmapause steepens and moves to lower L-values with increasing activity (CHAPPELL, 1972)

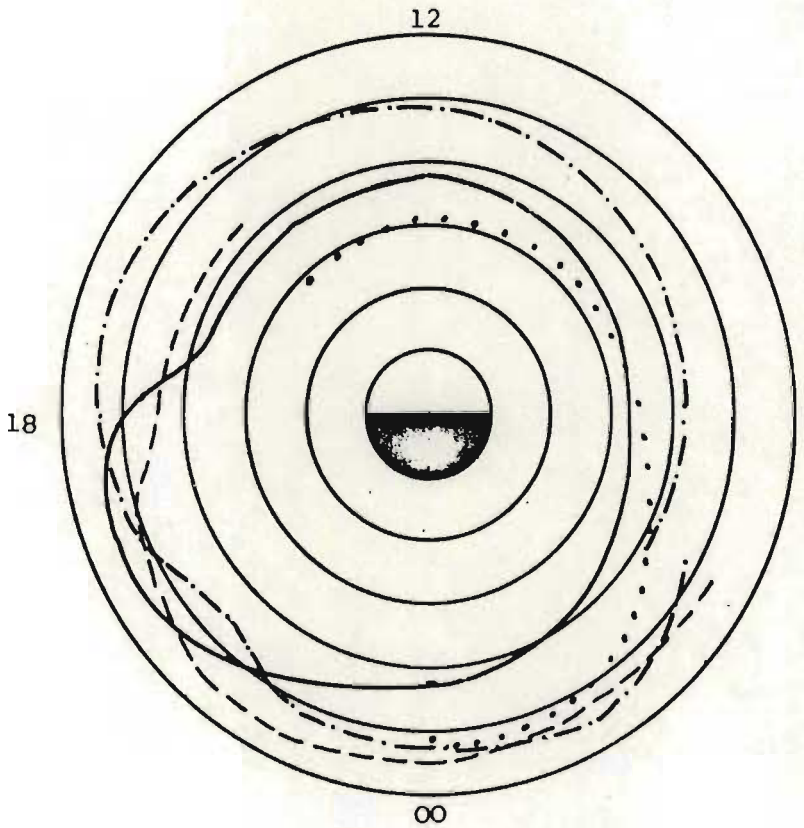

Figure 3.5 Equatorial cross-section of the plasmasphere:

Moderate steady state plasmapause K_p = 2 - 4 (———)

Plasmapause profile with decreasing activity (– – –)

Plasmapause profile with increasing activity (·····)

(CARPENTER, 1966)

Quiet time plasmapause with double bulge (–·–·–)

(RABE and SCOURFIELD, 1975)

the geomagnetic equatorial plane. The plasmasphere corotates with the earth and undergoes positional changes according to local time, and erosions and additions according to magnetic activity. In equatorial plane cross-section as shown in Figure 3.5, the plasmasphere exhibits a dawn to dusk assymetry in that it bulges outwards on the dusk side. Figure 3.5 shows the average position of the plasmapause as determined by whistlers (during a period of constant, steady magnetic agitation when K_p varied from 2 to 4) as given by the solid line (CARPENTER, 1966).

The plasmapause (solid line in Figure 3.5) is observed to move inwards during the period midnight to 0300 LT. The changing character of whistler components indicates that whistler ducts also move inwards suggesting a compression of the plasmasphere rather than an erosion of plasma. During the 1800 LT sector CARPENTER (1966) found that the observed outward movement of the plasmapause, to accommodate the dusk bulge region shown in Figure 3.5, was caused not by the expansion of the plasmasphere in that ducts convected outwards, but by the addition of 'new' plasma which tacked on to the plasmasphere at the dusk sector. Also illustrated in Figure 3.5 is the response of the plasmapause to changes in magnetic activity. The dotted line shows the inward movement of the plasmapause on a particular occasion involving increasing magnetic agitation. The dashed line shows an example of decreasing agitation.

When magnetic activity increases, the plasmapause moves to lower L-values, but retains a bulge region which rotates sunwards so that its onset occurs well before 1800 LT (CARPENTER, 1970). With decreasing magnetic activity the bulge region rotates towards the midnight sector and becomes less pronounced. The plasmapause moves to higher L-values and has been observed to extend almost symmetrically out to 6 or 7 R_E.

CARPENTER (1966) found evidence for a double bulge, the first occurring in the midday sector and the main one occurring in the evening

sector. RABE and SCOURFIELD (1975) made a quiet time whistler study of duct convection patterns following a period of moderate activity. They found a double bulge, with the first bulge occurring in the dusk sector, and the main one in the midnight sector, as indicated by the dotted-and-dashed line of Figure 3.5. They also showed that their bulge regions are not 'new' plasma, because whistler ducts convect outwards in the bulge regions.

3.2.6 Satellite observations

CHAPPELL (1972) presented a comprehensive review of satellite observations of the plasmapause. He found that the nightside region between 2200 and 0600 LT is characterised by the close correlation between plasmapause position and K_p. A number of typical plasmapause profiles are plotted in Figure 3.4 for various levels of magnetic activity. It may be seen that the plasmapause steepens and moves to lower L-values with increasing activity.

Study of the dayside region (0600 - 1500 LT) gave the important result that the plasmapause location in this local time sector depends on the value of K_p during the formative period of the previous night. Thus once a sector of plasmasphere has rotated past dawn, the plasmapause location is fixed regardless of the subsequent development of magnetic conditions.

In the dayside region, filling of plasmasphere flux tubes takes place from the underlying ionosphere. CHAPPELL (1972) presented evidence which was consistent with an upward flux of 3×10^8 ions cm^{-2} s^{-1} through the 1000 km level. This figure agrees with whistler observations (PARKS, 1970). CHAPPELL (1972) observed regions of detached plasma throughout the dayside plasma trough, but most often in the afternoon dusk sector. Most of the detached regions appeared after moderate to

high magnetic activity.

Ion density profiles in the bulge region (1500 - 2000 LT) were seen to exhibit an R_E^{-4} dependence. With increasing magnetic activity the bulge was observed to move inwards to lower L-values and the plasma outside the bulge appeared to be depleted or 'peeled away' during high K_p. In the following section some plasmapause formation theories are considered.

3.2.7 Magnetospheric plasma convection models

Present theories on the formation of the plasmapause stem from a magnetospheric convection model proposed by AXFORD and HINES (1961). They considered the possible bulk motion impressed on magnetospheric plasma by a viscous interaction with the solar wind at the magnetospheric boundary. Their model is represented in Figure 3.6 which shows a continuously circulating flow of plasma in a closed magnetosphere. The flow pattern comprises an anti-sunwards movement inside the boundaries of the magnetosphere and a sunwards movement through the inner magnetosphere to complete the flow pattern. Imposing the effect of the earth's rotation on the convection pattern of Figure 3.6, several important features become apparent as shown in Figure 3.7. The features to be noted are the boundary shell A, inside which no traverse convection takes place, the region of stagnation B and the bunching up of convection flow lines on the late night-to-dawn side of the forbidden region A. This bunching opens out again towards the afternoon sector. The existence of the plasmapause was not known when this model was proposed and subsequently the forbidden region A become identified with the plasmasphere and the stagnation region B with the bulge region. Also consistent is the identification of the bunching of convection lines with the diurnal post-midnight compression of the plasmasphere.

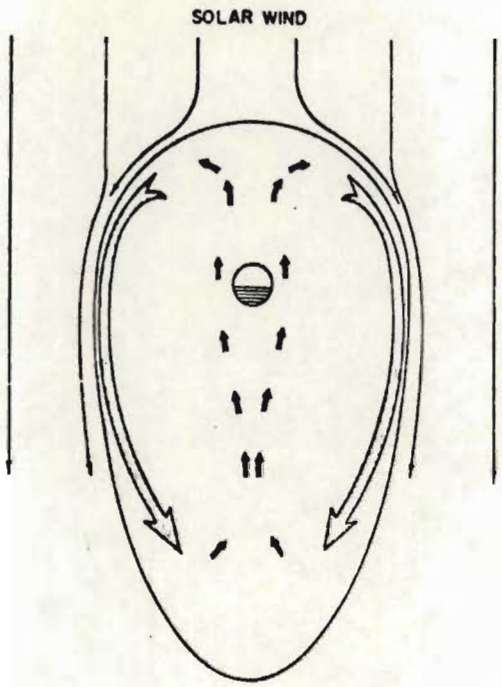

Figure 3.6 The motion imposed on the magnetospheric plasma by a viscous interaction with the solar wind (AXFORD and HINES, 1961)

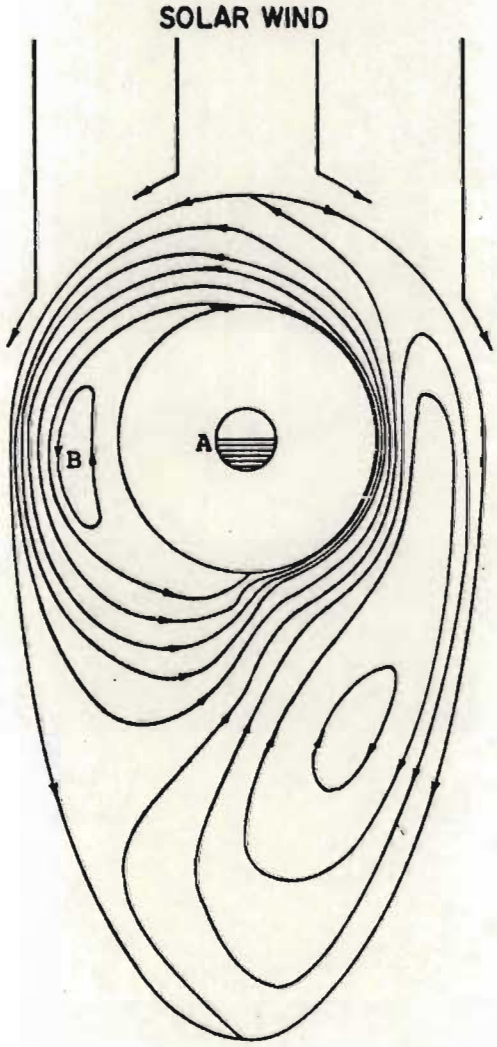

Figure 3.7 When the effect of the earth's rotation is impressed on the model of Figure 3.7, a composite motion appears as above, with a forbidden region A and a stagnation region B (AXFORD and HINES, 1961)

After the discovery of the plasmapause, NISHIDA (1966) extended the model of AXFORD and HINES (1961) to explain its formation. He assumed an open magnetosphere in which high latitude field lines, which are closed on the dayside, are swept back into the tail in the late afternoon and reconnected in the post-midnight sector. An importance consequence of this open model was that plasma could diffuse along the open field lines, so depleting the inner regions of plasma. The rate of replenishment of plasma from the ionosphere during the day when these field lines were closed, would be insufficient to establish the high density levels such as existed on field lines which had remained closed for a week or more. An interpretation of the plasmapause was thus to be the boundary between field lines which remained closed all the time and those field lines which, as part of the general convection pattern, have recently come in from the tail.

The predicted behaviour of NISHIDA's plasmapause model and CARPENTER's whistler results compare favourably, particularly as far as response to K_p is concerned. ANGERAMI and CARPENTER (1966) showed that the plasmasphere to plasma trough electron density ratios varied from a maximum of about 30 - 100 between 0100-0400 LT to a minimum of about 10 on the dayside. This is consistent with a gradual filling of plasma trough field lines during the day which had been open the previous evening.

KAVANAGH *et al* (1968) presented a mathematical model of magnetospheric convection in the equatorial plane. They superimposed a large scale uniform electric field on the geomagnetic field to represent sunwards plasma flow from the tail, and included a corotation electric field in the plasmasphere. They arrived at a dawn-to-dusk electric field of approximately 0,3 m Vm^{-1} to form a forbidden zone, (to sunward convection of thermal plasma), the size and shape of the

plasmasphere. A qualitative agreement with this model was indicated by CHAPPELL (1972). Figure 3.8 shows equatorial flow paths within the magnetosphere. Dotted lines indicate convection paths around shells of closed field lines within the plasmasphere, dominated by corotation, and dashed lines show the flow directions of flux tubes dominated by sunward convection. The flow lines are equivalent to electric equipotential curves on the equatorial plane. All magnetic field lines passing through a given curve define an equipotential surface, so that the plasmapause separates the set of closed equipotentials from the set of open equipotentials.

The flux tubes within the plasmasphere corotate concentrically to about 2,5 R_E as shown in Figure 3.9. Beyond 2,5 R_E the bulge region affects their course through the afternoon and dusk sectors so that the flux tubes or ducts move to higher L-values with associated volume increases. CHAPPELL (1972) showed that such behaviour, combined with dayside filling from the ionosphere, should result in an R_E^{-4} fall-off of plasma density in the plasmasphere beyond 2,5 R_E in the bulge sector. The experimental measurement of this profile in the dusk sector,but not in other LT sectors,supports the model of KAVANAGH *et al* (1968).

The sharp tip of the bulge as shown in Figure 3.8 is a stagnation point where the convection and corotation fields cancel. It is likely that a shear mechanism brings about a breakdown in strict corotation along the plasmapause with the greatest shear effect caused in the bulge at the stagnation point.

Because the convection electric field is enhanced with increasing magnetic activity, the plasmapause moves inwards. The outer flux tubes that were corotating under quiet condtions are therefore convected away from the plasmasphere. CHAPPELL (1972) detected regions of detached

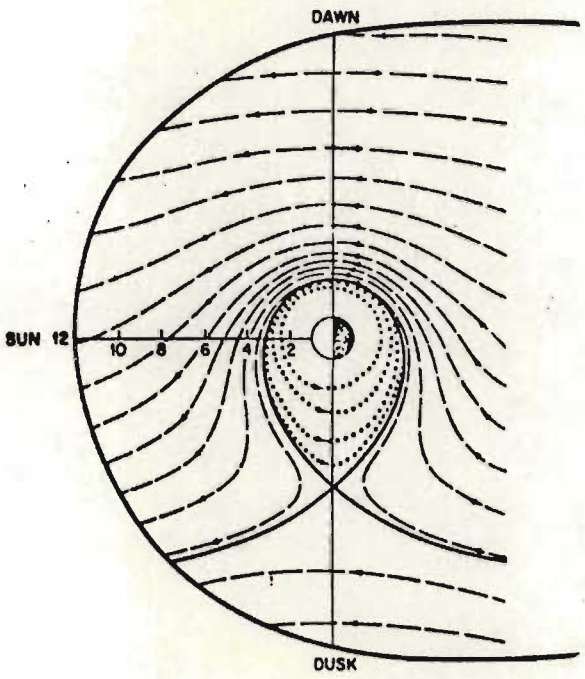

Figure 3.8 The equatorial flow paths within the magnetosphere of magnetic tubes of force containing thermal plasma. The dashed lines indicate convectional flow, the dotted lines corotational flow
(CHAPPELL, 1972)

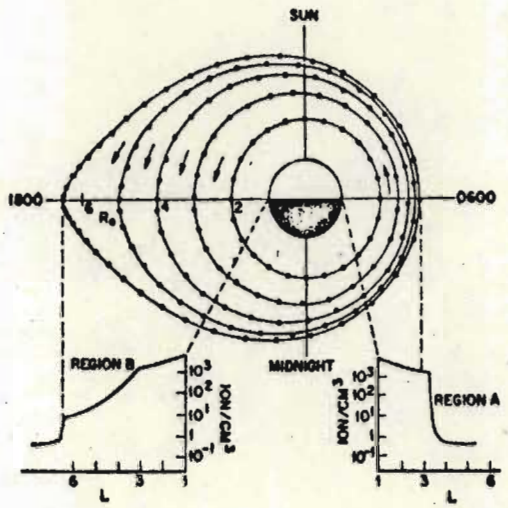

Figure 3.9 The motion of the flux tubes inside the plasmasphere. The distance between dots gives the approximate drift distance of the flux tube in one hour. The expansion in the dusk region transforms the sharp profile at L = 3 and L = 6,5 in region B (CHAPPELL, 1972)

plasma that appeared to have been 'peeled away' from the plasmasphere with increasing magnetic activity. With quietening magnetic conditions flux tubes that have just convected earthwards from the tail become captured in corotation, and gradual filling from the ionosphere takes place. Thus the recent storm time plasmapause may be observable for some time, until the outer regions to the new plasmapause position have filled to comparable density levels. Such double boundaries have been observed (CHAPPELL, 1972).

3.2.8 The dawn-to-dusk electric field

The existence of a large scale electric field directed from dawn to dusk across the magnetosphere is predicted by magnetospheric models. This electric field results from the combined effect of georotation and the solar wind - magnetosphere interaction. The electric field also changes with changing magnetic activity. CHEN and WOLF (1972) computed the effects of such changes on the plasmapause. They found that a single sudden decrease in the convection electric field (a reduction of magnetic activity) causes the region of strict corotation to expand, so that flux tubes that were moving in from the tail become trapped and commence filling from the dayside ionosphere. The filling rate is sufficiently small that the boundary of the original plasmapause remains evident for a week or so. Following the decrease in the convection field the relatively stronger corotation field causes the bulge to rotate towards the night sector and the plasmapause becomes nearly circular. This result is consistent with observations of CARPENTER (1970). CHEN and WOLF (1972) found that if the quiet conditions persist, the duskside bulge remnant wraps itself around the midnight sector as a tail which, as time progresses, becomes thicker in the dusk sector as shown in Figure 3.10. Detached regions of plasma have been observed in the evening sector by satellites (CHAPPELL, 1974) but no evidence of longtails has as yet been found. CHEN and WOLF (1972) also computed the effect of various regular and irregular changes in the convection

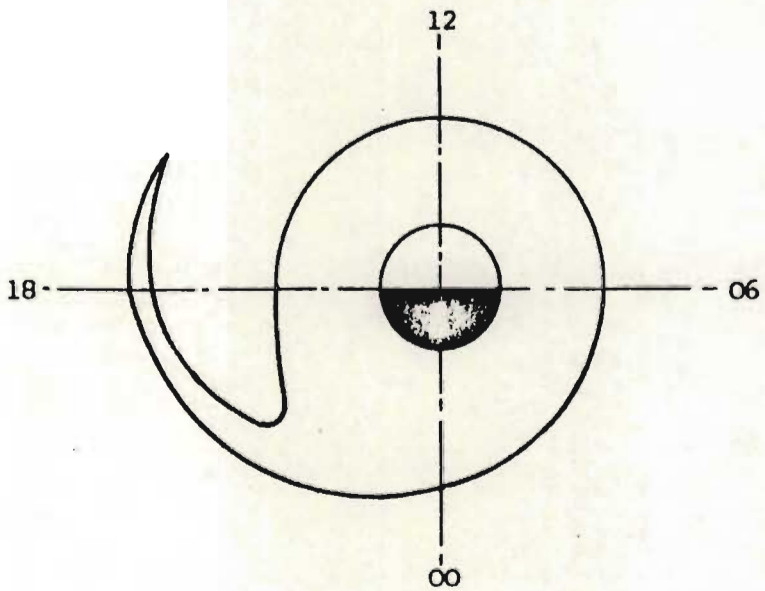

Figure 3.10 Theoretical distortion of the plasmapause to form a tail, shown on the 5th day after the causative decrease in the convection field
(Adapted from CHEN and WOLF, 1972)

electric field and,they show that a spatially uniform, 'gusty', westward electric field leads to a reasonably good agreement with the observed plasmapause shape.

3.2.9 Summary

The plasmapause exhibits predictable response to changes in magnetic activity abd is a permanent feature of the magnetosphere. Ground based whistler observations and *in situ* satellite probes have been used to investigate it. To account for its formation, several theories have been developed but the compexity of magnetospheric processes has precluded the development of complete theories.

The points pertinent to work appearing later in this thesis are:

(i) Well-defined whistler components provide information as to the equatorial radius of their ducts of propagation and equatorial electron density in the ducts.

(ii) A diffusive equilbrium model of electron density is appropriate within the plasmasphere. Beyond the plasmapause a collisionless model behaving as $N_e \propto R_E^{-4}$ should be used.

(iii) A centred dipole magnetic field model which is used in the whistler calculations is appropriate for quiet magnetic conditions, therefore corrections must be made to the whistler results for disturbed conditions.

(iv) The plasmapause is a magnetic field aligned surface representing the boundary between the dense thermal plasma of the plasmasphere and the tenous thermal plasma in the plasma trough.

(v) The plasmapause exhibits a dawn-dusk assymetry in that it bulges outwards on the dusk side.

(vi) Under the onset of quiet magnetic conditions the plasmapause

expands and under disturbed conditions it can contract to L < 3.

(vii) The plasmasphere corotates with the earth except, possibly, at high latitudes, where shear effects may become evident.

3.3 Auroral morphology

The visual aurora consists of emissions from sources at heights between 100 and 200 km above the earth. Such emissions are usually horizontally distributed in arcs and bands aligned, approximately, geomagnetic E-W. Their longitudinal extent is for hundreds of kilometres with horizontal widths of 10-20 km. Field aligned structure in the form of rays is often apparent and may extend for some tens of km upwards. The auroral zones, defined as the regions of maximum occurrence probability for auroral activity, lie about the circumferences of circles of approximately 22° radius centred on the geomagnetic poles. In addition to light, the auroral production mechanism generates; X-ray emission detectable down to balloon altitudes, VLF radio emissions detectable on the ground and by satellites above the aurora, high levels of ionization detectable by radar and heating of the auroral ionosphere.

3.3.1 The auroral oval

On basis of IGY all sky camera observations, FIELDSTEIN (1963, 1964) introduced the concept of the auroral oval. This is a statistically defined region on a geomagnetic latitude - local time plot, where the probability of auroral occurrence exceeds 75%. He specified the probability of auroral occurrence as the ratio of the number of 30 minute time intervals including aurora, within a 60° angle of the zenith, to the total number of time intervals under observation. The geometry of the auroral oval is fixed with respect to the sun and the earth rotates once a day under the oval. The auroral zone is simply the locus of the midnight part of the oval where intense auroral displays are most frequently seen. The location of the N-hemisphere auroral oval is shown

in Figure 3.11 which is reproduced from AKASOFU (1968). The auroral oval shown in Figure 3.11 is the mean oval for the IGY observations. If Fieldstein's concept is applied to subsets of all-sky data for various ranges of magnetic disturbance, it is found that during prolonged quiet periods the auroral oval contracts. During intense geomagnetic storms the auroral oval expands to locations as low as dipole latitude 50^{o} in the midnight sector, (FIELDSTEIN and STARKOV, 1967). The size of the oval is taken to reflect the recent history of magnetic activity.

Most discussion of the oval is limited to the N-hemisphere, but BOND and THOMAS (1970) published a determination of the southern auroral oval and concluded that the mean locations and the equatorward and poleward limits of the auroral ovals are similar in both hemispheres. However, they noted a tendency for the southern auroral oval to show greater broadening for the higher levels of K_p. Figure 3.12 illustrates the change in auroral oval location in the S-hemisphere as magnetic agitation increases.

The auroral oval has been widely accepted as a natural coordinate system (AKASOFU, 1968) for dealing with polar geomagnetic disturbances. EATHER (1973) presented a re-evaluation of the auroral oval in which the concept is shown to have serious limitations in representing characteristics of particle precipitation. He concluded that particle precipitation patterns were a more reasonable basis for any natural coordinate system as most auroral data represented the effect of particles (directly or indirectly). The auroral oval, however, remains a useful concept, particularly for long term observations such as the DSMP satellite auroral imaging data.

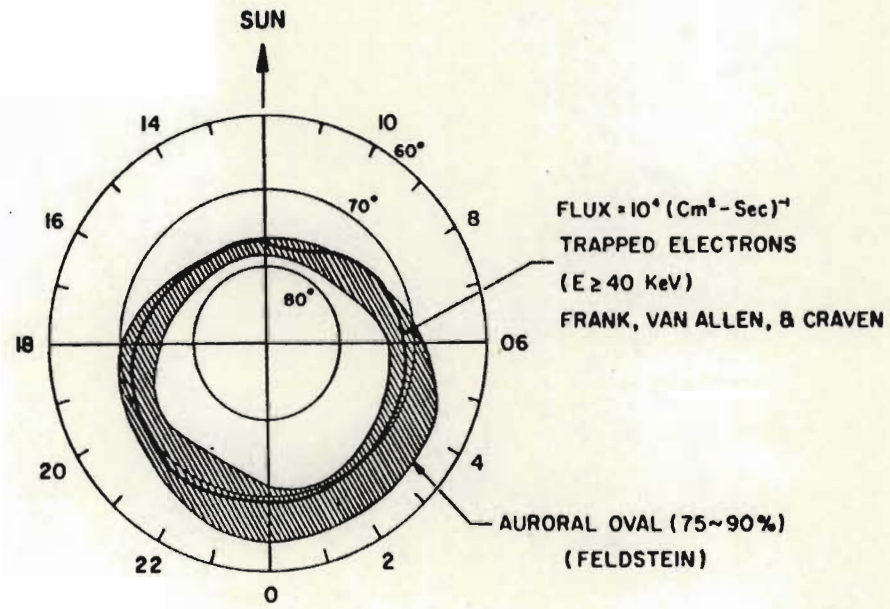

Figure 3.11 The auroral oval and the outer boundary of the trapping region

(AKASOFU, 1968)

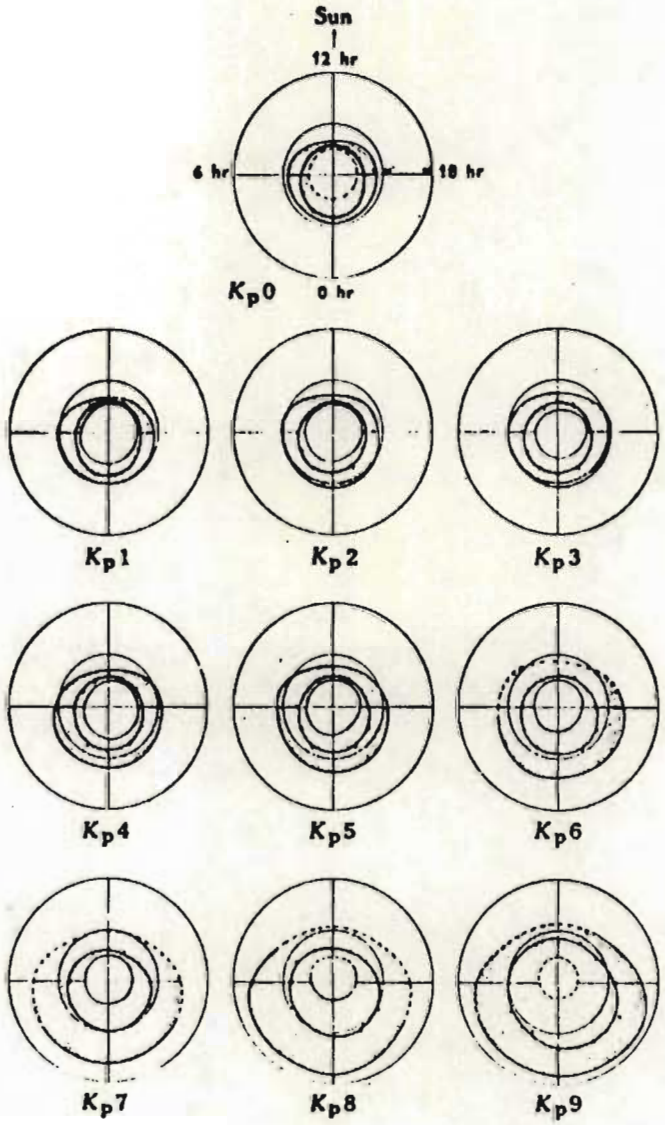

Figure 3.12 Smoothed mean locations of the southern auroral oval together with its inner and outer envelopes for K_p = 0 - 9
(BOND AND THOMAS, 1970)

3.3.2 Auroral forms

The many variations in auroral structures and the pattern changes evident during a typical auroral display may be resolved into a few elementary structures.

The *quite arc* is the basic stable auroral form with an elongation approximately geomagnetic E-W. Horizontally, they extend hundreds of km and arcs more than 1000 km long have been observed, (AKASOFU, 1963). MAGGS and DAVIS (1968) showed that auroral arcs with typical widths of 10 km have a fine structure of parallel arc elements of typical width 200 m. The mean altitude of the lower borders of arcs is between 95 and 105 km, (EGELAND and OMHOLT, 1967). The visual colour of a quiet arc is green unless its intensity falls below the colour threshold of the eye, in which case the sensation is usually white. A transition from the quiet arc to an active form takes place when field aligned rayed structure and/or distortion of the lower border becomes evident. A *rayed arc* has rays present yet the lower border is not distorted. HALLINAN and DAVIS (1970) found that arc elements often form tightly wound cylindrical field aligned forms which they called *curls*. When seen from the side, curls undoubtedly constitute rays which are spaced at 2 to 10 km intervals with horizontal extents of 200 to 300 m.

When the lower border becomes distorted it is termed a *homogeneous band* which becomes a *rayed band* when rays are present. Distortions in the lower border propagate simultaneously East to West and West to East along the band and on occasions the quiet arc becomes rayed along its entire length. Green homogeneous bands occur at a mean height of 100 km. The presence of a red lower border indicates an altitude of 80 - 100 km while an overall red appearance may mean that the lower border is at 250 km. However these occur rarely and a height of 100 km is usually assumed for auroral bands.

Rays may also be seen in patches isolated from bands. Their vertical extent can vary from a few tens to several hundred km (OMHOLT, 1971) and they are always field aligned. Distortion or folds, and rays may propagate along the length of a band with measured velocities of up to 50 km s^{-1} (OMHOLT, 1971). Colour appearances may be the same as for homogeneous bands and intensities vary from subvisual to bright levels capable of casting distinct shadows. (See Section 4.3.1).

Coronas occur when auroral forms with vertical extent (rays or folded bands for example) appear in the magnetic zenith which is indicated by the perspective convergence of the auroral structure along magnetic field lines.

Diffuse aurora usually appears as an extensive homogeneous area of faint luminosity covering much of the field of view. Its equatorward and poleward edges are often sharply defined depending on the position of the observer relative to the diffuse aurora. It may exhibit a patchy structure or polewards extending structure (AKASOFU, 1974) in the post-midnight sector. Diffuse aurora is often below the sensitivity threshold of all-sky cameras.

Fast aurora waves are E-W aligned waves of luminosity that often appear to emanate from bands or glows and rapidly travel equatorwards. In appearance they are similar to flaming but, because they propagate horizontally, they are observed to move through the zenith, which is the factor distinguishing them from the field aligned motion of flaming.

Flaming describes waves of luminosity which move rapidly upwards from the base of an auroral form in the direction of the magnetic field lines. It may recur rapidly and affect large parts of the sky. Flaming is usually associated with pulsating surfaces and patches.

Flickering is the term applied to describe the effect when large parts of a display undergo rapid, irregular changes in brightness as if lit by flickering flames.

Pulsating aurora includes intensity pulsations of all the forms reviewed above except, by definition, a quiet arc. They are characterised by quasi-periodic pulsations of periods ranging between 2 s and $^{1}/_{10}$ s. Whole bands may pulsate and pulsating patches are a common occurrence in the morning sector following the break-up phase.

3.3.3 Electron and proton aurora

Whereas aurora resulting from proton precipitation must be diffuse, electron aurora may be either discrete or diffuse. This arises because of two fundamental differences in the behaviour of these particles. For example, 5 keV protons, the radius of gyration in the earth's magnetic field is about 200 m compared with ~10 m for electrons of similar energy. Secondly incident protons spiralling about a field line can capture an electron in colliding with neutral atmospheric particles. This is illustrated in Figure 3.13 which shows the behaviour of a proton spiralling down a field line to capture an electron at which point it is a neutral H-atom. It can now move unaffected by the magnetic field until it loses an electron again through a loss collision. DAVIDSON (1965) showed that a linear sheet of incident 10 keV isotropic protons could be broadened to a distribution with a half width of the order of 100 km.

3.3.4 Auroral substorms

A model describing the development of the auroral substorm was introduced by AKASOFU (1964). Simultaneous all sky camera records from auroral zone locations across Siberia, Alaska and Canada indicated that the aurora shows various active features at different locations. He called the sequence of auroral events over the entire polar regions, during the passage from auroral quiet through the various active phases

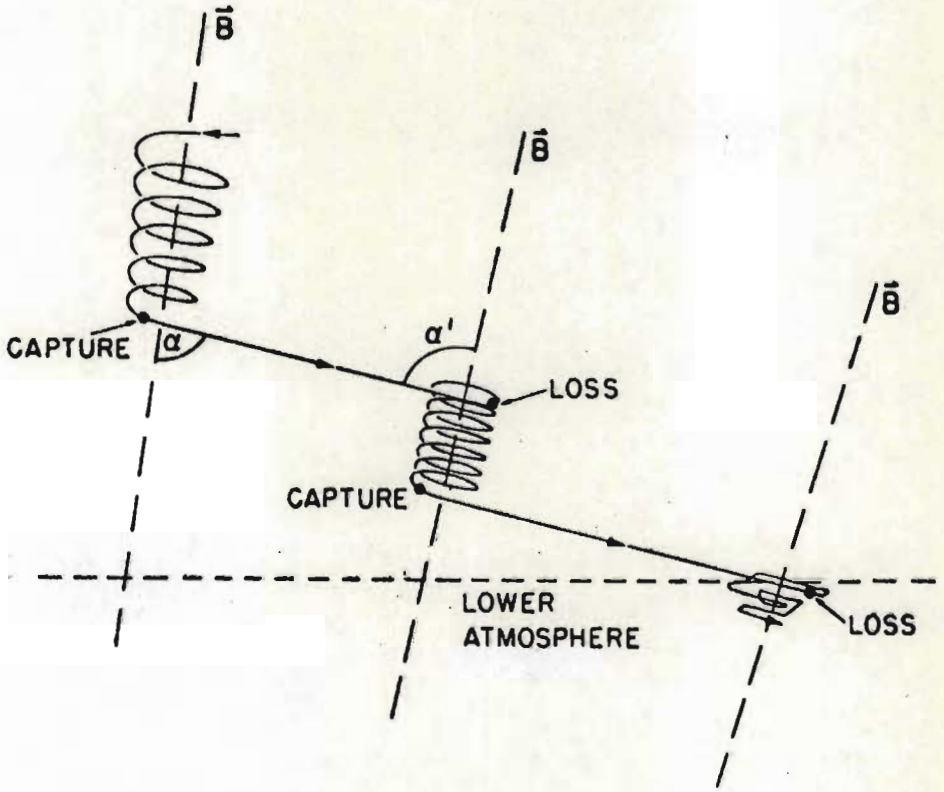

Figure 3.13 **Typical schematic path of a proton entering the atmosphere**

(VALLIANCE JONES, 1974)

to subsequent calm, an auroral substorm.

Each auroral substorm has a life time of 1-3 hr and consists of an expansive phase, lasting 10-30 min, followed by a recovery phase which may take more than 2 hrs before quiet conditions are achieved again. During the course of a day several substorms may take place, sometimes the expansive phase of one commencing during the recovery phase of the preceding substorm.

During a substorm quiet arcs which lie along the auroral oval are activated. The activation usually originates in the local midnight sector of the oval and its effects spread rapidly in all directions. Various characteristic displays occur in different LT sectors of the oval. A schematic representation of a typical substorm is given in Figure 3.14 reproduced from AKASOFU (1964). The six diagrams are plots of dipolar coordinates against local time with the sun at the top of each diagram. Part A of Figure 3.14 shows the quiet situation between substorms. Quiet arcs are arranged around the dark sector of the auroral oval and the so called polar cap auroras are seen to be sun aligned over the pole. Part B is the onset of the expansive phase of a substorm characterised by the sudden formation of an arc or the brightening of an existing quiet arc into a homogeneous band in the midnight sector. In most cases the band moves rapidly polewards forming a bulge in the midnight sector, as shown in part C. The characteristic break-up of an auroral substorm takes place in this bulge with the scattering throughout it of quiet curtain-like forms. Part D is the end of the expansive phase with the bulge expanding E and W. In the evening or west side of the bulge a large scale fold, referred to as a westward travelling surge, propagates with a speed of about 1 km s^{-1}. In the E sector the aurora often disintegrates into patches which drift E with speeds of hundreds of m s^{-1}. When the poleward expanding bulge has attained its highest latitude the recovery phase commences as illustrated in part E, and the bulge begins to contract. The westward travelling surge disintegrates

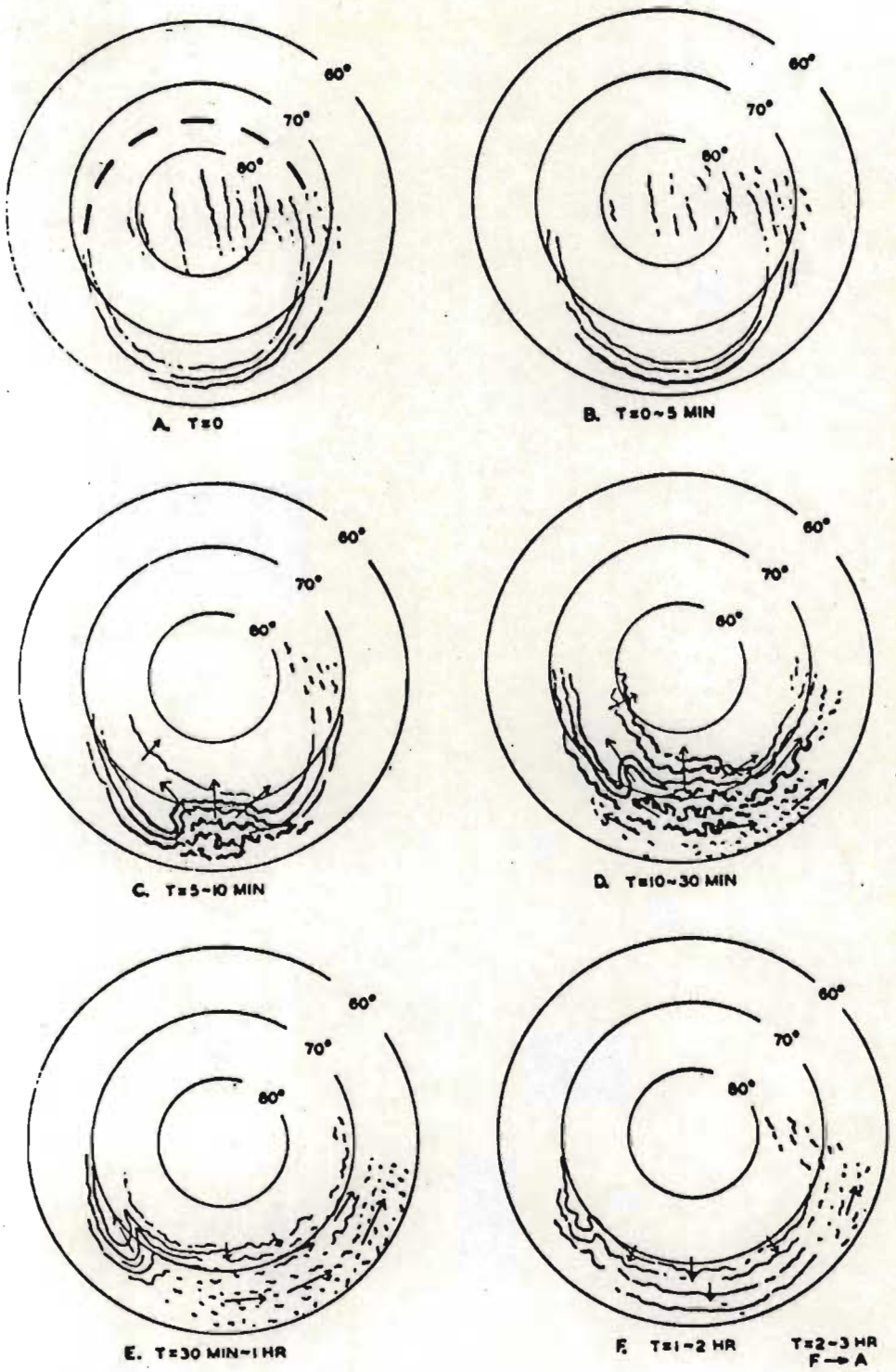

Figure 3.14 The development of an auroral substorm in a dipole-local time coordinate system. The sun is towards the top of the diagram

(AKASOFU, 1964)

into irregular bands and in the morning sector E-drifting patches pulsate and remain until obscured by dawn. The relative timings of the above events are indicated in Figure 3.14.

A typical auroral zone station rotates with the earth under the oval so that it travels under the midnight sector. In this way, depending on magnetic activity and the size of the oval, until about 2100 LT the station will be equatorwards of the oval. Towards the midnight sector it passes under the oval, and from about 0300 LT it will again be equatorwards. Thus an observer will see auroral displays, the nature of which will depend on his location, relative to the midnight sector of the oval, and on the stage of the auroral substorm. For example an auroral substorm occurring at 1900 LT may appear to be just an enhanced glow on the poleward horizon, while a substorm at midnight would appear as a break-up across his whole field of view. When the interplanetary magnetic field is directed northwards there is a decrease in the rate of merging of geomagnetic and interplanetary magnetic field lines. The result is the contraction of the auroral oval to dipole latitude 70° or above. Conversely, the southward directed interplanetary magnetic field leads to expansion of the oval. Most ground-based auroral observations are carried out in the auroral zone. AKASOFU (1975) pointed out that the general conclusion from such observations was that the aurora and its associated magnetic disturbances occurred only when the interplanetary field was southwards directed.

The advent of satellite auroral imaging showed that in fact auroral phenomena were present when the interplanetary magnetic field was directed northwards, but they were beyond the field of view of ground based stations.

3.3.5 Satellite imaging of aurora

Great progress in auroral morphology was made with ISIS-2 scanning photometer studies (LUI and ANGER, 1973) and DAPP/DMSP imaging studies (PIKE and WHALEN, 1974; AKASOFU, 1974). One of the most striking and persistent features of auroral displays as seen from ISIS-2 is a fairly uniform belt of diffuse auroral emission extending along the equatorward part of the auroral oval right around the pole, even when discrete forms are absent. The fact that diffuse aurora did not feature prominently in AKASOFU's (1964) model of auroral substorms is due to its generally low intensity, lack of structure and low contrast. Thus it was not recorded by all-sky cameras.

SNYDER *et al* (1974) tested the concept of the auroral substorm and concluded that the DMSP photographs verified the two important aspects of a substorm; namely auroras in the night sectors undergo intermittent activation and that auroral activity after activation consists of the expansive and recovery phases. However they found a number of important auroral features which were missing in the AKASOFU (1964) pattern of substorm. These include the general behaviour of the diffuse aurora, and the relationship between polar cap auroras and diffuse auroras. Figure 3.15 illustrates the major additions to the substorm model as shown in Figure 3.14. They may be summarized as follows:

(i) Normally satellite observations can distinguish between diffuse and discrete aurora. Diffuse aurora forms an integral part of the auroral substorm.

(ii) In the evening sector diffuse aurora appears as a relatively uniform belt of luminosity with a sharply defined equatorward border.

(iii) After midnight the diffuse aurora degenerates into a patchy structure.

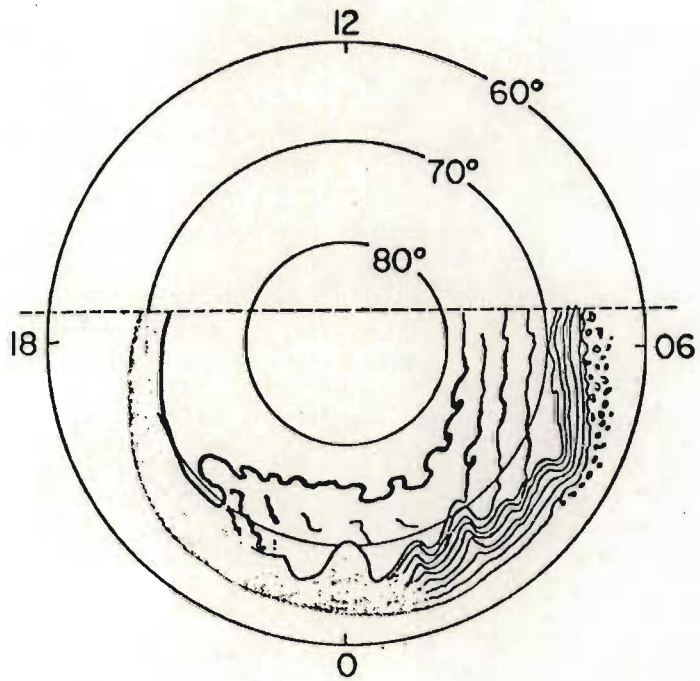

Figure 3.15 Dipole-local time schematic of auroral phenomena occurring near substorm maximum. This diagram summarizes the additional diffuse aurora features seen on DMSP photographs (SNYDER and AKASOFU, 1974)

(iv) In the late morning sector the diffuse aurora develops into a number of discrete aurora.

(v) Certain features are associated with diffuse aurora in the post midnight sector during the expansive and recovery phases. These include patches, large scale wave structures and omega bands.

(vi) Discrete auroral arcs appear to develop from the 'crests' of the wavy structure of diffuse aurora in the morning sector. These sun-aligned auroras often spread over the entire morning half of the polar cap.

(vii) The equatorward boundary of the diffuse aurora is the most stable auroral characteristic during substorms. The transition from the well defined premidnight boundary to the degenerate morning boundary occurs most often in the midnight or early morning sectors.

DMSP satellite photographs reproduced in Figure 3.16 from AKASOFU (1974) illustrate some of the features already discussed. Figure 3.16(a) shows discrete and diffuse auroras. (b) is an example of a poleward expanding bulge with bright diffuse aurora in the evening sector. (c) and (d) show eastward drifting patches in the morning sector and a torch-like diffuse structure respectively.

3.3.6 Characteristics of diffuse aurora

The charcteristics of the diffuse belt of auroras coincide with several well known characteristics of the proton aurora (EATHER, 1967). They are both steady, broad (3°-7° of latitude) regions of diffuse emission equatorward of the discrete electron precipitation in the evening sector. Bright discrete auroras may be superimposed on them. LUI and ANGER (1973) concluded however, that the proton contribution to the diffuse auroras seen from ISIS-2 was minimal. The filters

they used were centred at λ 558,1 nm and λ 391,5 nm with bandwidths of 1,8 and 2,6 nm respectively. Further they stated that the observed intensities of the diffuse aurora at λ 557,7 nm (1-2 KR at quiet times to 5 KR during a substorm are too high to be accounted for by proton precipitation , and the measured ratio of intensities of λ 391,4 nm emission to λ 557,7 nm emission indicated that the diffuse aurora was not dominantly proton excited. They concluded that the proton aurora (EATHER, 1967) and the mantle (electron) aurora (SANDFORD, 1964; 1968) together constitute the diffuse aurora in the midnight sector.

On the other hand, FUKUNISHI (1975) in his investigations of the dynamic relationship between proton and electron auroral substorms, found that the diffuse precipitation in the evening sector consists only of proton precipitation (H_β intensity 10-30 R constant over the evening and morning sectors) and that electron precipitation appears only in the postmidnight sector of the diffuse aurora. He found that the equatorward edge of the proton diffuse aurora in the evening sector moves equatorwards at 200 - 300 m s^{-1} on the initiation of the expansive phase of a substorm.

3.3.7 Morphology of the diffuse aurora

Satellite observations (LUI and ANGER, 1973; SNYDER and AKASOFU, 1974) have identified two diffuse and broad bands of luminosity. One of these is a quasi-circular belt, centred on the geomagnetic pole approximately along the line L = 6 and the other is an oval belt, partially overlapped with and located slightly equatorwards of the discrete auroral oval. They lie closely together in the midnight sector, but are separated by a dark gap in the noon sector, where they should be regarded as two separate precipitation regions (LUI *et al*, 1975). The observation of the outer belt of auroral emission was not unexpected since there was clear evidence of another zone of precipitation located equatorwards of the oval of discrete aurora (HARTZ and BRICE, 1967;

BURCH, 1968). This zone is characterised by a structureless precipitation of 'hard' electrons and corresponds approximately to the mantle aurora of SANDFORD (1968) and the drizzle zone of HARTZ and BRICE (1967), which is reproduced in Figure 3.16. As can be seen from the figure there is an appreciable gap between the drizzle zone (dots) and the splash zone (triangles) at noon.

In the evening sector the diffuse aurora is a relatively uniform band of luminosity with a smooth poleward and a sharp equatorward boundary. This is illustrated in Figure 3.15 to which reference should be made in the following descriptions. AKASOFU (1974) pointed out the smooth equatorward boundary of the auroral oval is often very clearly delineated by diffuse aurora which brightens during substorms, particularly in the evening sector.

In the midnight sector the general nature of the diffuse aurora changes and it loses its uniformity. Dark E-W gaps may appear in it and by the morning sector it may become a set of densely packed diffuse arcs aligned E-W around the auroral oval in that region. During a substorm the poleward boundary becomes very disturbed and develops a series of waves (omega bands) and sun-aligned arcs over the morning half of the polar zone (polar cap aurora). Often during a substorm the E-W aligned morning sector diffuse arcs appear to degenerate into E-drifting patches moving at about 300 m s^{-1}.

3.3.8 Relationship between diffuse aurora and the plasmasheet

FRANK and ACKERSON (1972) conducted a local time survey of plasma at low altitudes over the auroral zones during magnetically quiet periods. They found that a simplified picture of particle precipitation could be described in terms of two zones, located relative to the trapping boundary

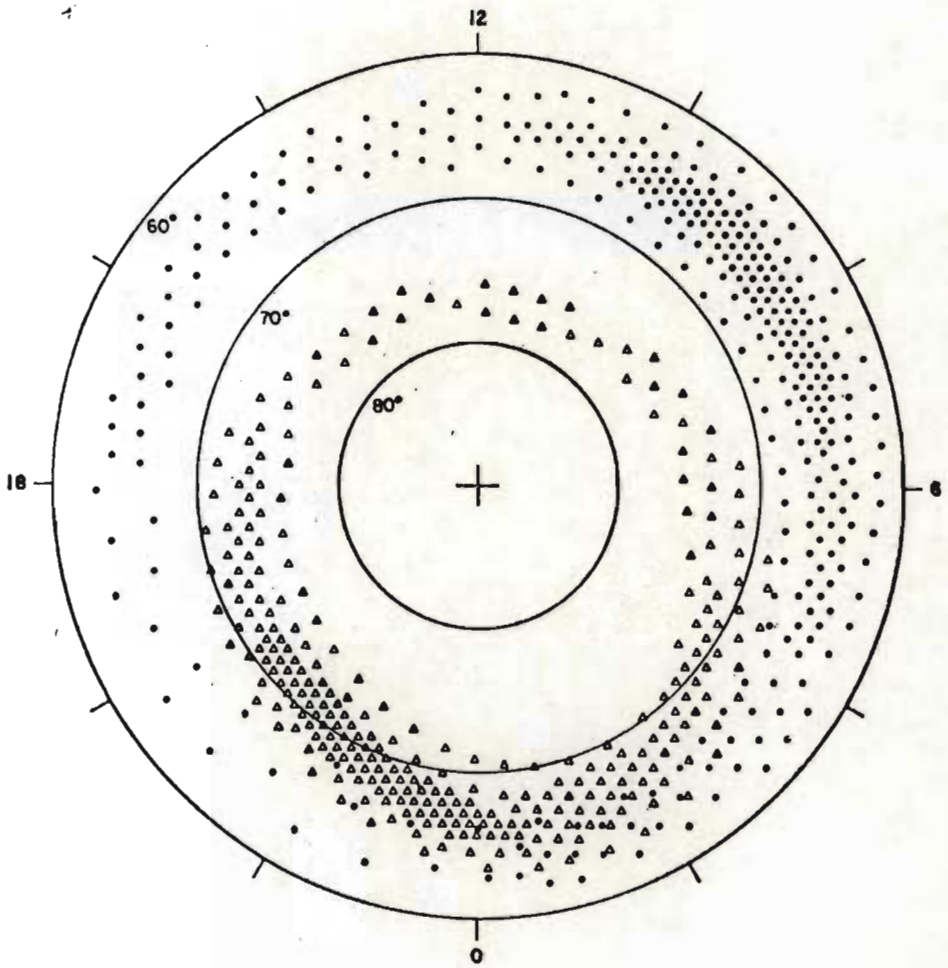

Figure 3.16 The two main zones of auroral particle precipitation: dots symbolize the drizzle precipitation, and triangles the splash type

(HARTZ and BRICE, 1967)

for the more energetic (E > 45 keV) electrons. Poleward of the trapping boundary they found that the electron precipitation pattern was dominated by inverted 'V' events. Equatorward of the trapping boundary they found that the most intense electron precipitation occurs in the midnight and early morning sectors. It is clear from the survey that the precipitation equatorward of the trapping boundary is identified with plasmasheet electron intensities because of their spatial location, overall intensities, average energies, and relatively broad energy spectra.

WINNINGHAM *et al* (1975) investigated the latitudinal morphology of 10 eV to 10 keV electron fluxes during magnetically quiet and disturbed times in the 2100 - 0300 LT sector. Their satellite data (ISIS-1 and 2) showed characteristic and repeatable morphological precipitation regions. A summary of their results is shown in Figure 3.17. They described this as an amplified version of the precipitation pattern proposed by HOFFMAN and BURCH (1973) reproduced in Figure 3.18. WINNINGHAM *et al* (1975) and DEEHR *et al* (1976) found three precipitation regions which they called central plasmasheet (CPS), boundary plasmasheet (BPS) and polar rain (PR). The CPS region corresponds to electron fluxes originating in the near-earth plasmasheet. Thus the equatorward limit to the CPS region is formed by the inner surfaces of the cusps of the plasmasheet as illustrated in Figure 3.20. Poleward of the CPS region they found a region of precipitation in which the average electron energy, intensity and morphology are extremely variable from orbit to orbit. They speculated that this region is associated with the outer boundaries of the plasmasheet cusps and thus named it the BPS region. The BPS region is associated with inverted 'V' events and is very dependent on magnetic activity. On the other hand the CPS region is more stable. BURROWS and McDIARMID (1972) showed that energetic solar flare electrons could reach the BPS but not the CPS region. The

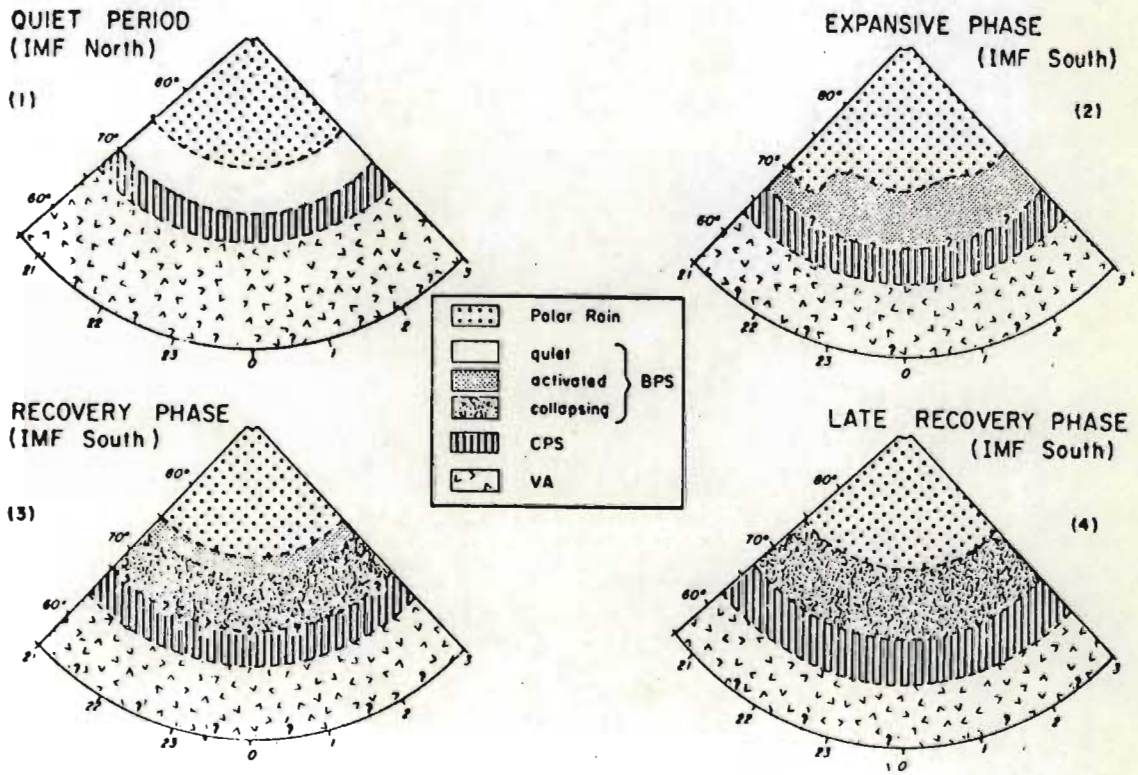

Figure 3.17 Polar plot of electron precipitation morphology for various substorm phases from 2100 to 0300 MLT based on ISIS 1 and 2 data

(WINNINGHAM et al, 1975)

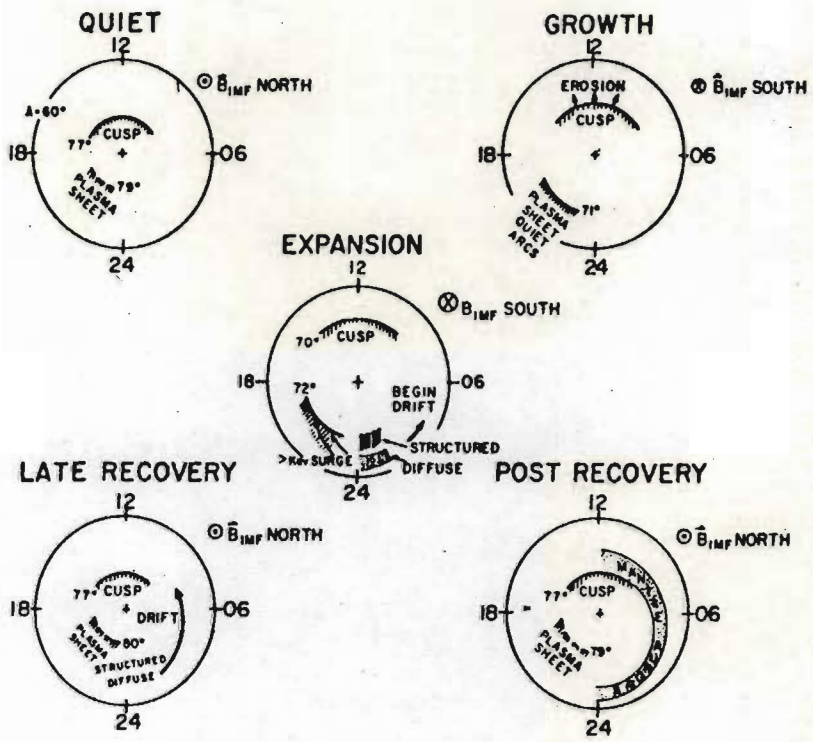

Figure 3.18 Polar plots in invariant latitude and magnetic local time which summarize the electron precipitation patterns of the five substorm phases
(HOFFMAN and BURCH, 1973)

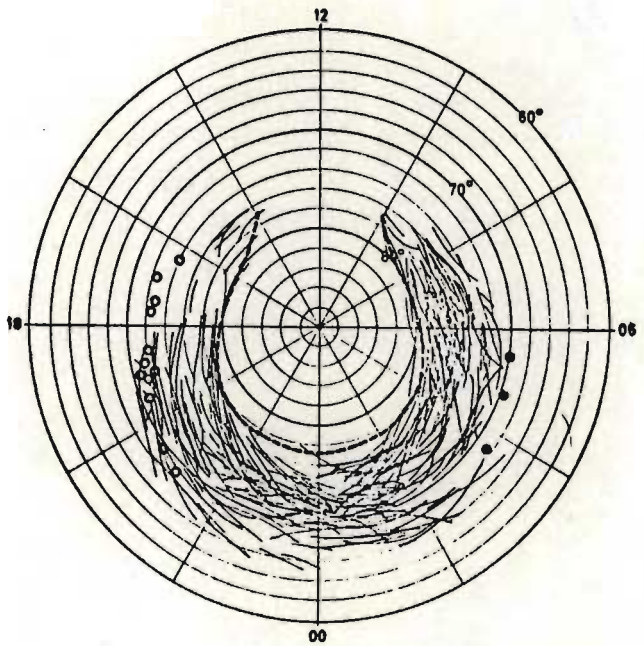

Figure 3.19 Relationship between auroral forms representing the auroral oval and the inner and outer boundaries of the plasma sheet

The outer boundary mapped from observations at 18 R_e (-----)

The inner boundary mapped from observations in the equatorial plane (O) and from 2,7 - 3,0 R_E (●)

(LASSEN, 1974)

PR region lies polewards of the BPS region. Weak electron fluxes precipitating here may be magnetosheath electrons.

VASYLIUNAS (1970) showed that the inner edge of the plasmasheet, projected along the magnetic field lines to the ionosphere, coincides with the equatorward boundary of the auroral oval. AKASOFU *et al* (1973) determined the outer boundaries of the plasmasheet using Vela 5 and 6 satellite data. LASSEN (1974) mapped these outer boundaries onto the polar ionosphere and superimposed auroral data recorded over a 2-month period by a network of 6 all-sky cameras in Greenland. His results are reproduced in Figure 3.19. The determination of the outer boundary of the plasmasheet is shown as a dashed line and the boundary of the inner edge is shown by open circles (mapped from observations at the equatorial plane) and filled circles (mapped from observations at 2,7 - 3,0 R_E). Lassen's auroral data is shown as representing discrete forms. There is a discrepancy in that discrete forms should delineate the poleward section of the auroral oval and diffuse forms the equatorward section. Discrete forms are plotted throughout the oval in Figure 3.19. He ascribed the discrepancy to the difficulty of distinguishing a diffuse aurora on all-sky camera records and concluded that some of the arcs plotted near the equatorward boundary of the oval represent elements of diffuse aurora.

Finally, LUI (1975) clearly showed that the region of diffuse auroral precipitation was directly associated with the centre of the plasmasheet (CPS) and that discrete events were associated with the outer boundary of the plasmasheet (BPS). A summary of the results of recent satellite surveys of the morphology of auroral precipitation by LINSCOTT (1975) is represented in Figure 3.20. Inverted 'V' events and discrete auroras occur at the outer boundary of the plasmasheet while diffuse aurora occurs from the discrete regions to an equatorward boundary at the inner edge of the plasmasheet.

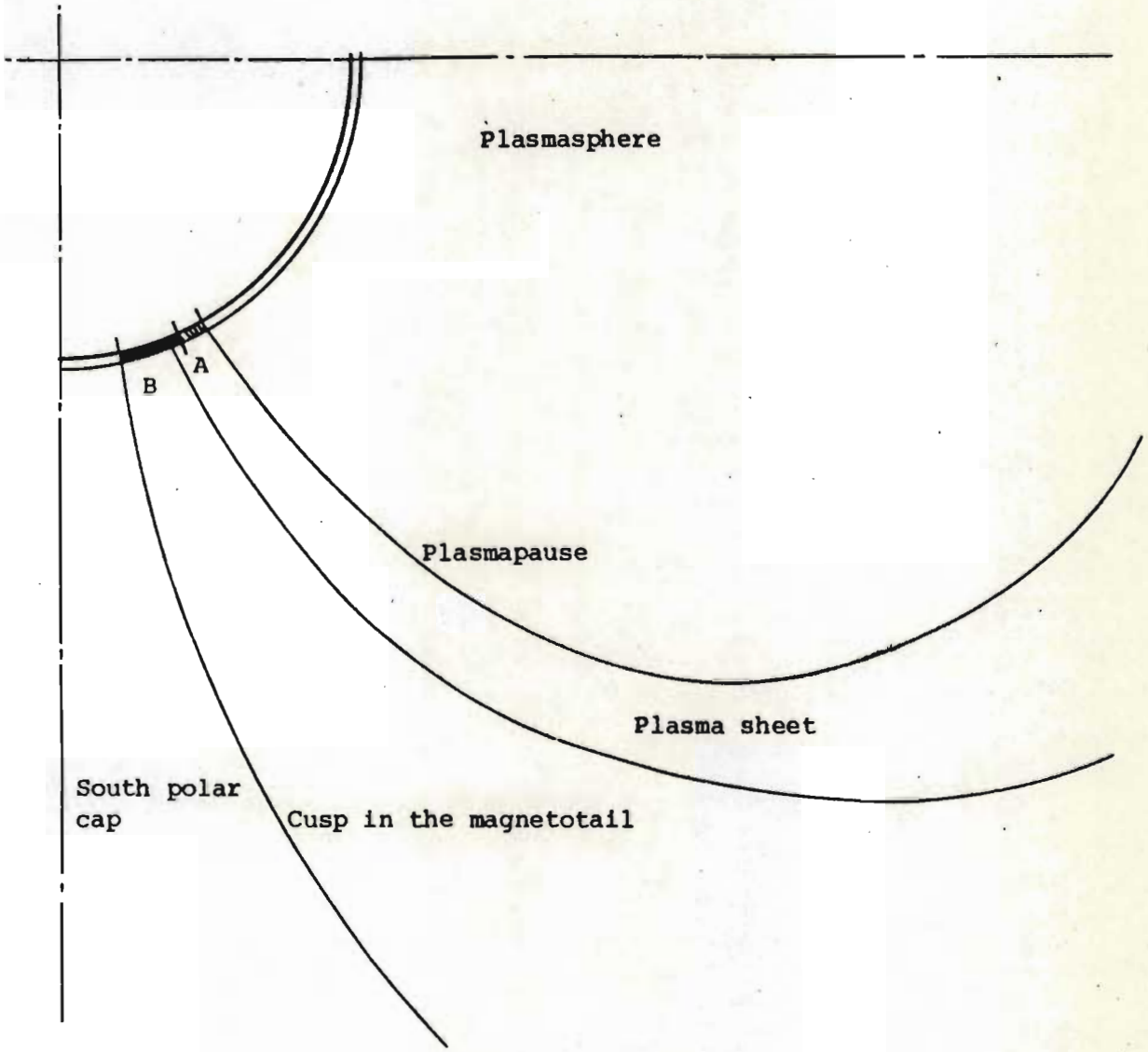

Figure 3.20 Relation of diffuse and discrete auroral regions to magnetospheric topology
Diffuse aurora - cross-hatched, A
Discrete aurora - solid, B

3.3.9 Summary

The relevant points to note in the section concerning the auroral morphology and, in particular, diffuse aurora are:

(i) The auroral oval is a topological concept derived statistically. The continuity of the oval around the pole does not imply that the precipitation mechanisms around the pole are all the same.

(ii) Auroral forms seen during a typical auroral display may be resolved into a few standard forms.

(iii) For ordering a sequence of auroral events, the concept of the auroral substorm can be used.

(iv) Auroral observations depend on the substorm phase as well as the observer's position relative to the auroral oval.

(v) Electron auroras may be classified as discrete or diffuse.

(vi) Diffuse aurora show a well defined equatorward boundary in the local evening sector and are relatively stable.

(vii) The equatorward boundary coincides with the equatorward boundary of the auroral oval and with the inner boundary of the plasmasheet.

(viii) Diffuse aurora brightens with the onset of discrete activity.

3.3.10 The characteristics of pulsating aurora

A modulation of intensity is often found to be superimposed on the gross features of a precipitation event. The source of modulation may be a process which redistributes the pitch angles of particles into the loss cone such as in a wave-particle interaction. A close investigation into the characteristics of pulsating aurora and its association with phenomena, such as precipitating particles and VLF emissions, can help in the understanding of the mechanisms involved.

Pulsating auroras are a post-breakup phenomenon, Figure 3.21 which exhibits quasiperiodic temporal variations with frequencies ranging from 0,01 to 10 Hz; they are low in intensity, 10 kR; the pulsating forms can be arc-like or irregular in shape with a horizontal extent between 0,1 to perhaps more than 100 km; pulsating auroras typically drift eastward at low speed, 1 km s^{-1} or less (e.g. PAULSON and SHEPHERD (1966); JOHANSEN and OMHOLT (1966); CRESSWELL and DAVIS (1966); SCOURFIELD and PARSONS (1969); CRESSWELL (1972).

Power spectral analysis of auroral pulsations presents a rather complex problem. The complexity arises from the fact that the intensity of many pulsating forms vary not only temporally but also spatially. JOHANSEN and OMHOLT (1966) found different types of pulsations exhibited different power spectra of intensity variations over frequencies ranging from 0 Hz to 3 Hz. A typical record of a very regular series of pulsations in auroral luminosity is shown in Figure 3.22 and power spectra of luminosity pulsations as observed by JOHANSEN and OMHOLT (1966) is presented in Figure 3.23. OMHOLT and PETTERSON (1967), from an investigation into power spectra over a frequency range of 1 - 20 Hz found a rapid decrease in power with increasing frequency. An interesting observation is that the spectral shape varied more rapidly with time with the fast pulsations (1 - 20 Hz) than with the slow pulsations (0 - 3 Hz). The appearance of fast pulsations also seem to be more irregular in time and shape than slow pulsations. Power spectral shape also seems to be dependent on local time (OMHOLT, KVIFTE and PETTERSEN 1969), but not strongly dependent on latitude (SHEPHERD and PEMBERTON, 1968).

Interesting work on isolated pulsating patches was done by INNES (1973). He found that optical emissions at different points within the pulsating patch showed detailed similarities as revealed by

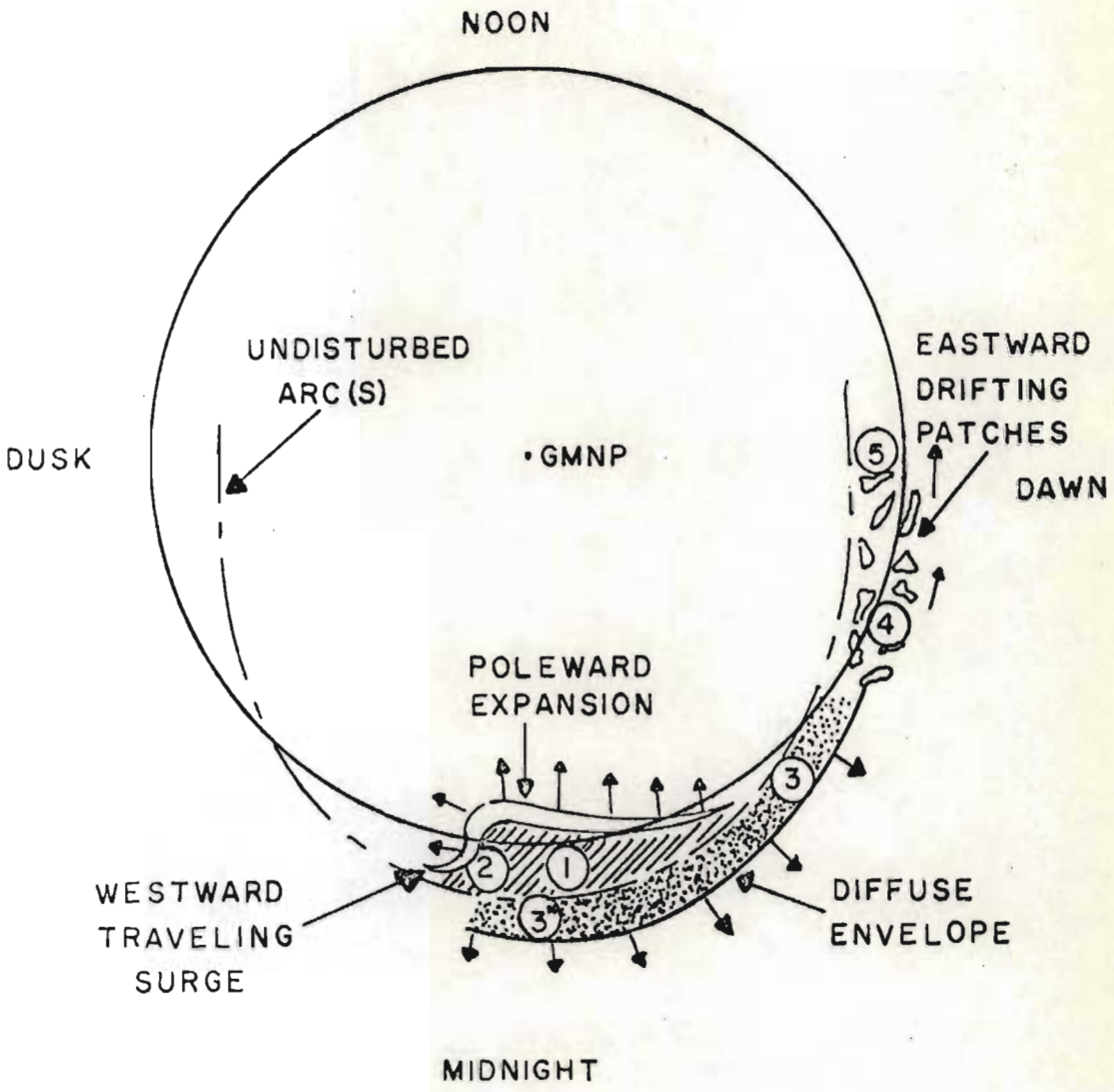

Figure 3.21 Schematic diagram showing the undisturbed arc just prior to a substorm onset and the subsequent idealized substorm in progress. The numbers refer to the manner in which the pulsating display would be observed to start at that point.

(REPRODUCED FROM CRESSWELL, 1968)

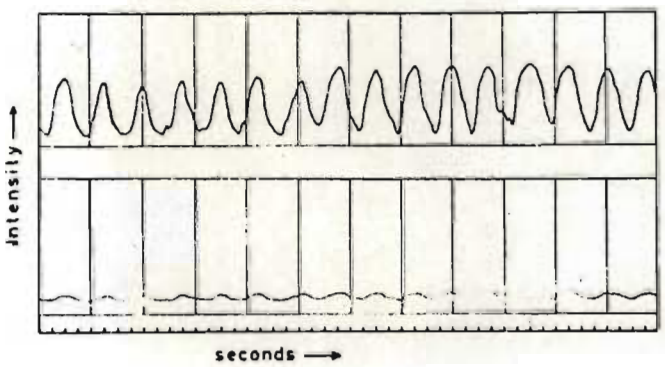

Figure 3.22 Typical record of pulsations in auroral luminosity. The lower record shows total intensity, whereas in the upper record the zero level has been removed off scale by a bucking current, and the signal is amplified an additional 10 times. 1 sec between division marks.
(JOHANSEN and OMHOLT, 1966)

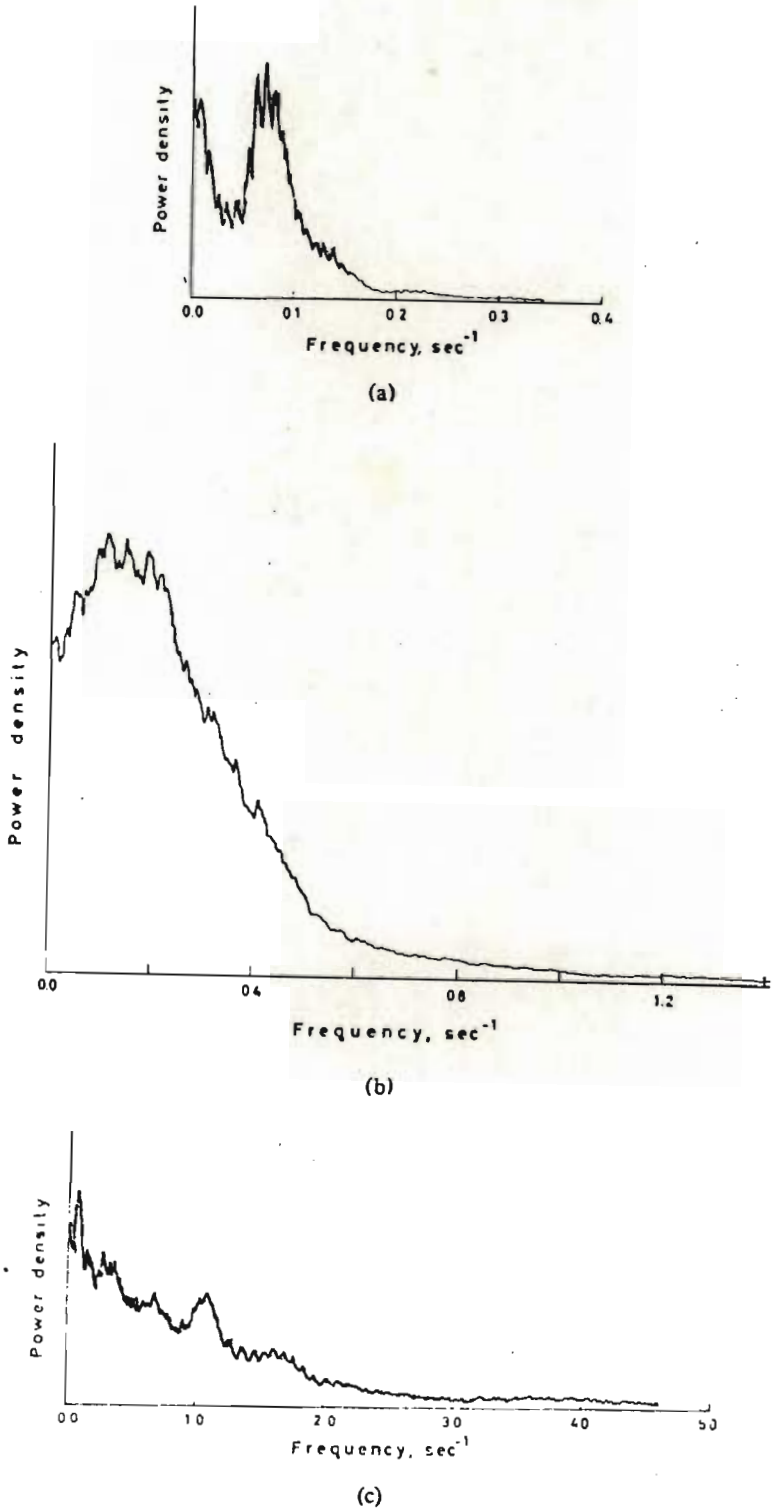

Figure 3.23 Power spectra of luminosity pulsations.
(JOHANSEN and OMHOLT, 1966)

the power spectral density plots but that the frequency components become randomly phased with increasing spatial separation of the points observed. There was furthermore no preferred direction in which frequency components progressed, INNES (1973) felt that this gave conclusive evidence of several minor modulation mechanisms being superimposed on a major mechanism.

3.3.11 Modulation of auroral electrons

Groundbased, satellite and sounding rocket observations have shown that auroral light is primarily due to electrons in the 1 - 10 KeV range e.g. HARANG and OMHOLT,(1960); CHRISTENSEN and KARAS,(1970). The following section concern the characteristics of these auroral electrons and their precipitation into the ionosphere.

Fluctuations in the flux of precipitating electrons have been observed during the breakup phase of an auroral display by rocket techniques, e.g. EVANS (1967); JOHNSTONE and DAVIS (1974); BRYANT *et al* (1971,1975). BRYANT *et al* (1971) measured 4,6,>22 KeV electron intensities above a pulsating band whose light intensity was recorded through a 3914 Å filter by a photometer on the ground below the pulsating auroral form. Figure 3.24 shows the similarity between the simultaneous electron intensity and optical illuminosity records of BRYANT *et al* (1971). The reason for the simultaneous observations of the two phenomenae was to establish whether the variations in electron intensity were temporal and not spatial. The assumption is made by several workers JOHNSTONE and DAVIS (1974), BRYANT *et al* (1971, 1975), that at the source of the electron intensity pulsations the modulation is simultaneous for particles of all energies, and that following the modulation, the speeds of the particles are constant until they are detected. On the basis of this assumption the distance along particle trajectories to the source of modulation is deduced. The results of such

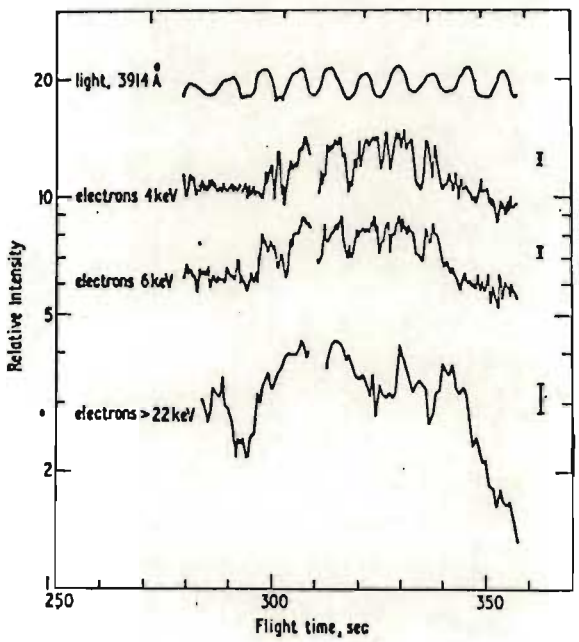

Figure 3.24 Electron intensities recorded at the rocket, and optical intensities recorded at the ground, from 280 to 360 sec. All intensities are on the same scale but the normalization is arbitrary. The 4 and 6 keV electron intensities are 0,5 sec averages and the > 22 keV intensities are 1 sec averages. Error bars show statistical uncertainties (±σ). The similarity of the measurements made from the rocket and from the ground shows that the observed changes of electron intensity were temporal rather than spatial in origin.

(BRYANT *et al*, 1971)

analyses have fallen into two groups. JOHNSTONE and DAVIS (1974) proposed a low-altitude mechanism such as acceleration as produced by an electric field parallel to the geomagnetic field for the precipitation of particles during a transient visible auroral event and a mechanism such as pitch angle diffusion or convection electric fields for the subvisual background precipitation. However, BRYANT *et al* (1971, 1975), place the modulating mechanism in the equatorial region and suggest that precipitation, which was observed during the expansive phase of an auroral substorm, was caused by pitch angle scattering of plasmasheet electrons into the loss cone as a result of wave-particle interactions. Wave-particle interactions have their greatest effect at the geomagnetic equator where the geomagnetic field strength is weakest.

It appears, therefore, that there exist different modulating mechanisms and there is debate as to the location of the source of modulation of auroral electrons and illuminosity.

3.3.12 Motion of energetic electron for L = 4,11

In the following section the time taken for electrons of various energies to travel from the equator to their mirror points in the atmosphere will be calculated. The results will be used later in the auroral date in Section

Consider first the oscillation of a trapped particle between mirror points M and M' in the northern and southern hemispheres.

The magnetic moment μ associated with the particle and its motion is invariant, ALVEN (1950).

$$\mu = \frac{1}{2} m \omega_n^2 / H$$

$$= \frac{1}{2} m \omega^2 / H_m \qquad (\omega_s = 0 \rightarrow \omega_n = \omega)$$

m = mass of trapped particle

ω = speed of trapped particle

ω_s = component of ω perpendicular to H

ω_n = component of ω normal to H

H = magnitude of magnetic vector

H_m = magnitude of magnetic vector at mirror point M

Thus at M

$$H_m = \left(\frac{\omega}{\omega_{ne}}\right)^2 H_e \qquad \text{(e denotes conditions at equatorial plane)}$$

$$= \frac{H_e}{\sin^2 \theta_e} \qquad (\theta_e = \text{angle between } \bar{\omega} \text{ and } \bar{H}, \text{ i.e. pitch angle})$$

$$\therefore \quad \sin^2 \theta_e = \frac{H_e}{H_m} \qquad 1.0$$

The height h_m of M above the ground is given by the equations

$$h_m = r_m - a \qquad 2.0$$

where r_m = radial distance from centre of earth to M

a = earth's radius

$$\text{and } \sin^2 \theta_e = \left(\frac{r_m}{r_e}\right)^3 / \left(4 - 3 \frac{r_m}{r_e}\right)^{\frac{1}{2}} \qquad 3.0$$

Figure 3.25 has been constructed from equations 2.0 and 3.0 to show how h_m, L_e and θ_e are related, AKASOFU and CHAPMAN (1961).

Two points are noteworthy. If we consider a number of particles of different energies all mirroring at some altitude in some McIlwans

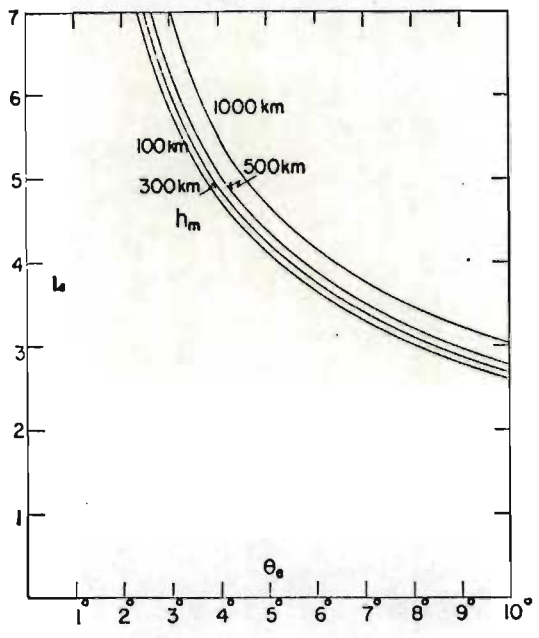

Figure 3.25 The graphs show for what combinations of L and θ_e the mirror points have heights of 100, 300, 500, and 1000 km above the ground; $L = r_e/a$, and r_e is the distance at which a particle crosses the equatorial plane with pitch angle θ_e.

(AKASOFU and CHAPMAN, 1961)

L shell, they will by equation 1.0 all have the same pitch angle in the equatorial plane and will follow the same spiral path. Secondly, from equation 3.0, the smaller r_e, the larger the range of pitch angle for which the particles can penetrate the atmosphere.

The time T_o required for one complete oscillation between the two mirror points M and M', is given by

$$T_o = \frac{4\ell}{\omega}$$

where ℓ denotes the arc length of the *spiral* path of the particle from the point where the path intersects the equatorial plane to the point M or M'. ℓ has been calculated by WENTWORTH *et al* (1959).

For $L = 4,11$

$\theta e = 4,94$

$\therefore \quad \text{Sin } \theta_e = 0,086$

From WENTWORTH *et al* (1959)

$\therefore \quad s = \ell = 1,268\ r_e$

and $r_e = 4,11a$

$\ell = 1,268 \times 4,11 \times a$

$$\therefore \quad T_o = \frac{4 \times 4,11 \times 1,268 \times a}{\omega}\ s$$

$$= \frac{132,997 \times 10^6}{\omega} \qquad (\omega \text{ in m s}^{-1})$$

For electrons of energy n KeV

$$\frac{1}{2} m\omega^2 = \left(n \times 10^3\right) \times \left(1,6 \times 10^{-19}\right) \text{ Joules}$$

$$\therefore \quad \omega = \sqrt{3,52n} \times 10^7 \text{ m s}^{-1}$$

For energies > 5 KeV the above must be modified for relativistic correction.

∴ The bounce time or time required for one complete oscillation, T_o, is the following:

$$T_o = 7{,}09/\sqrt{n}\ s$$

Below is a table of T_o for electrons of various energies.

Energy (KeV)	T_o(s)	$T_o/4$(s)
1	7,09	1,77
2	5,01	1,25
3	4,09	1,02
4	3,55	0,89
5	3,20	0,80
6	2,90	0,73
7	2,69	0,67
8	2,52	0,63
9	2,38	0,59
10	2,26	0,56
20	1,61	0,40
30	1,33	0,33

3.3.13 Summary

The following points from the sections concerning pulsating aurora are noted in lieu of the work to be presented later in this thesis.

(i) The power spectral determination of pulsating aurora is a complex procedure due to the fact that a pulsating forms fluctuation in intensity is not only temporal but also spatial.

(ii) Variations of intensity with an isolated patch have frequency components which are randomly phased.

(iii) 1 - 10 KeV electrons are primarily responsible for pulsating auroral emissions.

(iv) The study of the modulation mechanisms governing auroral electrons throws light on the modulation mechanisms responsible for pulsating patches.

(v) Time taken for an electron with m KeV energy on the field line L = 4,11 to travel from the equator to an altitude of 100 km has been determined to be

$$T = \frac{1}{4} T_o = 1,77/\sqrt{n} \text{ s}$$

3.4 Hiss

3.4.1 Introduction

Magnetospheric radio wave emissions observed with satellite and ground receivers are the results of wave-particle interactions, although details of the interaction mechanisms are not well understood. The association between auroral or precipitating particles and very low frequency emissions has since been established by satellite measurements, for example JORGENSEN (1966) and LAASPERE and HOFFMAN (1976). Ground based observers have also noted a correlation between auroral light intensity and VLF emissions e.g. BURTON and BOARDMAN (1933) and OGUTI (1975). The following review mainly concerns a specific VLF emission known as hiss.

3.4.2 Classification and morphology of hiss

VLF phenomena have been classified by GALLET (1959) and HELLIWELL (1965). Hiss may occur as a narrow band of noise, typically of a few kilohertz bandwidth, or as a wide band noise extending up to tens of kilohertz. It can be identified aurally by a hissing sound when

amplified and played through a loud speaker.

When one investigates VLF hiss in terms of intensity and of location in magnetic coordinates, it becomes apparent that there are two ranges of invariant latitudes where emissions are most commonly observed; high invariant latitudes of between about 70° and 80° and medium invariant latitudes, between 50° and 60°. The behaviour of VLF emissions, including hiss, differs greatly in these two regions e.g. see HUGHES (1970) and HAYAKAWA *et al* (1975). They must therefore be considered separately. In view of the fact that the location of SANAE is ($= 60^{\circ}$) in the medium latitude belt and that the VLF hiss data to be analysed is associated with aurora (auroral hiss), which usually occurs in the high latitude belt, it is appropriate that this review embraces both regions of observed hiss.

3.4.3 Morphology of medium latitude and high latitude hiss

High latitude hiss:

Before the advent of satellites, ground observations made at high latitude stations showed that two types of hiss were commonly observed; daytime hiss below 2 kHz, and hiss above 2 KHz which occurs mainly at night. MARTIN *et al* (1960) found an association between hiss at frequencies greater than 4 kHz and aurora. He called the VLF emissions 'auroral hiss' a very broad band hiss extending to hundreds of kHz. Since then, many other workers, for example ELLIS (1957, 1959), DOWDEN (1961), JORGENSEN (1964, 1968), MOROZUMI and HELLIWELL (1966), TANAKA (1972), OGUTI (1975) and HAYAKAWA *et al* (1975) have made observations of hiss and noted its association with auroral luminosity.

However, when VLF emissions are recorded at groundbased stations, they frequently exhibit complex behaviour. The reason for this could be

the propagation of high latitude hiss to low latitudes or vice-versa. in the ionosphere-earth waveguide so that a station at 60° invariant latitude, for example, may receive both low and high latitude emissions, resulting in a complex picture. Ionospheric absorption also plays a part in complicating a morphological study of hiss on the ground.

Satellite studies carried out with Injun, Alouette, Ogo, FR-1 and Ariel satellites have greatly enhanced our knowledge of hiss above the ionosphere.

As mentioned earlier the high latitude hiss zone is found to be situated between $\wedge = 70^{\circ}$ and $\wedge = 80^{\circ}$. This is supported by e.g. GURNETT (1966), HUGHES (1970), LAASPERE *et al* (1971). The location of the hiss zone peak intensity depends on magnetic activity and magnetic local time. Under disturbed conditions, the zone peak moves equatorwards but never as far as the medium latitude hiss zone. This has been attributed to the expansion of the auroral oval but satellite data suggests the development of emission at medium latitudes during a magnetic storm which is quite separate and distinct from the high latitude zone of emission. HUGHES (1970). Figure 3.26 illustrates the high latitude zone (northern hemisphere) plotted in invariant latitude against magnetic local time.

Various satellite studies have been carried out on the occurrence and correlation of energetic particles and hiss emissions. GURNETT (1966) concluded from INJUN 3 results that VLF hiss events were associated with fluxes of electrons having energies of about 10 KeV or less. LAASPERE *et al* (1971) and HARTZ (1971) have suggested that VLF hiss on the dayside of the magnetosphere is associated with an influx of low energy, 0,1 to 1 KeV electrons in a region identified as the 'soft-electron' precipitation zone by JOHNSON and SHARP (1969) and EATHER (1969). Published results by

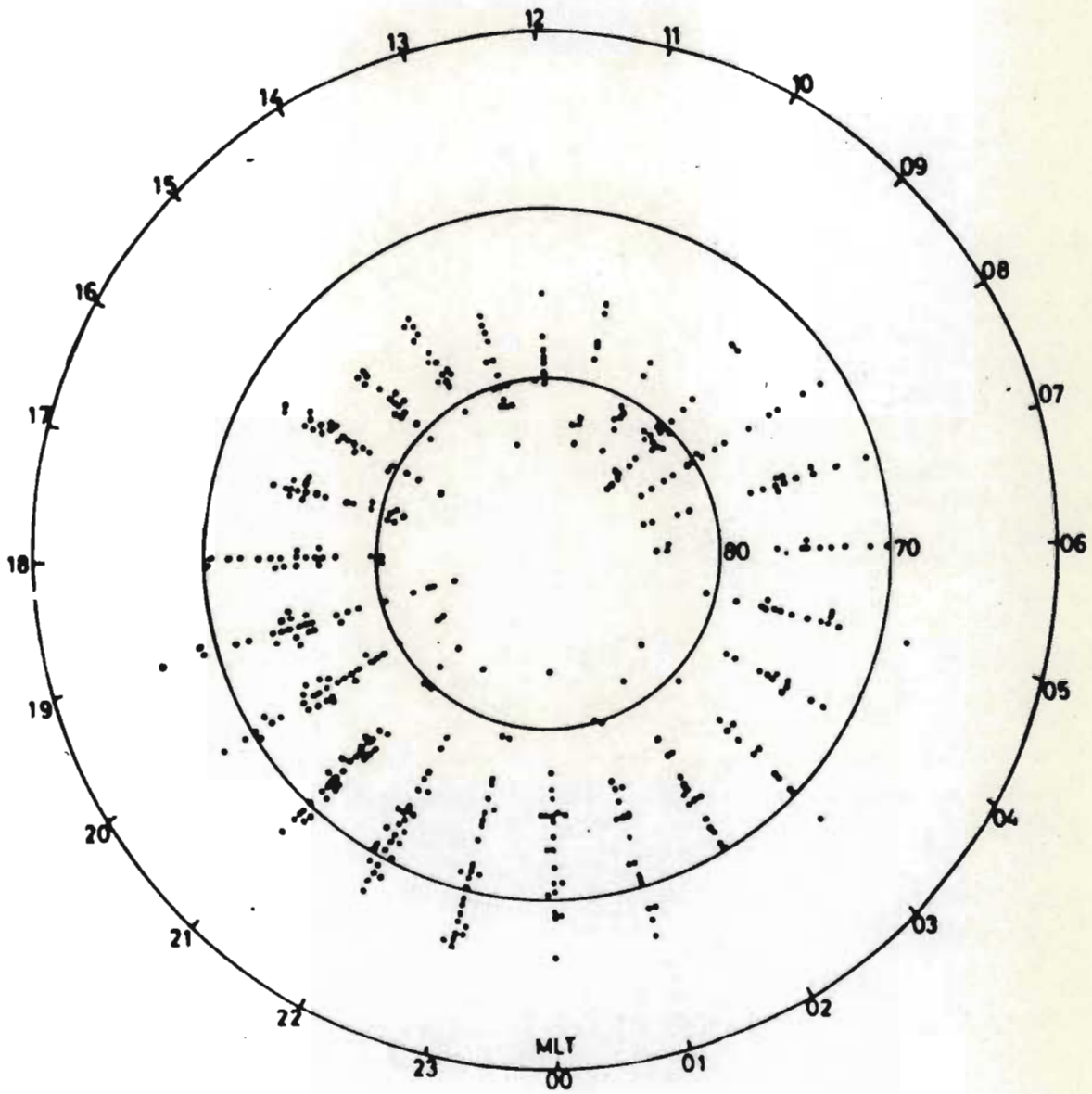

Figure 3.26 Position of high latitude zone (northern hemisphere) plotted in invariant latitude against magnetic local time.

(HUGHES, 1970)

HOFFMAN and LAASPERE (1972), GURNETT and FRANK (1972), HARTZ (1971) and JAMES (1973), clearly show that on the dayside of the earth the whole auroral hiss band (VLF - HF) is generated by very soft (few 100 eV) 'cleft region' electrons. LAASPERE and HOFFMAN (1976) concluded from OGO 6 data analysis that the predominant source for the whole auroral hiss on the nightside was electrons of energies below about 0,7 keV.

The close association between aurora and hiss has been reported by a number of observers e.g. BURTON and BOARDMAN (1933), JORGENSEN (1962) and OGUTI (1975), HARANG and LARSEN (1965), MOSIER and GURNETT (1972). Simultaneous occurrences on large and small time scales have been studied depending on the sophistication of the equipment used to observe the two phenomena. With the advent of low-light level imaging by sensitive TV cameras the resolution of data is in the order of a few milliseconds.

That a one-to-one correlation between the occurrence of aurora and VLF hiss does not exist has been established e.g. GURNETT (1966), MOROZUMI (1963) and MARTIN *et al* (1960). The absence of hiss during intense auroral displays has often been attributed to absorption in the ionosphere but ROSENBERG (1968) found a lack of one-to-one correlation even when ionospheric absorption was low. In addition many magnetospheric radio waves may also undergo total internal reflection at the base of the ionosphere, SRIVASTAVA (1974), thus limiting the information on the association between aurora and hiss gained from a ground-based station. An interesting experiment by MOSIER and GURNETT (1972), comparing all-sky camera data with INJUN 5 satellite VLF hiss data supports findings by GURNETT (1966) that indicated that VLF hiss and auroral light emissions are produced by electrons of somewhat different energies. Thus, depending on the detailed energy spectrum of precipitated electron flux

there may be a predominance of low energy ($\sim$400 eV) electrons which lead to the generation of VLF hiss but which does not contribute greatly to the auroral light emission. Also, for more energetic ($\sim$10 KeV) electron precipitation events there may be little VLF hiss generated, but strong auroral-light emissions observed. Thus if a broad enough energy spectrum of precipitated flux exists, both phenomena can be found to occur simultaneously.

SIREN (1972) reports the existence of dispersive auroral hiss, bursts of hiss which show whistler-mode dispersion. No accompanying auroral light was mentioned in this report although they were observed in the auroral zone. Their dispersive nature indicated various source positions ranging from altitudes of 10 000 km to 22 000 km.

From observations made at Syowa Station (high latitude) HAYAKAWA *et al* (1975) noted that there was a positive correlation between the occurrence probability of auroral hiss at 12 kHz and geomagnetic activity during slightly and moderately disturbed periods. This positive correlation dropped with further enhancement of geomagnetic activity which the author reports to be the possible result of ionospheric absorption. Figure 3.27 shows the dependance of occurrence probability of auroral hiss on magnetic activity observed at Syowa. Analysis of ARIEL 3 data shows a significant displacement of the mean position of the zone maximum to lower latitudes with increasing level of magnetic disturbance, the most and least displacement occurring at the noon and midnight meridians respectively HUGHES (1970). The mean position of zone maximum, however, does not move down to medium or low latitudes as other high latitude phenomena, such as aurora, during a magnetic storm.

Medium or low-latitude hiss

Medium latitude hiss is quite different from high latitude hiss, both in its behaviour with magnetic disturbance and the location of its occurrence.

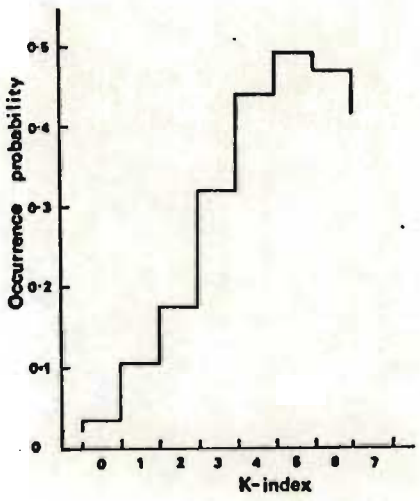

Figure 3.27 Dependence of occurrence probability of auroral hiss on magnetic activity.

(HAYAKAWA *et al*, 1975)

HUGHES (1970) summarizes the general features of medium latitude hiss as follows:

(a) The peak intensity zone lies between $\Lambda = 50^{\circ}$ and $\Lambda = 60^{\circ}$.

(b) It has a very sharp high latitude boundary between $\Lambda = 60^{\circ}$ and $\Lambda = 65^{\circ}$, the position being frequency dependent.

(c) The zone is often known to extend to lower latitudes on the evening side of the earth.

(d) Zone intensity and position are a marked function of local time and magnetic disturbance.

(e) There is always a separation of a well defined minimum in signal intensity between the medium and high latitude hiss zones.

(f) The frequency spectra of low latitude hiss is found to be always narrow band in frequency usually of the order of 1 kHz e.g. HAYAKAWA *et al* (1975).

A conclusion made by some observers e.g. JORGENSON (1968), that VLF emissions were observed at medium latitudes after propagation from high latitudes via the ionospheric-earth waveguide was questioned by HUGHES (1970) on various counts. ARIEL 3 data shows that intense emissions were observed in the morning almost immediately after a sudden storm commencement and there was no storm time delay as reported by HARANG (1968) which would indicate a propagation time delay. Also from this data it appears that the source of VLF emissions is confined to an angular width (in longitude) of between 15° and 30° because of the localisation of morning emissions.

Just as high latitude emissions move equatorwards during magnetic disturbance so do the emissions at medium latitudes but the two regions of emissions always remain separated by a deep minimum in signal intensity

It is generally considered (AKASOFU, 1969) that aurora observed at medium latitudes is due to the expansion of the oval towards the equator but, as HUGHES (1970) mentions, an alternative explanation, because of the two distinct zones of hiss, may be that during magnetic storms the precipitation of particles from the radiation belts is greatly increased giving rise to 'a medium latitude aurora' and at high latitudes the aurora is produced by particle coming in from the tail of the magnetosphere; these two phenomena being quite separate. However, it is debatable whether the radiation belts can support aurora of long duration.

3.5 Hiss generation mechanisms

The generation mechanism of VLF hiss emissions should be explicable for various parameters, but the two on which the most effort has been concentrated have been frequency versus time spectra and the intensity of the emissions. A number of different mechanisms have been considered to explain hiss. This review will concentrate on two popular mechanisms, namely Cérenkov radiation and cyclotron emission.

3.5.1 Cérenkov radiation

When charged particles in a medium move with a velocity greater than the phase velocity of propagation of electromagnetic waves in the medium then electromagnetic waves are radiated, known as Cérenkov radiation. FRANK and TAMM (1937) and FRANK (1939) gave the fundamental theory of Cérenkov radiation produced by a point charge moving with a uniform velocity through an isotropic medium. The first attempt to consider the condition of coherent radiation and calculate the total radiated power is due to KOLOMENSKII (1956). MACKENZIE (1963), LIEMOHN (1965), MANSFIELD (1967) and TAYLOR (1973) have also formulated the theory and shown its applicability to ionospheric and magnetospheric plasma.

The basic assumptions in these formulations of Cérenkov theory are the following:

(i) The medium is assumed to be cold, collisionless, dispersive and anisotropic.

(ii) The plasma is neutral.

(iii) Permeability of the medium equals that of free space

(iv) The dielectric tensor is complex and Hermitian.

(v) A static magnetic field permeates the medium and the magnetic field vector is comparatively very small.

(vi) The change in velocity of the particle is independent of spatial and temporal changes in the density of the medium.

3.5.2 A comparison of the properties of Cérenkov radiation and observed hiss characteristics

LIEMOHN (1965) and MANSFIELD (1967) using a plasma model with the above assumption and specific parameter values appropriate for trapped electron orbits at sample points in the geomagnetic field, calculated frequency and angular spectra of the power emitted by Cérenkov radiation. The frequency and angular spectra of Cérenkov radiation in the whistler mode for a 10 KeV electron with pitch angle $\psi = 30^{\circ}$, at a magnetospheric locus of $L = 3,0$ and geomagnetic latitude $\gamma = 30^{\circ}$ as calculated by MANSFIELD (1967) is presented in Figures 3.28 and 3.29. MANSFIELD (1967) makes the following conclusions:

(i) Theories using the longitudinal form of the index of refraction cannot be correct because the largest part of the radiation is emitted at large angles to the field line.

(ii) To explain the observed power levels of VLF emissions at least partial coherence among the radiating electrons is necessary.

(iii) VLF emissions with very narrow instantaneous bandwidth necessitates the postulation of some means of frequency selection.

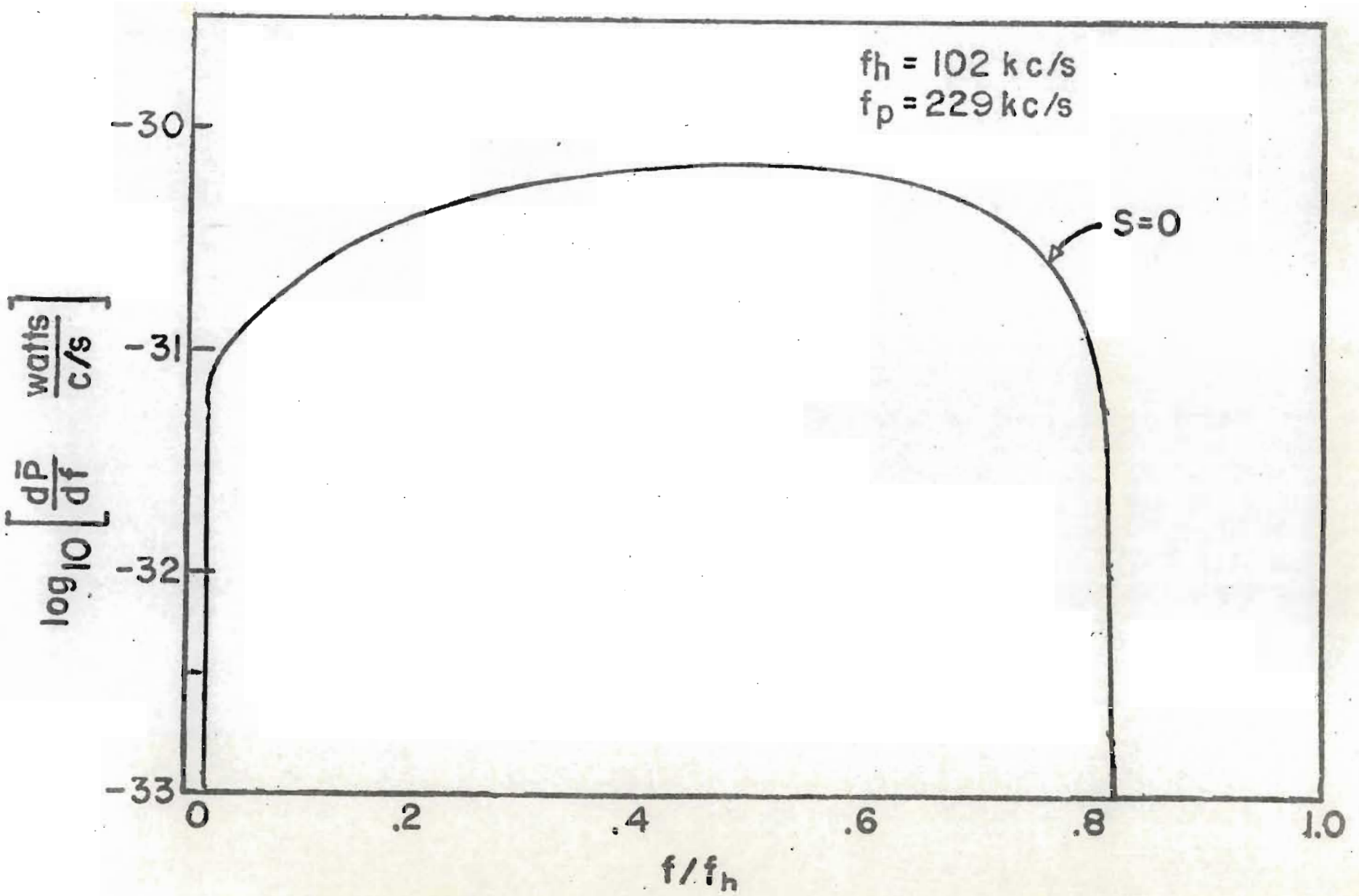

Figure 3.28 Frequency spectra of Cérenkov (s = 0) in the whistler mode for a 10 keV electron with $\psi = 30^{\circ}$, f_h = 102 kc/s, and f_p = 229 kc/s.

(MANSFIELD, 1967)

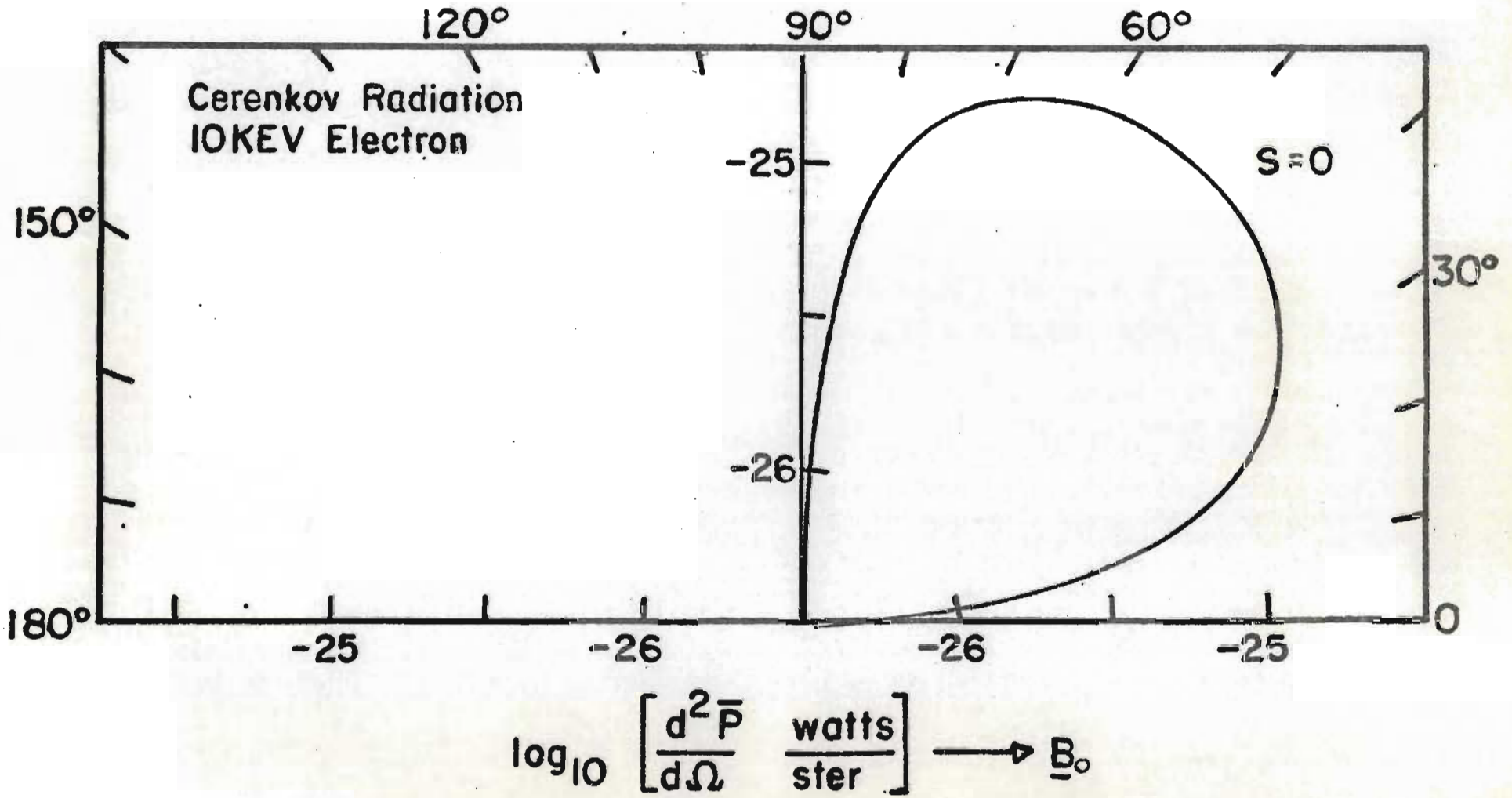

Figure 3.29 Angular spectrum for Cérenkov (s = 0) radiation in the whistler mode with $\psi = 30^{\circ}$, f_h = 102 kc/s, and f_p = 229 kc/s. (MANSFIELD, 1967)

JORGENSEN (1968) calculated a VLF hiss spectrum appropriate for the lower ionosphere using MANSFIELD's (1967) theoretical results and incorporating an intense but reasonable electron spectrum determined by EVANS (1966) for electrons with energies above 1 KeV. His calculated spectrum is shown in Figure 3.30. Although OGO 2 observations of VLF hiss showed an average spectral density of the same order as his theoretical results, INJUN 5 hiss spectral density was 3 orders of magnitude greater. In reviewing Jorgensen's paper, TAYLOR and SHAWHAN (1974) are critical of firstly, JORGENSEN's (1968) calculation of OGO 2 power spectral densities and secondly of his assumption that the hiss is perfectly guided.

Using MCKENZIE's (1963) formulation the dipole approximation for the geomagnetic field and electron density distribution supported by most experimental measurements, SINGH and SINGH (1969) plotted frequency and angular spectra for electrons of various energies. These are illustrated in Figures 3.31 and 3.32. Having calculated the incoherent Cérenkov power for different points in the magnetosphere they were able to integrate the effects of all radiating electrons in a tube of force and thus determine the total power received at the bottom of a tube of force having 1 m^2 base area on the earth surface and crossing the equator at L = 3. Their results were comparable with observed values of hiss power received at low latitudes as reported by JORGENSEN (1966). There is an overall agreement between their results and that of JORGENSEN's (1968).

LIM and LAASPERE (1972) modified MANSFIELD's (1967) formula by placing a limit of 400 on the index of refraction, corresponding to the condition that the phase velocity of the emitted wave be twice the thermal velocity of the background electrons for their assumed electron temperature of 5000° K. Their hiss spectrum is also shown in Figure 3.34 and it is seen that two orders of magnitude still separate the

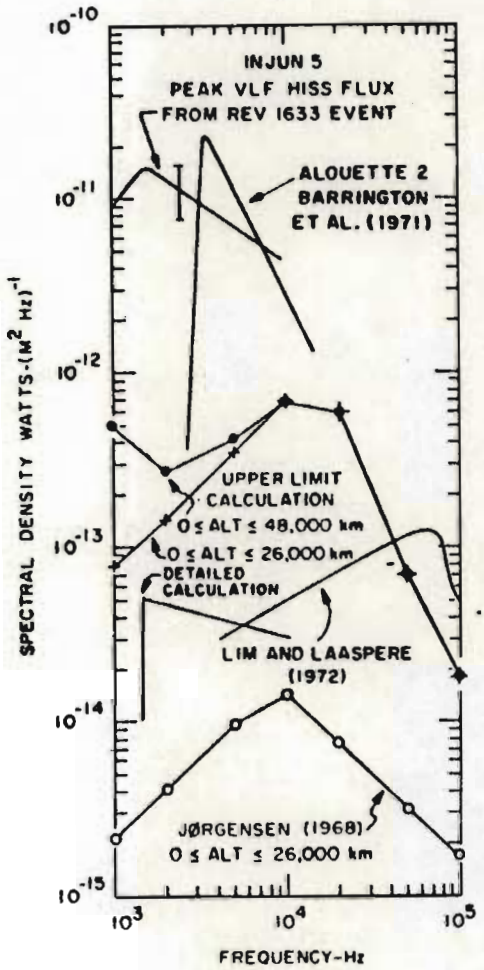

Figure 3.30 Spectral densities of observed VLF hiss and of calculated incoherent Cérenkov radiation.

(TAYLOR and SHAWNAN, 1974)

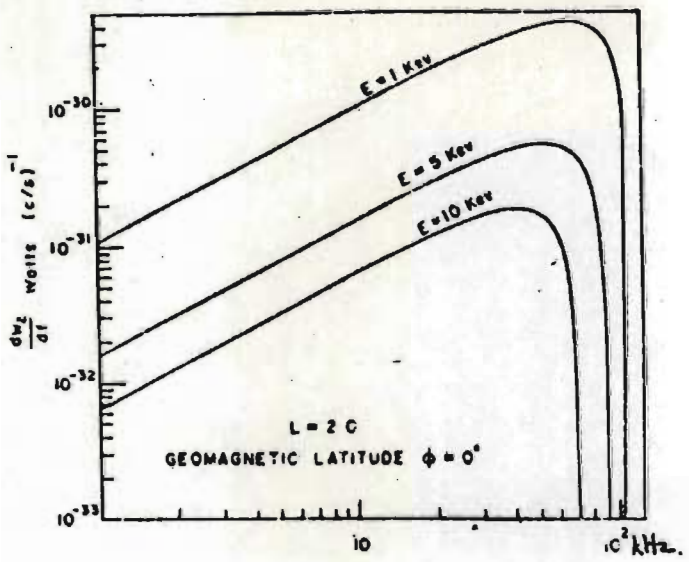

Figure 3.31 Cérenkov power variation with frequency radiated from an electron of various energies.

(SINGH and SINGH, 1969)

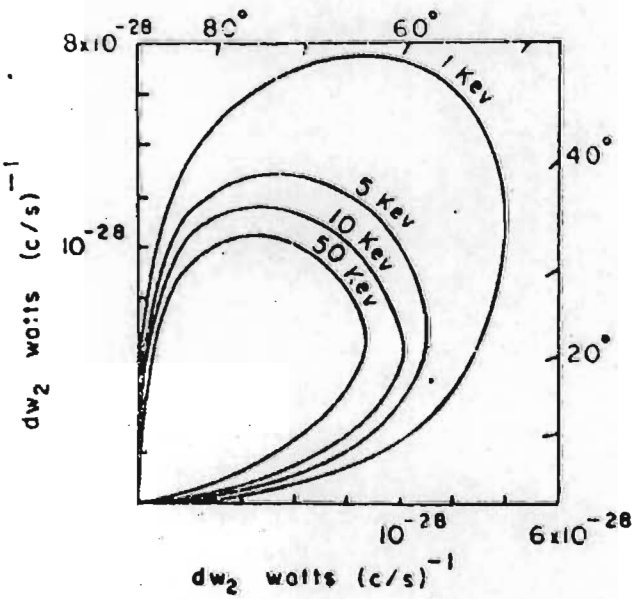

Figure 3.32 Polar diagram of Cerenkov Radiation from electrons of various energies.

(SINGH and SINGH, 1969)

maximum observed INJUN 5 fluxes and their calculated VLF fluxes. TAYLOR and SHAWHAN (1974) felt that they underestimated the power at the lower frequencies. It is noted by TAYLOR and SHAWHAN (1974) that large fluxes of low-energy electrons in the auroral zone will emit significant amounts of energy in the Cérenkov mode only for frequencies that may propagate with a large index of refraction. This condition holds for frequencies in the VLF range between the local lower hybrid resonance frequency and the minimum of the electron gyrofrequency/2π and electron plasma frequency/2π.

TAYLOR and SHAWHAN (1974) did calculations which included a wave normal angle dispersion calculation and a calculation for a wave normal angle distribution peaked near 6° from the resonance cone. They found theoretical and observed power spectra were still very different for VLF hiss although their spectralshapes were in agreement. They concluded that it seemed unlikely that VLF hiss is generated by incoherent Cérenkov radiation from electrons and because of the agreement in spectral shape and the non-linear dependance of wave power on particle flux, they suggest a partially coherent or amplified Cérenkov source (SINGH, 1972) or an instability with initial wave normal angles near the resonance cone at a source altitude of 3000 to 10 000 km.

A instability mechanism caused by an electron beam was investigated by SWIFT and KAN (1975). The instability could be viewed as a *coherent* Cérenkov radiation that is excited when the streaming velocity of the beam exceeds the phase velocity of the wave parallel to the magnetic field. It is successful in explaining the greater frequency of hiss observations by satellite than those on the ground.

3.5.3 Cyclotron radiation

When a charged particle spirals in a magnetoplasma it generates normal cyclotron radiation due to its continuous acceleration while spiralling and if its velocity component parallel to the magnetic field is smaller than the phase velocity of light in the medium, then it can also emit anomalous cyclotron radiation.

MANSFIELD (1967) rigourously formulated the cyclotron radiation theory using the basic assumptions underlined in Section 3.5.1 and discussed the applicability of doppler-shifted cyclotron radiation theory to the search for a source of VLF emissions. Plots of frequency and angular power spectra for cyclotron radiation by a 10 KeV particle with pitch angle $\psi = 30^{\circ}$ and magnetospheric locus of $L = 3,0$ and geomagnetic latitude $\phi = 30^{\circ}$ are presented in Figures 3.33 and 3.34 and these curves reveal noteworthy points as mentioned by MANSFIELD (1967).

Normal cyclotron radiation

(i) The maximum power density is around 10^{-30} watts/c/s/electron for the first harmonic.

(ii) The higher harmonics have lower power densities and peak at higher frequencies.

(iii) Most of the radiation is emitted at large angles to the magnetic field line in the backward hemisphere and essentially no emission is in the direction of the field line.

(iv) It appears that when the frequency spectra of the individual harmonics are summed the radiation will have a broad maximum.

Anomalous cyclotron radiation

(i) The maximum power density for the fundamental harmonic is 3×10^{-31} watts/c/s/electron.

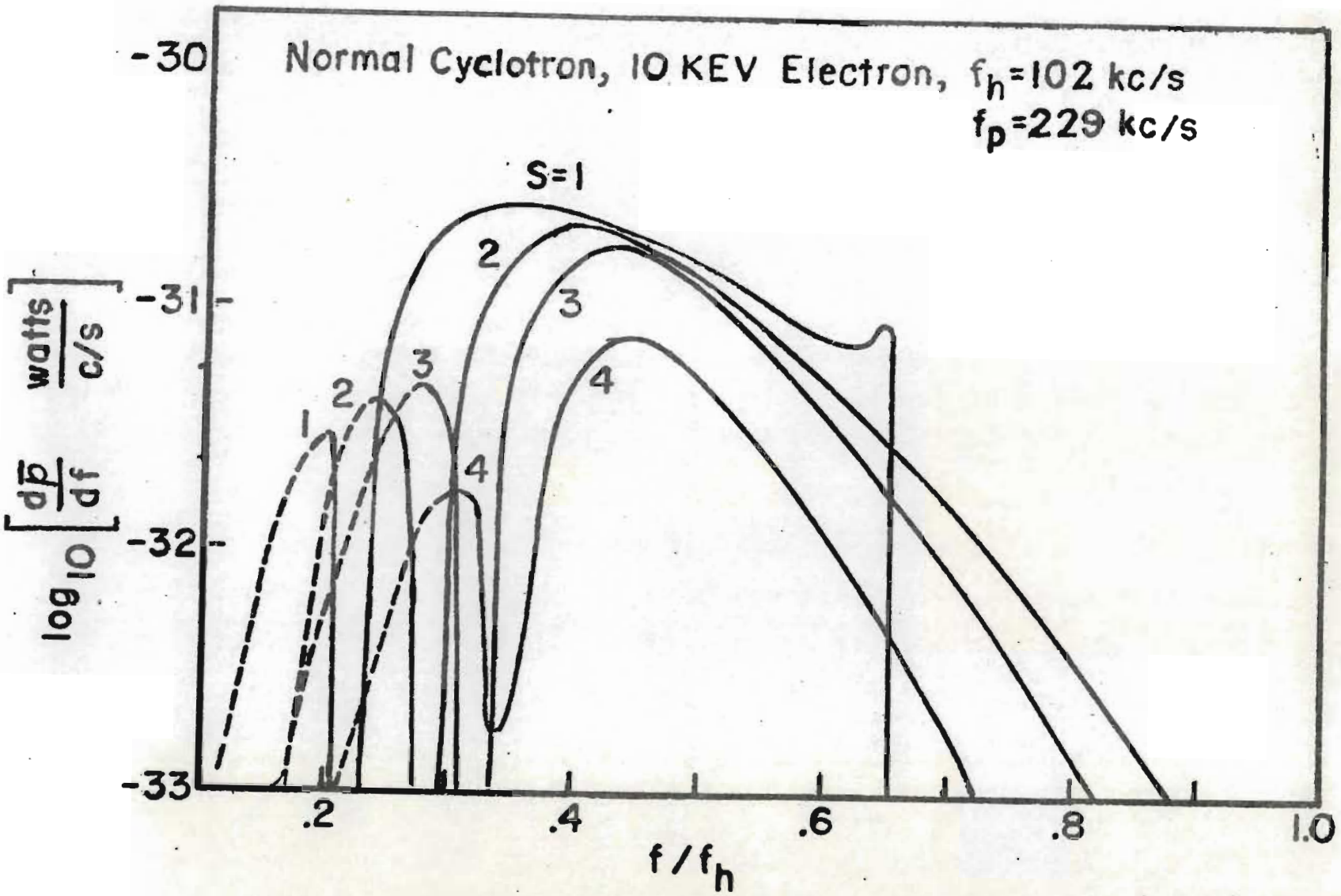

Figure 3.33 Frequency spectra for normal (s => 0) cyclotron radiation in the whistler mode for a 10 keV electron with $\psi = 30^{\circ}$, f_h = 102 kc/s, and f_n = 229 kc/s.

(MANSFIELD, 1967)

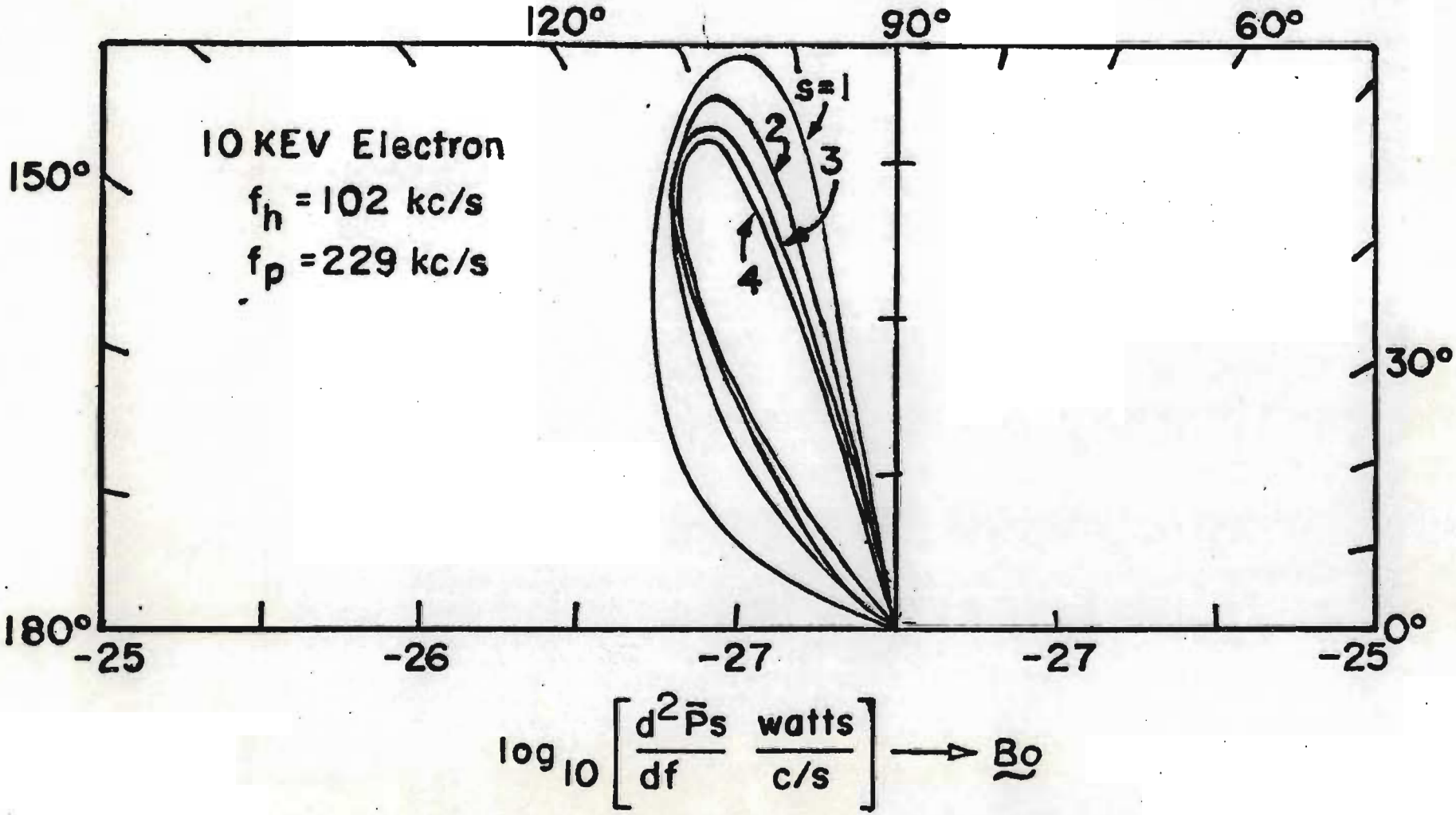

Figure 3.34 Angular spectra for normal s > 0) for 10 keV electron with $\psi = 30^{\circ}$, f_h = 102 kc/s, and f_p = 229 kc/s.

(MANSFIELD, 1967)

(ii) Higher harmonics have lower power densities but peak at the same frequency.

(iii) It is expected, as in normal cyclotron radiation, that the radiation will reach a broad maximum.

(iv) Radiation is emitted at large angles to the magnetic field and there is essentially no emission in the direction of the field line.

(v) The anomalous radiation is in the forward hemisphere.

SINGH and SINGH (1969) mention that assuming charged particles are emitting cyclotron frequencies and the change in frequency is due to spiralling motion upward or downward along the geomagnetic field, then the expression for the shifted frequencies can be obtained. (DOWDEN (1962) and NANSEN (1963)). The doppler-shifting of the cyclotron frequency depends on the velocity of radiating charged particles along the geomagnetic field lines. The doppler shifted frequency f_s is written as

$$f_s = f_H/(1 + \frac{V}{V_p})$$

where phase velocity $V_p = c/\mu$ which can be easily obtained from the ambient plasma. Frequencies received by the observer on the ground have been doppler-shifted down if the particles are travelling away and up if the particles are approaching the observer as in the case of precipitating particles.

From calculations, using THORNE and KENNEL's (1967) suggested electron density model, SINGH and SINGH (1969) concluded that cyclotron radiations were well suited for electromagnetic wave interaction with streaming or ambient magnetospheric plasma as they possessed the wave propagation direction along and opposite to the direction of spiralling electrons. Again, though, the calculated power in general falls short of the observed power.

3.5.4 Coherent Cérenkov and cyclotron radiation

As can be seen from the previous sections Cérenkov and cyclotron radiation from electrons cannot adequately explain the mechanism of VLF emissions from the point of view of intensity unless there is an additional mechanism which is able to make the radiation coherent.

The following sections discuss various conditions for the radiations from individual sources to propagate coherently.

3.5.5 Coherent Cérenkov radiation

Cérenkov radiation is emitted when the refractive index n satisfies the Cérenkov condition, KIMURA (1967).

$$1 - \frac{V_{\parallel}}{c} n \cos\theta = 0 \tag{1}$$

Using the approximation of the Appleton-Hartree equation for the square of the refractive index of plasma,

$$V_{\parallel}^{2} = \left[\frac{\omega(\omega - \omega_{ge}\cos\theta)}{\omega(\omega - \omega_{ge}\cos\theta) - \omega_{pe}^{2}}\right] \cdot \frac{c^{2}}{\cos^{2}\theta}$$

for longitudinal propagation ($\theta = 0$),

$$V_{\parallel}^{2} = \left[\frac{\omega(\omega - \omega_{ge})}{\omega(\omega - \omega_{ge}) - \omega_{pe}^{2}}\right] \cdot c^{2} \tag{2}$$

The emitted frequency ω is then given by the following expression

$$\omega = \frac{\omega_{ge}\cos\theta}{2\pi}\left(1 \pm \left(1 - \frac{4\,\omega_{pe}^{2}\,V_{\parallel}^{2}}{\omega_{ge}^{2}\,c^{2}}\right)^{\frac{1}{2}}\right) \tag{3}$$

$V_{\parallel}$ = electron velocity in the direction of the static magnetic field

c = speed of light

n = refractive index

θ = angle between wave normal and the external magnetic field

ω_{ge} = electron gyrofrequency

ω_{pe} = electron plasma frequency

If the electron's parallel velocity $V_{\parallel}$ satisfies a relation

$$V_{\parallel} = \frac{\omega_{ge}\, c}{2\, \omega_{pe}}$$

two frequencies coalesce to a single frequency

$$\omega = \frac{1}{2}\, \omega_{ge} \cos \theta$$

At this frequency the group velocity V_g of the wave becomes identical with the phase velocity V_p by lieu of the equation of the refractive index of the whistler mode (right-handed polarized) which is expressed by

$$n^2 = 1 - \frac{\omega_{pe}^2}{\omega(\omega - \omega_{ge} \cos \theta)}$$

given for example by KIMURA (1967).

We then have the condition that from the Cérenkov condition

$$1 - \frac{V_{\parallel}}{c}\, n \cos \theta = 0$$

and $V_p = V_g$ $\qquad$ V_p = phase velocity
V_g = group velocity

that the electron and the radiated energy are always on the same wave front as seen in Figure 3.35. GENDRIN (1960) was the first to point this out and STURROCK (1962), BRICE (1964) and ONDOH (1965) did further investigation into it.

What is noteworthy is that the condition does not require a number of particles to radiate coherently but that the radiation from a single particle be summed up coherently to give a solitary impulse. However, though the wave energy traverses with a constant angle to the

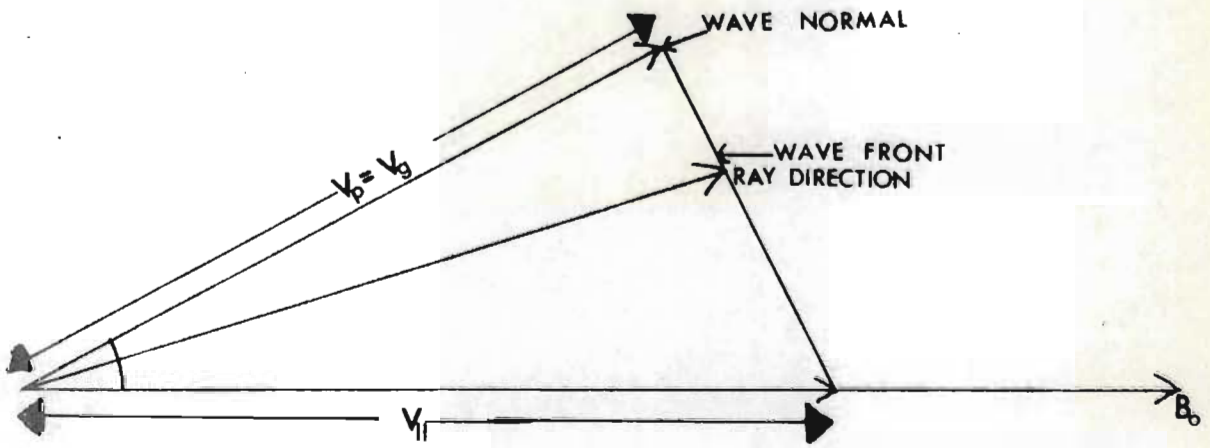

Figure 3.35 Condition in which Cerenkov radiation is coherently emitted.

(KIMURA, 1967)

magnetic line of force, the energies successively emitted do not always travel along a single ray path, so that the intensity of the solitary impulse would not attain a very high value.

3.5.6 Coherent cyclotron radiation

KIMURA (1967) notes that if the cyclotron radiations from individual particles constituting a beam are to be observed coherently, then the phase of the transverse velocity of the particles should change periodically in space and time like a wave, the wavelength of which should have a particular relation with that of the radiation in the medium. He found that the phenomena of coherent cyclotron radiation emitted from a beam can be identical to an electron beam interacting with a whistler mode wave to excite the cyclotron instability.

The latter will be discussed in the following section.

3.5.7 Cyclotron instability (gyroresonance)

BRICE (1964) classified suggested mechanisms for the generation of VLF emissions and noted that all the mechanisms involve either longitudinal or transversal resonance conditions for interactions between whistler-mode electromagnetic waves and energetic particles.

Cérenkov radiation by individual particles and travelling wave tube amplification plasma instability satisfy the longitudinal resonance condition, RYCROFT (1972), but it is the transverse resonance or gyroresonance which this section is devoted to and which is also treated in more detail by RYCROFT (1972) and BRICE (1964).

The exchange of energy from an energetic electron in the

magnetosphere to electromagnetic radiation propagating in the whistler mode is considered. A change in energy ΔW of an electron of charge $q = -e$, moving a distance $\underline{\Delta s}$ at velocity $\underline{V}$ in time $\underline{\Delta t}$, in an electric field $\underline{E}$ and magnetic field $\underline{B}$ is given by

$$\Delta W = q\ (\underline{E} + \underline{V} \wedge \underline{B}) \cdot \underline{\Delta s}$$

$$= q\ \underline{E} \cdot \underline{V}\ \Delta t \qquad (1)$$

An electron moves in a helix of varying pitch angle α in geomagnetic field with velocity components $V_{\parallel} = V \cos \alpha$ parallel to the magnetic field and $V_{\perp} = V \sin \alpha$ perpendicular to the magnetic field.

Two resonant conditions are possible

(a) $\underline{E}_{\parallel} \cdot \underline{V}_{\parallel} = \text{constant}$

or (b) $\underline{E}_{\perp} \cdot \underline{V}_{\perp} = \text{constant}$ (2)

Let us consider case (b). If a gyrating electron experiences the electric vector of a wave rotating about the geomagnetic field in the same sense and at the same frequency as its cyclotron motion, it 'feels' the wave Doppler-shifted to its gyrofrequency. As the propagation of whistler mode waves only occurs at $f < f_{ge}$ (electron gyrofrequency), the wave frequency must be Doppler-shifted up to the electron gyrofrequency. Alternatively, the electron gyrofrequency must be Doppler-shifted down to the frequency of the whistler mode radiation. The electrons and whistler mode waves must be travelling in opposite directions for a gyroresonance interaction to take place. Equation (2) becomes thus

$$V_\phi \frac{f_{ge} - f}{f} = - \gamma V_{\parallel} \cos \theta$$

V_ϕ = phase velocity of the wave

$\gamma = (1 - V_{\parallel}{}^2/c^2)^{-\frac{1}{2}}$

The minus sign is an indication that the waves and electrons are moving in opposite directions and will be omitted in what follows. In terms of the refractive index n, for resonance at the Doppler-shifted fundamental gyrofrequency, the resonance occurs when

$$n \left(\frac{\omega}{\omega_{ge} - \omega}\right) \frac{V_{\parallel}}{c} \cos \theta = 1 \qquad (\omega = 2\pi f) \qquad (3)$$

for longitudinal propagation ($\theta = 0$)

$$n \left(\frac{\omega}{\omega_{ge} - \omega}\right) \frac{V_{\parallel}}{c} = 1$$

$$\therefore \quad V_{\parallel} = \frac{c}{n} \left(\frac{\omega_{ge} - \omega}{\omega}\right) \qquad (4)$$

RYCROFT (1972) notes that this condition as a coherent collective effect leads to the transverse resonance plasma instability (KNOX (1964)).

By rearranging (4) one gets an expression for the parallel component of the energy $W_{\parallel}$ of the electrons resonating with whistler mode radiation of frequency f, at a point where the electron gyrofrequency is f_{ge} and the refractive index of the plasma is n

$$W_{\parallel} = \frac{mc^2}{2} \frac{(\omega_{ge} - \omega)^2}{n^2 \omega^2} \qquad (5)$$

Using the approximation of the Appleton-Hartree equation for the square of the refractive index of plasma and inserting

ω_{pe} = plasma frequency $= \sqrt{\frac{Ne^2}{\varepsilon_o m}}$

and $\omega_{ge} = eB/m$

and $c^2 = (\varepsilon_o \mu_o)^{-1}$

(5) gives

$$W_{\parallel} = \frac{B^2}{2 \mu_o N} \frac{\omega_{ge}}{\omega} \left(1 - \frac{\omega}{\omega_{ge}}\right)^3 \qquad (6)$$

In the region where the geomagnetic field approximates to a dipole field, B is proportional to L^{-3}

$$W_{\parallel} \simeq \frac{2.45 \times 10^6}{L^6 N} \frac{\omega_{ge}}{\omega} \left(1 - \frac{\omega}{\omega_{ge}}\right)^3 \text{ keV}$$

with N in cm^{-3} and L in earth radii.

BRICE (1964) calculated that the decrease of the transverse energy of the electrons was greater than the decrease of their total energy by a factor of f_{ge}/f which is greater than 1. Thus during this wave-particle interaction or gyroresonant instability the longitudinal energy of the electrons is increased leading to a change (decrease) in the electron's pitch angle which in turn could cause trapped electrons to be transferred to the 'loss cone' in the equatorial region and precipitate into the atmosphere.

KENNEL and PETSCHEK (1966) considered the situation regarding trapped electrons precipitating and showed that provided the pitch angle distribution of trapped electrons is sufficiently anisotropic, whistler mode noise will be generated. The pitch angles would then be scattered into the loss cone by this noise, increasing particle precipitation and the anisotropy of the pitch angle distribution. They found that the rate of pitch angle diffusion into the loss cone is proportional only to the wave energy, and the wave growth rate depends only on the number of

resonant particles, thus a limiting situation is reached for the number of stably trapped particles and the magnitude of whistler mode energy generated.

DUNGEY (1963) suggests that whistlers may account for the scattering of electrons into the loss cone by gyroresonance interaction. The essential different between Dungey's work and that of KENNEL and PETSCHEK (1966) is that the latter propose that whistler mode noise is generated within the magnetosphere.

It was shown by HUGHES (1970) from ARIEL 3 data that emissions at high latitudes are associated with low energy particle precipitation while at medium latitudes the emissions are due to trapped particles causing them to become 'untrapped' and to precipitate.

3.5.8 Conclusion

It is apparent that the generation mechanism for VLF hiss is still highly debatable. The reasons stem from the disagreement between theoretical and experimental results, lack of sufficient satellite VLF data to determine the effect of the absborbing ionosphere and the possibility of different mechanisms being responsible for hiss observed at different altitudes.

Coherent Cerenkov radiation and cyclotron instability (gyroresonance) at present seem to be the more likely generation mechanisms responsible for the hiss. The cyclotron instability (gyroresonance) and Cerenkov radiation mechanisms are shown to be unacceptable sources of the hiss analysed in Chapter Six.

CHAPTER FOUR

INSTRUMENTATION

4.1 INTRODUCTION

A detailed account of both the whistler and auroral low light level systems, used to acquire the data described in this thesis, has been given elsewhere WOODS (1974) and LINSCOTT (1975). The more important features of these systems will be presented together with those modifications made by the author.

Also described here in detail is the Video Analyser used in the analysis of the auroral data.

4.2 WHISTLER SYSTEM

Whistlers are bursts of very-low-frequency (VLF) electromagnetic radiation, varying smoothly over a frequency range of 300 Hz to 30 kHz. Also interspersed in this frequency range are other VLF phenomena such as impulsive atmospherics, hiss and 'dawn chorus'. A broadband VLF receiver is used to detect these signals and the output of the receiver recorded on magnetic tape.

4.2.1 Sanae whistler system

Figure 4.1 shows a block diagram of the system. It consists of two identical channels of which the sections marked 'aerial site' and 'auroral hut' constitute a single channel. The two aerials were orientated perpendicular to each other. A distance of 600 m separates the aerial site and auroral hut, which is 400 m south of the base office.

A 12 m aluminium mast supports a triangular vertical loop aerial

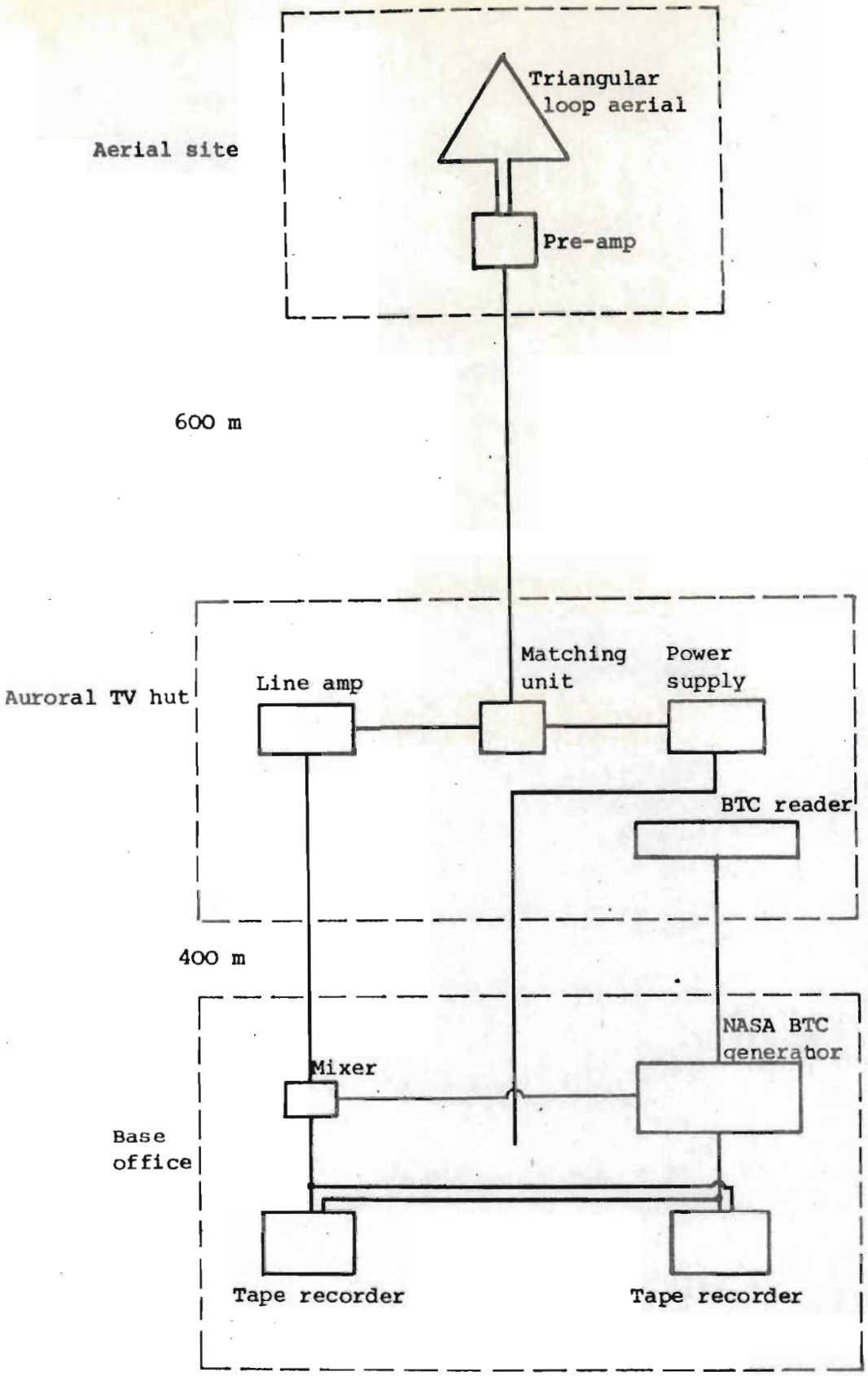

Figure 4.1 Block diagram of one channel of the SANAE whistler system, 1974. All items except the NASA BTC equipment and the tape recorders are duplicated in a second channel

which is 50 m in perimeter. Designed specifically for an environment notable for mains hum interference and the absence of an electrical earth, is a preamplifier with a balanced input and output.

The preamplifier power requirements and the VLF signal output are taken along a common 3-core rubber covered cable between the aerial site and the auroral hut. The VLF signal is then extracted in the auroral hut through a transformer coupled impedance matching unit from which it is available for direct recording in the hut, or for onward transmission to the base office via a line amplifier and coaxial cable.

Base office instrumentation consists of two Revox recorders and a NASA binary time code (BTC) generator. The latter supplies a visual time readout, generates a 5,3 kHz time pip every second and provides the NASA binary time code. The time pip is mixed with the VLF signal for recording on the one channel of the tape recorder while the binary time code is recorded simultaneously on the second channel. A binary time code reader is connected to the tape recorder's playback head which not only insures that the time code is being recorded but also provides a visual display of the time. The NASA BTC generator may be set with a standard radio time signal to an accuracy of 10 m s.

4.2.2 Whistler analysis system

WOODS (1974) gives a detailed description of the data analysis techniques which were used in the present study.

A real-time continuous output low frequency spectrum analyser (Ubiquitous-model UA6B) is used in conjunction with an oscilloscope display and a cine camera with a fixed aperture, shutterless lens to produce a 16 mm film output of frequency components as a function of

time. The output of the spectrum analyser is displayed as a horizontal line of intensity modulated spots on the oscilloscope screen. The t-me and frequency resolution of the spectrum analyser is such that the audio range from 0 kHz to 8 kHz is swept in 10 m s with a bandwidth of 80 Hz. One hundred spots, each representing a 80 Hz frequency 'window', are displayed on the oscilloscope screen, the intensity of modulation representing the amplitude of the signal. Transport of the film provides the time dimension of the film output.

The film records facilitate surveillance of whistler trends over several hours and for monitoring changes in the VLF noise patterns. When portions of data have been chosen for analysis, they are spectrum analysed on a Sonagraph spectrum analyser which produces plots of frequency components as a function of time. Each plot represents the frequency components 80 - 8000 Hz with a resolution of 45 Hz and a time scale of 2,4 s and takes about a minute and half to produce. These plots or sonagrams are then digitized by a Hewlett-Packard 9815A digitizer which punches whistler component (frequency, time) points on punch paper tape which is then fed into the computer to be processed. A computer program using the HO and BERNARD (1973) method and incorporating a weighting factor as given by WALKER and DEANE (1974) the calculates the position of the initiating sferic and determines various parameters such as equatorial electron density, L - values and tube content for the whistlers whose frequency, time information is on the punch paper tape.

4.3 LOW LIGHT LEVEL IMAGING

A problem encountered in experiments to study precipitating electrons of various energies, is the difficulty in distinguishing, unambiguously, between spatial and temporal fluctuations e.g. rocket and satellite measurements. The morphology of low-ebergy electron precipitation patterns can be studied from ground-based recordings of auroral optical emissions which they produce. Photometers have been fairly successful in this field but there are restrictions with regards to the interpretation of photometer records. For example if s sub-visual patch, which is not pulsating, drifts through the field of view of the photometer, this could

be interpreted from the output of the photometer as being a pulsation of an auroral form.

In the systems employing very sensitive photoelectric devices for high speed imaging of auroral emissions with exposures of a fraction of a second, the spatial and temporal ambiguities discussed above do not arise, DAVIS (1966); SCOURFIELD and PARSONS (1969). The system selected for auroral research at Sanae is based on such a device, namely a silicon intensified target tube.

4.4 SANAE TELEVISION SYSTEM

The system selected and used for auroral cinematography at Sanae since 1975 is a monochrome TV chain which operates on the 625 line standard at 25 frames per second. A block diagram of the system is given in Figure 4.2. It consists of the camera head housing the silicon intensifier tube (SIT), the camera control unit (CCU), a video tape recorder (VTR) and two display monitors. System calibration is performed by means of the low brightness source (LBS). Each unit is described in more detail by LINSCOTT (1975).

A modification was made during 1975 by the author with regards to the interface built into the CCU to supply a 2VP-P sine wave to the locking circuitry of the sync pulse generator from the VTR 50 Hz vertical drive pulses. It was found that this interface was unnecessary if the VTR is operated in the TV mode and not the camera mode facilitated by a switch on the side of the VTR.

A further modification involved the connection of one of the monitors to the output of the first video amplifier stage of the VTR. This assured the operator that the composite video signal was being fed into the circuitry of the video tape record.

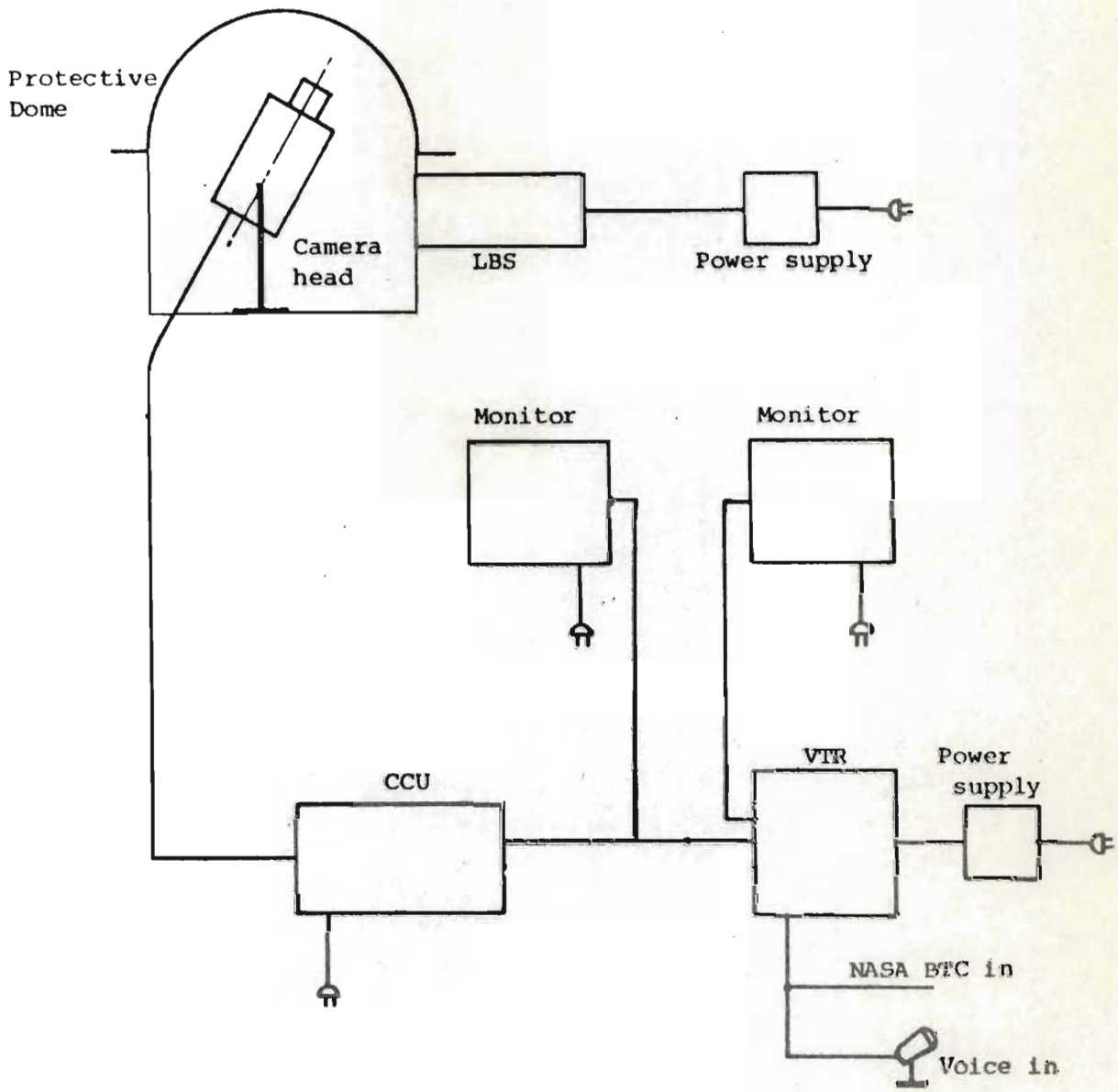

Figure 4.2 Block diagram of the SANAE auroral TV system, 1974

When the intensity of the aurora was sufficiently high it was viewed and recorded through a wide band blue filter made of Corning CS-5605543 glass. The combined response of the filter and the S20 photocathode of the SIT tube, which determines the spectral response of the system, is plotted in Figure 4.3. The filter has a peak transmission of 65% at λ 419 nm with a full width-half maximum bandpass of 95 nm. Thus the principle emissions of the nitrogen N_2^+ 1NG band system are transmitted, notably the intense (0-0) system at λ 391,4 nm. The upper cut-off of the filter is λ 520,0 nm. Thus the intense metastable O(1s) λ 557,7 nm emission with theoretical half life of approximately 0,75 is completely excluded. In this way the 'smoothing' effects of long lifetime emissions are eliminated from the data and recorded intensity variations should directly follow processes since the lifetime of the N_2^+ 1NG band is of the order of 10^{-8} s.

In conclusion the auroral imaging system used at Sanae has the following capabilities, LINSCOTT (1975). It is capable of:

(i) imaging auroral forms down to < 0,2 kR,

(ii) resolving 300 lines per picture height which is 10 lines per picture height per degree of field of view with a 12,5 nm lens. This is an angular resolution of $0,1^{o}$ equivalent to a form of dimension of hundreds of metres at an altitude of 100 km, as required. It can be improved however by using a lens with narrower field of view,

(iii) a dynamic range of about 100.

4.5 AURORAL ANALYSIS SYSTEM

A detailed diagram of the video chain in the playback (analysis) mode is shown in Figure 4.4. The system is capable of recording on

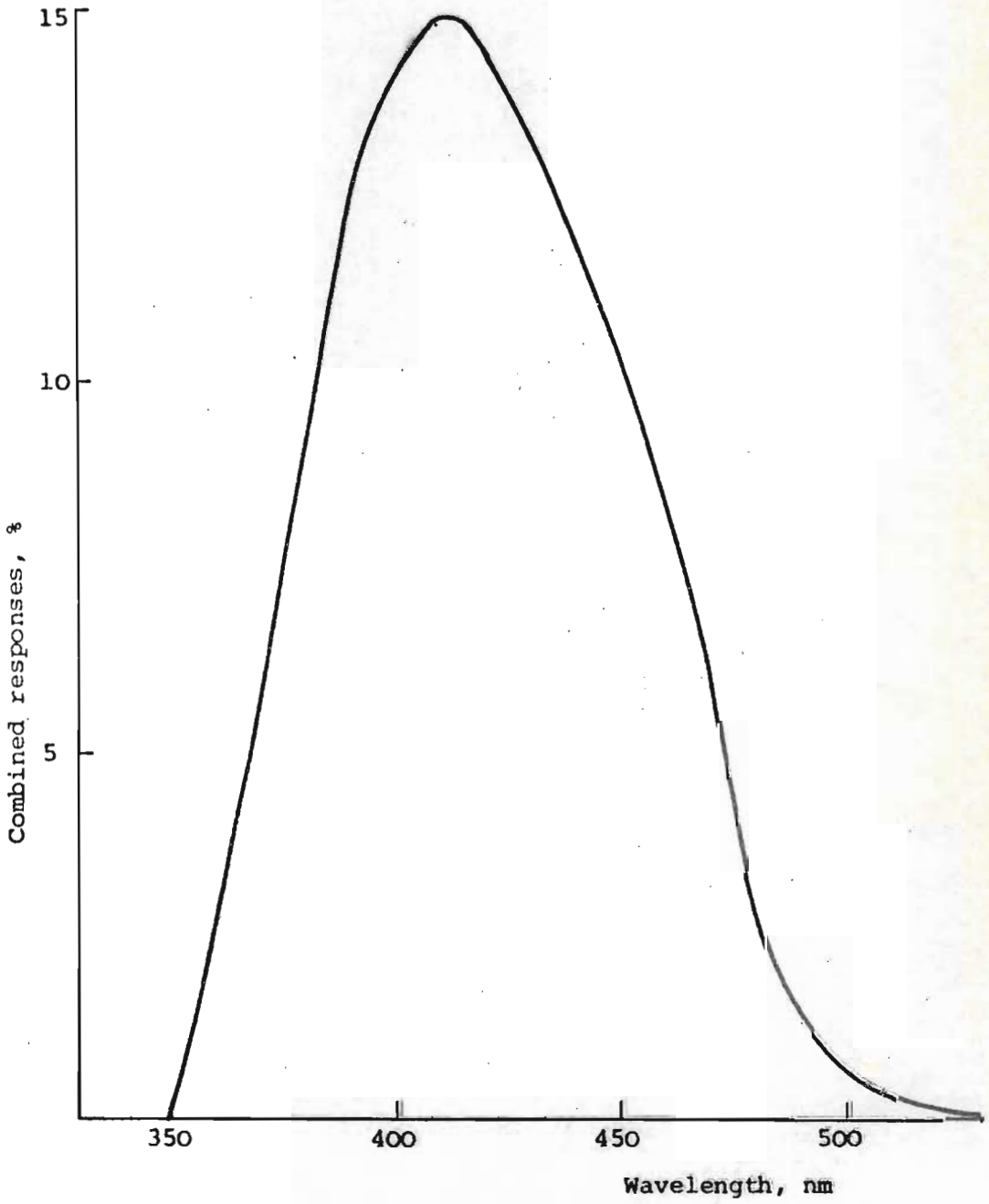

Figure 4.3 Combined responses of the 5-60 blue filter and S-20 photocathode as a function of wavelength

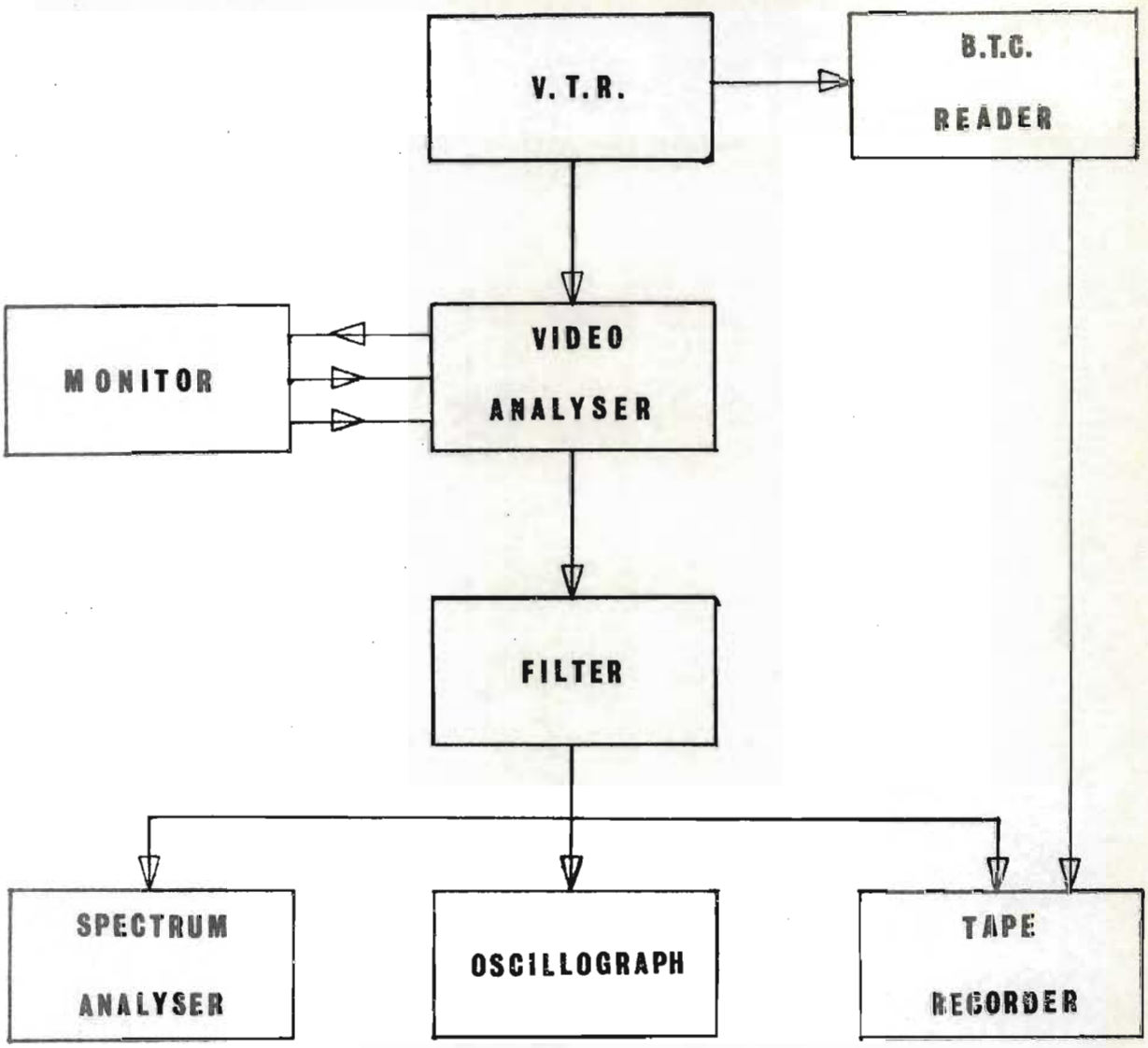

Figure 4.4 Diagram of the video chain in the playback (analysis) mode.

paper or magnetic tape, the integrated light intensity variations within a window, of any dimensions, in the recorded video picture or frame. A description of the Video Analyser is given in the following section.

4.5.1 Video analyser

The design, circuit diagram and evaluation of the video analyser will be described in some detail since this information does not appear elsewhere.

The video analyser (VA) is able to provide an analogue output (≃ 50 - 100 mV) which approximates the integrated light intensity within a preselected rectangular window as displayed on a monitor screen. A maximum of seven independent such outputs are available and the rectangular window corresponding to each channel may be continuously varied both in size and position.

The output impedance is low (≃ 50 Ω) and the VA is inserted in the video link between the video tape recorder and the video monitor. In addition the VA requires the horizontal and vertical synchronizing pulses which may be taken from the circuitry of the monitor.

The following paragraphs deal firstly with a circuit description together with circuit diagrams, board connections, a description of the sample and hold circuitry and secondly a full investigation of the performance of the analyser, including linearity, frequency response.

(a) Circuit operation

A stage-by-stage breakdown of the circuit, describing circuit components, design criteria and functioning of the various elements will be presented. Reference will be made to the

circuit diagrams that appear in Figures 4.5 and 4.6. As there are seven identical channels, stages identical in each channel are indicated as such.

(i) Interface and pulse shaping circuits

This stage consists of two sections, with minor component and component value differences. The two sections are the vertical (VERT) and horizontal (HORZ), each of which deal with their respective scan signals.

The vertical and horizontal take off points (located after the sync. separator in the monitor circuit), are suitably isolated by R_1, R_2 from the interface transistors T_1, T_2. D_1 and D_2 serve to protect the transistors from high transients and clip the inputs to $\simeq$ 0,6 V. C_3 provides negative feedback to T_1 to attenuate ringing in the switching waveform. From the collectors of T_1, T_2 the waveform is then squared by a couple of Schmidt triggers (with switching times of $\simeq$ 18 n s), which will accept slow edges and so provide jitter free triggering for the monostables. The Schmidt triggers have a maximum fan-out (low logic level) of 10 and so can comfortably drive the seven channels. A dual SN7413 Schmidt trigger I.C. is used.

(ii) Monostable timing circuits

Considering for the moment the horizontal section, the first monostable, M_1, (-ive edge triggered corresponding to the beginning of the line scan from the left hand side of the screen) provides a variable time delay (determined by C_{T_1} and variable R_1 located on the front panel) which fixes

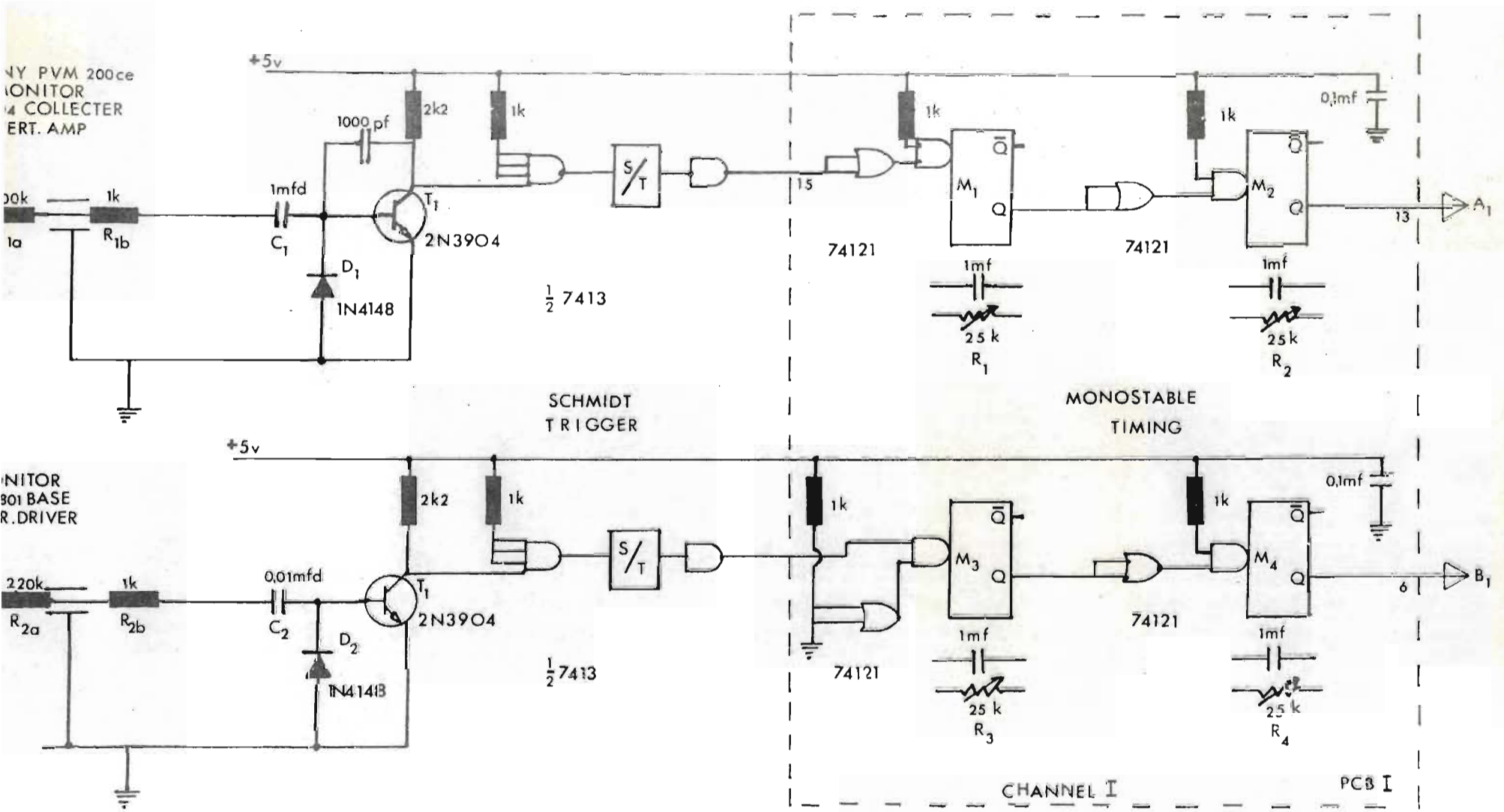

Figure 4.5 Circuit diagram of the interface, pulse shaping and monostable timing circuits for the video analyser.

the left hand side of the window on the screen. The second monostable, M_2, is triggered by M_1 and its delay period (adjustable by R_2) determines the width of the window.

The vertical section follows the same description *mutatus mutandis* with the sync. pulse determining the top of the window. SN74121 monostables are used. The outputs from M_2, M_4 each describe a path (horizontal and vertical) on the screen which, when ANDed, produce the required window.

(iii) AND circuitry (Figure 4.6)

The horizontal and vertical pulse chains would, if injected back into the video signal straight away, produce a crossed pathway on the monitor screen. If these two paths are ANDed (using SN7400 NAND gates G_1 - G_8), the required window would be produced. This window from each of the seven channels is then OR-gated by a 8-input NAND gate (SN7430) and the combined signal is then injected back into the video signal via two attenuators one in each of the switched pathways. The one path goes directly into the video line whilst the other is inverted, thus enabling either a light or dark window to appear on the screen.

(iv) Sample and hold circuitry

A field effect transistor (FET, p-channel 2N5485) is used to gate the video signal corresponding to the intra-window intensity into the integrating capacitor C_I, which is a low leakage polycarbonate type. Three values of C_I (0,1 mfd; 0,1mfd; 0,01 mfd) can be selected from the front panel. The gating signal for the FET is taken from

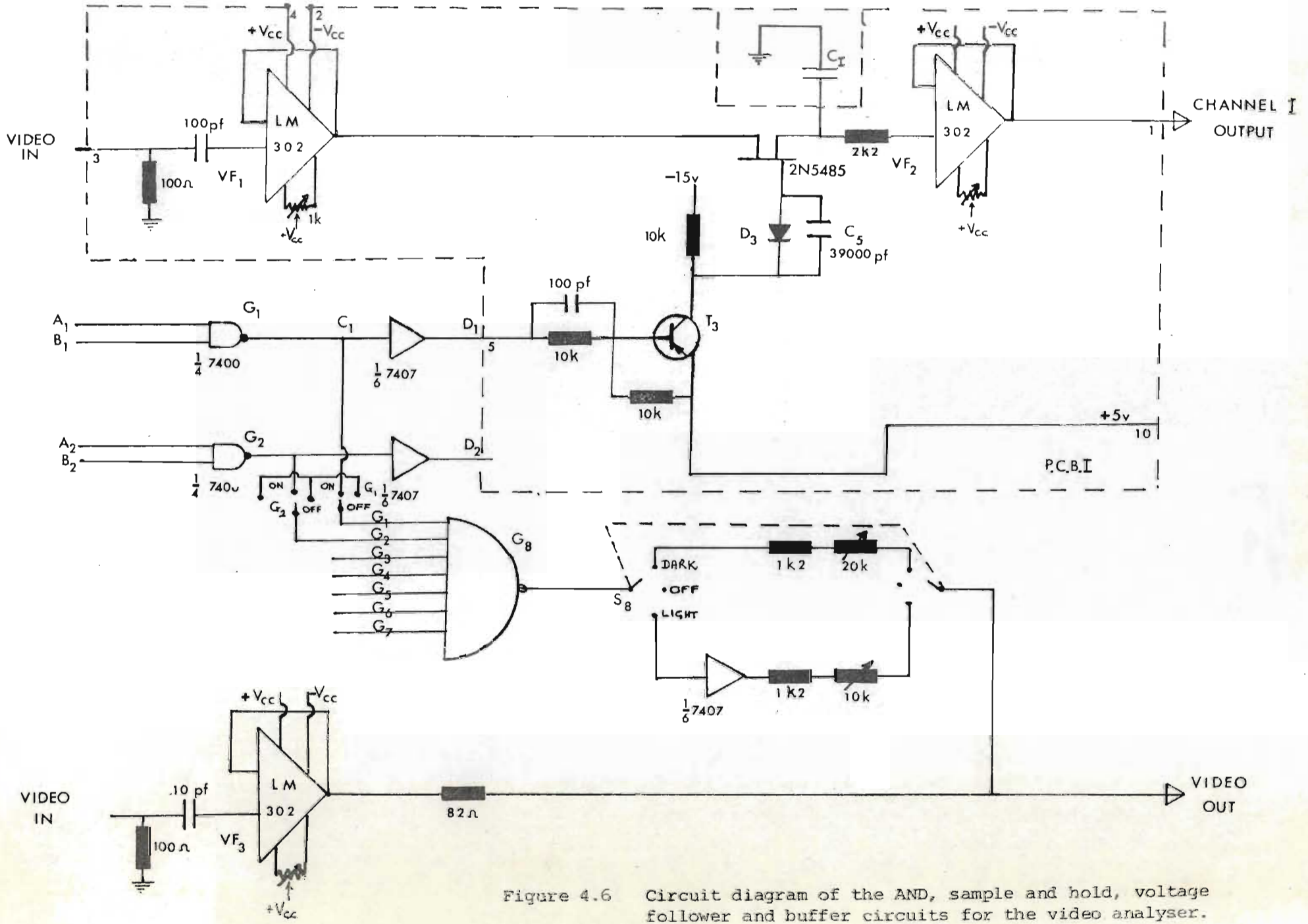

Figure 4.6 Circuit diagram of the AND, sample and hold, voltage follower and buffer circuits for the video analyser.

the NAND gates just before the 8-input OR gate i.e. point C_1 in Figure 4.6. To isolate this point from the transistor switch T_3, an open collector buffer is used ($^1/6$ SN7407). The collector of T_3 switches between +5 V, -15 V and is clipped by D_3 to a 0 V, -15 V signal which is more than sufficient to gate the FET.

(v) Voltage-follower, buffer circuits

Monochrome video circuitry requires a bandwidth of at least 3 - 4 MHz. The LM302 voltage follower adequately performs this task. As the video signal is fed to each of the seven channels in the sample and hold circuitry, the LM302 (VF_1) is used to isolate each FET from the common take-off point. In addition, to prevent the window pedestal from breaking through to the video signal (which would then unfortunately be sampled), a voltage follower is used here as well (VF_3). The main advantage in using the LM302 is its excellent buffer capability. It is this property which is used by buffer VF_2 in Figure 4.6.

(vi) Power supply

The circuit diagram is indicated in Figure 4.7. The circuit is straight forward supplying the necessary +15 V, -15 V and +5 V needed.

(vii) Circuit boards

Those components which appear within the dotted area in Figures 4.5 and 4.6 are all located on one printed circuit board (PCBI). This board is repeated for each channel. All other components, except those in the power supply and the front panel controls, are located on the main PC board PCB II.

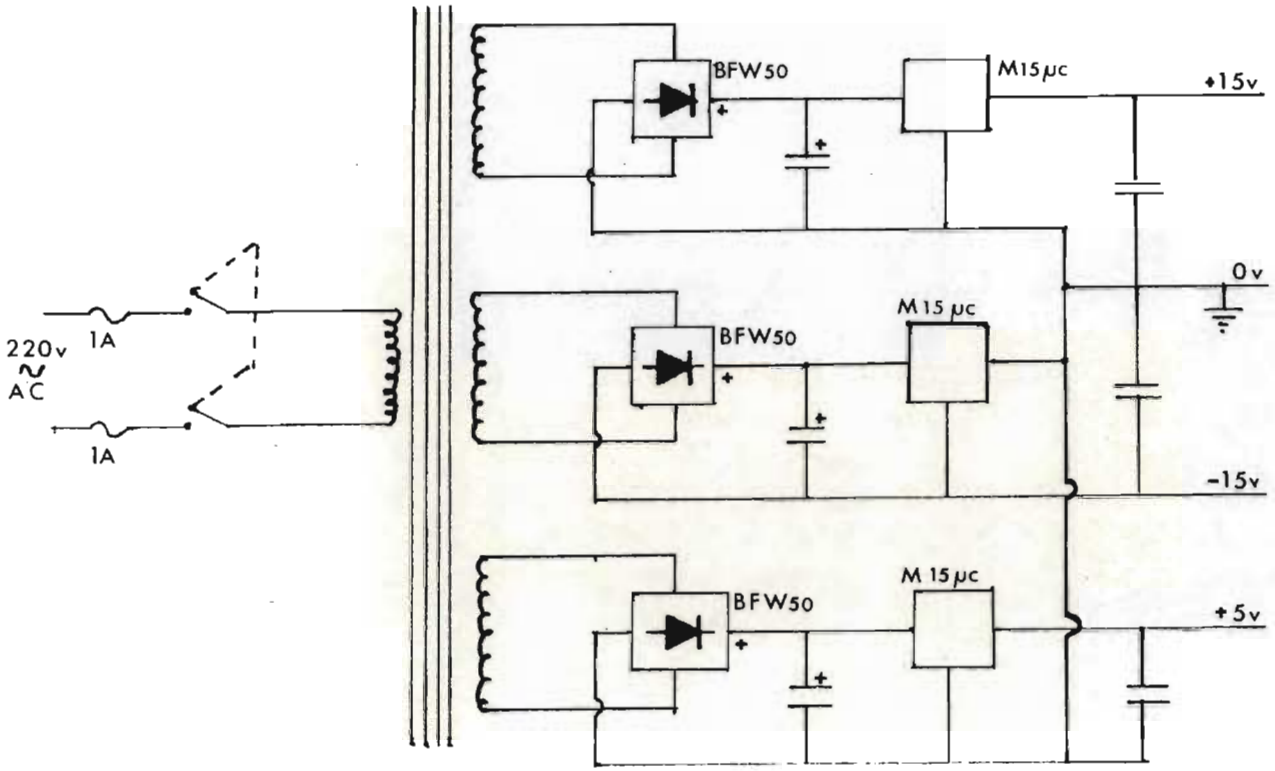

Figure 4.7 Circuit diagram of the power supply for the video analyser.

(b) Performance tests

(i) Linearity

In order to determine the linearity of the VA circuit, and the effect of different values of the integrating capacitor, a photographic board was constructed. It was sprayed matt black and two white-paper rectangles were glued to its surface. Under suitable ambient lighting, a rectangular window was recorded using the Sony AV3670CE video tape recorder and Philips LDH 150/08 camera.

Figure 4.8 shows the relative locations of the rectangular windows and the target rectangles. The shaded rectangles represent the analyser window and unshaded block, the rectangular image target. By using a graticule on the surface of the monitor screen, the position of the window relative to that of the target could be measured. The window was moved across the target and the output from the analyser was measured with a voltmeter. This was done for the vertical and horizontal cases and for C_I equal to 1,0 mfd and 0,1 mfd capacitance.

The results are shown in Figures 4.9 and 4.10. The recording for these results was made using ambient lighting that did not cause streaming at the target boundary. For the 1,0 mfd capacitor, the response was approximately linear in the horizontal and vertical directions. However, for the 0,1 mfd capacitor, the vertical response was distinctly non-linear.

Assuming that the effective *on* resistance of the FET and the output impedance of the voltage follower of the RC bandpass filter associated with the sample and hold capacitor is 1 KΩ

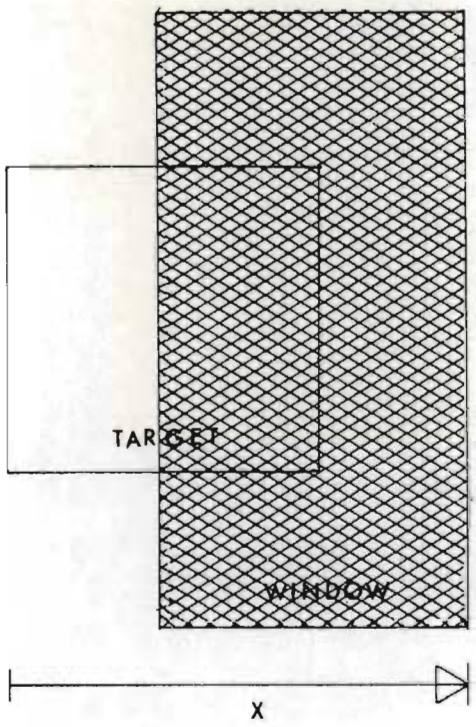

HORIZONTAL

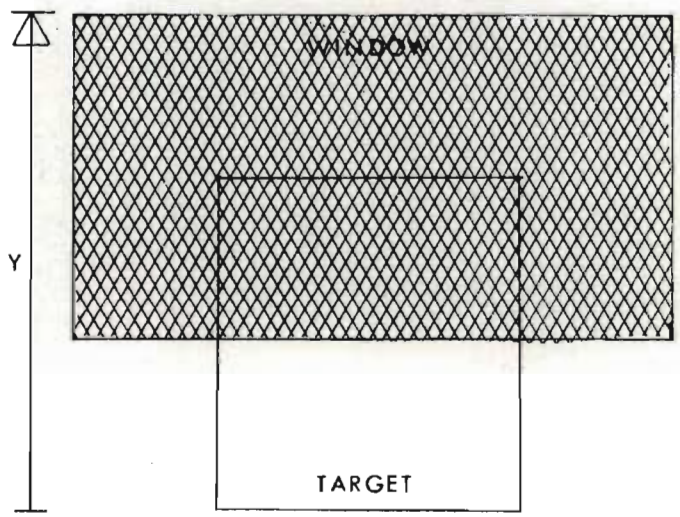

VERTICAL

Figure 4.8 The relative locations of the rectangular windows and target rectangles.

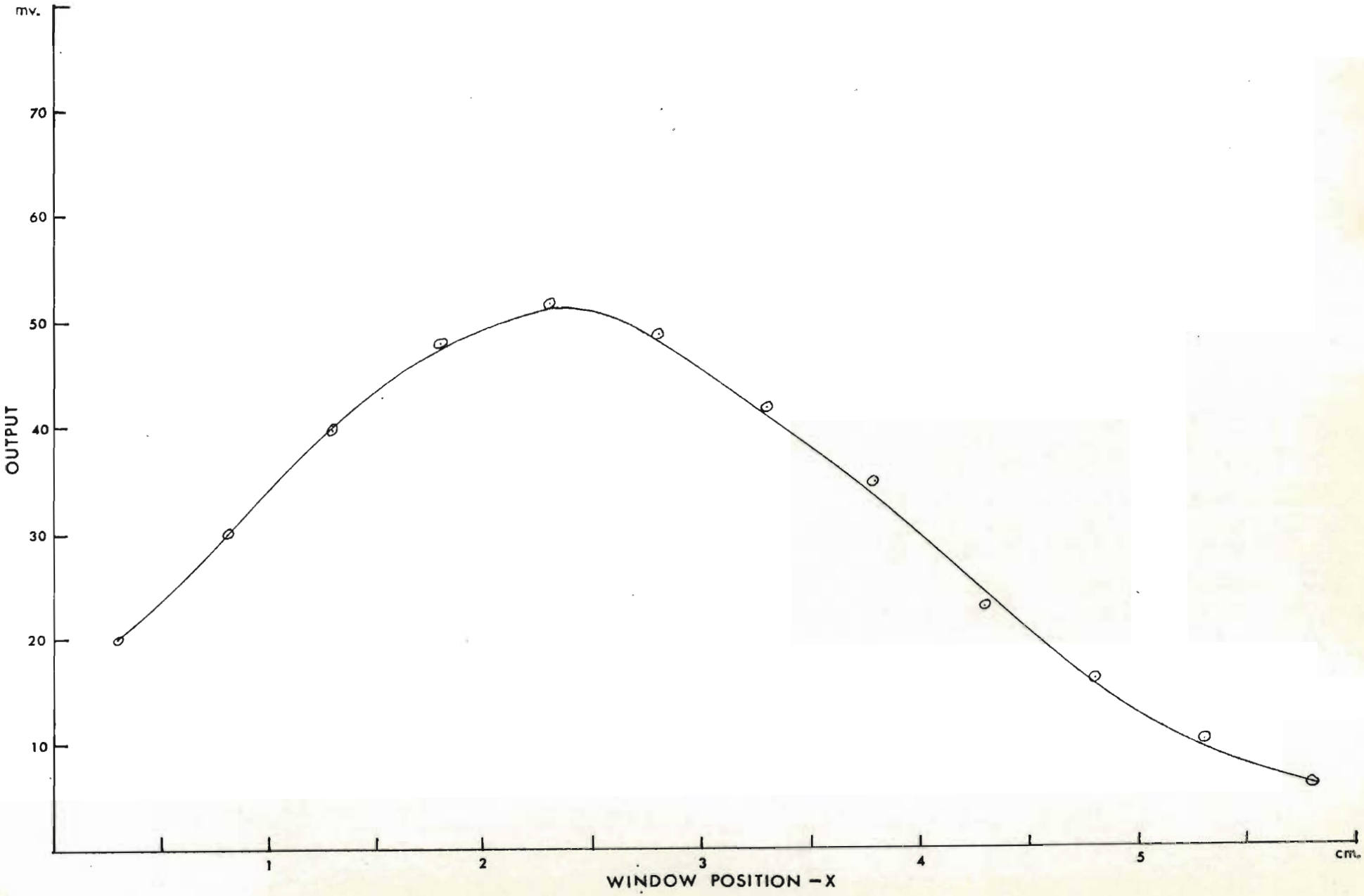

Figure 4.9 Plot of the video analyser output (mV) versus the window position (cm) relative to the rectangular target for the horizontal case.

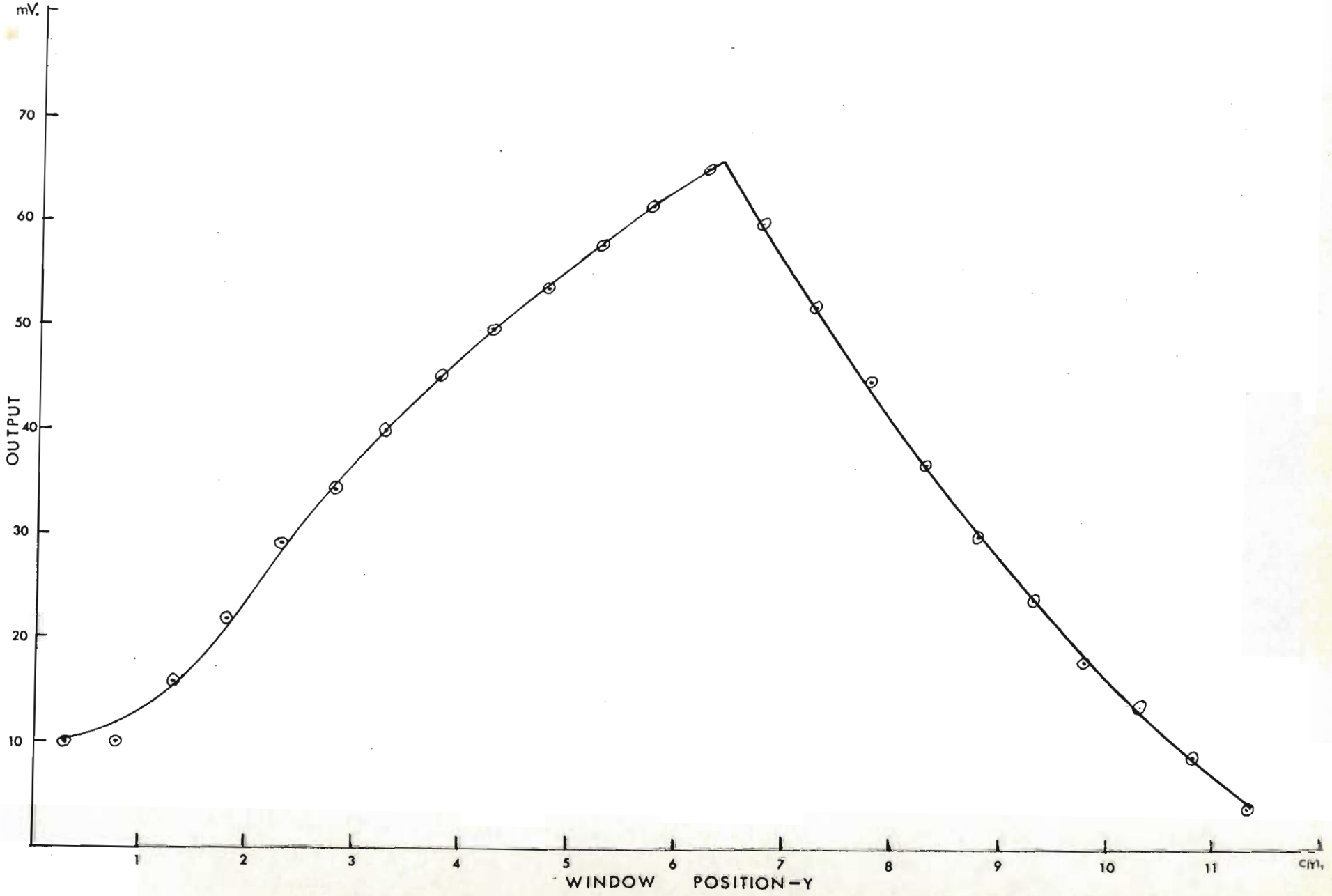

Figure 4.10 Plot of the video analyser output (mV) versus the window position (cm) relative to the rectangular target for the vertical case.

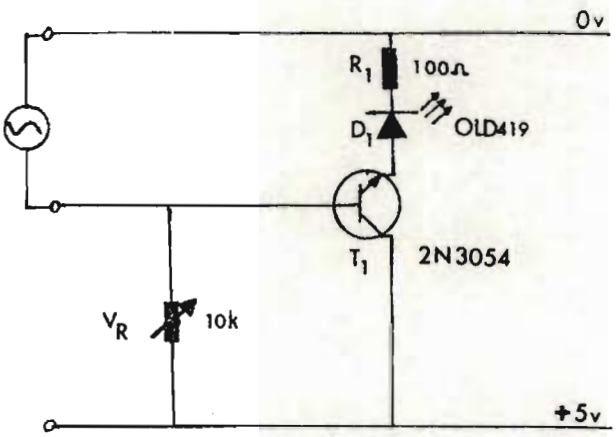

Figure 4.11 LED circuitry.

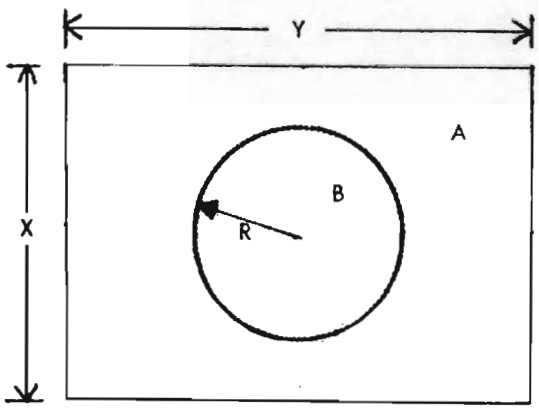

Figure 4.12 Dimensions of window and central circle of uniform illuminosity.

then this provides an attenuation of -4×10^{-5} dB. This is an insignificant attenuation so the integrating capacitor could be easily increased to 50 - 100 mfd without an appreciable increase in the attenuation of the frequencies under consideration to provide a more linear response.

(c) Integration of intensity versus area

An investigation of the system's response to a central bright area superimposed on a background of constant brightness, was made in order to determine the system's accuracy in approximating the integral of the intensity over the dimensions of the window.

The central bright area was spherical in shape being the image of an out of focus light emitting diode (LED) mounted on a black board. The image was not focussed so that the dimensions of the LED as they appeared on the screen were larger than they would normally have been if the image had been focussed properly. In this way a circle of approximately uniform brightness of diameter ≈ 2 cm was recorded. Windows of various sizes were placed over this area and the integrated output displayed on an X-Y plotter. The diode was modulated at an arbitrary frequency of 0,5 Hz. Figure 4.11 shows the LED circuitry. The windows were adjusted so that the smallest window just contained the central circle. Ambient lighting was such as to make the background uniformly grey. The output from the video analyser was analysed by the Ubiquitous Model UA 6B spectrum analyser.

Consider the areas A and B in Figure 4.12, then

$$V_A = \alpha A$$
$$V_B = \beta B$$

where V_A, V_B = integrated intensities for areas A and B of uniform brightness

and α, β = constants.

The integrated intensity V_{AB} over the window is

$$V_{AB} = \frac{V_A + V_B}{A + B}$$

$$= \frac{\alpha(xy - \pi R^2) + \beta \pi R^2}{xy}$$

$$= \alpha + \frac{\gamma \pi R^2}{xy}$$

where

$\gamma = (\alpha + \beta)$ = constant.

Therefore the graph of V_{AB} versus $\frac{1}{xy}$ should be a straight line. Figure 4.13 shows the plot of V_{AB} verses $\frac{1}{xy}$ for four window sizes. The relation is clearly linear.

(d) Frequency response

In order to gauge the circuit's response to a time varying signal a synthetic 'pulsating aurora' was constructed by changing the current through the LED at a frequency of 5 Hz with the aid of a signal generator and circuitry as shown in Figure 4.11. V_R was adjusted in order that the transistor was correctly biased. The specification of the LED OK10CD419 are such that the diode exhibits linear light output versus current characteristics.

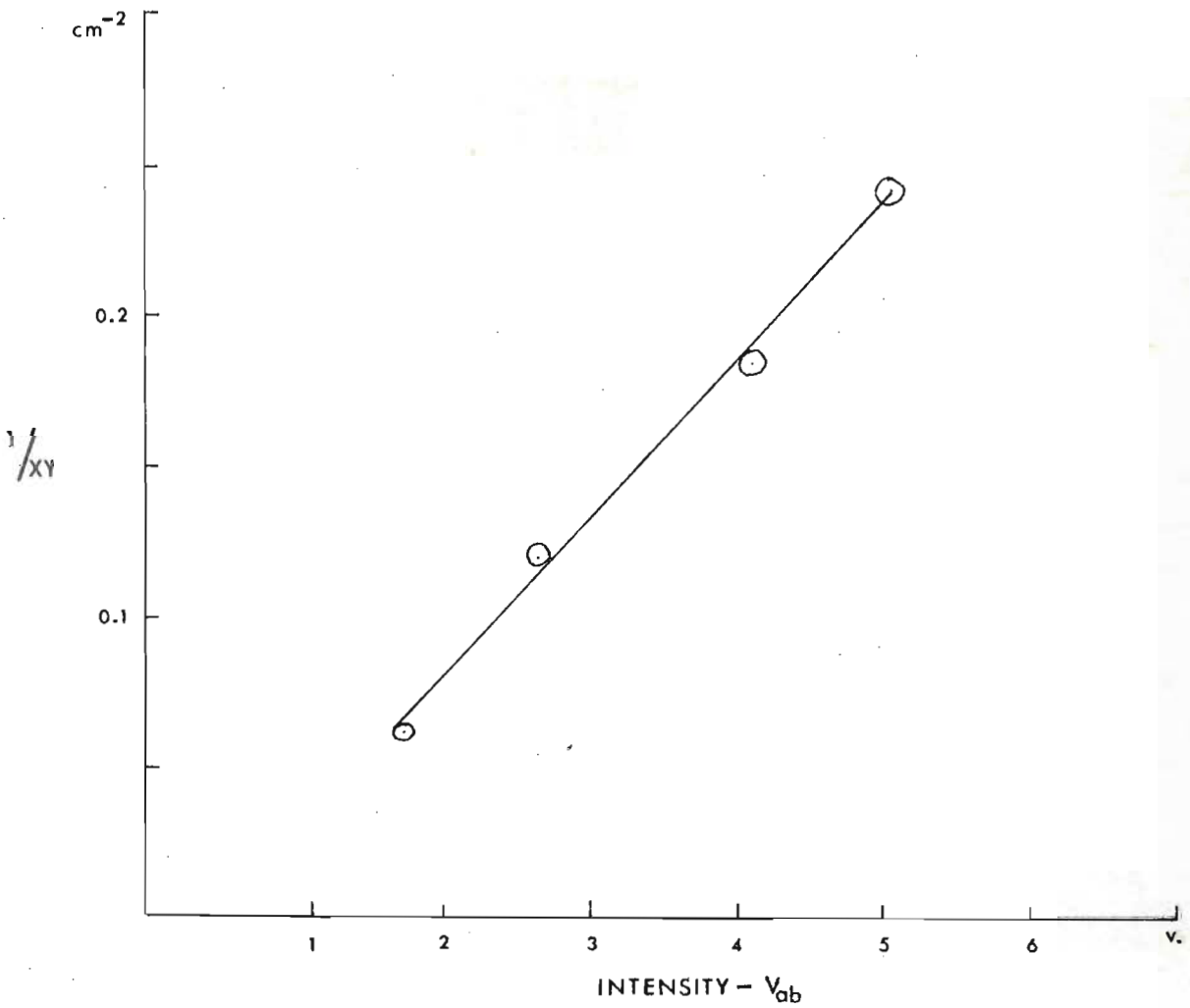

Figure 4.13 Plot of $^{1}/_{XY}$ (cm^{-2}) versus V_{AB}(V).

The spectrum of the signal obtained from video analyser of the pulsating image showed very little broadening when compared with the spectrum of a 5 Hz signal from the signal generator. Various frequencies were used and the same frequency response was found.

4.6 HISS AND AURORA ANALYSIS

When the Ubiquitous spectrum analyser is used in the calibrate stop mode it can act as a filter of 80 Hz bandwidth centred at any frequency from 0 - 40 kHz. The intensity of the VLF signal at a frequency, for e.g. 4 kHz, is then available at the linear output of the Ubiquitous when the VLF signal is applied to the input of the Ubiquitous. This facility was used in the analysis of Hiss.

Both the signal containing the intensity of Hiss at a chosen frequency and the signal containing the integrated light intensity of a window positioned in an auroral form was fed through a bandpass filter, and recorded on a FM tape recorder capable of recording frequencies down to 0 Hz.

These recorded signals were then sampled at a high rate and analysed by the Hewlett-Packard 5451B Fourier Analyser system which computed power spectra, cross-correlation functions and coherencies between the signals of the intensities of hiss and auroral light. Figure 4.14 shows a block diagram of the analysis system described above.

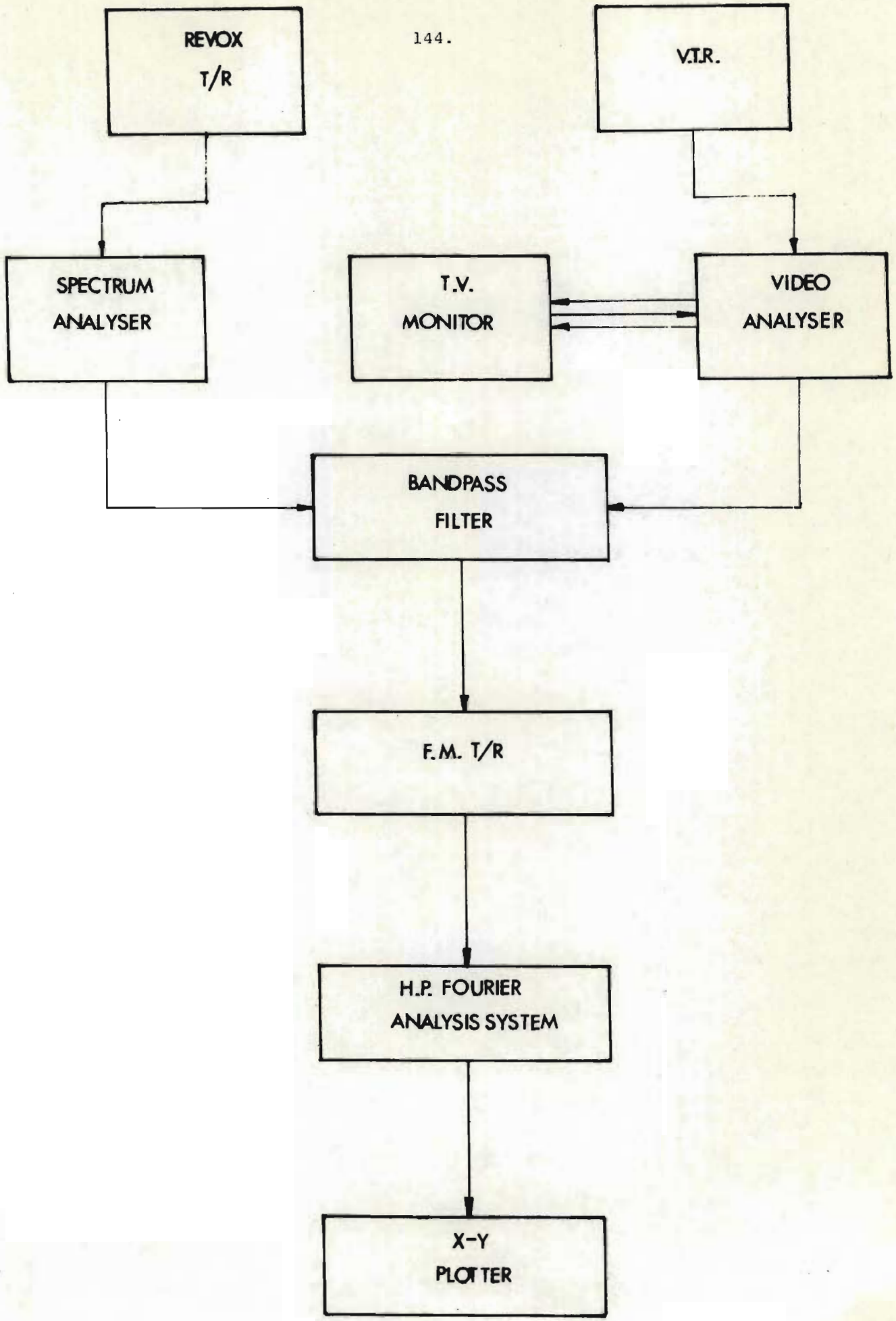

Figure 4.14 Block diagram of anylsis system for the simultaneous analysis of hiss and aurora.

CHAPTER FIVE

THE SPATIAL RELATIONSHIP BETWEEN AURORAL FORMS AND CLOSED MAGNETIC FIELD LINES

5.1 INTRODUCTION

As discussed in Chapter Three the nose frequency of whistlers propagating along a closed field line can be used to determine the L-value of the field line. Hence, from simultaneous ground based recordings of aurora and whistlers the position of an auroral form can be related to the position of a closed field line. Some of the work to be described here has already been published elsewhere, (Duthie and Scourfield (1977)).

5.2 WHISTLER DATA

In a detailed study of the plasmapause, Carpenter (1966), indicated that about 15% of the whistler spectrograms from the Antarctic station at Eights (L = 3,89) showed clearly visible knee components. Carpenter and Park (1973) subsequently recommended that the optimum station location from which to observe, direcly overhead, any events associated with the plasmapause was at L = 3,7. In a synoptic study of more than 2490 hourly recordings at SANAE (L = 3,98) Woods *et al* (1974) found that less than 0,7% clearly showed visible knee components, even though SANAE is located close to the optimum position. However, components travelling on field lines to the plasmapause will more than likely have very low nose frequencies (< 5 KHz) and the determination of a density profile from the group of whistlers which these low nose frequency components belong too, will be indicative of how close to the plasmapause the field lines, along which these low nose frequency components travelled, are.

5.2.1 Data Analysis

16 mm film records of continuous whistler data were obtained as described in Section 4.2.2. The data were divided into 15 minute intervals, commencing at the hour, as described in a similar study by Rabe and Scourfield (1975) and Linscott (1975). During any 15 minute interval, the dispersion characteristics of successive whistler groups remain essentially unchanged. As many whistler groups as possible (usually about five) were chosen per interval for computer analysis. Rabe and Scourfield (1975) indicated that at least ten groups are required, but often during magnetically disturbed conditions, the whistler rates are not high enough to satisfy this.

Three points in coordinates of frequency, and of time relative to an arbitrary origin, were scaled off each whistler component of each group. By fixing a reference component for each 15 minute interval, successive whistler groups within the interval shared the same arbitrary time origin. The method of Ho and Bernard (1973) was used to calculate the position of the initiating sferic for each component in all groups in an interval. A mean initiating sferic position was then obtained for each 15 minute interval. Because the absolute error in the Ho and Bernard (1973) method increases with increasing nose delay, t_n, a weighting factor of t_n^{-2}, as given by Walker and Deane (1974), was used to favour the components with smaller nose delays.

From initiating sferic positions values of duct equatorial geocentric distances and electron densities were calculated, using a centred dipole magnetic field model. The DE-1 diffusive equilibrium model of electron density distribution was used in the calculations for ducts, inside the plasmapause. This model was given by Park (1972) as discussed in Section 3.2.2.

5.2.2 Whistler Data Selected

All VLF data coincident with recorded auroral data during 1975 was selected for reduction to 16 mm film records. From these records three nights, 12th June, 14th July and 16th July, were chosen for analysis following a criteria of relatively high whistler activity. The reason for this criteria was because experience showed that when good auroral data was available, the whistler rate was very poor and more than often non-existent.

The three periods chosen were:

(i) 0130 UT - 0400 UT 12th June ($K_p = 3^o, 3^+$)
(ii) 0000 UT - 0400 UT 14th July ($K_p = 3^o, 2^+$)
(iii) 0100 UT - 0400 UT 16th July ($K_p = 3^+, 3^o$)

There were no knee components present in this data. However, there were very low nose frequency components present which gave one access to information over a spread of closed field lines, extending to the proximity of the plasmapause.

5.2.3 Results of the Whistler Analysis

For every 15 minute interval during the nights selected the average L-values of the duct, along which the whistler component with the lowest nose frequency travelled, is calculated and plotted in Figure 5.0.

Due to the ring current effect discussed in Section 3.2.4 it was necessary to correct the duct L-values using the curves of Figure 3.3. The upper diagram (diffusive equilbrium conditions), was used for the correction. Curve (a) in the diagram represents the effect of the ring current for $D_{ST} = 25$ nT. During the periods under

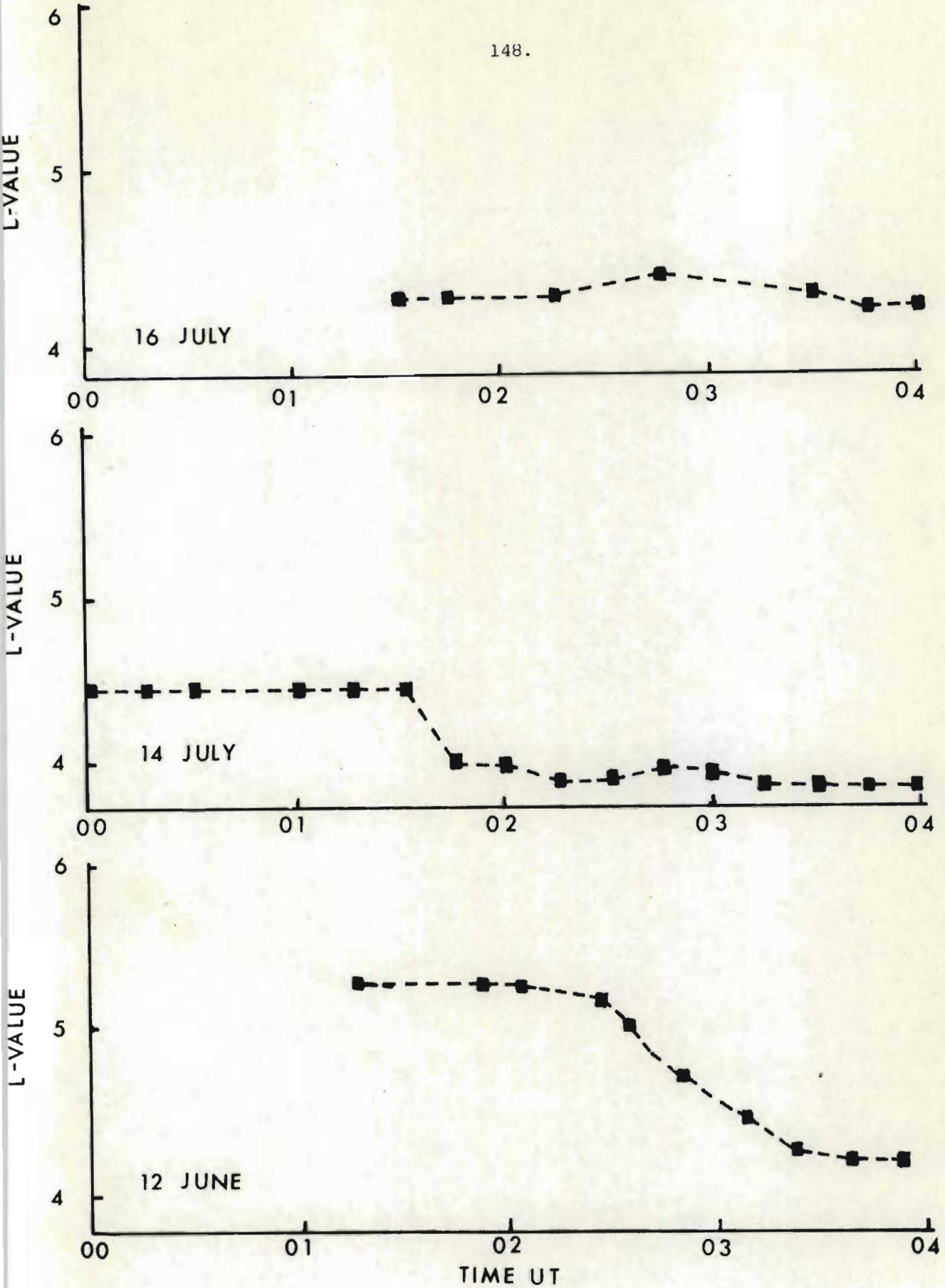

KEY : ■–■–■ HIGHEST LATITUDE WHISTLER COMPONENTS.

Figure 5.0 Plots of the L-values of the highest latitude whistler components vs Universal Time on the 16 July, 14 July and 12 June, 1975. The vertical side of each solid rectangle represents the error in whistler method (Section 5.2.4).

consideration the D_{ST} values ranged from -6 to 9 on 12th June, -14 to -21 on the 14th July and -10 to -11 on the 16th of July. Consequently the L-value corrections were interpolated between curve (a) and the dipole curve.

Instantaneous equatorial density profiles for the period 0215 - 0245 UT on 12th June 1975 is presented in Figure 5.1. Also calculated is an equatorial density profile for 0015 to 0045 UT on 14th July, 1975 as plotted in Figure 5.1. Because of the lack of the number of well defined components in the whistler groups of the 16th July, an equatorial density profile was not calculated for this period.

5.2.4 Errors in the Whistler Method

Errors in the whistler method of calculating duct L-values and N_e(eq) are both systematic, due to electron density distribution model approximations, and experimental due to errors in measurement. Park (1972) provided information for the calculation of the systematic errors in the DE-1 model used in the present analysis. Details of the calculations of these errors are given in Appendix A1, and the results are summarized in Table 5.1 together with Park's (1972) estimate of experimental errors. Park discussed uncertainties due to ionospheric dispersion and subionospheric propagation. Because these errors are very small or negligible in L-value and smaller than measurement errors for N_e(eq), they are not considered in the present analysis.

The systematic errors of the data plotted in Figure 5.1 are very much smaller than the duct symbols in L-value, and comparable to the symbols in N_e(eq). Experimental errors, as indicated by the standard deviations calculated for each duct were the same size as the

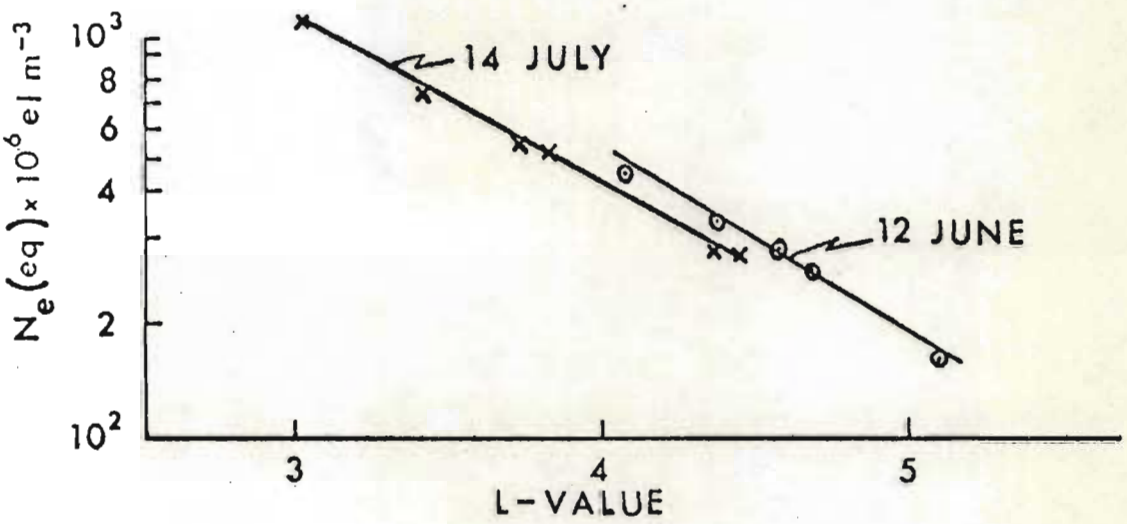

Figure 5.1 Plot of electron density, $N_e(eq)$, vs. L-value for the highest latitude whistler components observed during 0015 - 0045 UT, 14 July, and 0230 - 0245 UT, 12 June, 1975.

Nature of error		Max error in L-value (%)	Max error in N_e(eq) %
Systematic	DE - 1	0,05	0,84
	R^{-4}	0,1	2,4
Experimental		1	8

Table 5.1 Uncertainties in the whistler method of calculating L-value and N_e(eq) of ducts

symbols, never exceeding a standard deviation in L-value of 0,04 L.

5.2.5 Discussion

The dashed line in Figure 5.0 represents a 15 minute plot of the L-value of the duct along which the whistler component, with lowest nose frequency received at SANAE, travelled. Care must be taken in identifying this plot as a plot of the L-value of the last closed field line because a whistler propagating along a field line of higher L-value than the dashed line may not have been received at SANAE due to poor ionospheric propagation conditions which is typical of disturbed magnetic conditions which existed throughout the periods of observation Figure 5.2. However, one definite conclusion is that all field lines with L-values lower than the dashed curve are closed over the periods of observation.

During the nights of the 14th and 16th July the L-value of the ducts represented by the dashed line change very little. On the 14th July the L-value changes by 0.1 L and on the 16th July the L-value changes by 0.5 L. There is, however, a drastic change from L = 5.2 to L = 4.2 between 0230 UT and 0330 UT on the 12th June.
The change in L-value can be interpreted in three ways:

(i) The last observed closed field line has moved towards the earth from L = 5.2 to L = 4.2 in L-value, or

(ii) Ducts along which the lowest nose frequency component propagated are no longer closed, or

(iii) The whistler components previously travelling along field lines with L-value L = 5.2 are no longer received on the ground due to poor ionospheric propagating conditions.

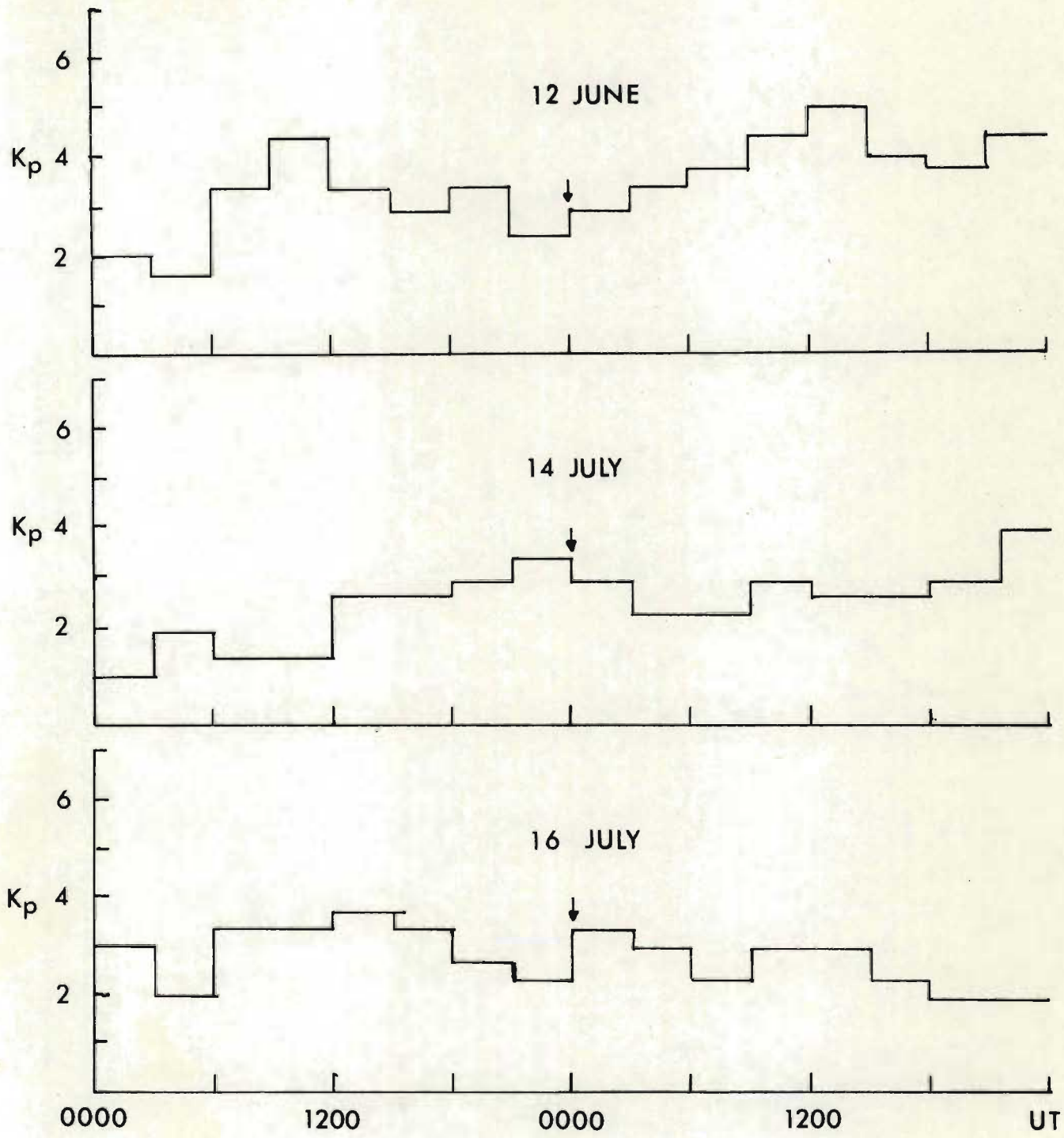

Figure 5.2 Plots of k_p-values versus Universal Time particular to the 16 July, 14 July and 12 June, 1975.

The first interpretation would indicate a fast variation in plasmapause position which has not previously been observed and is therefore an unlikely explanation.

The whistler groups over the period 0230 UT to 0330 UT also indicate 'dropping out' of whistler components rather than a gradual movement of the component with the lowest nose frequency to higher nose frequencies.

Carpenter (1966), showed that the ducts could be expected to have lifetimes of the order of a day, so that in the present case it is likely that some rapid decay mechanism affected observations of existing ducts. Such a mechanism may involve wave-particle interactions or whistler attenuation in the coupling between the duct and the earth ionosphere waveguide. This would support interpretations (ii) and (iii).

These interpretations will be discussed in greater detail in Section 5.3.2 when the auroral data over this period is investigated in conjunction with the whistler data.

Due to the absence of knee whistler components the position of the plasmapause cannot be found directly. However, the equatorial density profiles of the 12th June and 14th July indicate that the high latitude whistler components (whistler components travelling along ducts with high L-values) are propagating near the outer boundary of the plasmasphere. This is evident from the correspondence of the highest latitude whistler component to an electron density of 300×10^6 el m^{-3} on the 14th July and 170×10^6 el m^{-3} on the 12th June (Figure 5.1), which are electron densities typical of the outer plasmasphere. Thus, although the plasmapause position cannot be determined precisely, it must be situated at a slightly higher L-value than the dashed lines in Figure 5.0.

The question of longitudinal spread of the present data cannot be satisfactorily resolved because it was recorded without direction finding facilities. Carpenter stated that the longitudinal spread of ducts excited by a single whistler group appears to vary with local time, being relatively small at night. However, he pointed out that a spread of up to 15^{o} in longitude about the observation station was sometimes excited by separate whistler groups.

5.3 AURORAL DATA

Visual aurora was observed on 30 nights during 1975 and recorded on video tape using the TV system described in Section 4.4. On some nights there were indications of activity, but cloud cover or bright moonlight masked the aurora.

5.3.1 The Location of Auroral Forms

The L-value of a point in an auroral form may be calculated as a function of its geographic latitude and longitude and its height above the surface of the earth. To determine the geographic latitude and longitude of a point in space as recorded in a video picture, the latitude and longitude of the TV camera and the direction in which the camera is pointed in terms of elevation and azimuth has to be known. The calculation of the position of stars in a known star pattern, also recorded in the video picture, is an accurate and convenient way of making such a determination.

Once the star pattern had been identified with the help of a Star Atlas and the time of the observation noted from the time code recorded on the sound channel of the video record, a program 'ELEVAZI' calculated the angle of elevation and azimuth with respect to SANAE of any star.

By interpolation, the video picture and also the monitor screen was graduated into angles of elevation and azimuth. The angle of elevation and angle of azimuth of any auroral form was then obtained to an accuracy of $\pm 1^{o}$. A subroutine 'ANGEOG' converted these parameters of the auroral form into the corresponding geographic latitude and longitude of the auroral form with an added input parameter of height. Finally the L-value of the aurora was computed using program 'L VALUE' (Appendix B2) which makes available the choice of seven main magnetic field models and a facility for using updated models such as the model of the main magnetic field for epoch 1975 as given by Barraclough *et al* (1975) which is used in this analysis.

The plot of L-values versus geographic longitude and latitude in the vicinity of SANAE is shown in Figure 5.3 as determined by using the main magnetic model for epoch 1975 given by Barraclough *et al* (1975). A grid is provided which, when superimposed on Figure 5.3, gives contours of equal elevation from SANAE for a height of 100 km above the earth's surface. The oval lines represent the loci of points which have equal angles of elevation from SANAE and the radial lines are loci of points with equal angles of azimuth from SANAE. With the aid of the grid and Figure 5.3, one can determine the L-value of any point 100 km above the earth's surface whose angles of elevation and azimuth are known.

The error in L-value due to a measurement error of $\pm 1^{o}$ in the angles of elevation was typically 0,3 L at low angles of elevation and 0,2 L at high angles of elevation. An error of $\pm 1^{o}$ in the angle of azimuth resulted in an error in L-value much smaller than 0,2 L. If an altitude of 110 km were chosen, it would involve an error in L-value whose size depends on the geographic position of the point of which the L-value is desired. This is discussed in more detail under the auroral data Section 5.3.2.

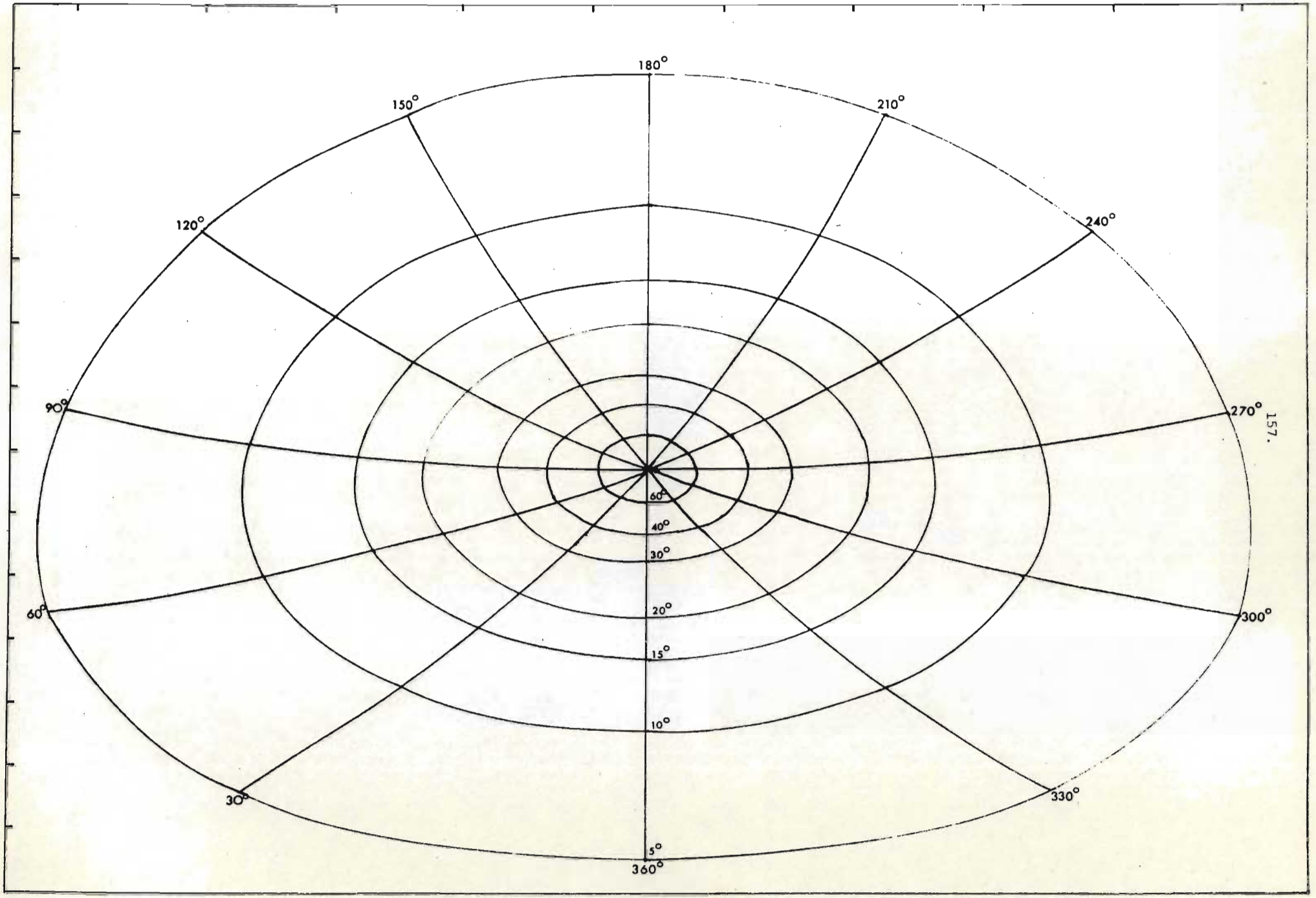

Grid for Figure 5.3.

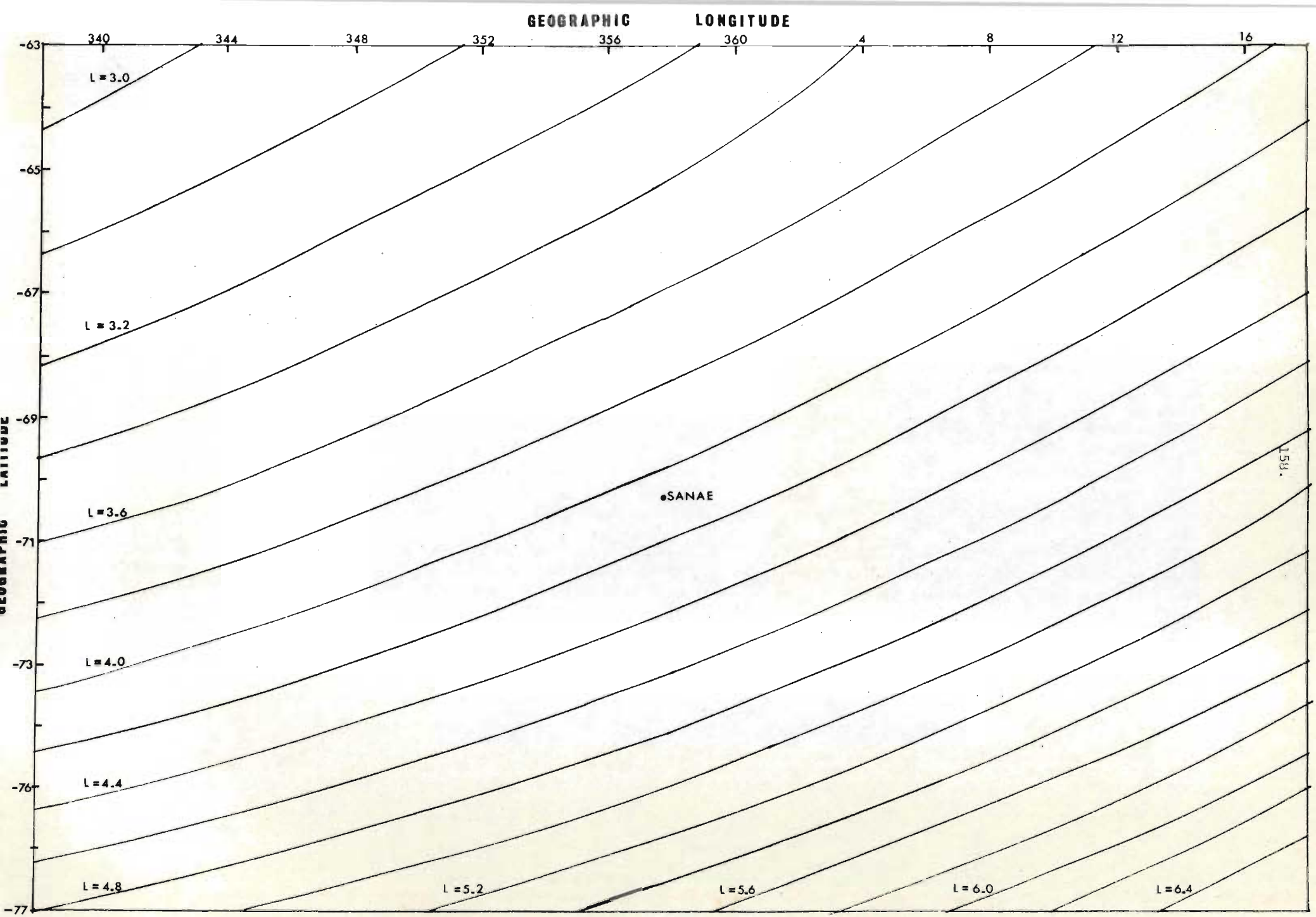

Figure 5.3 Plot of L-values versus geographic longitude and latitude in the vicinity of Sanae for 1975.

5.3.2 Auroral Activity on 12th June, 14th and 16th July

Periods 2345 to 0400 UT, 14th July and 0115 to 0400 UT 16th July, 1975.

The results of analysis of the auroral data for these periods are summarized in the plots of L-value against time shown in Figure 5.4 .

Diffuse aurora, represented by dark shading in the plots, was observed throughout these periods with well-defined equatorward and poleward edges. There is little change in position of the poleward and equatorward edges, the averaged position of the equatorward edge being at L = 4,8 on 14th July and L = 4,6 on 16th July. The latitudinal extent of the diffuse aurora varies between 250 km and 320 km.

The region poleward of the diffuse aurora was partially occupied by auroral bands of varying activity and position. This region is represented in Figure 5.4 by vertical lines. A dark area usually separated the diffuse auroral from the bands but when the latter were very active they moved into the diffuse aurora.

At $\sim$ 0250 UT on 14th July and $\sim$ 0230 UT on 16th July band activity gave way to pulsating patches. These are depicted in Figure 5.4 by the black spots. The patches were embedded in the diffuse aurora and pulsated with periods varying between 5 s and 10 s. The intensity of the diffuse aurora was, typically, $\sim$ 1,5 KR dropping to $\sim$ 0,5 KR at the time when the pulsating patches appeared. Pulsating patches switched off to background from a maximum intensity of $\sim$ 0,5 KR above background.

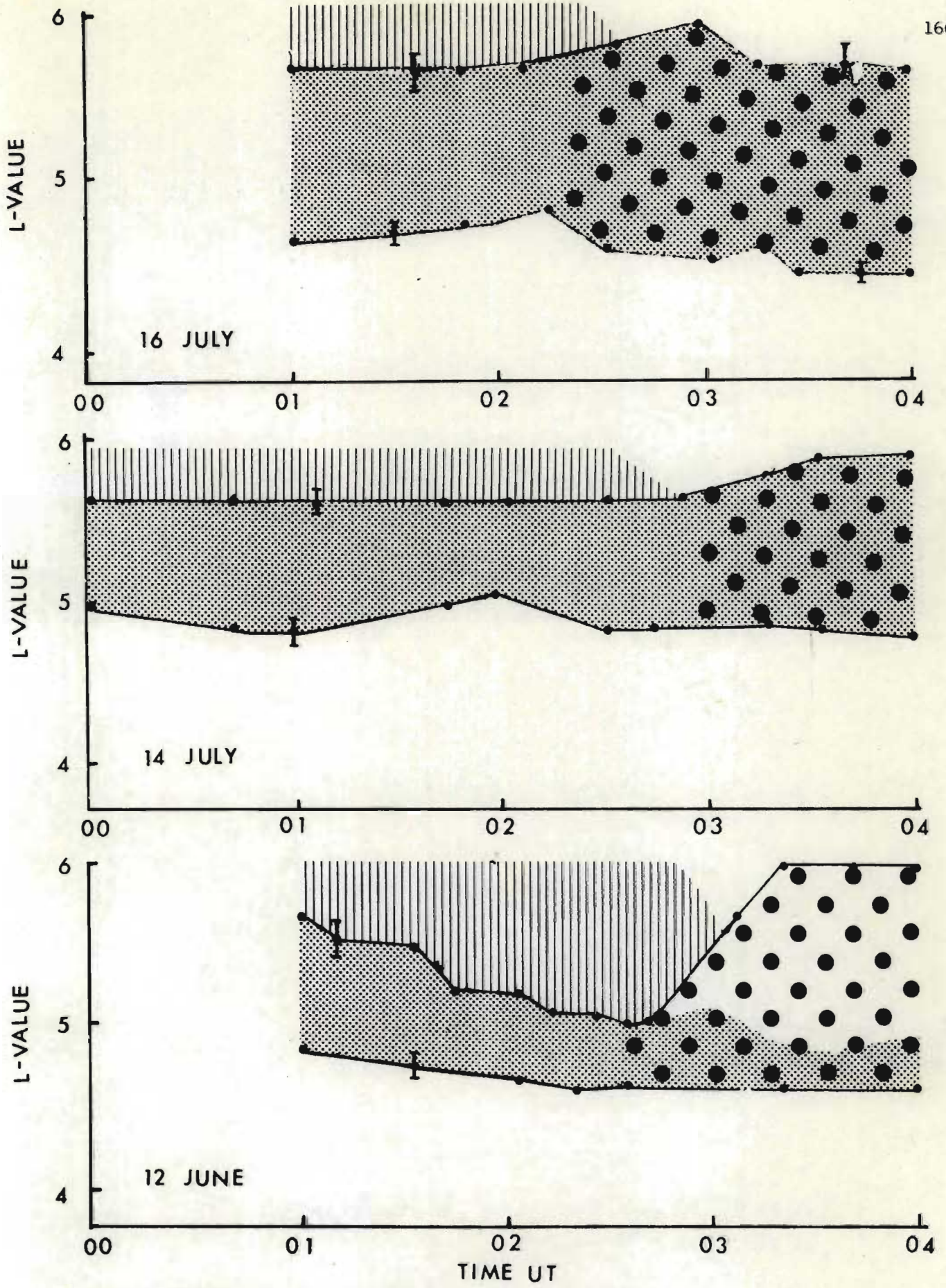

Figure 5.4 Plots of L-values of auroral forms versus Universal Time on the 16 July, 14 July and 12 June, 1975.

The error bars in Figure 5.4 are based on the uncertainty of $\pm 1^{o}$ in measuring auroral positions as discussed in Section 5.3.1. Also if a height of 120 km had been assumed, this would result in the equatorward edge of the diffuse aurora being displaced by $\sim$ 0,1 L in the poleward direction.

Period 0100 to 0415 UT, 12th June 1975.

The auroral results for this period are summarized in the L-value against time plot in Figure 5.4. In many respects the development of the auroral display for this period is similar to that of the two periods described above. For example, active bands poleward of the diffuse aurora again give way to a region of pulsating patches embedded in the diffuse aurora and the intensities of these forms do not differ significantly from those of the previous two periods. Moreover, although there is a systematic change in latitudinal extent of the diffuse aurora from 370 km to 150 km in Figure 5.4, the equatorward edge again shows little change in position being located at L = 4.6.

5.4 COMPARISON OF WHISTLER AND AURORAL DATA

A comparison of the spatial distribution of auroral data and whistler ducts for this period has already been reported (Duthie and Scourfield, 1977).

5.4.1 The Combined Data

The auroral data of Figure 5.4 and the ring current corrected data of Figure 5.0 for the three periods of observation analysed, are superimposed on the L-value versus time plots of Figure 5.5. As before, the dashed lines joining the solid squares indicates the location of

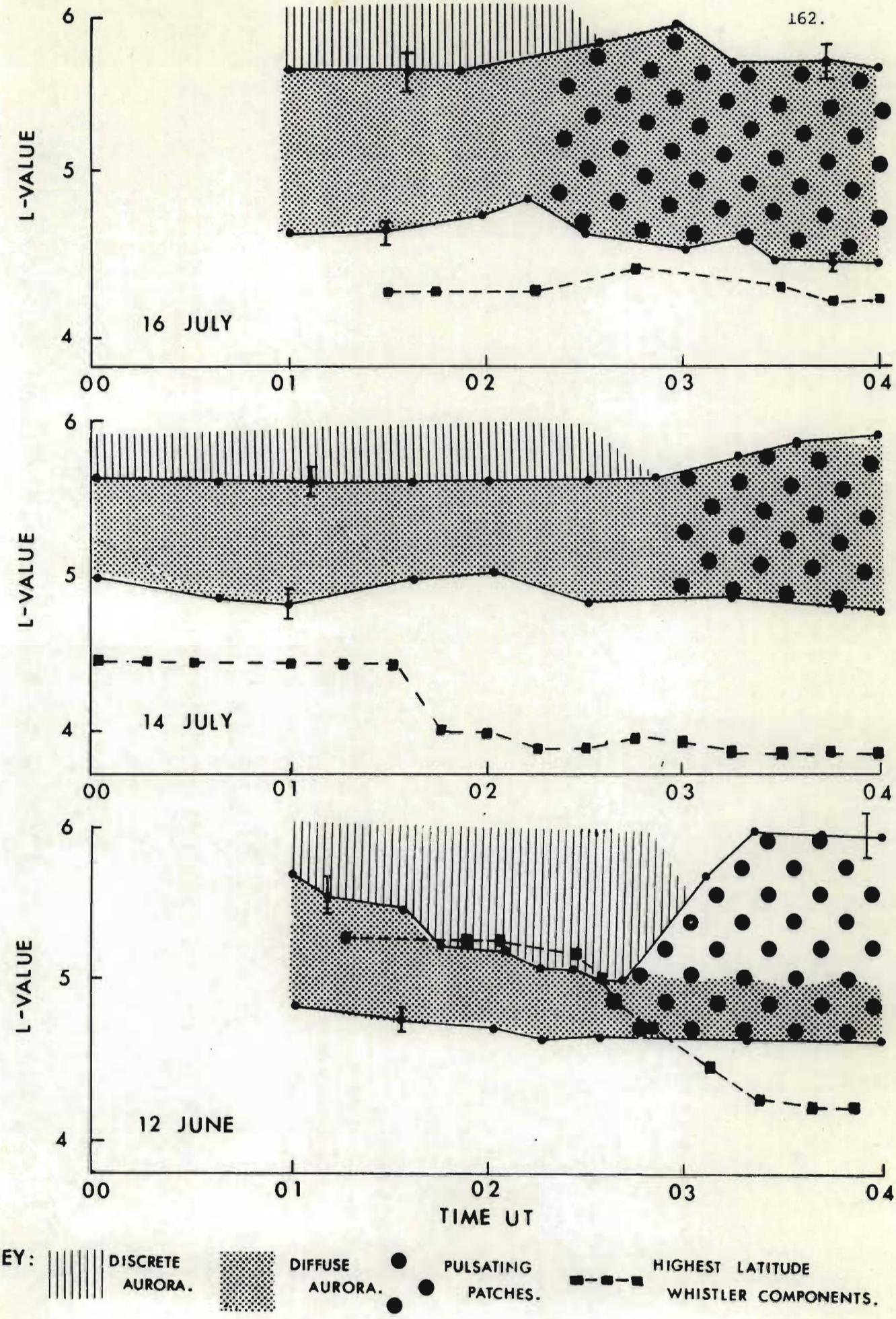

Figure 5.5 Plots of L-values of auroral forms and highest latitude whistler components versus Universal Time on the 16 July, 14 July and 12 June, 1975.

those whistlers propagating at the highest L-values i.e. closed field lines are known to exist up to L-values represented by the dashed line. Diffuse aurora is represented by dark shading, discrete aurora by vertical lines and pulsating patches by black spots.

It is necessary to justify a comparison of the position of auroral forms based on a model of the main magnetic field at epoch 1975 with the position of whistlers based on a dipole field model. Such a comparison is valid since whistler position is derived from nose frequency which is primarily determined in a very limited region of the propagation path centred on the equatorial plane and it is here that the dipole model closely approximates the field configuration of the main magnetic field, with due allowance made for the effect of the ring current.

Periods of 14th and 16th July

There is no direct evidence that any of the auroral forms occur on closed field lines since the whistlers identifying such lines are alwars equatorward of the forms during these two periods of observation.

From equatorial electron density measurements in Figure 5.1 it has been established that the highest latitude whistlers are located near the boundary of the plasmasphere. Thus although the plasmapause position cannot be determined since no knee whistlers were observed, it must be situated at a slightly higher L-value than the dashed line on 14th and 16th July in Figure 5.5.

Assuming maximum error in the location of the auroral forms the separation of both diffuse and pulsating aurora from the plasmapause

ranges from < 0.9 L (0330 UT, 14th July) to 0,2 L (0245 UT, 16th July). This close proximity, coupled with the fact that closed field lines are known to exist beyond the plasmapause suggests that diffuse and pulsating aurora occurs on closed field lines.

Feriod of 12th June

The most striking feature of the 12th June in Figure 5.5 is that from 0100 to 0230 UT much of the diffuse aurora occurs equatorward of the dashed line representing the high latitude occurrence of whistler components and hence, of the plasmapause. In whistler work it is important to bear in mind that, although the nose frequency gives the L-value of propagation, the longitude is not known in the absence of direction finding information. From an analysis of 24 hours of continuous whistler recordings at SANAE (Rabe and Scourfield, 1977) one can infer that the 'effective field of view of the VLF receiver is not greater than 15° of longitude i.e. the unknown longitudinal spread in time is ± 1 hour. Nevertheless if the whistler data point for the 15 minute interval following 0200 UT on 12th June in Figure 5.5 for example is shifted by ± 1 hour it is always 0,5 L poleward of the equatorward edge of the diffuse aurora. The evidence clearly points to the occurrence of diffuse auroral on closed field lines.

From the fact that the diffuse aurora occurs equatorwards of the dashed line in Figure 5.5 one may conclude, at least for this portion of the data, that the plasmapause is poleward of the diffuse aurora. This in turn implies that the inner edge of the plasmasheet is within the plasmasphere. This result is somewhat surprising since it is generally accepted (e.g. LUI *et al* (1975); FRANK (1971); WINNINGHAM *et al* (1975) that the inner edge of the plasmasheet is situated beyond the plasmasphere and also the hotter interplanetary plasma from the plasmasheet cannot

penetrate as far into the earth's magnetic field as the terrestrial plasma trapping boundary, i.e. the plasmapause, under the same electric field that traps the relative colder terrestrial plasma in the earth's magnetic field. A possible explanation lies in the relative movement of the plasmapause and precipitation region of electrons after a storm. RUSSELL and THORNE (1970) show that during a storm the plasmapause assumes a new position at lower radial values and a proton ring current builds up just external to the new plasmapause. The energetic electrons also appear just external to the plasmapause but not necessarily as close to it as the ring current. For electrons, energies greater than 35 KeV, the new position of maxima flux can lie in the previous quiet time minimum. After the storm the plasmapause expands and the ring current protons decay at a rate such that the maximum flux essentially keeps pace with the motion of the plasmapause. The electrons, however, decay much more slowly and the outer zone maximum created by the storm may lie several earth radii inside the quiet time plasmapause. The net result is an injection of low energy electrons well into the plasmasphere. If this flux of low energy electrons is sufficient to maintain a diffuse aurora, the diffuse aurora would occur in the plasmasphere, hence equatorwards of the plasmapause.

It is felt that more cases of this type need to be found and studied to make a worthwhile interpretation of the problem presented above.

5.5 Conclusion

The results of the analysis of the present data can be summarized as follows:

(a) Diffuse aurora occurs on closed magnetic field lines and indirect evidence shows that this is also the case for pulsating aurora.

(b) For two periods of data the separation of diffuse aurora from the plasmapause ranges from < 0,9 L to < 0.2 L but during a third period the diffuse aurora lies at least partially, within the plasmasphere.

CHAPTER SIX

POWER SPECTRA, CORRELATION AND COHERENCY OF PULSATING AURORAL PATCHES AND SIMULTANEOUSLY OBSERVED VLF HISS

6.1 Introduction

Hiss closely related to aurora is known as 'auroral hiss'. First reported by BURTON and BOARDMAN (1933), the relation between auroral activity and VLF emission has been studied for a number of years, e.g. MOROZUMI (1965); JORGENSEN (1966); HIRASAWA and NAGATA (1972); KOKUBUN *et al* (1972), HAYAKAWA *et al* (1975); OGUTI (1975) and SWIFT and KAN (1976). A study closely linked to auroral hiss research is the effort made to clarify the close relationship between auroral particles and hiss at satellite altitudes e.g. GURNETT and FRANK (1972); LAASPERE and HOFFMAN (1976). JORGENSEN (1968) and LIM and LAASPERE (1972) hypothesize that auroral hiss may be generated by incoming or precipitating auroral electrons during polar substorms.

Research on both ground and satellite observations of hiss and associated auroral light intensity and auroral particle flux has concentrated on the determination of the emission mechanism and the location of the emission source of auroral hiss.

This chapter concerns the power spectral, cross-correlation and coherency analysis of an event of pulsating auroral patches and simultaneously occurring pulsating auroral hiss observed at Sanae.

6.2 Auroral hiss data

Auroral hiss observed on the ground is more likely to be observed when a westward travelling surge in an auroral band moves across the

field of view, the peak intensity coinciding with the overhead passage of the surge, SWIFT and SRIVASTAVA (1972). On some occasions it is also reported, however, that no hiss is present when very intense westward travelling surges have passed overhead. Bursts of hiss closely correlated to sudden enhancements of auroral form illuminosity was investigated by OGUTI (1975). He found that necessary conditions for the emission of auroral hiss were the rapid brightening and rapid movement of the auroral forms associated with the hiss. High correlation between auroral luminosities and hiss was rarely obtained unless the brightening auroral form was in the zenith and then only when there was general auroral activity near the zenith.

The auroral hiss analysed in the past, for example by OGUTI (1975), has mostly been associated with discrete auroral forms such as arcs and bands and not pulsating aurora. Pulsating auroral hiss has, to the author's knowledge, not been reported and analysed before and therefore seems to be a rare event. Data of this nature was recorded at Sanae on the 10th of September, 1975 and lasted for approximately 16 minutes.

6.2.1 Data analysis

The presence of the time code on both the magnetic tape holding the VLF data and video tape holding the auroral data, afforded the author the facility of playing back both data synchronised in time. Once synchronised, one could watch the aurora on the TV monitor and listen simultaneously to the VLF using headphones. This is a rather rigorous procedure but proved to be valuable as the hiss did not show up clearly on the 16 mm film records due to the profusion of atmospherics amongst the hiss 'patches'. This can be seen from a section of the hiss record reproduced on a spectrogram in Figure 6.1.

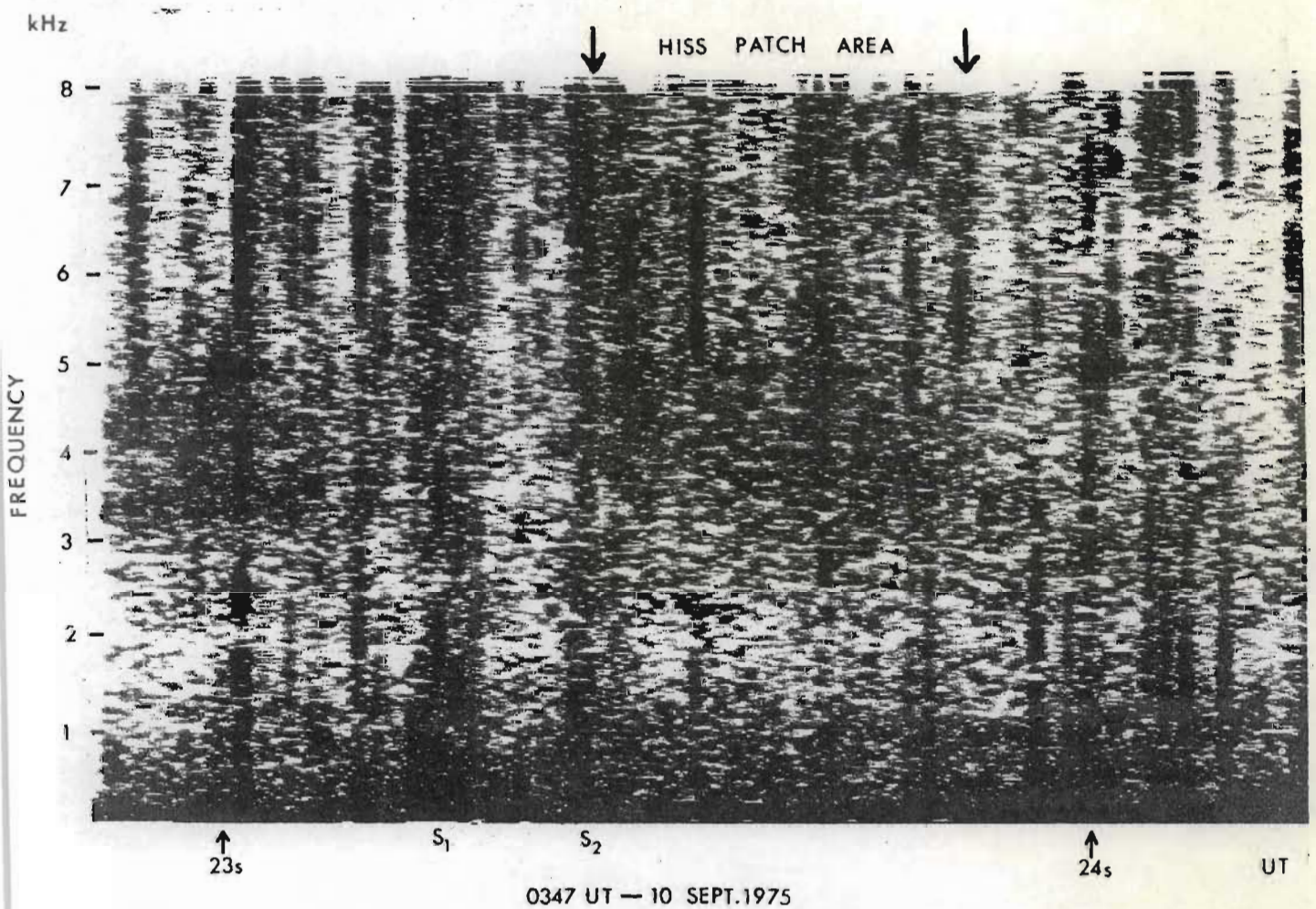

Figure 6.1 Spectrogram of pulsating hiss 'patches' received at Sanae at 0347 UT, 10 September, 1975.

(a) Pulsating hiss bandwidth

The VLF data was passed through bandpass filters of various centre frequencies and the power spectra of the outputs were determined. The centre frequencies of these filters covered a frequency range of approximately 1 kHz to 8 kHz. Each power spectrum was calculated over a frequency range of 0 - 10 Hz with a bandwidth resolution of 0,02 Hz. To acquire a power spectrum over this low range of frequencies the Ubiquitous Spectrum Analyser required a record of data 50 seconds long.

Two typical studies will be presented here.

1 kHz bandpass filter

The interval 0350-20 UT to 0051-10 UT was chosen. Centre frequencies of 1 kHz bandpass filters were positioned beginning at 1,5 kHz and ending at 6,0 kHz and placed 0,25 kHz apart. For example, the first filter's centre frequency was 1,5 kHz, the second 1,75 kHz; the third 2,00 kHz; etc. until 6,0 kHz. The output of each filter was spectrum analysed and plotted. The spectra of the outputs of six bandpass filters centred at 3,0 kHz; 3,5 kHz; 4 kHz; 5,0 kHz; 5,5 kHz; and 6,0 kHz are plotted in Figures 6.2 (a) and 6.2 (b).

Figure 6.3 shows a graph of the height of the 1,34 Hz frequency component peak in each spectrum plotted against the centre frequency of the filter whose output is responsible for the spectrum.

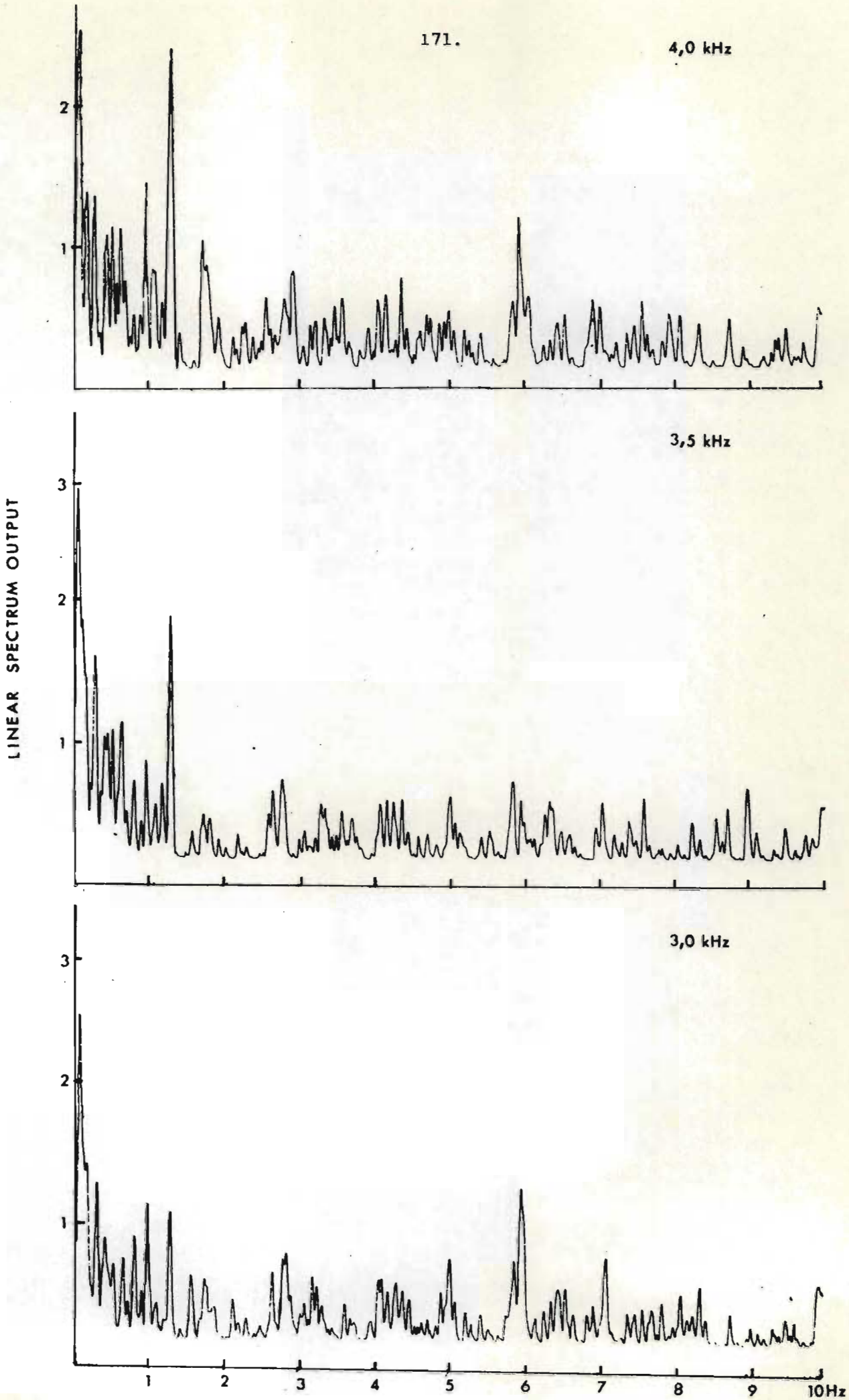

Figure 6.2(a) Spectra of the outputs of 1 kHz bandpass filters

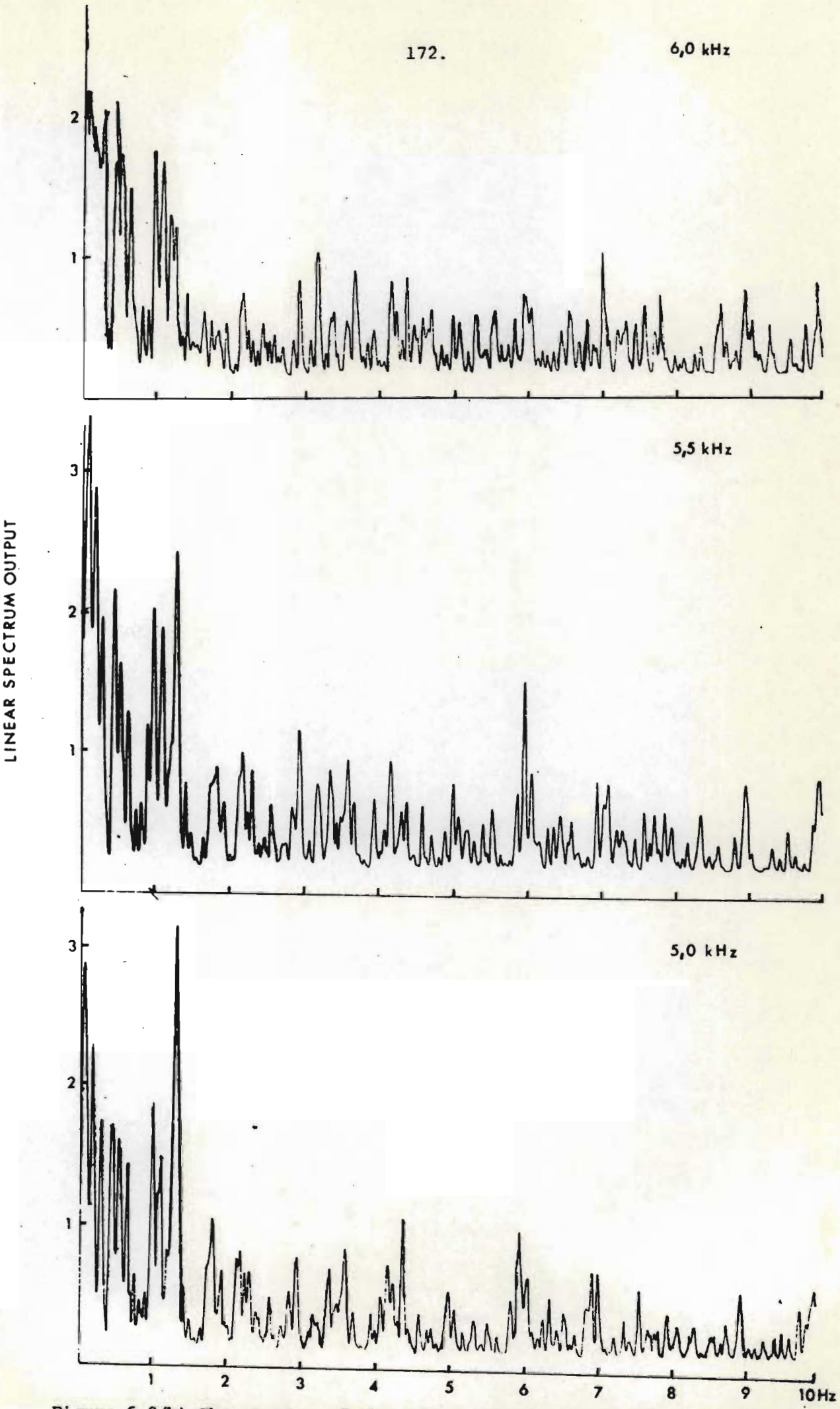
6,0 kHz
5,5 kHz
5,0 kHz
LINEAR SPECTRUM OUTPUT
1
2
3
1
2
3
4
5
6
7
8
9
10Hz

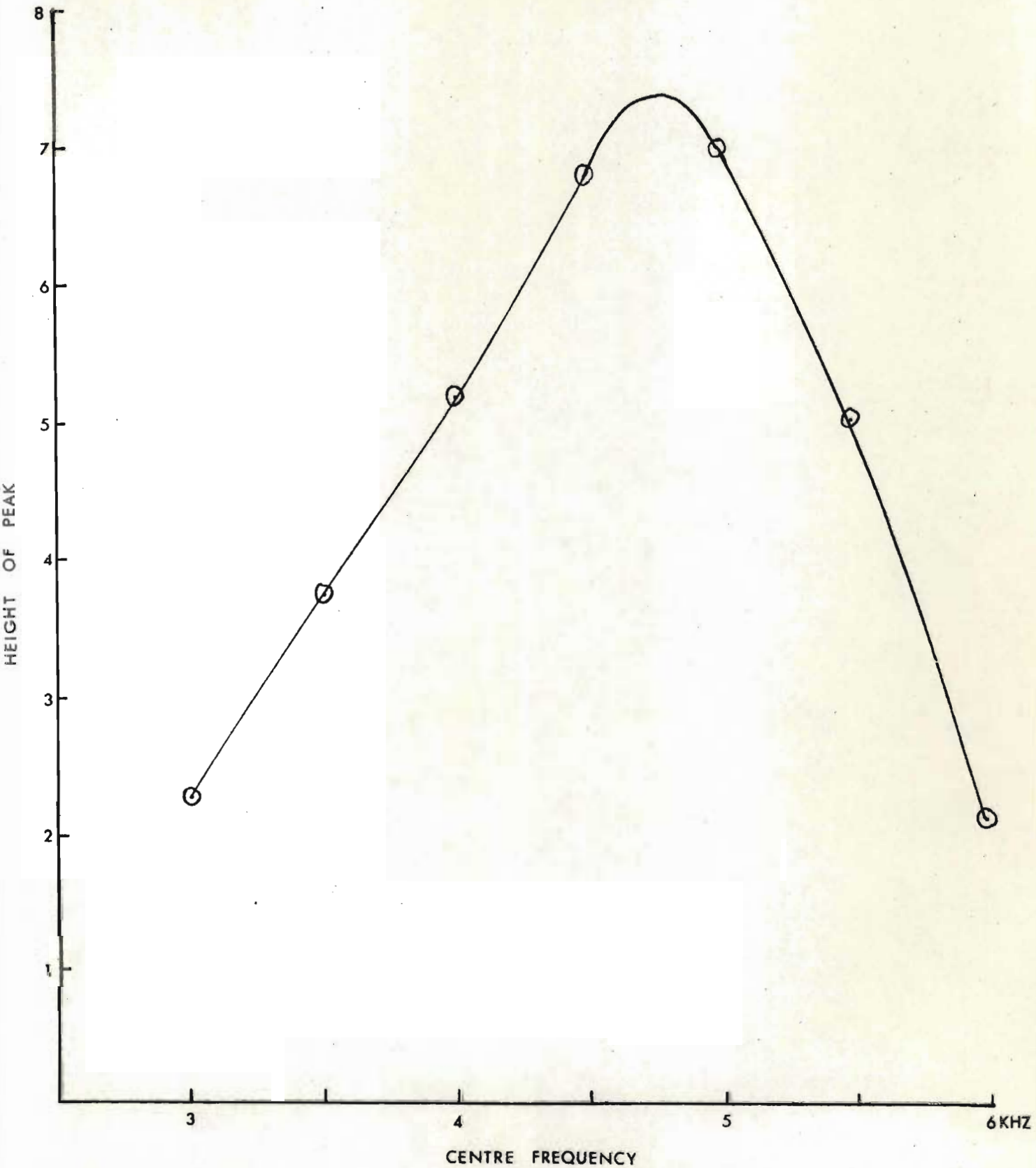

Figure 6.3 Plot of the height of the 1,34 Hz frequency component peak in each spectrum versus the centre frequency of each bandpass filter for the period 0350-20 UT to 0051-10 UT.

80 Hz bandpass filter

As in the 1 kHz bandpass filter study, power spectra were determined at various frequencies. In this case 80 Hz bandpass filters were used and the frequency range of the centre frequencies was from 2,2 kHz to 5,4 kHz. Sets of spectra at various frequencies were plotted for consecutive 50 second periods and a contour plot of the heights of the 1,34 Hz peak in the frequency spectra for the time period 0343-00 UT to 0358-50 UT is presented in Figure 6.4. The darker the shading, the higher the peak.

Approximately 290 spectra were plotted and measured to attain a resolution of 160 Hz in the determination of the kHz bandwidth of the hiss and its variation in width with time.

Spectrum criteria

When interpreting the variation in height of the peak at 1,34 Hz in the spectra, it is important to note the capabilities of the spectrum analyser set up for analysing over the frequency range of 0 - 10 Hz. For example, if a sinusoidal signal of 1,34 Hz of constant amplitude was applied to the input for the full length of the processing time of 50 s, the spectrum analyser would realise its maximum resolution of 0,02 Hz and the height of the peak at 1,34 Hz in the spectrum would clearly be representative only of the amplitude of the signal. If, however, the duration of the signal was of shorter length than the processing time of 50 s, the height and half-bandwidth of the peak at 1,34 Hz would be indicative of, not only the amplitude of the signal but also the duration of the signal. This is shown in Figure 6.5. In the top diagram of Figure 6.5 the

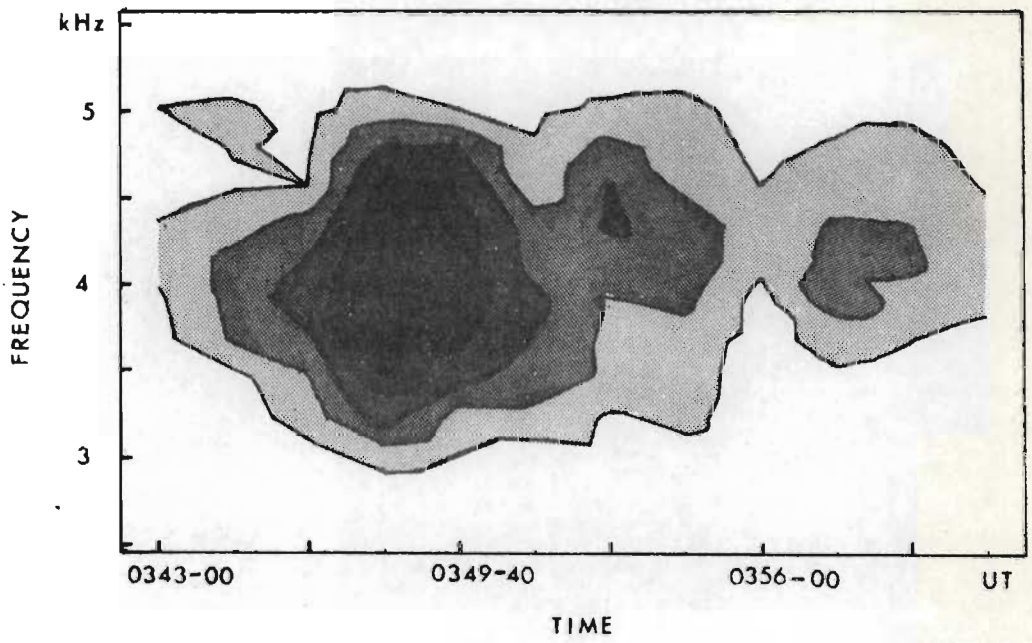

Figure 6.4 Contour plot of the heights of the 1,34 Hz peak in the frequency spectra derived from 80 Hz bandpass filters versus the centre frequency of each bandpass filter for the period 0343-00 UT to 0358-50 UT. The darker the shading, the higher the peak.

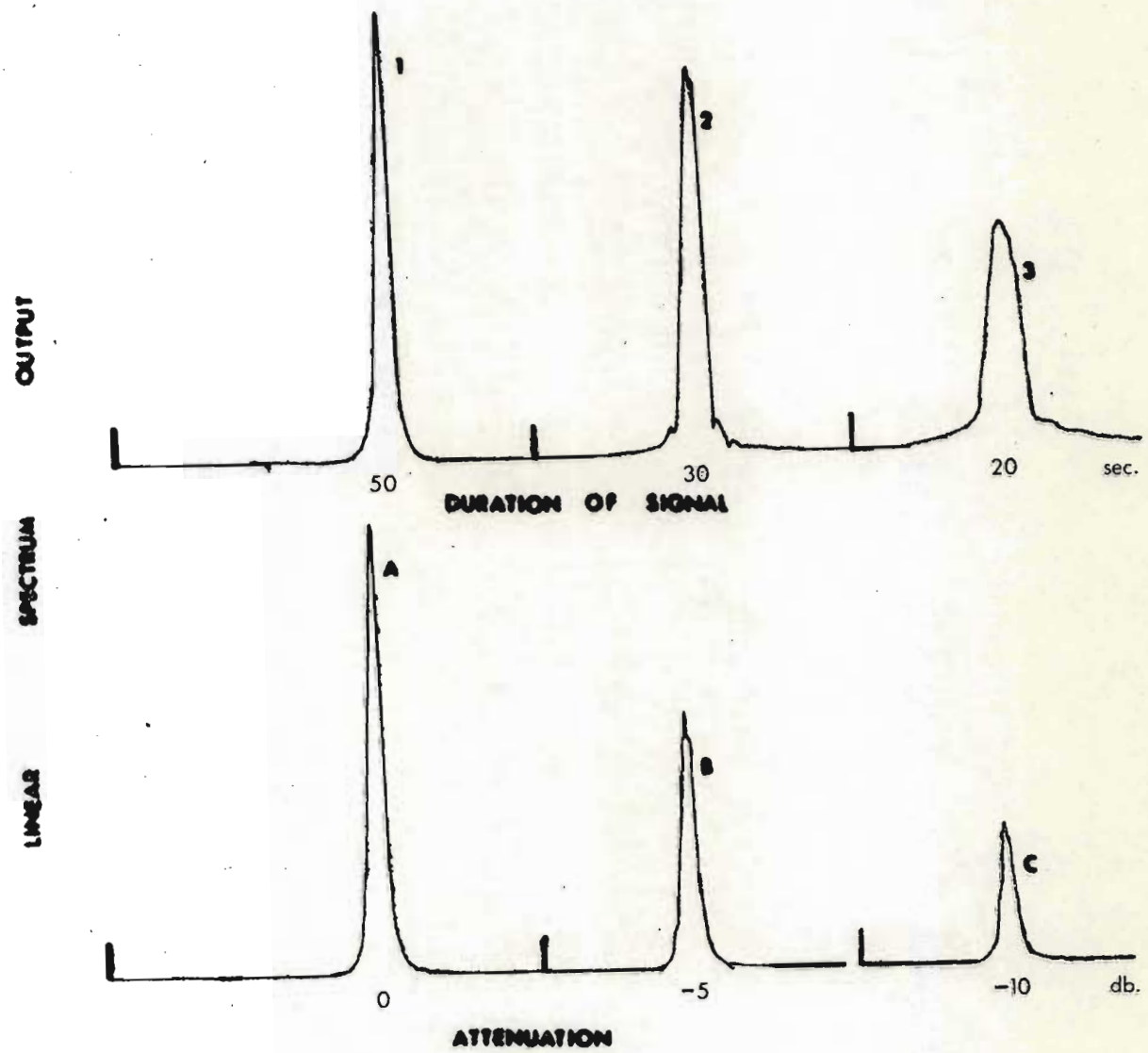

Figure 6.5 Linear spectrum output plots for the variation in firstly, the processing time and secondly, the attenuation, of a sinusoidal signal applied to the Ubiquitous input.

linear spectra, (Nos. 1, 2 and 3), have been plotted for a signal of constant amplitude but of different lengths of duration and in the lower diagram the signals' durations have been 50 s in each case, but the amplitude of the input signal has been changed. It can be seen that in the top diagram where the duration of the signal has changed the height of the peak *and* the effective resolution have changed i.e. the half-bandwidth has changed whereas, when the duration is constant, only the height of the peak has decreased with decreasing amplitude of the signal.

On inspection of Figure 6.2 and in view of the above paragraph, it is felt that the 1,34 Hz component of the VLF signal analysed, was present for the whole duration of 50 s due to the fact that the narrow half-bandwidth of the 1,34 Hz peak in the spectra is constant throughout. Unfortunately plots of the actual signals analysed do not reveal the 1,34 Hz component on visual inspection due to the presence of sferics, but on listening to the original VLF record, the pulsating hiss is heard to be present throughout the whole 50 s period i.e. 0350-20 UT to 0351-10 UT. Figures 6.3 and 6.4 therefore represent the actual kHz frequency spectrum of the pulsating hiss.

Discussion

A prominent characteristic of auroral hiss observed on the ground by other workers, e.g. OGUTI (1975), is its broadband nature, sometimes extending over a frequency range of 100 kHz. The pulsating auroral hiss analysed here has a relatively narrow band ranging from 1 kHz to 2 kHz in width extending from 2,7 kHz to 5,2 kHz. It is also interesting to note from Figure 6.4 that

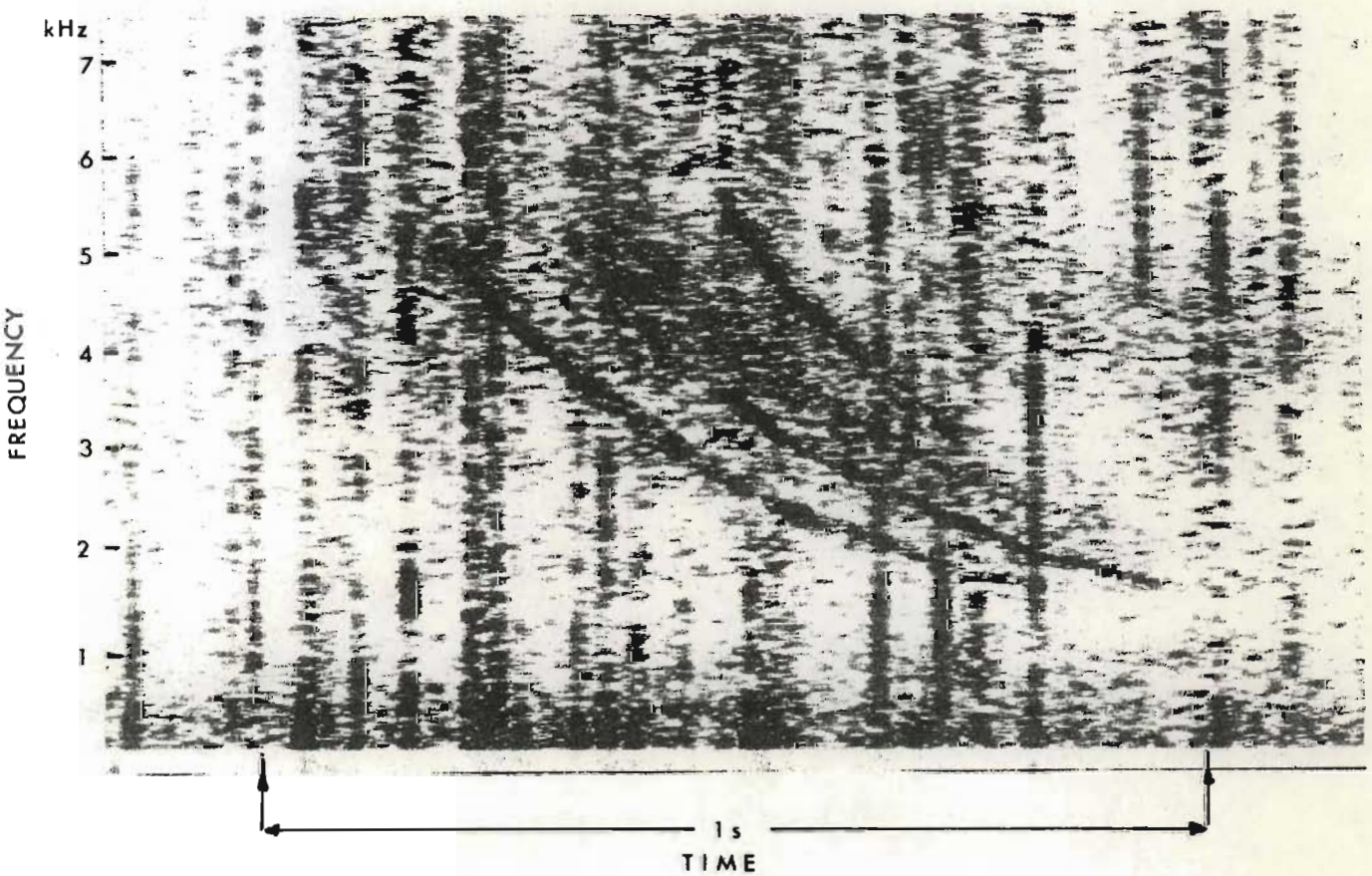

Figure 6.6 Spectrograms of whistlers received at Sanae at 0347-00 UT, 10th September, 1975.

the bandwidth of the pulsating hiss 'patch' broadens when its intensity increases, for example over the period 0347-10 UT 0348-00 UT. The narrow bandwidth nature of the pulsating hiss suggests a frequency selection process, MANSFIELD (1967). However, the mechanism responsible for the bottom and top cut-offs of the hiss also seems to act on the whistlers received during the same time period, for example Figure 6.6.

HELLIWELL (1965) discusses various factors influencing whistler cut-off frequencies. Factors such as collisional absorption in the ionosphere, duct properties and thermal (Landau) damping near the top of the whistler path, all affect the upper cut-off whereas the lower cut-off is affected by properties of the earth-ionosphere waveguide and ion resonances. It is interesting to note that SMITH (1961) suggests that the upper cut-off frequency of a whistler may be limited as a result of the failure of the duct along which the whistler propagates, to trap the energy above a certain frequency. However, the predicted upper cut-off frequency, in the vicinity of half the minimum gyrofrequency, is usually much higher than the observed upper cut-off frequency. Another possible explanation for the upper cut-off frequency is the effect of thermal damping associated with cyclotron resonance between the whistler wave and electrons i.e. wave-particle interactions. LIEMOHN and SCARF (1962) found that thermal loss should increase very rapidly with frequency.

From Figures 6.4 and 6.6 it is seen that the upper cut-off frequency for the hiss 'patch' is approximately the same as that of the whistlers observed over the same period, which suggests that the same mechanism, duct propagation or thermal loss, is responsible for the cut-off frequency of both phenomena.

The difference in their lower cut-off frequencies is probably ascribable to the fact that the earth-ionosphere waveguide was responsible for the lower frequency cut-off of some of the whistlers and that the hiss did not propagate in the waveguide between the exit point and receiving station. Some whistlers have, however, lower cut-off frequencies similar to that of the hiss 'patches'. HELLIWELL,(1965) suggests a property of propagation in the magnetosphere as a control of low frequency cut-off such as the effective diameter of the duct in wavelengths becoming too small for trapping to occur. This mechanism could be active on both the whistlers and hiss analysed in this case.

(b) Dispersion

Very low frequency electromagnetic waves guided by the lines of force of the earth's magnetic field are dispersed along the path which they travel. This means that the different frequency components of the wave travel at different velocities. If one assumes that waves,with the same frequencies as present in the hiss, are generated simultaneously in the equatorial region and that they propagate along a line of force at L = 4,11, then the waves would arrive at the receiving station at the bottom of the field line at different times depending on their frequencies.

PARK (1972) gives an empirical formula for the relationship between the equatorial electron density N and the L-value, L, of the path along which a whistler with nose frequency f_n and time delay t_n, propagates using a dispersive equilibrium model. The time taken for a VLF wave with frequency f_n, to travel from the equatorial plane to the earth can then be found using the following formula:

$$t_f = t_{n/2} = \frac{1}{2} \times \sqrt{\frac{N_{eq} L^5}{24 f_n}}$$ PARK (1972) p52.

A table showing the travel times for VLF waves of frequencies 2,70 kHz, 3,20 kHz, 3,92 kHz, 4,48 kHz and 5,20 kHz for various equatorial electron densities is given, in Figure 6.7.

An equatorial electron density profile was determined from the whistlers received over the period 0343 UT to 0351 UT and although the quality of the whistlers was not good, as expected with high magnetic activity, the equatorial electron density was estimated to be 200 ± 100 eℓ cm^{-3} at L = 4,11.

If the hiss waves propagate and are duct-guided as the whistlers are, the signals of the different frequencies present in the hiss would be delayed by the times as indicated in Figure 6.7, that is to say, the hiss would have a dispersive characteristic or profile similar to a whistler generated in the equatorial plane. From Figure 6.7 the difference in travel times between a 3,20 kHz signal and 4,48 kHz signal is of the order of 300 m s and 100 m s for equatorial densities of 1000 eℓ cm^{-3} and 200 eℓ cm^{-3} respectively and must be kept in mind with regards to the following analysis.

Two methods were employed to determine whether the hiss patches possessed dispersive characteristics. They will be described in the following paragraphs.

(i) Spectrum analysis of an isolated hiss 'patch'

A hiss 'patch' relatively free of atmospherics was identified and chosen from a sequence of spectrograms made from the period 0347 UT to 0348 UT. The hiss 'patch' is shown in

N_{eq} (el cm^{-3})	f_n (kHz)	t_f (s)
1000	2,70	2,127
	3,20	1,954
	3,92	1,765
	4,48	1,651
	5,20	1,532
300	2,70	1,165
	3,20	1,070
	3,92	0,967
	4,48	0,904
	5,20	0,840
200	2,70	0,951
	3,20	0,874
	3,92	0,789
	4,48	0,738
	5,20	0,685
100	2,70	0,673
	3,20	0,618
	3,92	0,558
	4,48	0,522
	5,20	0,485

Figure 6.7 Table showing the travel times of emissions of various frequencies from the equatorial plane to Sanae along the field line L = 4,11, for various equatorial electron densities.

the spectrogram in Figure 6.1 and the visual estimation of its position is indicated by the arrows on the spectrogram. Spectra of consecutive 16 m s intervals of the hiss patch were plotted in Figure 6.8 with the aid of an HP Fourier Analyser system and HP Signature Analysis system from the time period 0347-23,320 UT to 0347-23,880 UT. As the frequency band of the hiss was found in Section 6.2.1(a) to extend from 2,7 kHz to 5,2 kHz, the VLF data was first fed through a bandpass filter with lower cut-off at 2,5 kHz and top cut-off at 5,3 kHz and then spectrum analysed, hence the lack of peaks below 2,5 kHz and above 5,3 kHz in the spectra in Figure 6.8. The atmospherics S_1 and S_2 in Figure 6.1 show up clearly in Figure 6.8.

The linear spectrum outputs of consecutive frequency slices over the same period of time (0347-23,320 UT - 0347-23,880 UT) were plotted and,presented in Figure 6.9 ,are the linear spectrum outputs of the frequency 'slices' ranging from 3,70 kHz to 4,10 kHz.

(ii) Cross-correlation between two signals whose amplitude is representative of the intensities at two different frequencies

The broadband VLF signal, (0-16 kHz), containing the hiss 'patches' was fed through three bandpass filters, each with a bandwidth of 80 Hz, centred at 3,20 kHz, 3,92 kHz and 4,48 kHz. Outputs of the three filters were cross-correlated to determine whether there was a time delay between the intensities at 3,20 kHz and 4,48 kHz or between the intensities at 3,20 kHz and 3,92 kHz. The correlation-functions of the signals representing the intensities at 3,20 kHz and 4,48 kHz were calculated for three time intervals,(0347-00 UT

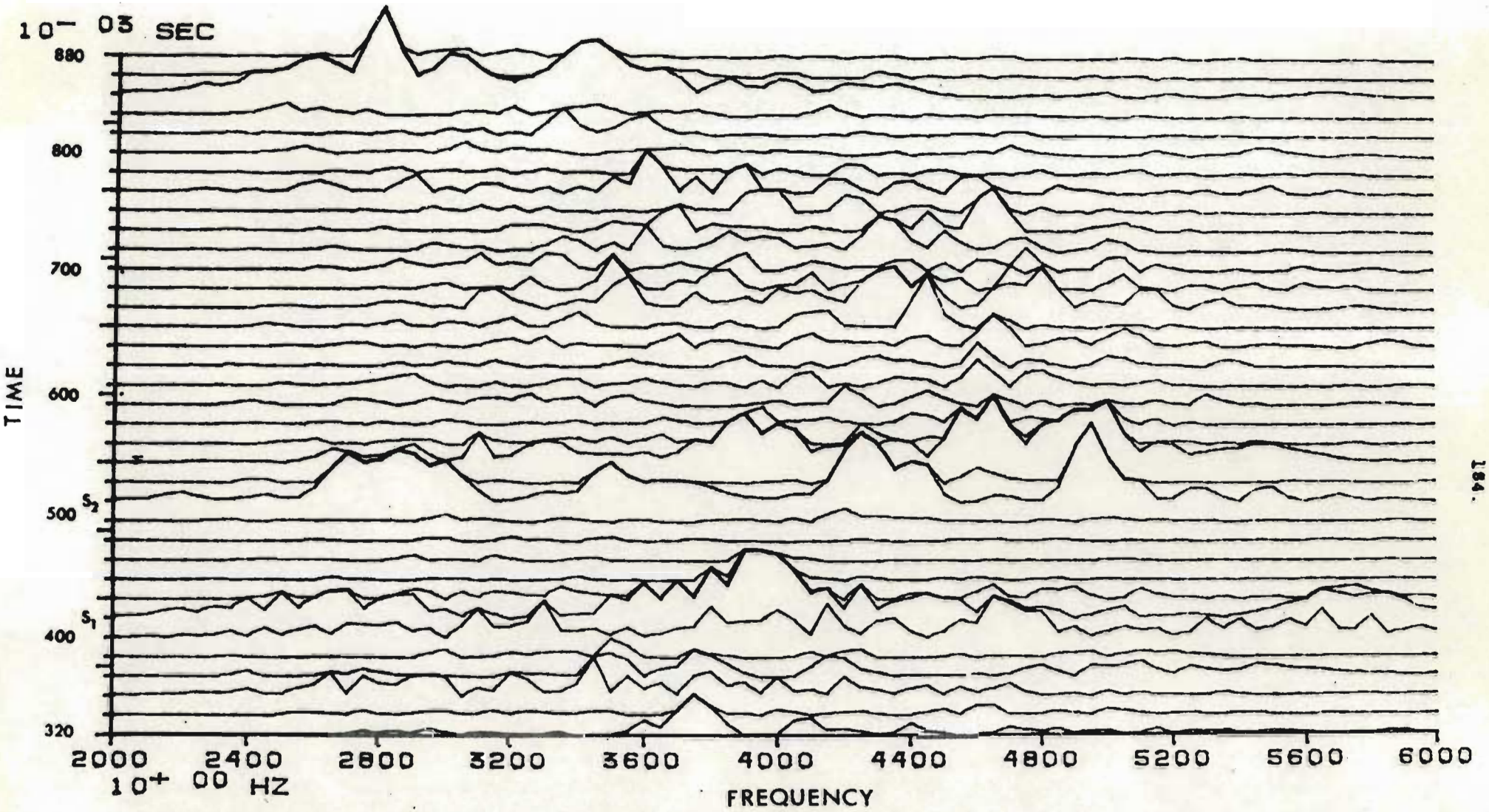

Figure 6.8 Digital spectrogram of a hiss 'patch' between 0347-23,320 UT to 0347-23,880 UT. Each spectrum was plotted at 16 m s intervals. S_1 and S_2 are the spectra of the sferics as indicated in Figure 6.1.

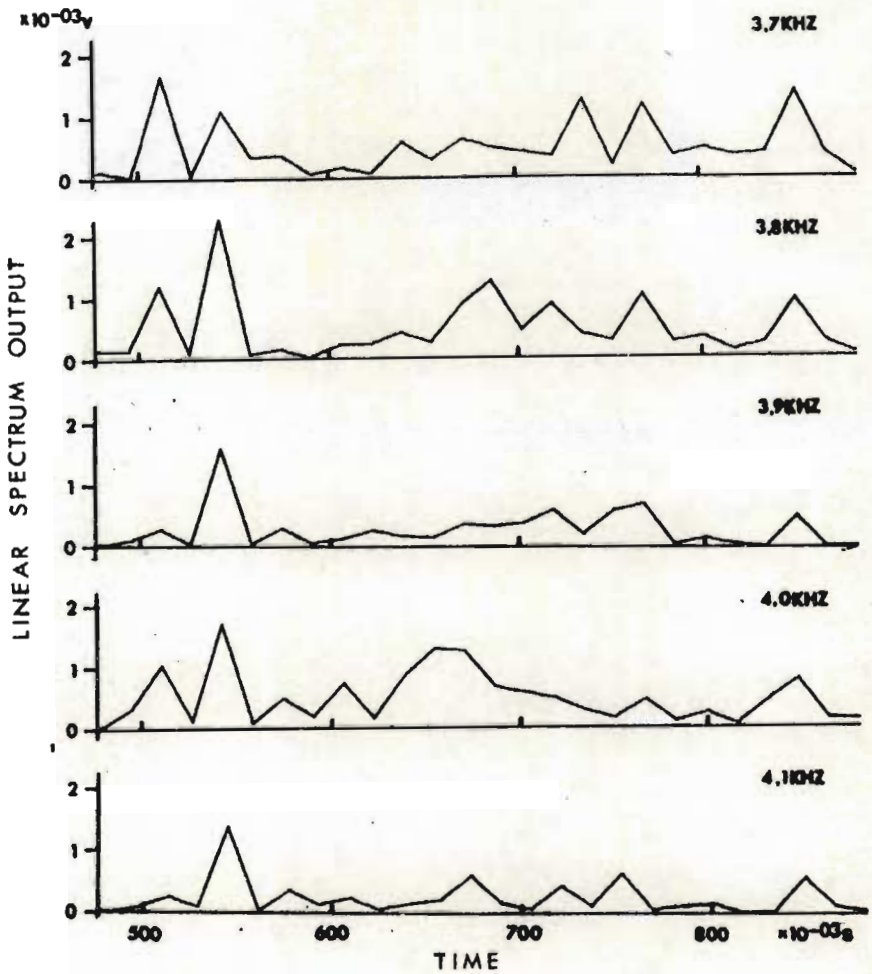

Figure 6.9 Linear spectrum outputs of consecutive frequency slices ranging from 3,70 kHz to 4,10 kHz over the period 0347-23,32 UT to 0347-23,880 U.T.

to 0347-08 UT, 0347-10 UT to 0347-18 UT and 0347-20 UT to 0347-28 UT), and are shown in Figure 6.10. A similar correlation function was determined for the frequencies 3,20 kHz and 3,92 kHz for the period 0347-00 UT to 0347-08 UT and plotted in Figure 6.11.

A short summary of the correlation function program, as described in detail in the Operating Manual of the HP5451B Fourier Analysis system, is presented in the following paragraph.

Two analogue signals, S_1 and S_2, are digitally sampled at a frequency(f_s) and stored in data blocks 0 and 1 respectively, the size,(N) of which, is selected according to the size of memory available (see Figure 6.12(a)). The length of time for which the analogue signals are each sampled, is T, ($T = N \cdot \Delta t$ where $t = 1/f_s$). The digitally sampled signal(S_2) stored in positions 0 to $\frac{N}{3}$ and $\frac{2N}{3}$ to N in data block 1 is brought to zero, Figure 6.12(b). The signal left between positions $\frac{N}{3}$ and $\frac{2N}{3}$ in data block 1 is then consecutively shifted by Δt in real time and the correlation function is determined between S_1 in data block 0 and the signal data block 1 for each shift of Δt and plotted, for example Figure 6.12(c).

The signals from the outputs of the frequency channels, of which the correlation functions are shown in Figures 6.10 and 6.11, were sampled at a frequency of f_s = 500 Hz and stored in data blocks with block size N = 4096. The duration T of the signal sampled is therefore 8,192 s ($T = 4096 \cdot \Delta t$, $\Delta t = 1/500$). When the signal in data block 0 is well correlated to the signal in data block 1, as it is shifted in jumps of 2 m s, the correlation function has a relatively large

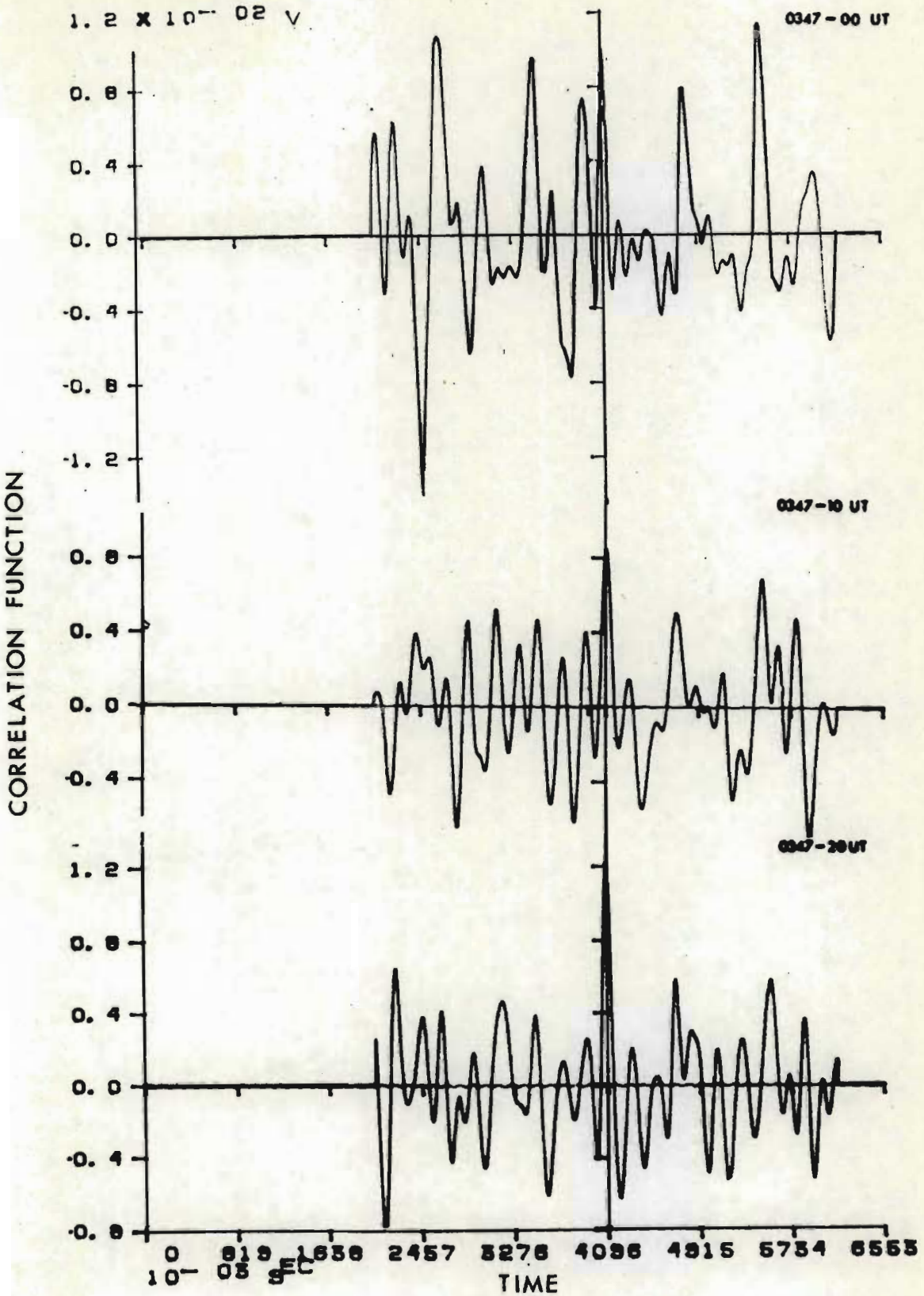

Figure 6.10 Plots of the cross-correlation functions of the signals representing the intensities at 3,20 kHz and 4,48 kHz for the periods 0347-00 UT to 0347-08 UT, 0347-10 UT to 0347-18 UT and 0347-20 UT to 0347-28 UT.

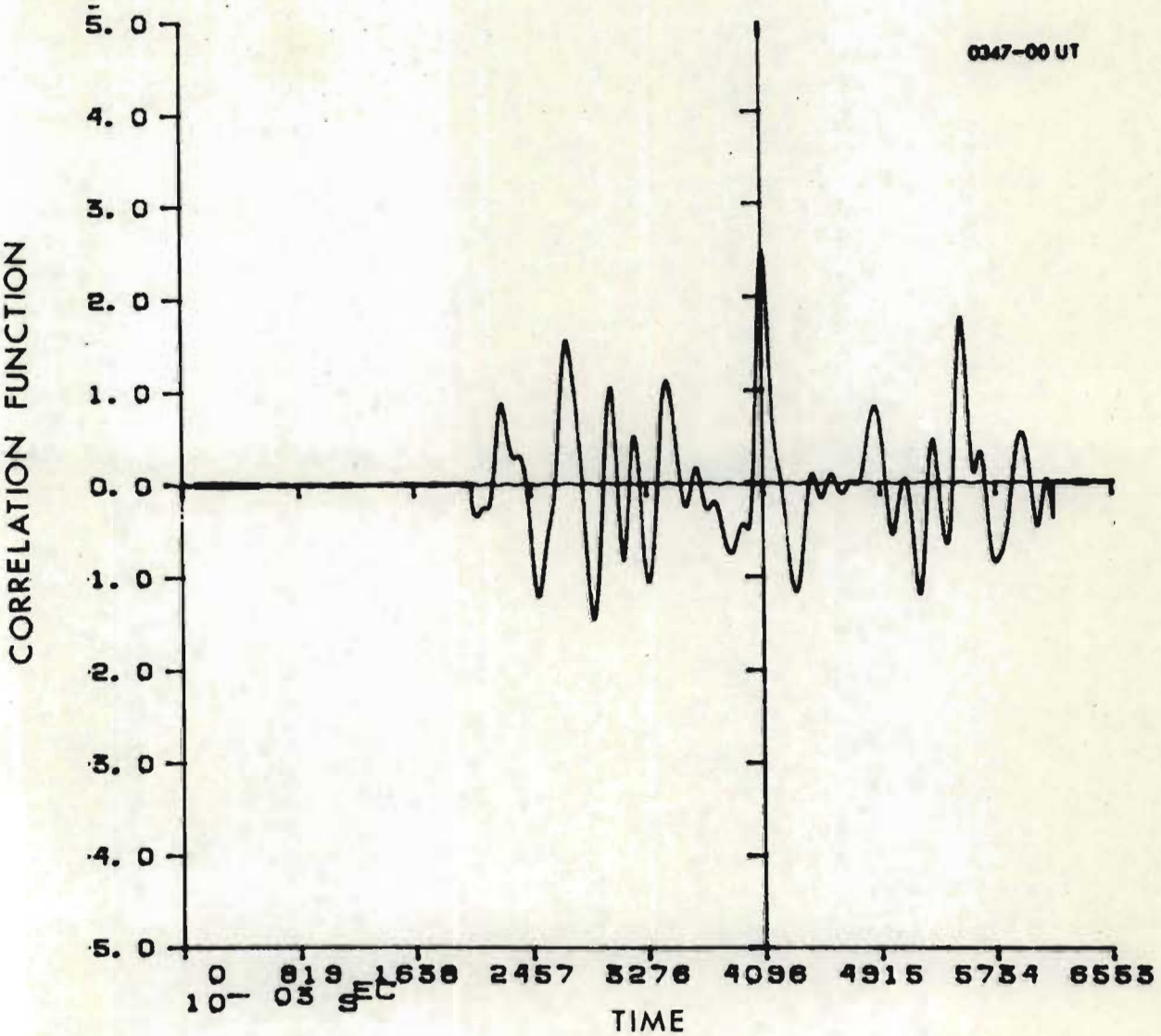

Figure 6.11 Plot of the cross-correlation functions of the signals representing the intensities at 3,20 kHz and 3,97 kHz for the period 0347-00 UT to 0347-08 UT.

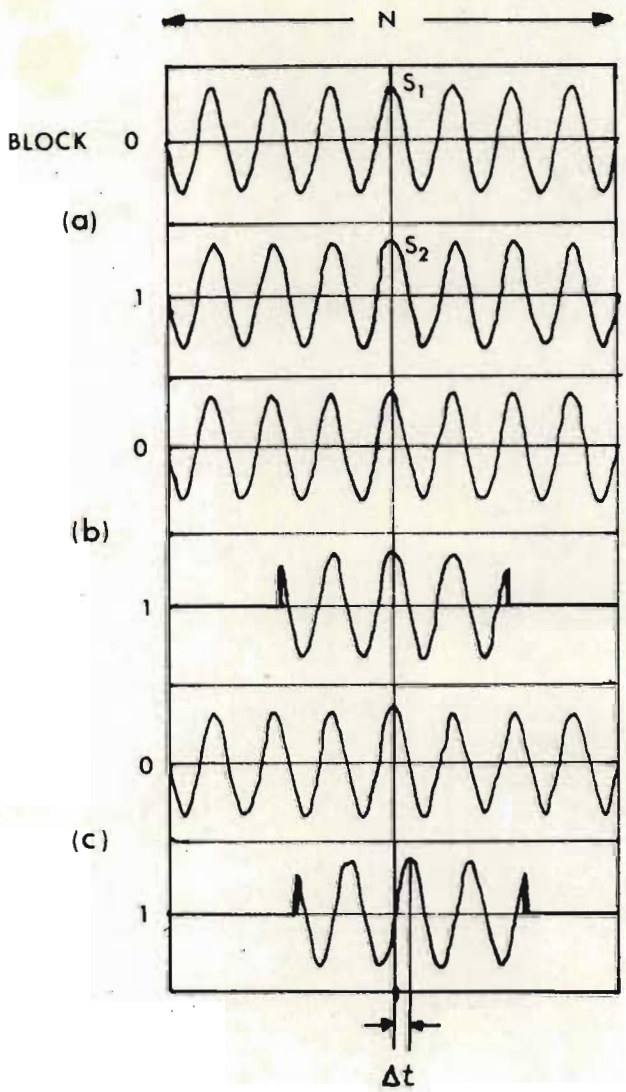

Figure 6.12 Determination of cross-correlation function of signals S_1 and S_2.

positive value. If data block 0 contains a signal with a square pulse situated in position 2040 and data block 1 contains a signal with a square pulse situated at 2050, i.e. the square pulses are separated by 20 m s in real time, then the graph of the correlation function will peak 20 m s to the *left* of the centre line. Therefore it can be said that the square pulse in data block 0 leads the square pulse in data block 1 by 20 m s or there is a time delay of 20 m s between the two signals.

Discussion

Let us first consider the detailed spectral picture of one hiss patch as presented in Figures 6.8 and 6.9 . It is difficult to detect a repetitive and continuous displacement of peaks along the frequency-axis as one goes up the time axis. The presence of atmospherics in the hiss 'patch' does not aid detection either, because of the relatively low intensity of the hiss. Figure 6.8 does however give an indication of the frequency-time 'shape' of the hiss patch. The lower frequency cut-off appears to be approximately 3,30 kHz which again (see Discussion, Section 6.2.1(a)) is higher than that of the whistlers received over the same period. Further similar analysis of other hiss 'patches' did not yield definite dispersive information either.

From Figures 6.10 and 6.11 it is seen that the signals are well correlated and there appears to be no time delay between their intensities. However, one must again consider the relative intensities of the atmospherics and the periodically changing intensity of the pulsating hiss. If the 1,34 Hz intensity variation of the hiss was dominant in the determination of the correlation function, the correlation function would peak periodically every 0,75 s. This characteristic is not clearly noticeable in Figures 6.10 and 6.11 where 0,75 s is represented by 15,22 mm on the time axis. If the peaks were present and one of them was the peak

on the centre line, one could conclude that there was no time delay between the signals and hence no dispersion in the pulsating hiss. Therefore, again, there seems to be no conclusive evidence with regards to dispersion in the hiss 'patches'. However, the structure characteristic of rising or falling tones as observed in 'dawn chorus' or triggered emissions, HELLIWELL, (1965)), is not noticeably present here as it is in spectrograms of 'dawn chorus' and whistlers which suggests an incoherent generation mechanism.

6.3 Auroral pulsating patch data

Various analysis techniques have been employed in determining power spectra of pulsating patches. SCOURFIELD, (1967, 1970) and McINNES, (1973) used calibrated photocells placed on a TV monitor in selected positions. The output of a photocell represented the light intensity within the field of view of the photocell. The system used by the author has been described in Section 4.5.1.

The prominent feature of pulsating auroral patches is that they are not only temporal but spatial. This must always be borne in mind when doing auroral patch analysis. The data analysed in the following section was recorded in the zenith at Sanae on the 10th September 1975 during the post break-up phase of an auroral display. The field of view of the camera was 25° and the aurora was viewed through a blue bandpass filter (see Figure 4.3). During the period of observation that the following analysis covers, (0342-10 UT to 0358-50 UT), three types of pulsating forms existed in the zenith. Two forms moved rapidly across the screen from South to North pulsating at about 3 Hz and a pulsating patch moved slowly East to West pulsating at about 1,3 Hz. A video analyser 'window' was placed across the whole field of view of the camera and the spectra of consecutive 50 s periods of the integrated light intensity within the window were determined and plotted. Six power spectra of consecutive 50 s periods starting at 0347-50 UT and ending

at 0353-30 UT are presented in Figures 6.13 and 6.14. The units on the Linear Spectrum Output axes have been arbitrarily chosen. The three dominant and ever present peaks are situated at 1,34 Hz, 3,00 Hz and 3,28 Hz. To represent the power in the 1,34 Hz component for the whole period of interest, i.e. 0342-10 UT to 0358-50 UT, a time plot of the height of the peak at 1,34 Hz in each spectrum is shown in Figure 6.15(a). It is interesting to compare the variation in the power of the intensity of the 1,34 Hz pulsating patch and the variation in the power at different frequencies of the 1,34 Hz pulsating hiss patch as shown in Figure 6.15(b).

Discussion

The noticably constant feature present in the power spectra is the peak at 1,34 Hz. Its bandwidth at half maximum is constantly narrow and its centre frequency remains at 1,34 Hz during the whole 16 minute period. The bounce period for electrons with energies in the 1 to 10 KeV range, which are felt to be responsible for pulsating aurora, CHRISTENSEN and KARAS (1970), passing through the equatorial plane at L = 4,11, is of the order of 7,0 to 2,0 s (Section 3.3.12) and is therefore not a plausible explanation for the 0,75 s period of the pulsating patches observed.

The same power spectral peak at 1,34 Hz occurs in the power spectra of the auroral hiss over the same time period, (0347-10 UT to 0358-00 UT), e.g. Figure 6.1 . Because the frequency modulation of the auroral electrons is the same as that for the VLF emissions constituting the auroral hiss, a wave-particle interaction is strongly supported by the data analysed as a generation mechanism. When comparing the variation in power of the 1,34 Hz component of both the hiss and auroral data, it is noticed that there is no corresponding auroral, 1,34 Hz component over the period 0342-10 UT to 0347-10 UT. This can be explained

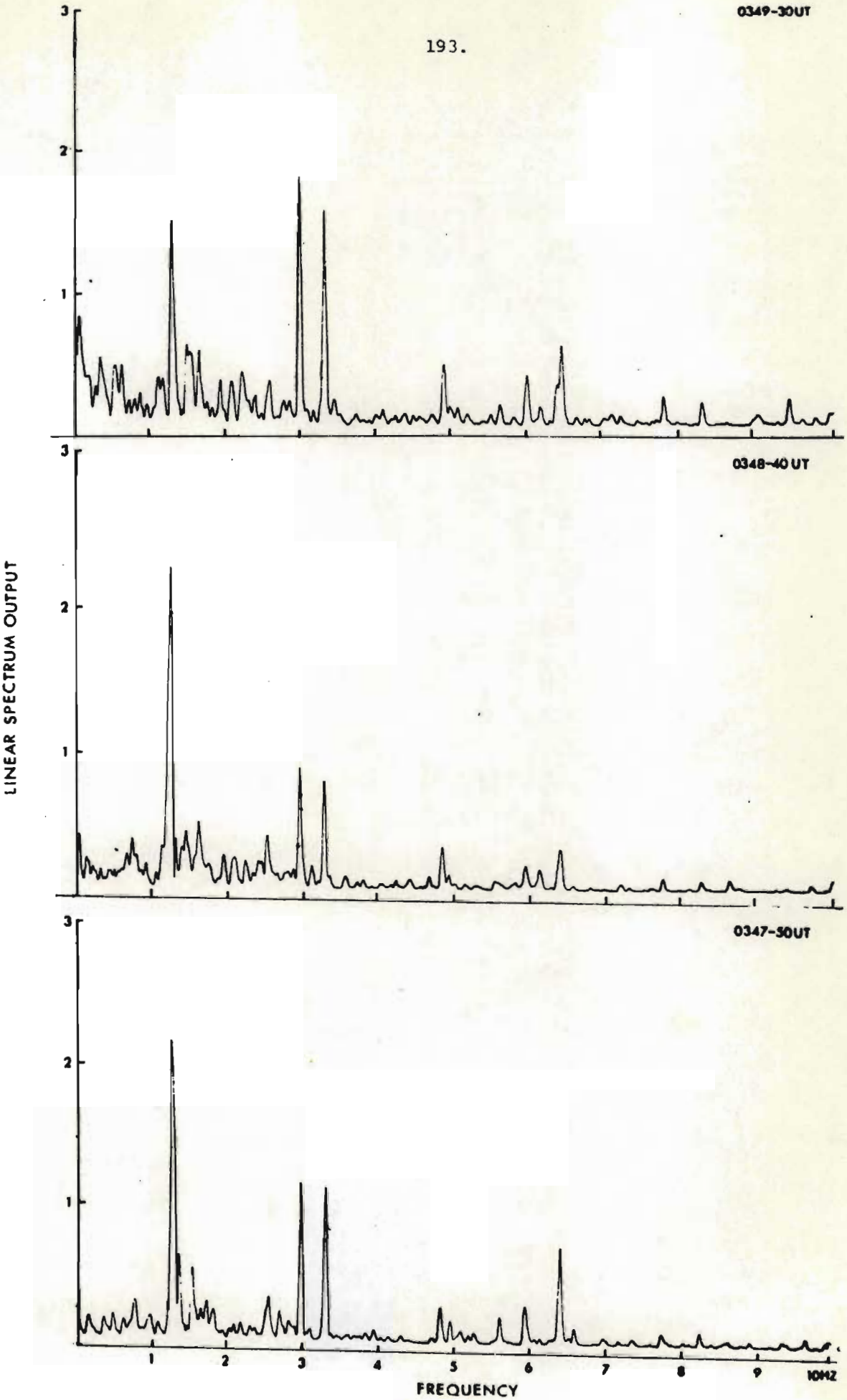

Figure 6.13 Linear spectra of the integrated light intensity within the full field of view of TV camera 1

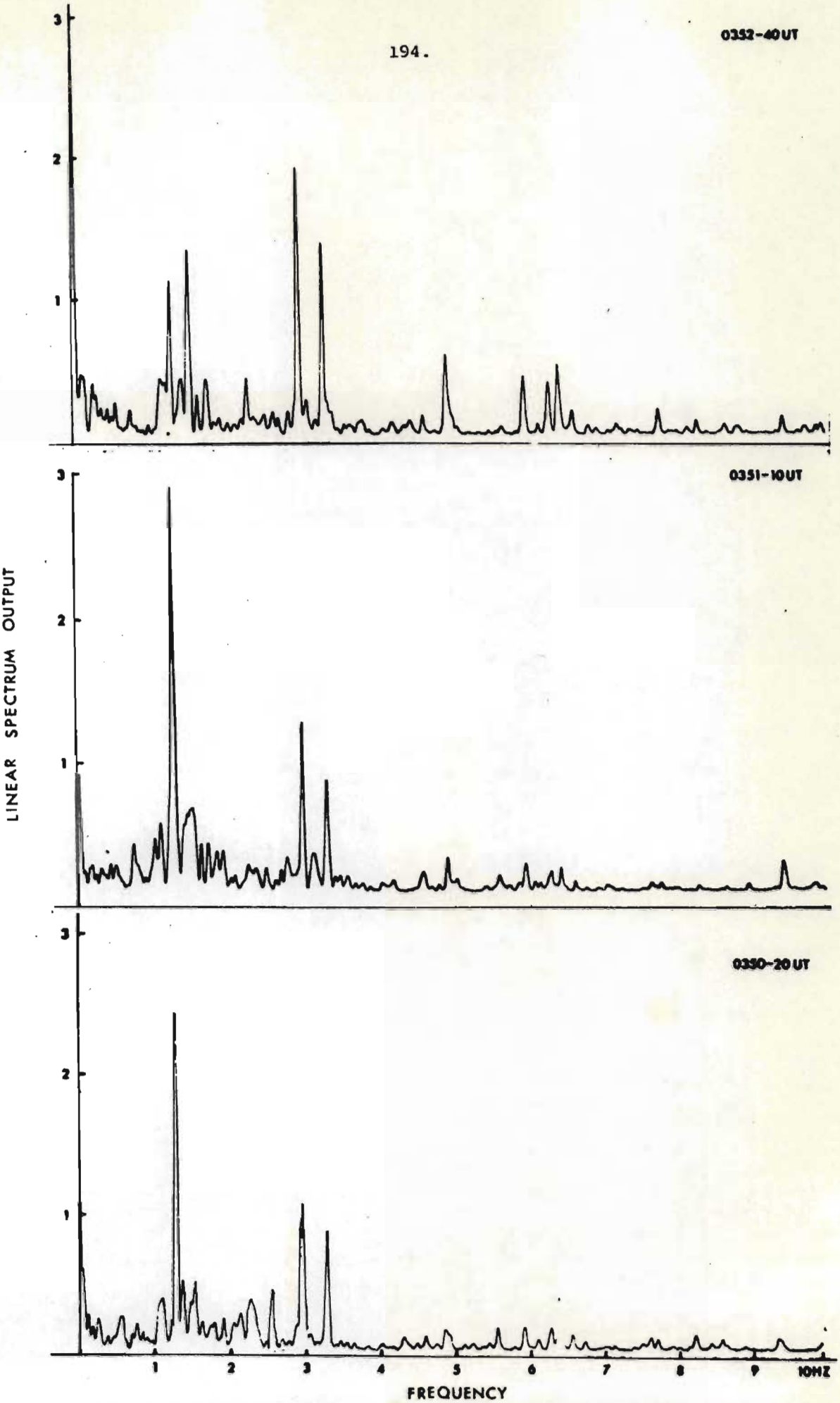

Figure 6.14 Linear spectra of the integrated light intensity within the full field of view of TV camera during consecutive 50 s

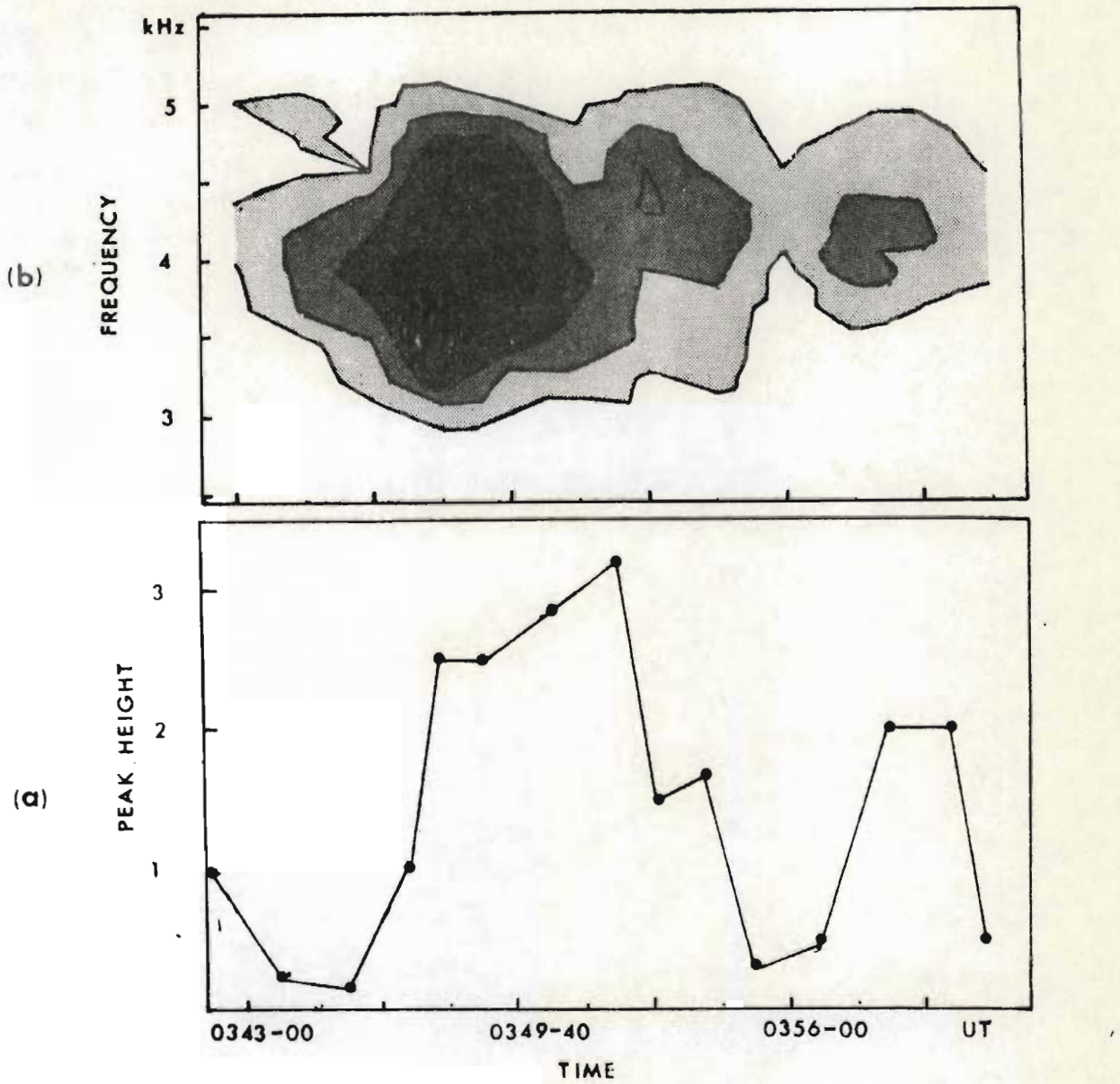

Figure 6.15(a) Plot of the height of the 1,34 Hz frequency component peak in each auroral spectrum for the period 0343-00 UT to 0358-50 UT.

6.15(b) Contour plot of the heights of the 1,34 Hz peak in the frequency spectra derived from 80 Hz bandpass filters versus the centre frequency of each bandpass filter for the period 0343-00 UT to 0358-50 UT. The darker the shading, the higher the peak.

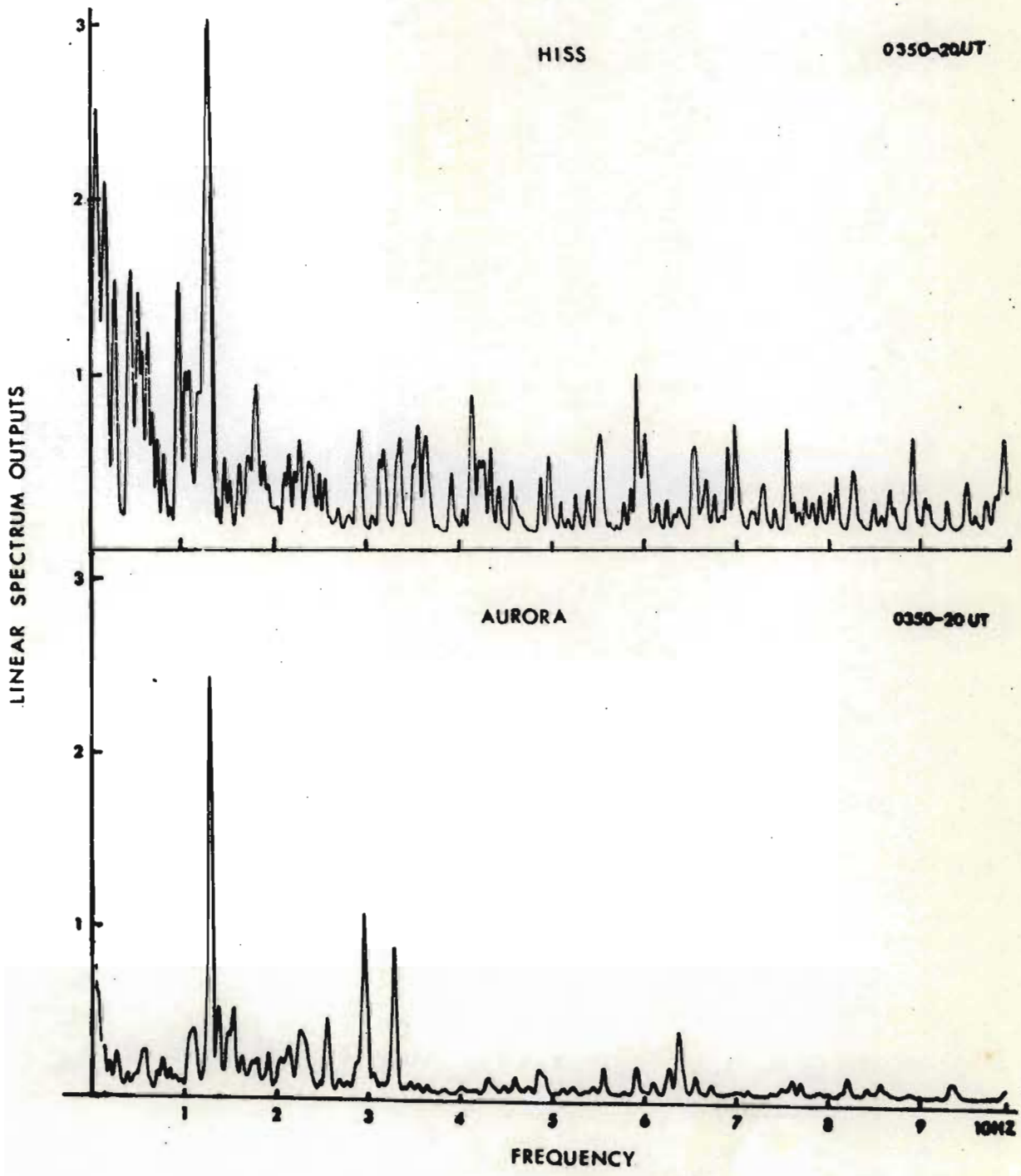

Figure 6.16 Linear spectra of the intensity of hiss at 3,92 kHz and the integrated light intensity within the full field of view of the TV camera over the period 0350-20 UT to 0351-10 UT.

by the possibility of the patch, pulsating at 1,34 Hz, to be out of the field of view of the camera over that period. Otherwise the variations in power of the two phenomena, the pulsating patch and the pulsating auroral hiss, follow each other fairly closely, which is indicative of a common power control source.

6.4 Cross-correlation and coherency between pulsating patch light intensity and pulsating auroral hiss intensity

Simultaneous auroral and hiss data for the periods 0348-15 UT to 0348-43 UT, 0348-40 UT to 0349-10 UT, 0349-15 UT to 0349-43 UT, 0350-40 UT to 0351-20 UT and to 0351-20 UT were cross-correlated and tested for coherency. A square video analyser window, with a vertical and horizontal extent of $3,5^{o}$, was placed in the centre of a pulsating patch during each period and the integrated light intensity within the window was recorded, digitally sampled and stored on disc in data blocks of size 4096 each of which are equivalent to a data realtime of 8,192 sec. Similarly stored was a signal representative of the intensity of the hiss at 3,92 kHz, (bandwidth of the filter - 80 Hz). With the aid of the HP5451B Fourier Analysis System, it was then a simple procedure to determine the cross-correlation function and the coherency between data blocks containing simultaneous auroral and hiss data. In the following paragraphs the analysis of one 8,192 s period will be dealt with in detail and a summary of the results of the other periods will then be presented.

0348-40 UT to 0349-10 UT

The auroral patch signal and hiss signal during the period 0348-45,000 UT to 0348-53,192 UT are shown in Figure 6.17. The power spectrum of each signal was determined and is represented by the plots in Figure 6.18. The frequency range is 0-3,91 Hz and the peaks marked A are at 1,34 Hz. Figure 6.19 shows the phase angles of the two signal

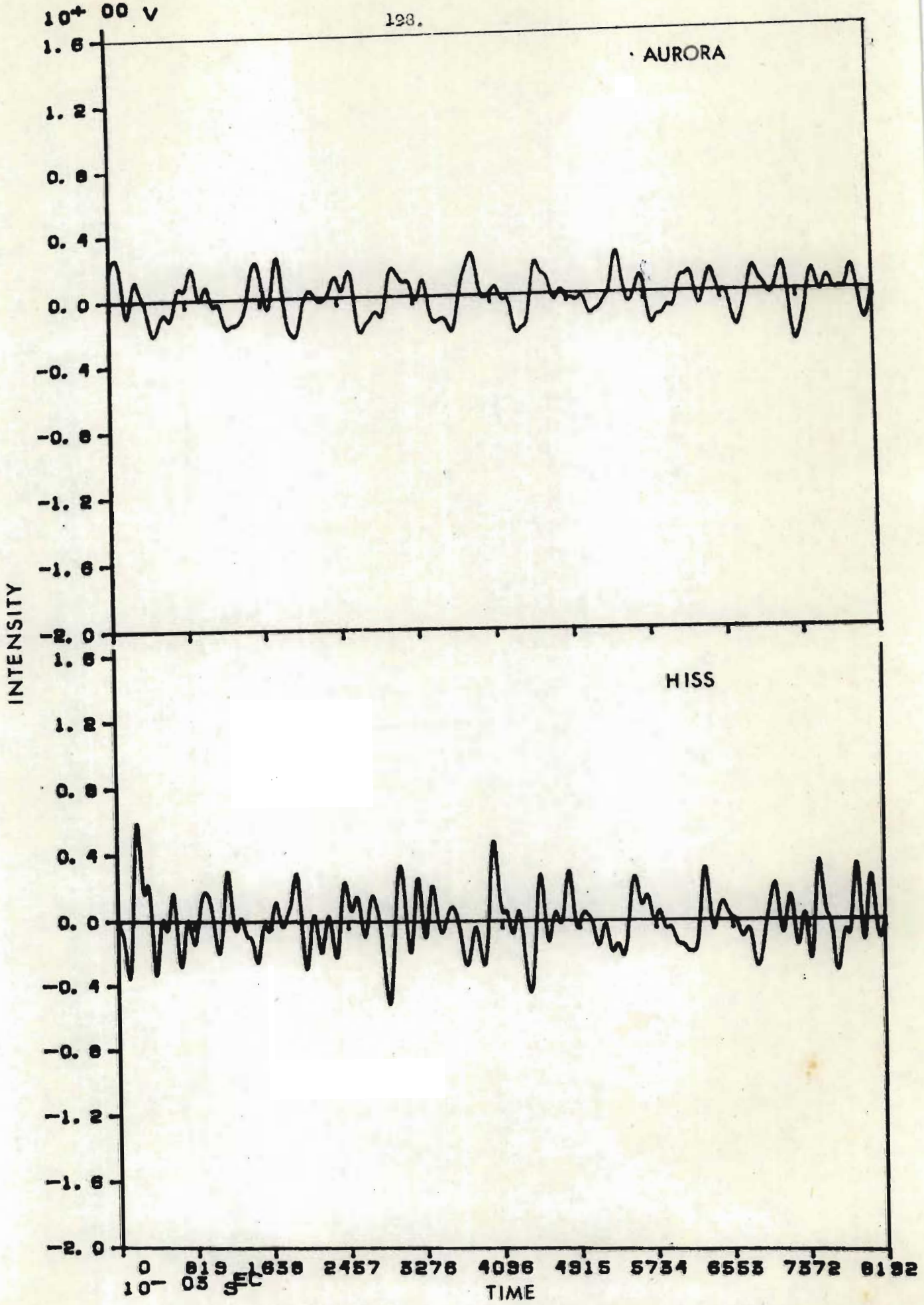

Figure 6.17 Signals representing the light intensity of a pulsating auroral patch and the intensity of the hiss at 3,92 kHz for the period 0348-45,000 UT to 0348-53,192 UT

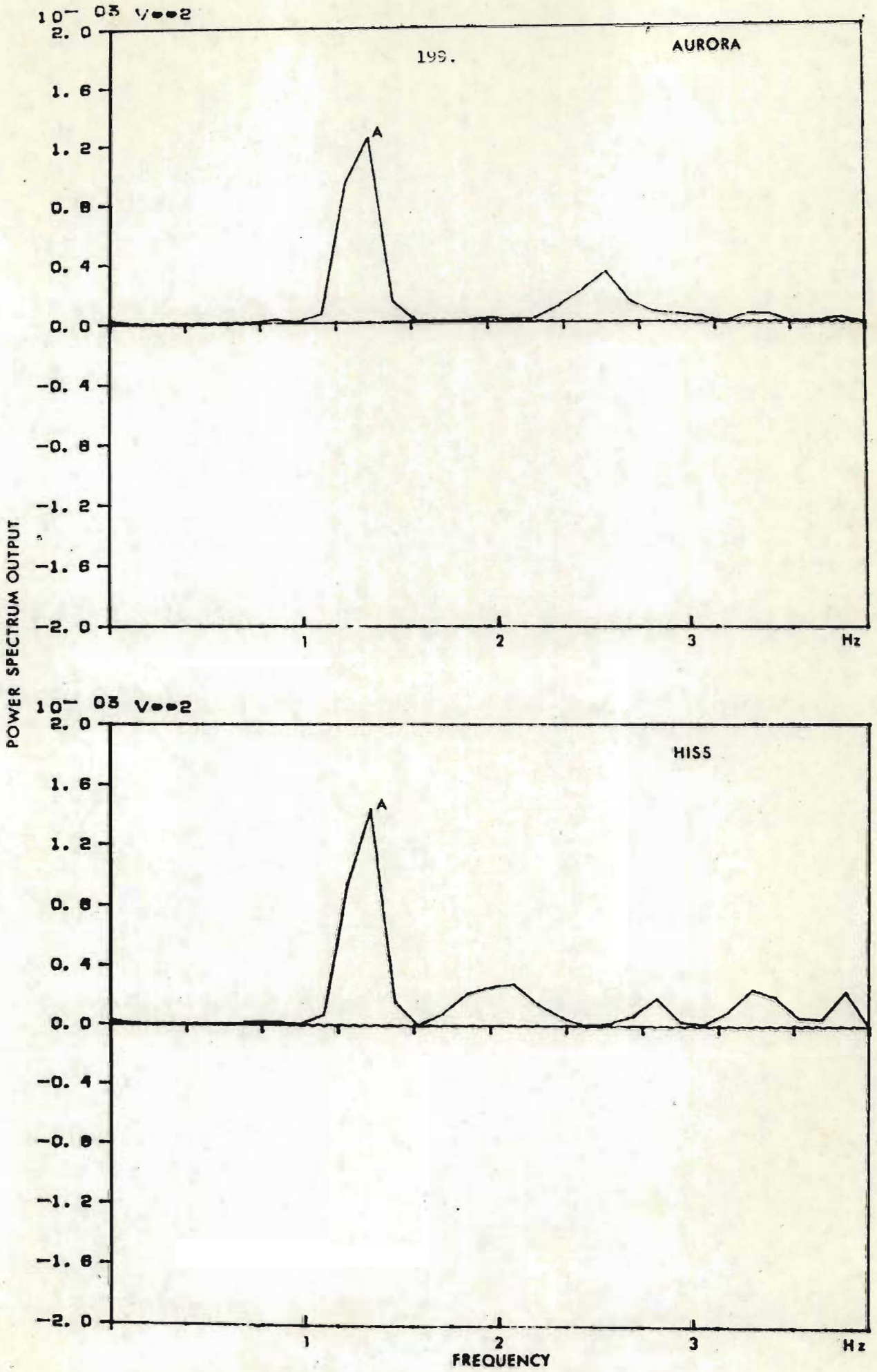

Figure 6.18 Power spectra of the auroral and hiss intensity signals represented in Figure 6.17 for the period 0348-45,000 UT to 0349-53,192 UT.

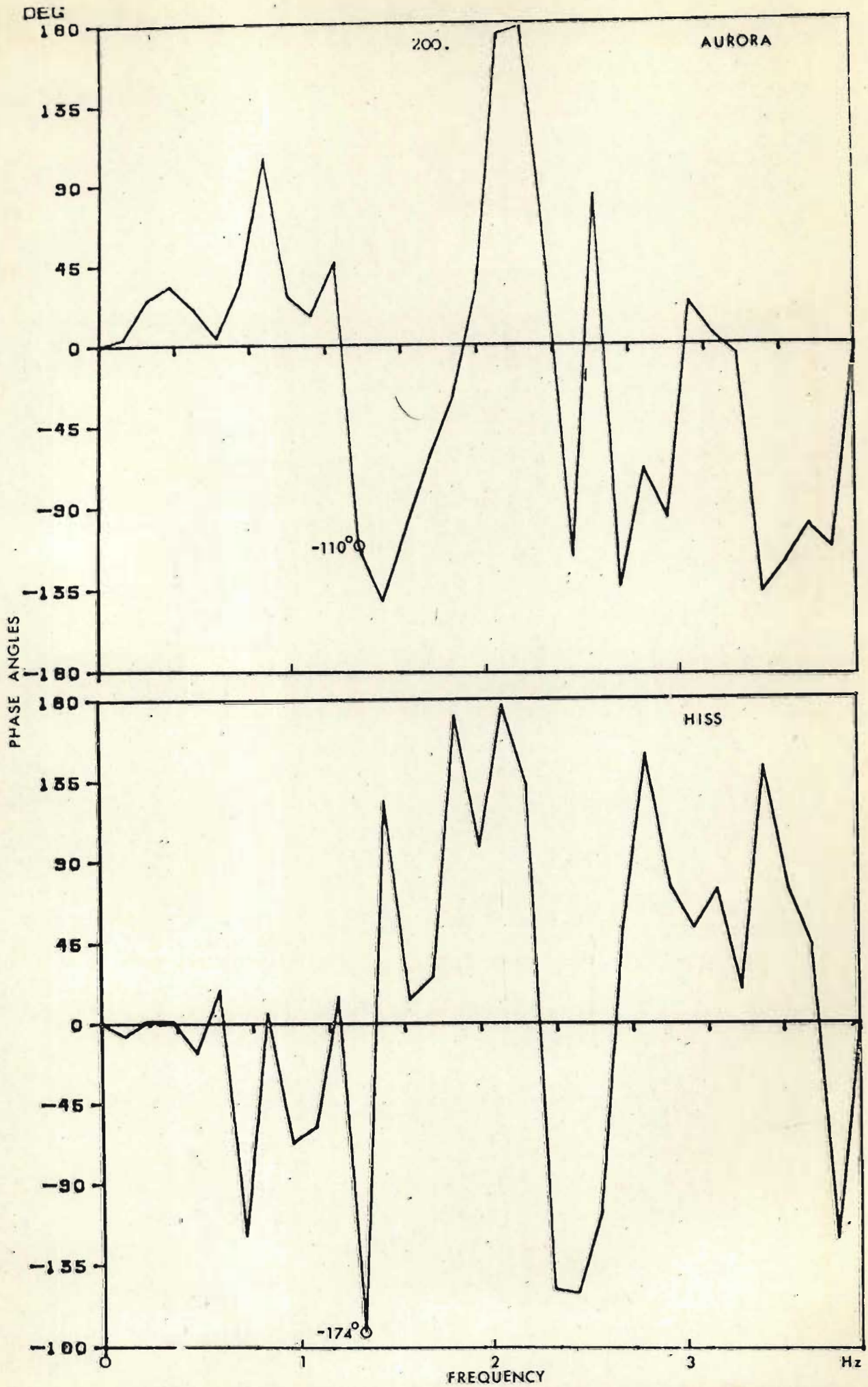

Figure 6.19 Phase angle plots of the auroral and hiss intensity signal represented in Figure 6.17 for the

over the same frequency range. It is seen from Figure 6.18 that at the frequency 1,34 Hz, the two signals are 64° out of phase. This means that the auroral signal leads the hiss signal at 1,34 Hz by 64° and that there is a time delay of 132 m s between them. The plots of the cross-correlation and coherency functions are shown in Figure 6.20. Here the frequency range (x-axis) in the coherency plot is 0 Hz to 15,64 Hz and at 1,34 Hz the two signals have a coherency of 0,77. From Figure 6.20 the time delay between the auroral patch light intensity and pulsating hiss intensity at 3,92 kHz was found to be 135 m s. This measurement is found by calculating the amount along the time axis that the correlation function graph must be shifted such that the peaks are symmetrical about the centre axis. Because the results from this method of time delay determination were within 10 m s of the values obtained from phase angle information, it was decided to rely on the correlation function for time delay calculations for the rest of the analysis. A similar study is done for the period 0348-55,000 UT to 0349-03,192 UT for which the cross-correlation and coherency plots are presented in Figure 6.21.

The results of the periods analysed are summarized in the table in Figure 6.22. Points of interest are the following:

(i) The delay between the auroral and hiss signals is not constant.
(ii) When the signals are highly coherent for a 8,192 s period, the delay lies between 90 m s and 157 m s.

Discussion

Considering cyclotron instability (gyroresonance) and Cerenkov radiation, (See section 3), as a possible generation mechanism for the pulsating auroral hiss analysed in this chapter, two factors come under discussion, namely the energies of electrons which may be responsible for the hiss emmission

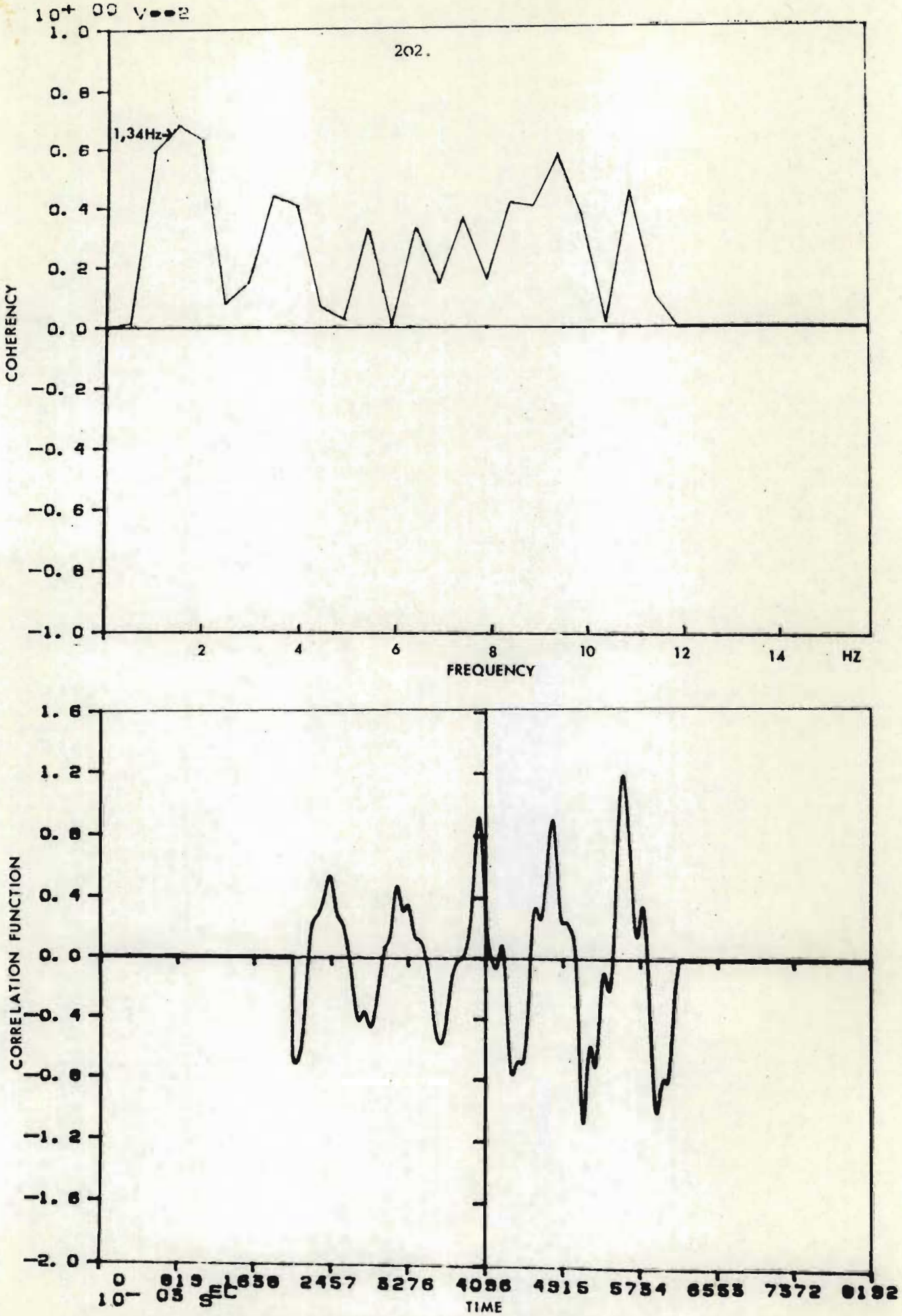

Figure 6.21 Coherency and cross-correlation function plots of the auroral patch light intensity at 3,92 kHz for the period 0348-55,000 UT

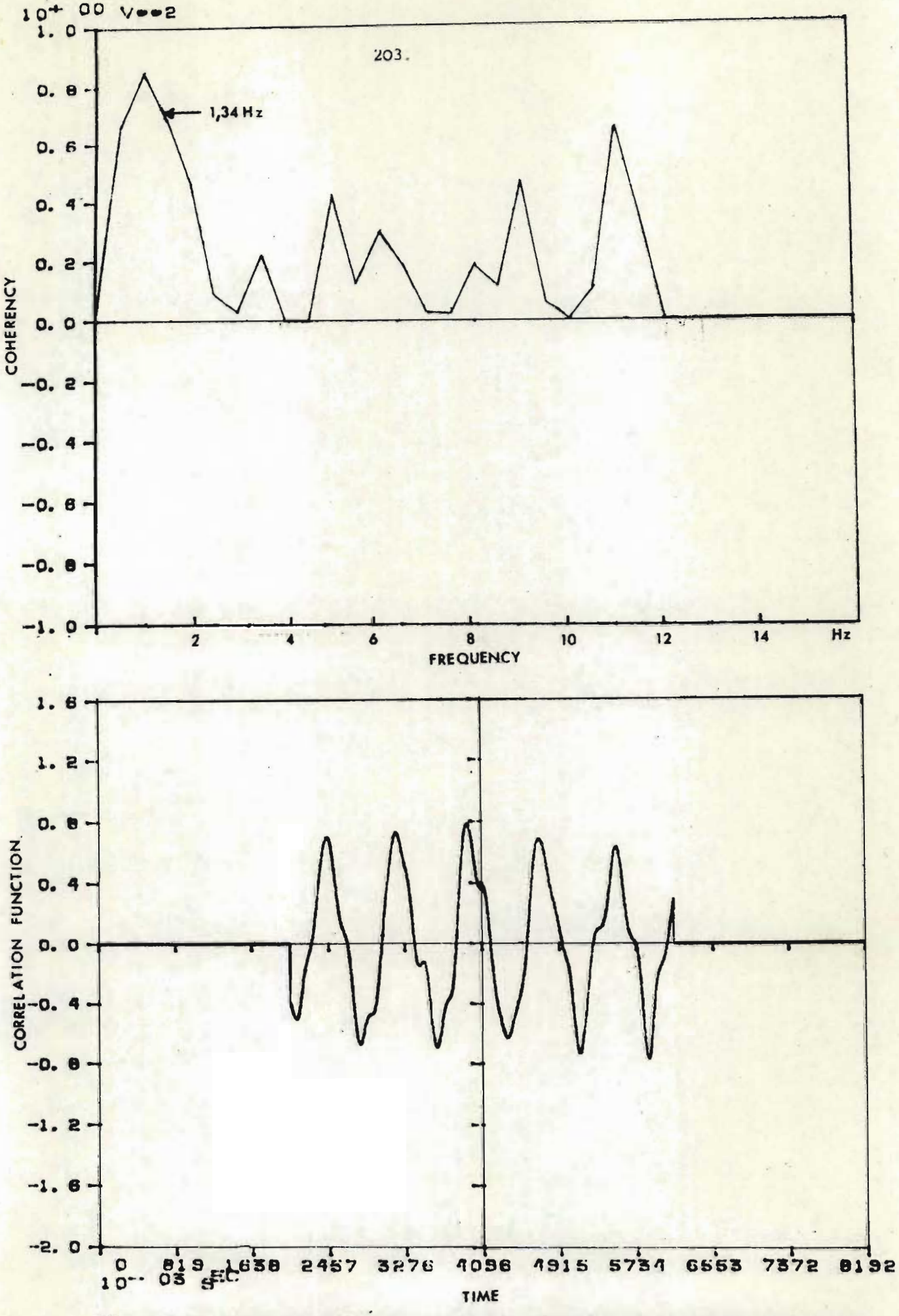

Figure 6.20 Coherence and cross-correlation function plots of the auroral and hiss intensity signals represented in Figure 6.17 for the period 0348-45.000 UT to 0348-53.192 UT.

Period (UT)	Coherency	Delay (ms)
0348-15,00 to 0348-23,19	0,74	157
0348-25,00 to 0348-33,19	0,54	62
0348-35,00 to 0348-43,19	0,79	136
0349-15,00 to 0349-23,19	0,40	-
0349-25,00 to 0349-33,19	0,75	107
0349-35,00 to 0349-43,19	0,10	-
0350-50,00 to 0350-58,19	0,65	40
0351-00,00 to 0351-08,19	0,52	40
0351-10,00 to 0351-18,19	0,50	62
0351-20,00 to 0351-28,19	0,52	157
0351-25,00 to 0351-33,19	0,75	90
0351-40,00 to 0351-48,19	0,50	40
0351-50,00 to 0351-58,19	0,34	-

Figure 6.22 Coherency and time delays between auroral patch light intensity and hiss intensity at 3,92 kHz for the periods of data analysed. The auroral signal leads the hiss signal in each period analysed.

over the observed range of frequencies (2,70 kHz to 5,20 kHz) and the lack of conclusive evidence with regards to the dispersive properties of the hiss.

The energies of electrons associated with hiss of frequencies 2,70; 3,92; and 5,20 kHz have been calculated for both cyclotron and Cerenkov radiation under the following assumptions:

(i) the emissions at these frequencies are generated simultaneously,
(ii) the source region is in the equatorial plane, and
(iii) the electrons in question are just outside the loss cone.

For cyclotron radiation

$$W = \frac{W_{\parallel}}{\cos \theta_e} \qquad (\theta_e = \text{electron pitch angle})$$

$$\simeq W_{\parallel} \qquad (\theta_e < 5^{\circ} \text{ for electrons in the loss cone at } L = 4,11) \quad \text{(See Section 3.7.5)}$$

$$= \frac{B_{eq}^2}{2 \mu_o N_{eq}} \frac{\omega_{ge}}{\omega} (1 - \frac{\omega}{\omega_{ge}})^3 \quad \text{Joules}$$

For Cerenkov radiation

$$W = \frac{W_{\parallel}}{\cos \theta_e}$$

$$\simeq W_{\parallel}$$

$$= \frac{mc^2}{2} \frac{\omega(\omega - \omega_{ge})}{\omega(\omega - \omega_{ge}) - \omega_{pe}^2} \quad \text{Joules} \qquad \text{(See Section 3.5.5)}$$

$$B_{eq} = 0,312 \ (L^{-3}) \ (1 + 3 \sin^2\phi)^{\frac{1}{2}} \times 10^{-4} \text{ Tesla (Dipole approximation, PARK (1972, p88))}$$

$\phi = 0^{\circ}$ at the equator

$$B = (0,312/L^3) \times 10^{-4} \quad \text{Tesla}$$

$$= 4,494 \times 10^{-7}\ T \qquad (L = 4,11)$$

N_{eq} = Electron density in equatorial region (el m^{-3})

$f_{ge} = \frac{\omega_{ge}}{2\pi}$ = electron gyrofrequency

$$= (8,736 \times 10^5/L^3)\ (1 + 3\sin^2\phi)^{\frac{1}{2}}\ \text{Hz}$$

$$= 12,6\ \text{kHz}$$

$f = \frac{\omega}{2\pi}$ = frequency of emitted radiation (kHz)

$$\omega_{pe} = \sqrt{\frac{N_{eq}\ e^2}{\varepsilon_o\ m}}\ \text{Hz}$$

The table in Figure 6.23 shows the relationship between the N_{eq}, f, and W and the travel times (t_e) of electrons with energy W from the equatorial plane to the earth along L = 4,11 (See Section 3.3.12). Also presented in Figure 6.23 are the travel times (t_f) of emissions of the various frequencies taken from Figure 6.7.

Assuming that the modulation mechanism, for example gyroresonance, to be acting simultaneously on electrons with similar energies travelling in the backward and forward hemispheres in the equatorial plane, it is seen from the table in Figure 6.23 that the emissions at 3,92 kHz have longer travel times than the electrons with the same energies as those responsible for the emissions. The difference in travel times range from 0,213 s to 0,674 s for equatorial electron densities of 100 el cm^{-3} and 1000 el cm^{-3} respectively. The results of the data analysed in this section, however, indicate a difference in travel times ranging from 0,090 s to 0,157 s with the auroral electrons travelling <u>faster</u> than the emissions at 3,92 kHz, which is contrary to the prediction of the cyclotron instability theory.

N_{eq} ($e\ cm^{-3}$)	f (kHz)	W Gyroresonance (keV)	t_e Gyroresonance (s)	W Cerenkov radiation (keV)	t_e Cerenkov radiation (s)	t_f (s)	$t_f - t_e$ Gyroresonance (s)	$t_f - t_e$ Cerenkov radiation (s)
1000	2,70	1,137	1,662	0,085	6,089	2,127	+ 0,465	- 3,962
	3,92	0,528	2,439	0,108	5,397	1,765	- 0,674	- 4,722
	5,20	0,247	3,566	0,122	5,076	1,532	- 2,034	- 3,544
300	2,70	3,790	0,910	0,282	3,337	1,165	0,255	- 1,172
	3,92	1,759	1,336	0,360	2,958	0,904	- 0,432	- 2,054
	5,20	0,822	1,955	0,407	2,782	0,840	- 1,115	- 1,942
200	2,70	5,685	0,743	0,424	2,725	0,951	+ 0,208	- 1,774
	3,92	2,639	1,091	0,539	2,416	0,789	- 0,302	- 1,625
	5,20	1,233	1,596	0,609	2,272	0,685	- 0,911	- 1,587
100	2,70	11,370	0,526	0,086	1,929	0,673	+ 0,147	- 1,256
	3,92	5,278	0,772	1,076	1,710	0,558	- 0,214	- 1,152
	5,20	2,466	1,129	1,216	1,608	0,485	- 0,644	- 1,123

Fig. 6.23 Table showing the travel times of emissions and the energetic electrons responsible for each emission, as predicted by the gyroresonance and cerenkov radiation theory, from the equatorial plane to Sanae along a field line L = 4,11 for various equatorial electron densities.

It is also worth noting that the difference in electron travel times range from 0,904 s (for N_{eq} = 1000 eℓ cm^{-3}) to 0,603 s (for N_{eq} = 1000 eℓ cm^{-3}). One would therefore expect a similar time duration for the enhancement of auroral luminosity whereas, in fact, the latter was observed to be ∿ 0,400 s.

As far as Cerenkov radiation is concerned it can be seen from the figures appearing in the final column of Figure 6.23 that the discrepancy noted above for cyclotron gyroresonence is even more marked.

Gyroresonance or Cerenkov radiation occurring in the equatorial plane do not therefore seem to be plausible mechanisms for the production of the pulsating auroral patches and auroral hiss analysed.

6.5 Conclusion

The close relation and correlation between auroral hiss and auroral light intensity of various auroral forms is well established e.g. OGUTI, (1975). Interest and research concerning auroral hiss is centred around the determination and location of the mechanism responsible for auroral hiss e.g. LIM and LAASPERE, (1972).

The results of the analysis of the data, as presented in this chapter, can be summarized as follows:

Auroral hiss

(a) The pulsating auroral hiss is band-limited and most likely duct-guided.

(b) There is no clear evidence of dispersion or structure in the hiss.

(c) The pulsation period of 0,75 s of the hiss remains constant for approximately 16 minutes.

Auroral patch light intensity

(a) A pulsation period of 0,75 s is a dominating feature during the 16 minute period of analysis.

(b) The length of the pulsation is not explained by the bounce period of energetic electrons travelling along the field line L = 4,11.

Simultaneous analysis of the auroral hiss and auroral patch light intensity

(a) The common identical pulsation period and high coherency between the two phenomena strongly suggests a wave-particle interaction as a modulation mechanism.

(b) Time delays, typically between 0,090 s and 0,157 s where the auroral electrons are observed to arrive before the auroral hiss emissions at the point of observation, are not explained by either cyclotron instability or Cerenkov radiation mechanisms occurring in the equatorial plane.

APPENDIX A1

SYSTEMATIC ERRORS IN L-VALUE AND $N_e(eq)$

Electron density distribution model systematic errors in L-value and $N_e(eq)$ may be calculated for the DE-1 and R^{-4} models, used in the present work, according to information given by PARK (1972). The formulas used in the calculation of L and $N_e(eq)$ are:

$$fH_{eq} = K f'_n \tag{1}$$

$$L = \left(\frac{8,736 \times 10^5}{fH_{eq}} \right)^{1/3} \tag{2}$$

$$N_e(eq) = Keq \frac{f'_n \, t'^2_n}{L^5} \tag{3}$$

Equations (1) to (3) may be written in differential form as follows:

$$\frac{\Delta f_{Heq}}{f_{Heq}} = \frac{\Delta K}{K} \tag{4}$$

$$\frac{\Delta L}{L} = -\frac{1}{3} \cdot \frac{\Delta K}{K} \tag{5}$$

$$\frac{\Delta N_e(eq)}{N_e(eq)} = \frac{\Delta K_{eq}}{K_{eq}} + \frac{5}{3} \cdot \frac{\Delta K}{K} \tag{6}$$

$\frac{\Delta K}{K}$ and $\frac{\Delta K_{eq}}{K_{eq}}$ in the above equations may be obtained from Tables 9

and 10 of PARK (1972) for the DE-1 and R^{-4} models respetively, giving for the DE-1 model:

$$\frac{\Delta K}{K} = 0,14\%$$

$$\frac{\Delta K_{eq}}{K_{eq}} = 0,61\%$$

and for the R^{-4} model:

$$\frac{\Delta K}{K} = 0,3\%$$

$$\frac{\Delta K_{eq}}{K_{eq}} = 1,9\%$$

From these K errors the calculated errors for the DE-1 model are:

$$\frac{\Delta L}{L} = 0,05\%$$

$$\frac{\Delta N_e(eq)}{N_e(eq)} = 0,84\%$$

and for the R^{-4} model are:

$$\frac{\Delta L}{L} = 0,1\%$$

$$\frac{\Delta N_e(eq)}{N_e(eq)} = 2,4\%$$

APPENDIX B1

THE DETERMINATION OF THE ANGLES OF ELEVATION AND AZIMUTH OF STARS IN A STAR PATTERN

An example of a star pattern at 0320 UT 12 June, 1975, traced off a Sony Video Monitor PVM-90CE is presented in Figure a. With the help of Norton's Star Atlas the stars were identified as shown in Figure a.

Conversion of Universal Time (UT) to Local Sidereal Time (LST)

		h	m	s
Greenwich Mean Sidereal Time at 00^h 12th June, 1975*		17	18	48
Reduction for Longitude of SANAE $= (17 + \frac{18}{60}) \div 24 \times 3{,}56$ m	+	00	02	34
Mean Sidereal Time		17	21	22
Universal time of observation	+	03	20	00
Local Sidereal Time of observation		20	41	22

* This can be obtained in the star ephemeris for 1975 under the section of universal and sidereal times.

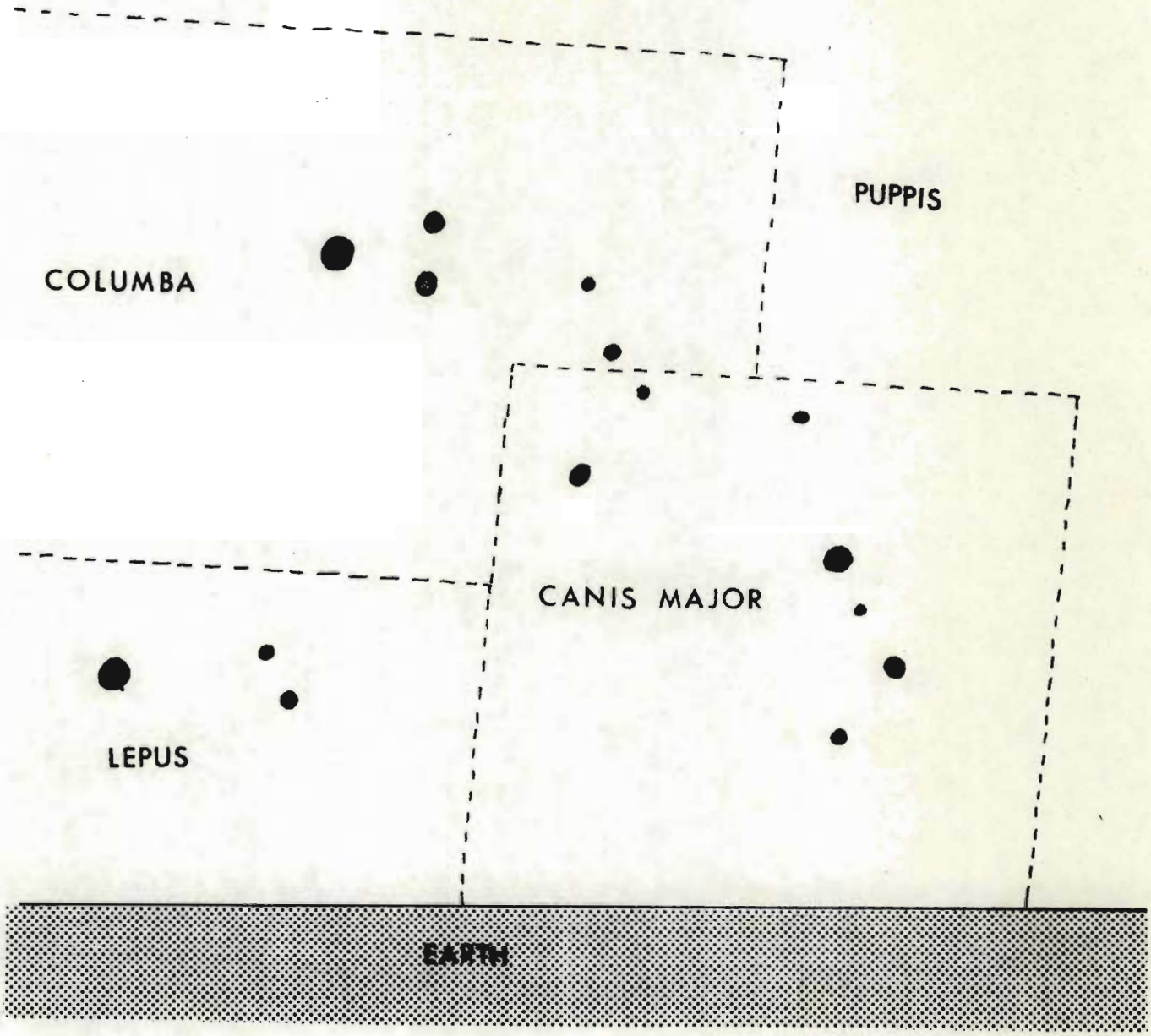

Figure (a) Star pattern as copied from the screen of a Sony Video Monitor PVM-90 CE showing a video picture recorded at 0320 UT on 12 June, 1975.

Calculation of the position of γ Canis Major at $20^h\ 41^m\ 22^s$ Local Sidereal Time with program ELEVAZI

The four input parameters needed for ELEVAZI are the following:

(i)	Right ascension of star	α
(ii)	Declination of star	δ
(iii)	Latitude of observing station	ϕ
(iv)	Local Sidereal Time	LST

For γ Canis Major*

(i)	ϕ	=	-70°	$-18'$	$-00''$
(ii)	L.S.T.	=	20^h	41^m	22^s
(iii)	α	=	06^h	19^m	21^s
(iv)	δ	=	-30°	$-03'$	$-05''$

* Obtained from the star ephemeris for 1975 under section for Mean Places of Stars, 1975,0.

Program 'ELEVAZI' was written for the HP9100B computor and is explained as follows:

00	20	CLEAR	21	01	1
01	01	1	22	05	5
02	41	STOP	23	36	X
03	44	GO TO( )( )	24	25	↓
04	77	SUB	25	23	x→( )
05	10	8	26	17	d
06	14	b	27	04	4
07	23	x→( )	28	41	STOP
08	14	b	29	44	GO TO( )( )
09	02	2	2a	77	SUB
0a	41	STOP	2b	10	8
0b	44	GO TO( )( )	2c	14	b
0c	77	SUB	2d	23	x→( )
0d	10	8	30	12	e
10	14	b	31	16	c
11	27	↑	32	27	↑
12	01	1	33	17	d
13	05	5	34	34	-
14	36	X	35	25	↓
15	25	↓	36	23	x→( )
16	23	x→( )	37	16	c
17	16	c	38	73	cos x
18	03	3	39	27	↑
19	41	STOP	3a	12	e
1a	44	GO TO( )( )	3b	73	cos x
1b	77	SUB	3c	36	X
1c	10	8	3d	14	b
1d	14	b	40	73	cos x
20	27	↑	41	36	X

42	25	↓	66	73	cos x
43	23	x→( )	67	36	X
44	17	d	68	16	c
45	12	e	69	70	sin x
46	70	sin x	6a	35	÷
47	27	↑	6b	40	y→( )
48	14	b	6c	17	
49	70	sin x	6d	14	b
4a	36	X	70	70	sin x
4b	17	d	71	27	↑
4c	33	+	72	16	c
4d	25	↓	73	44	GO TO( )( )
50	72	arc	74	34	-
51	73	cos x	75	00	0
52	23	x→( )	76	00	0
53	13	a	77	27	↑
54	44	GO TO( )( )	78	64	int x
55	77	SUB	79	34	-
56	07	7	7a	23	x→( )
57	07	7	7b	15	f
58	41	STOP	7c	06	6
59	00	0	7d	00	0
5a	27	↑	80	36	X
5b	16	c	81	27	↑
5c	50	IF X=Y	82	25	↓
5d	34	-	83	31	ROLL ↓
60	07	7	84	64	int x
61	00	0	85	34	-
62	12	e	86	31	ROLL ↓
63	71	tan x	87	36	X
64	27	↑	88	15	f
65	14	b	89	31	ROLL ↓

8a	77	RETURN	-10	67	x←( )
8b	22	ROLL ↑	-11	33	+
8c	23	x→( )	-12	16	c
8d	15	f	-13	70	sin x
90	06	6	-14	53	if x y
91	00	0	-15	02	2
92	35	÷	-16	00	0
93	31	ROLL ↓	-17	02	2
94	33	+	-18	07	7
95	25	↓	-19	00	00
96	30	x⇄y	-1a	44	GO TO( )( )
97	35	÷	-1b	02	2
98	15	f	-1c	02	2
99	33	+	-1d	35	÷
9a	37	clear x	-20	11	9
9b	27	↑	-21	00	0
9c	22	ROLL ↑	-22	27	↑
9d	77	RETURN	-23	67	x←( )
a→d	Registers		-24	33	+
-00	71	tan x	-25	15	f
-01	35	÷	-26	34	-
-02	67	x←( )	-27	25	↓
-03	33	+	-28	23	x→( )
-04	17	d	-29	33	+
-05	34	-	-2a	17	d
-06	25	↓	-2b	44	GO TO( )( )
-07	72	arc ↓	-2c	77	SUB
-08	71	tan -	-2d	33	+
-09	23	x→( )	-30	07	7
-0a	33	+	-31	07	7
-0b	15	f	-32	41	STOP
-0c	00	00	-33	01	1
-0d	7	↑	-34	05	5

-35	27	↑
-36	67	x←( )
-37	33	+
-38	14	b
-39	73	cos x
-3a	36	X
-3b	67	x←( )
-3c	33	+
-3d	17	d
-40	70	sin x
-41	36	X
-42	00	0
-43	30	x←→y
-44	27	↑
-45	25	↓
-46	41	STOP
-47	67	x←( )
-48	33	+
-49	14	b
-4a	73	cos x
-4b	27	↑
-4c	67	x←( )
-4d	33	+
-50	17	d
-51	73	cos x
-52	36	X
-53	67	x←( )
-54	33	+
-55	13	a
-56	71	tan x
-57	35	÷
-58	67	x←( )
-59	33	+

-5a	14	b
-5b	70	sin x
-5c	33	+
-5d	01	1
-60	05	5
-61	36	X
-62	25	↓
-63	41	STOP
-64	44	GO TO( )( )
-65	33	+
-66	0	0
-67	0	0
-68	0	0
→9d	0	0

Instructions for data Input and Output

	Registers		
	z	y	x
Press 'CONT'	0	0	1
Enter data (ϕ)	-70	-18	-00
Press 'CONT'	0	0	2
Enter data (L.S.T.)	20	41	22
Press 'CONT'	0	0	3
Enter data (α)	6	19	21
Press 'CONT'	0	0	4
Enter data (δ)	-30	-03	-05
Press 'CONT'			
(Elevation)	76	28	16
Press 'CONT'			
(Azimuth)	328	51	57
Press 'CONT'			
($d\theta'/dt$)	0	0	-2.6
Press 'CONT'			
($d\gamma/dt$)	0	0	-13.0

The symbols θ' and γ are explained in Figure b.

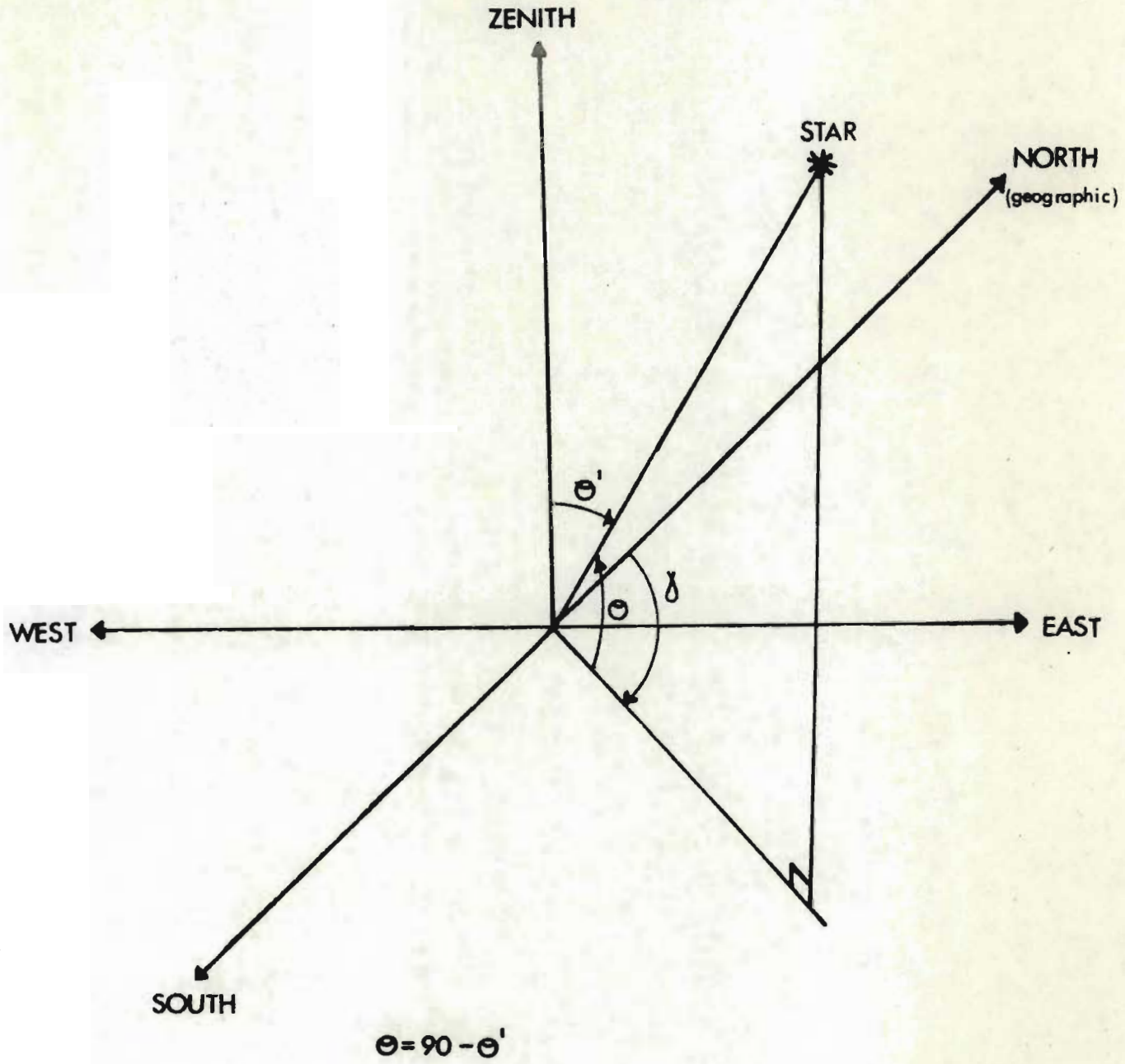

Figure (b) Diagram for the determination of the geographic latitude and longitude of a point with altitude h km above the earth and angles of elevation θ and azimuth γ relative to the observing station.

APPENDIX B2

MATHEMATICS FOR SUBROUTINE ANGEOG

The determination of the geographic latitude and longitude of a point with altitude h km above the earth and angles of elevation θ and azimuth γ relative to the observing station (calculations are made assuming that the earth is spherical).

In Fig c

$$\tan(\theta + \alpha) = \frac{(h + R) - R\cos\alpha}{R\sin\alpha}$$

$$h + r = \frac{R\sin\alpha\sin(\alpha + \theta)}{\cos(\alpha + \theta)} \qquad (\times R\sin\alpha)$$

$$h + r = R\left(\frac{\sin\alpha\sin(\alpha + \theta) + \cos\alpha\cos(\alpha + \theta)}{\cos(\alpha + \theta)}\right)$$

$$h + r = \frac{R\cos\left((\alpha + \theta) - \alpha\right)}{\cos(\alpha + \theta)}$$

$$\cos\theta = \frac{h + R}{R} \times \cos(\alpha + \theta)$$

$$\cos(\alpha + \theta) = \frac{R}{h + R}\cos\theta$$

$$\alpha + \theta = \cos^{-1}\left(\frac{R\cos\theta}{h + R}\right)$$

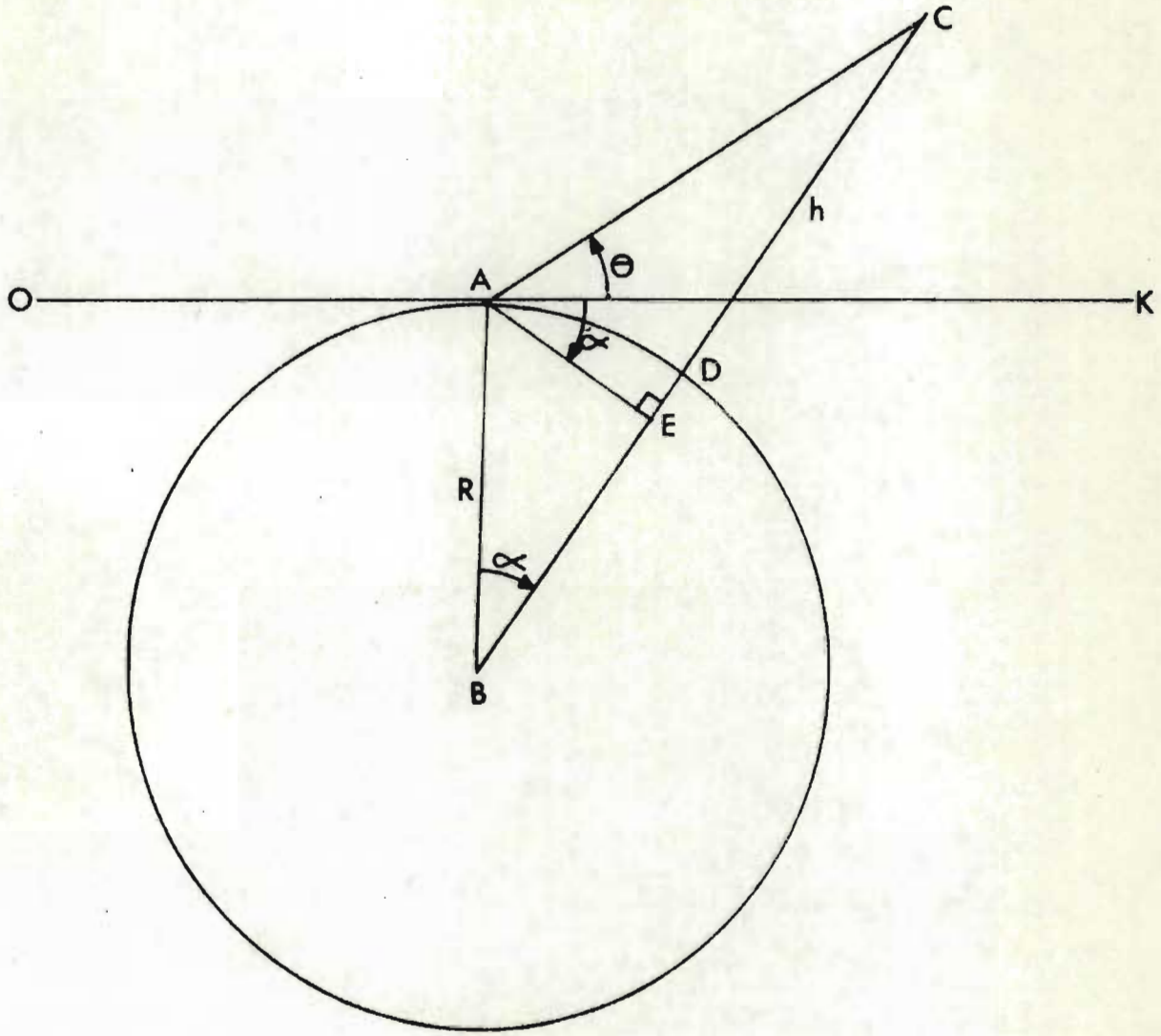

Figure (c) $\overline{OAK}$ is a line tangent to the earth through the observing station A

AB = R = earth radius = 6371 km

DC = h = height of point C above the earth

α = $\angle ABD$

$$\alpha = \cos^{-1}\left(\frac{R\cos\theta}{h+r}\right) - \theta \qquad (1)$$

In Figure d, spherical $\Delta\,\hat{\Theta}$ CSA

$$\cos \angle CAS = \frac{\cos/SOC - \cos/SOA \cdot \cos/COA}{\sin/SOA \cdot \sin/COA}$$

$$\cos(180-\gamma) = \frac{\cos \nu'_C - \cos \nu'_A \cos\alpha}{\sin\ '_A \sin\alpha}$$

$$-\cos\gamma = \frac{\sin \nu^\circ_C - \sin \nu^\circ_A \cos\alpha}{\cos \nu^\circ_A \sin\ \alpha}$$

$$(\sin 90 - A) = \cos A)$$

$$\nu^\circ_C = \sin^{-1}(\sin\lambda^\circ_A \cos\alpha - \cos\nu^\circ_A \sin\alpha\cos\gamma) \qquad (2)$$

Latitude of point C = ν°_C

In spherical $\Delta\,\Theta$ CSA

$$\frac{\sin/CSA}{\sin/COA} = \frac{\sin/CAS}{\sin/SOC}$$

i.e $$\frac{\sin\Delta L}{\sin\alpha} = \frac{\sin\gamma}{\sin\lambda'_C}$$

$$\Delta L = \sin^{-1}(\sin\alpha\sin\gamma/\cos\lambda^\circ_C)$$

Longitude of point C

$$= \Delta L - (360^\circ - \text{longitude of A}) \qquad (3)$$

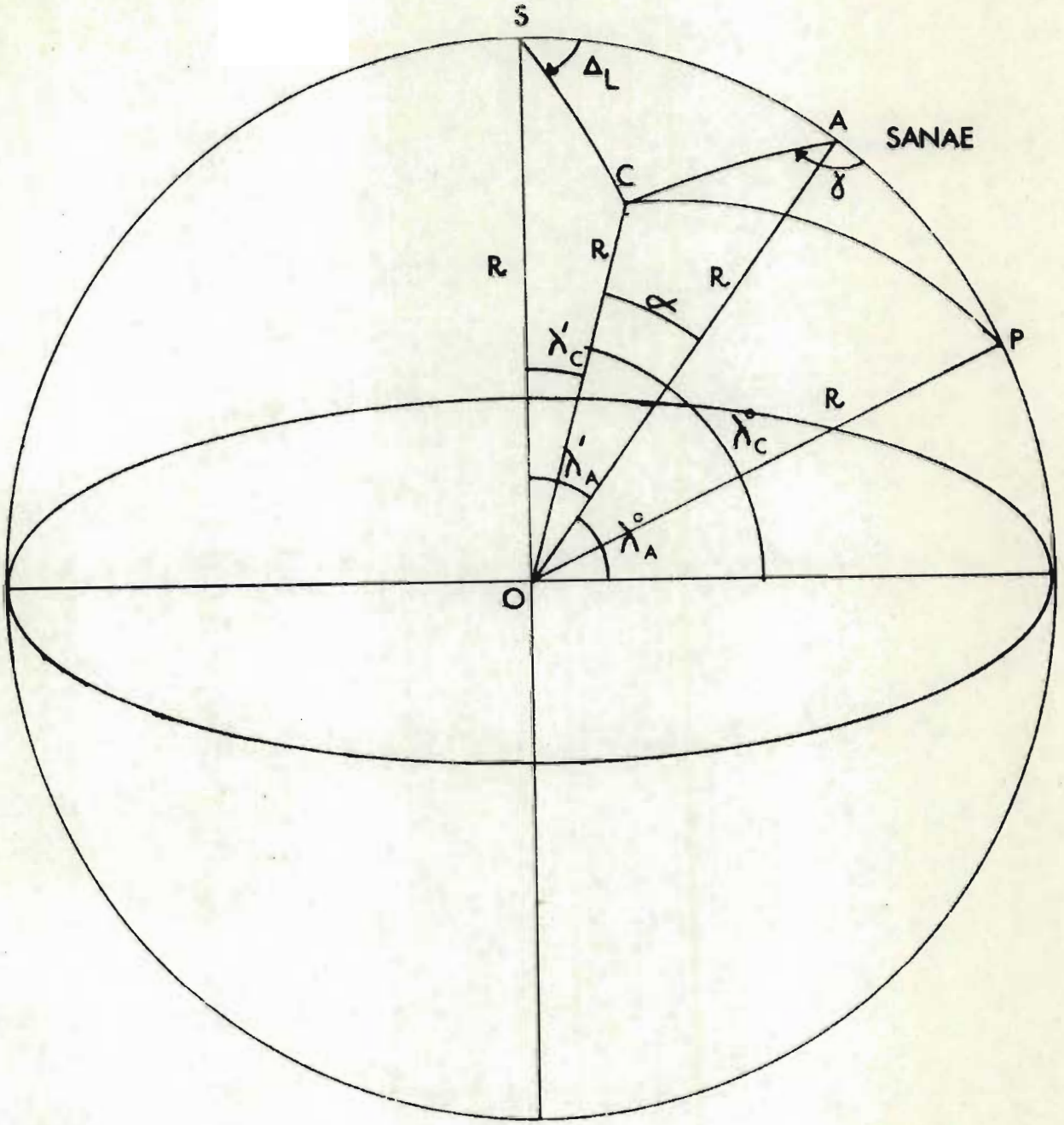

Figure (d)
C = point whose longitude is to be calculated
A = observing station
S = geographic south pole
ΔL = difference in longitude between points C and A
AP = line of longitude through A

L VALUE COMPUTER PROGRAM

(Modified version of a program by E. G. Stassinopoulos and G. D. Mead, (1972).
- NASA-GODDARD SPACE FLIGHT CENTRE, REPORT No. NSSDC72-12)

```
$ SET IBM026
FILE  5 =  INPUT                ,UNIT = READER
FILE  6 = OUTPUT, UNIT = PRINTER
C****  NBNBNB.....SEE DESCRIPTION OF LVALUE PROGRAM IN  A.R.U."S FILES.
C  ***  MAIN FOR INVARA USING ALLMAG AND THE COORDINATE CONVERSION
C  ***  INPUT:
C  ***  SINGLE PRECISION DECK FOR OCTAL MACHINES (BCD, 026 PUNCH)
C  ***                        =1 GEODETIC;  =2 GEOCENTRIC.
C*****                         =3GENERATES COORDINATES FOR ANGLESOF
C*****                       ELEVATION AND AZIMUTH FOR ANY STATION
C  ****                       FOR ANY HEIGHT. GCALT = HEIGHT ABOVE
C *******                        SURFACE EARTH. SEE SUBROUTINE ANGEOG
C  ****                       FOR INSERTING LATITUDE OF STATION.
CC*******                     = 4 GENERATES COORDINATES FOR GIVEN
C*****                        GRID  WITH ANY SIZE SQARES.
C  ***       ICOORD           REFERENCE SYSTEM OF INPUT COORDINATES
C  ***       MODEL            CHOICE OF 7 MODELS (FROM ALLMAG)
C  ***       TM               TIME IN YEARS FOR DESIRED FIELD
C***  N    AZIMUTH
C*****  GCALT    ALTITUDE

      DIMENSION SHMIT(13,13),G(13,13),EL(46),GLA(46),GLO(46)
     DATA RAD/57.2957795/,SHMIT(1,1)/0.0/,TMOLD/0.0/,MODOLD/0.0/
    2 FORMAT(3I5,2F10.3)
    3 FORMAT(1H0,7X,2F8.2,F8.1,1X,2F8.2,F8.1,2X,F12.5,F12.3,F12.3)
    4 FORMAT(3F10.3)
    5 FORMAT(8H1   MODEL,I3,/,7H    TIME,F8.1,/,9H    ICOORD,I3)
      READ(5,2)  ICOORD,MODEL,N,TM,GCALT
      WRITE(6,5) MODEL,TM,ICOORD
C
C     BRANCH TO  ICOORD SECTIONS
C      **************************
       GO TO (7,11,8,12),ICOORD
C
C      ICOORD = 1
C      **********
    7 READ(5,4,END=99)  GDLAT,GLON,GDALT
      CALL CONVRT(1,GDLAT,GDALT,GCLAT,RKM)
      CT= SIN(GCLAT/RAD)
      GCALT=RKM-6378.16/ SQRT(1.+.0067397*CT*CT)
      GO TO 9
C
C      ICOORD = 2
C      **********
 11    READ(5,4,END=99)GCLAT,GLON,GCALT
       CT=SIN(GCLAT/RAD)
      RKM=GCALT+6378.16/ SQRT(1.+.0067397*CT*CT)
      CALL CONVRT(2,GDLAT,GDALT,GCLAT,RKM)
    9 CALL INVARA(MODEL,TM,GCLAT,GLON,GCALT,0.01E0,BB,FL,
     *SHMIT,G,NMAX,MODOLD,TMOLD)
      WRITE(6,3)  GCLAT,GLON,GCALT,GDLAT,GLON,GDALT,BB,FL
       GO TO (7,11),ICOORD
C
C      ICOORD = 3
C      **********
  8    WRITE(6,100) N
```

```
      CALL ANGEOG(N,EL,GLA,GLO,GCALT)
      DO 10 K=1,46
      GCLAT=-GLA(K)
      GLON =GLO(K)
     CT= SIN(GCLAT/RAD)
     RKM=GCALT+6378.16/ SQRT(1.+.0067397*CT*CT)
     CALL CONVRT(2,GDLAT,GDALT,GCLAT,RKM)
     CALL INVARA(MODEL,TM,GCLAT,GLON,GCALT,0.01E0,BB,FL,
    *SHMIT,G,NMAX,MODOLD,TMOLD)
      ELEV=EL(K)
     WRITE(6,3)  GCLAT,GLON,GCALT,GDLAT,GLON,GDALT,BB,FL,ELEV
 10   CONTINUE
       GO TO 99
C
C      ICOORD = 4
C      **********
 12     READ(5,1) GLATBE,GLATEN,LATDEL,GLONBE,GLONEN,LONDEL
  1     FORMAT(2F10.3,I5,2F10.3,I5)
      CALL GENCOR(GLATBE,GLATEN,LATDEL,GLONBE,GLONEN,LONDEL,GLA,GLO)
      DO 14 I=1,46
       DO 13 J=1,46
       GCLAT=GLA (J)
        GLON= GLO(I)
       IF( GLON .EQ.0.0) GO TO 99
       CT=SIN(GCLAT/RAD)
     RKM=GCALT+6378.16/ SQRT(1.+.0067397*CT*CT)
     CALL CONVRT(2,GDLAT,GDALT,GCLAT,RKM)
     CALL INVARA(MODEL,TM,GCLAT,GLON,GCALT,0.01E0,BB,FL,
    *SHMIT,G,NMAX,MODOLD,TMOLD)
     WRITE(6,3)  GCLAT,GLON,GCALT,GDLAT,GLON,GDALT,BB,FL
 13     CONTINUE
  14    CONTINUE
   99 STOP
      END
```

```
      SUBROUTINE GENCOR (GLATBE,GLATEN,LATDEL,GLONBE,GLONEN,
     *LONDEL,GLAT,GLONG)
C*****  GLATEN = LAST LATITUDE COORDINATE.
C*****  GLATBE = FIRST LATITUDE COORDINATE.
C*****GLONEN = LAST LONGITUDE COORDINATE.
C*****GLONBE  = FIRST LONGITUDE COORDINATE.
C***** LATDEL = INTERVAL BETWEEN LAT. COORDINATES.
C***** LONDEL = INTERVAL BETWEEN LONG. COORDINATES.
      DIMENSION GLAT(46),GLONG(46)
      DO 1 I = 1,46
      GLAT(I)=0
      GLONG(I)=0
  1   CONTINUE
       DO 2 I = 1,46
        GLAT(I)=GLATBE + (I-1)*LATDEL
       IF(GLAT(I).GT.GLATEN) GO TO 3
  2   CONTINUE
  3   DO 4 J=1,46
       GLONG(J)=GLONBE + (J-1)*LONDEL
```

```
      IF(GLONG(J).GT.GLONEN)GO TO 5
4     CONTINUE
5     RETURN
      END
```

```
      SUBROUTINE ANGEOG(N,ELEV,GLAT,GLONG,HEIGHT)
C***SUBROUTINE ANGEOG TO CONVERT ANGLES OF ELEVATION AND AZIMUTH TO
C**** GEOGRAPHIC COORDINATES OF LATITUDE AND LONGITUDE.
C***  ELEVATION SCAN 1 TO 90 IN STEPS OF 2
C*** INPUT
C****  N   AZIMUTH
C*** OUTPUT
C***  ELEV,GLAT,GLONG           ANGLE OF ELEVATION,GEOGRAPHIC LATITUDE
C*****   HEIGHT =HEIGHT OF POINT ABOVE EARTH
C****          AND GEOGRAPHIC LONGITUDE.
C***  INCORPORATES FUNCTIONS AFUNC,BFUNC.
      DIMENSIONELEV(46),GLAT(46),GLONG(46)
      RAD=3.14159/180.0
C
C     CHANGE "70.3" TO GEOGRAPHIC LATITUDE OF STATION
C     ***********************************************
      SANAE = 70.3*RAD
      XI =N
         B=XI*RAD
      GHT=6371./(6371.+HEIGHT)
      DO 1 M = 1,6
      XJ=M*2 -2
      ELEV(  M)=XJ*RAD
       GAMMA=ARCOS(   GHT*COS(ELEV(  M)))-ELEV(  M)
      FLAMDA = AFUNC(GAMMA,B,SANAE)
      FDELTL = BFUNC(GAMMA,B,FLAMDA)
      GLAT(  M) =        FLAMDA/RAD
      GLONG(  M) =357.6 -FDELTL/RAD
1     CONTINUE
      DO 2 K=1,46
      ELEV(K)=ELEV(K)/RAD
2     CONTINUE
      RETURN
      END
```

```
      FUNCTION AFUNC(X,Y,SANAE)
      AFUNC=ARSIN(SIN(SANAE)*COS(X)-COS(SANAE)*SIN(X)*COS(Y))
      RETURN
      END
```

```
      FUNCTION BFUNC(A,B,C)
       BFUNC =ARSIN(SIN(A)*SIN(B)/COS(C))
       RETURN
      END
```

```
      SUBROUTINE INVARA(MODEL,TM,FLAT,FLONG,ALT,ERR,BB,FL,
     *SHMIT,G,NMAX,MODOLD,TMOLD)
****  SINGLE PRECISION DECK FOR OCTAL MACHINES (BCD, 026 PUNCH)          INVRA004
****  NEEDS SINGLE PRECISION SUBROUTINE ALLMAG                           INVRA006
****  PROGRAM MODIFIED JAN 1971 BY E G STASSINOPOULOS AND G D MEAD,      INVRA008
****  CODE 641, NASA GODDARD SPACE FLT CTR, GREENBELT, MD 20771          INVRA010
****  NOTE,ERROR IN L IS TYPICALLY LESS THAN 10.*ERR*L (PERCENT)         INVRA012
****  FLAT=LATITUDE IN DEGREES  , FLONG=LONGITUDE IN DEGREES             INVRA014
****  ALT=ALTITUDE=DISTANCE FROM SURFACE OF EARTH IN KILOMETERS          INVRA016
      DIMENSION V(3,3),B(200),ARC(200),VN(3),VP(3),BEG(200),BEND(200),   INVRA018
     1BLOG(200),ECC(200),R1(3),R2(3),R3(3),SHMIT(13,13),G(13,13)
      V(1,2)=ALT/6371.2                                                  INVRA022
      V(2,2)=(90.-FLAT)/57.2957795                                       INVRA024
      V(3,2)=FLONG/57.2957795                                            INVRA026
      ARC(1)=0.                                                          INVRA028
      ARC(2)=(1.0+V(1,2))* SQRT(ERR)*0.3                                 INVRA030
      DCLT=1.5708-0.2007* COS(V(3,2)+1.239)                              INVRA032
      IF(V(2,2)-DCLT)10,10,11                                            INVRA034
   11 ARC(2)=-ARC(2)                                                     INVRA036
   10 CALL STARTA(R1,R2,R3,B,ARC,V,MODEL,TM,SHMIT,G,NMAX,MODOLD,TMOLD)
      DO 12 I=1,3                                                        INVRA040
      VP(I)=V(I,2)                                                       INVRA042
   12 VN(I)=V(I,3)                                                       INVRA044
      CALL LINESA(R1,R2,R3,B,ARC,ERR,J,VP,VN,MODEL,TM,SHMIT,G,NMAX,
     *MODOLD,TMOLD)
      IF(J-200)16,17,17                                                  INVRA048
   17 FL=-1.0                                                            INVRA050
      GO TO 18                                                           INVRA052
   16 JUP=J                                                              INVRA054
      DO 40 J=1,JUP                                                      INVRA056
      ARC(J)= ABS(ARC(J))                                                INVRA058
   40 BLOG(J)=ALOG(B(J))                                                 INVRA060
      JEP=JUP-1                                                          INVRA062
      DO 21 J=2,JEP                                                      INVRA064
      ASUM=ARC(J)+ARC(J+1)                                               INVRA066
      DX=BLOG(J-1)-BLOG(J)                                               INVRA068
      DN=ASUM*ARC(J)*ARC(J+1)                                            INVRA070
      BCO    =((BLOG(J-1)-BLOG(J+1))*ARC(J)**2-DX*ASUM**2)/DN            INVRA072
      CCO    =(DX*ARC(J+1)-(BLOG(J)-BLOG(J+1))*ARC(J))/DN                INVRA074
      SA=.75*ARC(J)                                                      INVRA076
```

```
      SC=SA+.25*ASUM                                                    INVRA078
      DCO=BLOG(J-1)-CCO    *SA*SC                                       INVRA080
      ECO(J)=BCO    +CCO    *(SA+SC)                                    INVRA082
      BEG(J)= EXP(DCO+ECO(J)*.5*ARC(J))                                 INVRA084
   21 BEND(J)= EXP(DCO+ECO(J)*.5*(ASUM+ARC(J)))                         INVRA086
      BEG(JUP)=BEND(JEP)                                                INVRA088
      BEND(JUP)=B(JUP)                                                  INVRA090
      ECO(JUP)=(2.0/ARC(JUP))*ALOG(BEND(JUP)/BEG(JUP))                  INVRA092
      CALL INTEGA(ARC,BEG,BEND,B,JEP,ECO,FLINT)                         INVRA094
   27 CALL CARMLA (B(2),FLINT,FL)                                       INVRA096
   18 BB=B(2)                                                           INVRA098
      RETURN                                                            INVRA100
      END                                                               INVRA102
```

```
      SUBROUTINE STARTA(R1,R2,R3,B,ARC,V,MODEL,TM,SHMIT,G,NMAX,MODOLD,
     *TMOLD)
C ****  SINGLE PRECISION DECK FOR OCTAL MACHINES (BCD, 026 PUNCH)        STRTA004
      DIMENSION B(200),ARC(200),V(3,3),R1(3),R2(3),R3(3),SHMIT(13,13),
     1G(13,13)
      SIT= ABS( SIN(V(2,2)))                                            STRTA008
      AER=V(1,2)                                                        STRTA010
      SSQ=SIT*SIT                                                       STRTA012
      OER=(6356.912+SSQ*(21.3677+.108*SSQ))/6371.2                      STRTA014
      V(1,2)=AER+OER                                                    STRTA016
   10 IF(V(3,2))11,12,12                                                STRTA018
   11 V(3,2)=V(3,2)+6.283185307                                         STRTA020
      GO TO 10                                                          STRTA022
C**12 CALL MAGNET(AER,SIT,V(3,2),BR,BT,BP,R(2),V(2,2))                  STRTA024
   12 RKM=V(1,2)*6371.2                                                 STRTA026
      IF(MODEL.EQ.0) RKM=RKM+14.288-SSQ*(21.3677+.108*SSQ)              STRTA028
      COT= COS(V(2,2))                                                  STRTA030
      SIP= SIN(V(3,2))                                                  STRTA032
      COP= COS(V(3,2))                                                  STRTA034
      CALL ALLMAG(MODEL,TM,RKM,SIT,COT,SIP,COP,BR,BT,BP,B(2),
     1SHMIT,G,NMAX,MODOLD,TMOLD)
      R2(1)=BR/B(2)                                                     STRTA038
      DN=B(2)*V(1,2)                                                    STRTA040
      R2(2)=BT/DN                                                       STRTA042
      R2(3)=BP/(DN*SIT)                                                 STRTA044
      IS=0                                                              STRTA046
    1  DO 2 I=1,3                                                       STRTA048
    2 V(I,1)=V(I,2)-ARC(2)*R2(I)                                        STRTA050
      SIT= ABS( SIN(V(2,1)))                                            STRTA052
C**  3  SSQ=SIT*SIT                                                     STRTA054
C**     OER=(6356.912+SSQ*(21.3677+.108*SSQ))/6371.2                   STRTA056
C**     AER=V(1,1)-OER                                                 STRTA058
C**     CALL MAGNET(AER,SIT,V(3,1),BR,BT,BP,R(1),V(2,1))               STRTA060
    3 RKM=V(1,1)*6371.2                                                 STRTA062
      SSQ=SIT*SIT                                                       STRTA064
      IF(MODEL.EQ.0) RKM=RKM+14.288-SSQ*(21.3677+.108*SSQ)              STRTA066
      COT= COS(V(2,1))                                                  STRTA068
      SIP= SIN(V(3,1))                                                  STRTA070
      COP= COS(V(3,1))                                                  STRTA072
      CALL ALLMAG(MODEL,TM,RKM,SIT,COT,SIP,COP,BR,BT,BP,B(1),
```

```
     1SHMIT,G,NMAX,MODOLD,TMOLD)
       IF(B(1)-B(2))4,5,5                                              STRTA076
     4  ARC(2)=-ARC(2)                                                  STRTA078
       GO TO 1                                                         STRTA080
     5 R1(1)=BR/B(1)                                                   STRTA082
       ARC(3)=ARC(2)                                                   STRTA084
       DN=B(1)*V(1,1)                                                  STRTA086
       R1(2)=BT/DN                                                     STRTA088
       R1(3)=BP/(DN*SIT)                                               STRTA090
       DO 6 I=1,3                                                      STRTA092
     6 V(I,1)=V(I,2)-ARC(2)*(R1(I)+R2(I))/2.                           STRTA094
       SIT= ABS( SIN(V(2,1)))                                          STRTA096
       IS=IS+1                                                         STRTA098
       GO TO (3,7),IS                                                  STRTA100
     7  DO 8 I=1,3                                                     STRTA102
     8 V(I,3)=V(I,2)+ARC(3)*((1.5)*R2(I)-.5*R1(I))                     STRTA104
       RETURN                                                          STRTA106
       END                                                             STRTA108
```

```
       SUBROUTINE LINESA(R1,R2,R3,B,ARC,ERR,J,VP,VN,MODEL,TM,SHMIT,G,
      *NMAX,MODOLD,TMOLD)
C ****  SINGLE PRECISION DECK FOR OCTAL MACHINES (BCD, 026 PUNCH)        LINES004
       DIMENSION B(200),ARC(200),R1(3),R2(3),R3(3),VN(3),VP(3),RA(3),
      1SHMIT(13,13),G(13,13)
       CRE=0.25                                                        LINES008
       IF(ERR-0.15625)74,75,75                                         LINES010
    74 CRE=    (ERR**0.333333333)                                      LINES012
    75 A3=ARC(3)                                                       LINES014
       AAB= ABS(A3)                                                    LINES016
       SNA=A3/AAB                                                      LINES018
       A1=ARC(1)                                                       LINES020
       A2=ARC(2)                                                       LINES022
       AD6=A3*A3/6.0                                                   LINES024
       J=3                                                             LINES026
       ILP=1                                                           LINES028
       IS=1                                                            LINES030
       GO TO 87                                                        LINES032
    66 IS=1                                                            LINES034
       J=J+1                                                           LINES036
       AD6=A3*A3/6.0                                                   LINES038
       ARCJ=A1+A2+A3                                                   LINES040
       AD=(ASUM+A1)/AA                                                 LINES042
       BD=ASUM/BB                                                      LINES044
       CD=A1/CC                                                        LINES046
    36 DO 5 I=1,3                                                      LINES048
       DD=R1(I)/AA-R2(I)/BB+R3(I)/CC                                   LINES050
       GO TO(6,8),IS                                                   LINES052
     6 RT=R1(I)-(AD*R1(I)-BD*R2(I)+CD*R3(I)-DD*ARCJ)*ARCJ              LINES054
       RA(I)=R1(I)                                                     LINES056
       R1(I)=R2(I)                                                     LINES058
       R2(I)=R3(I)                                                     LINES060
       R3(I)=RT                                                        LINES062
       VP(I)=VN(I)                                                     LINES064
     8 RHAR=(R2(I)+R3(I))/2.-DD*AD6
```

```
      A2=A3                                                              LINES192
      A3=A3*.2*(8.+X)/(.8+X)                                             LINES194
      AM=(2.-R3(2)*VN(1))*VN(1)*CRE                                      LINES196
      IF( ABS(A3)-AM)84,84,72                                            LINES198
   72 A3=SNA*AM                                                          LINES200
   84 IF(SNA*R3(1)+.5)85,85,73                                           LINES202
   85 AM=-.5*SNA*VN(1)/R3(1)                                             LINES204
      IF( ABS(A3)-AM)73,73,86                                            LINES206
   86 A3=SNA*AM                                                          LINES208
   73 ARC(J+1)=A3                                                        LINES210
      AAB= ABS(A3)                                                       LINES212
      GO TO 66                                                           LINES214
   60 RETURN                                                             LINES216
      END                                                                LINES218
```

```
      SUBROUTINE INTEGA(ARC,BEG,BEND,B,JEP,ECO,FI)                       INTGA002
****  SINGLE PRECISION DECK FOR OCTAL MACHINES (BCD, 026 PUNCH)          INTGA004
      DIMENSION ARC(200),BEG(200),BEND(200),B(200),ECO(200)              INTGA006
    4 KK=JEP                                                             INTGA008
    6 IF(KK-4)14,11,20                                                   INTGA010
   11 KK=KK-1                                                            INTGA012
   14 A=B(KK-1)/B(2)                                                     INTGA014
      X2=B(KK)/B(2)                                                      INTGA016
      X3=B(KK+1)/B(2)                                                    INTGA018
      ASUM=ARC(KK)+ARC(KK+1)                                             INTGA020
      DN=ARC(KK)*ARC(KK+1)*ASUM                                          INTGA022
      BB=(-A*ARC(KK+1)*(ARC(KK)+ASUM)+X2*ASUM**2-X3*ARC(KK)**2)/DN       INTGA024
      C=(A*ARC(KK+1)-X2*ASUM+X3*ARC(KK))/DN                              INTGA026
      FI=.15707963E+01*(1.0-A+BB*BB/(4.0*C))/ SQRT( ABS(C))              INTGA028
      RETURN                                                             INTGA030
   20 T= SQRT(1.0E0-BEND(2)/B(2))                                        INTGA032
      FI=(2.0*T-ALOG((1.0+T)/(1.0-T)))/ECO(2)                            INTGA034
      IF(B(2)-BEND(KK))21,21,25                                          INTGA036
   25 KK=KK+1                                                            INTGA038
   21 T= SQRT( ABS(1.0-BEG(KK)/B(2)))                                    INTGA040
      FI=FI-(2.0*T-ALOG((1.0+T)/(1.0-T)))/ECO(KK)                        INTGA042
      KK=KK-1                                                            INTGA044
   22 DO 5 I=3,KK                                                        INTGA046
      ARG1=1.-BEND(I)/B(2)                                               INTGA048
      IF(BEND(I)/B(2).LT.1.E-7) ARG1=1.-1.E-7                            INTGA050
      IF(ARG1)26,26,27                                                   INTGA052
   26 TE=1.E-5                                                           INTGA054
      GO TO 28                                                           INTGA056
   27 TE= SQRT(ARG1)                                                     INTGA058
   28 ARG1=1.-BEG(I)/B(2)                                                INTGA060
      IF(BEG(I)/B(2).LT.1.E-7) ARG1=1.-1.E-7                             INTGA062
      IF(ARG1)29,29,31                                                   INTGA064
   31 TB= SQRT(ARG1)                                                     INTGA066
      GO TO 32                                                           INTGA068
   29 TB=1.E-5                                                           INTGA070
   32 IF( ABS(ECO(I))-2.E-5) 23,23,24                                    INTGA072
   23 FI=FI+((TE+TB)*(ARC(I)+ARC(I+1)))/4.                               INTGA074
      GO TO 5                                                            INTGA076
   24 FI=FI+(2.*(TE-TB)-ALOG((1.+TE)*(1.-TB)/((1.-TE)*(1.+TB))))/ECO(I)  INTGA078
```

```
 5 CONTINUE                                                              INTGA080
30 RETURN                                                                INTGA082
   END                                                                   INTGA084
```

```
   SUBROUTINE CARMLA (B,XI,VL)                                           CRMLA002
**** SINGLE PRECISION DECK FOR OCTAL MACHINES (BCD, 026 PUNCH)           CRMLA004
   COMPUTE L                                                             CRMLA006
   IF(XI-1.0E-30)14,14,15                                                CRMLA008
14 VL=(0.311653/B)**(1./3.)                                              CRMLA010
   RETURN                                                                CRMLA012
15 XX=3.0*ALOG(XI)                                                       CRMLA014
   XX=XX+ALOG(B/0.311653)                                                CRMLA016
   IF(XX+22.)1,1,8                                                       CRMLA018
 8 IF(XX+3.)2,2,9                                                        CRMLA020
 9 IF(XX-3.)3,3,10                                                       CRMLA022
10 IF(XX-11.7)4,4,11                                                     CRMLA024
11 IF(XX-23.)5,5,6                                                       CRMLA026
 1 GG=.333338*XX+.30062102                                               CRMLA028
   GO TO 7                                                               CRMLA030
 2 GG=(((((((((-5.1537735E-14*XX+8.3232531E-13)*XX+1.0066362E-9)*XX+     CRMLA032
  18.1048663E-8)*XX+3.2916354E-6)*XX+8.2711096E-5)*XX+1.3714667E-3)*     CRMLA034
  2XX+.01501724)*XX+.43432642)*XX+.62337691                              CRMLA036
   GO TO 7                                                               CRMLA038
 3 GG=(((((((((2.6047023E-10*XX+2.3028767E-9)*XX-2.1997983E-8)*XX-       CRMLA040
  15.3977642E-7)*XX-3.3408822E-6)*XX+3.8379917E-5)*XX+1.1784234E-3)*     CRMLA042
  2XX+1.4492441E-2)*XX+.43352788)*XX+.6228644E0                          CRMLA044
   GO TO 7                                                               CRMLA046
 4 GG=(((((((((6.3271665E-10*XX-3.958306E-8)*XX+9.9766148E-07)*XX-       CRMLA048
  11.2531932E-5)*XX+7.9451313E-5)*XX-3.2077032E-4)*XX+2.1680398E-3)*     CRMLA050
  2XX+1.2817956E-2)*XX+.43510529)*XX+.6222355E0                          CRMLA052
   GO TO 7                                                               CRMLA054
 5 GG=(((((2.8212095E-8*XX-3.8049276E-6)*XX+2.170224E-4)*XX-6.7310339E-3)CRMLA056
  1)*XX+.12038224)*XX-.18461796)*XX+2.0007187                            CRMLA058
   GO TO 7                                                               CRMLA060
 6 GG=XX-3.0460681                                                       CRMLA062
 7 VL=(((1.0+ EXP (GG))*0.311653)/B)**(1./3.)                            CRMLA064
   END COMPUTE L                                                         CRMLA066
   RETURN                                                                CRMLA068
   END                                                                   CRMLA070
```

```
   SUBROUTINE CONVRT(I,GDLAT,ALT,GCLAT,RKM)                              CNVRT002
SINGLE PRECISION DECK FOR OCTAL MACHINES (BCD, 026 PUNCH)                CNVRT004
CONVERTS SPACE POINT FROM GEODETIC TO GEOCENTRIC OR VICE VERSA           CNVRT006
REFERENCE GEOID IS THAT ADOPTED BY IAU IN 1964                           CNVRT008
A=6378.16, B=6356.7746, F=1/298.25                                       CNVRT010
```

```
C   I = 1  GEODETIC TO GEOCENTRIC                                          CNVRT012
C   I = 2  GEOCENTRIC TO GEODETIC                                          CNVRT014
C   GDLAT = GEODETIC LATITUDE IN DEGREES                                   CNVRT016
C   ALT = ALTITUDE ABOVE GEOID IN KILOMETERS                               CNVRT018
C   GCLAT = GEOCENTRIC LATITUDE IN DEGREES                                 CNVRT020
C   RKM = GEOCENTRIC DISTANCE IN KILOMETERS                                CNVRT022
      DATA A,RAD,AB2,EP2/6378.16,57.29578,1.0067397,.0067397/              CNVRT024
      IF(I.EQ.2) GO TO 2                                                   CNVRT026
    1 SINLAT = SIN(GDLAT/RAD)                                              CNVRT028
      COSLAT = SQRT(1.-SINLAT**2)                                          CNVRT030
      COSTH = SINLAT / SQRT((AB2*COSLAT)**2+SINLAT**2)                     CNVRT032
      SINTH = SQRT(1.-COSTH**2)                                            CNVRT034
      RGEOID = A / SQRT(1.+EP2*COSTH**2)                                   CNVRT036
      X = RGEOID*SINTH + ALT*COSLAT                                        CNVRT038
      Y = RGEOID*COSTH + ALT*SINLAT                                        CNVRT040
      RKM = SQRT(X*X+Y*Y)                                                  CNVRT042
      GCLAT = RAD * ATAN(Y/X)                                              CNVRT044
      RETURN                                                               CNVRT046
    2 RER=RKM/A                                                            CNVRT048
C   SEE ASTRON. J. VOL.66 P.15, 1961, FOR FORMULAS BELOW.                  CNVRT050
      A2=(((-1.4127348E-8/RER+.94339131E-8)/RER+.33523288E-2)/RER          CNVRT052
      A4=(((-1.2542063E-10/RER+.11760996E-9)/RER+.11238084E-4)/RER         CNVRT054
     1 -.2814244E-2)/RER                                                   CNVRT056
      A6=((54.939665E-9/RER-28.301730E-9)/RER+3.5435979E-9)/RER            CNVRT058
      A8=(((320.00/RER-252.00)/RER+64.00)/RER-5.00)/RER*.98008304E-12      CNVRT060
      SCL = SIN(GCLAT/RAD)                                                 CNVRT062
      CCL = SQRT(1.-SCL*SCL)                                               CNVRT064
      S2CL=2.*SCL*CCL                                                      CNVRT066
      C2CL=2.*CCL*CCL-1.0                                                  CNVRT068
      S4CL=2.*S2CL*C2CL                                                    CNVRT070
      C4CL=2.*C2CL*C2CL-1.0                                                CNVRT072
      S8CL=2.*S4CL*C4CL                                                    CNVRT074
      S6CL=S2CL*C4CL+C2CL*S4CL                                             CNVRT076
      DLTCL=S2CL*A2+S4CL*A4+S6CL*A6+S8CL*A8                                CNVRT078
      GDLAT=DLTCL*RAD+GCLAT                                                CNVRT080
      ALT = RKM - A/SQRT(1.+EP2*SCL*SCL)                                   CNVRT082
      RETURN                                                               CNVRT084
      END                                                                  CNVRT086
```

```
      SUBROUTINE ALLMAG(MODEL,TM,RKM,ST,CT,SPH,CPH,BR,BT,BP,B,
     1SHMIT,G,NMAX,MODOLD,TMOLD)
C ****  SINGLE PRECISION DECK FOR OCTAL MACHINES (BCD, 026 PUNCH)          ALMGL002
C ****  GEOCENTRIC VERSION OF GEOMAGNETIC FIELD ROUTINE                    ALMGL003
C ****  LONG DECK, THROUGH NMAX=13, FIXED INDICES WITHOUT DO LOOPS         ALMGL004
C ****  EXECUTION TIME PER CALL FACTOR OF THREE LESS THAN SHORT DECK       ALMGL005
C ****  PROGRAM DESIGNED AND TESTED BY E G STASSINOPOULOS AND G D MEAD,    ALMGL006
C ****  CODE 641, NASA GODDARD SPACE FLT CTR, GREENBELT, MD 20771          ALMGL007
C *****  INPUT: MODEL     CHOICE OF 7 MODELS - SEE BELOW                   ALMGL008
C *****         RKM       GEOCENTRIC DISTANCE IN KILOMETERS                ALMGL009
C *****         TM        TIME IN YEARS FOR DESIRED FIELD                  ALMGL010
C *****         ST,CT     SIN + COS OF GEOCENTRIC COLATITUDE               ALMGL011
C *****         SPH,CPH   SIN + COS OF EAST LONGITUDE                      ALMGL012
C ***** OUTPUT: BR,BT,BP  GEOCENTRIC FIELD COMPONENTS IN GAUSS             ALMGL013
C *****         B         FIELD MAGNITUDE IN GAUSS                         ALMGL014
```

```
*****  NOTE: FOR GREATEST EFFICIENCY, COMPLETE ALL CALCULATIONS WITH ALMGL015
   COMMON /DIPOLE/WLONG,COLAT                                        ALMGL//1
          ONE MODEL AND ONE TIME BEFORE CHANGING MODELS OR TIME.     ALMGL016
   DIMENSION TO(7),NMX(7),ISUM(7,3),G(13,13),LSUM(7,3)               ALMGL017
   DATA TO/4*1960.,2*1965.,1970./,NMX/10,11,12,11,9,9,13/            ALMGL018
   DATA    LSUM     /-1646106,-1795169,-1865298,-1777057,-158472,    ALMGL019
  A-156856,-2191704,-62661,-96778,-181519,-83555,-9569,-9599,        ALMGL020
  B-8593,1,-10618,5*1/                                               ALMGL021
   INTEGER   G1(13,13),GT1(13,13),GTT1(13,13),G2(13,13),GT2(13,13),  ALMGL022
  1 GTT2(13,13),G3(13,13),GT3(13,13),GTT3(13,13),G4(13,13),          ALMGL023
  2 GT4(13,13),GTT4(13,13),G5(13,13),GT5(13,13),GTT5(13,13),         ALMGL024
  3 G6(13,13),GT6(13,13),GTT6(13,13),G7(13,13),GT7(13,13),GTT7(13,13)ALMGL025
  4 ,LG(13,13,7),LGT(13,13,7),LGTT(13,13,7)                          ALMGL026
   REAL       GG(13,13,7),GGT(13,13,7),GGTT(13,13,7),SHMIT(13,13)    ALMGL027
   EQUIVALENCE (G1(1),GG(1),LG(1)), (GT1(1),GGT(1),LGT(1)),          ALMGL028
  A     (GTT1(1),GGTT(1),LGTT(1)),                                   ALMGL029
  B (G2(1),LG(1,1,2)), (GT2(1),LGT(1,1,2)), (GTT2(1),LGTT(1,1,2)),   ALMGL030
  C (G3(1),LG(1,1,3)), (GT3(1),LGT(1,1,3)), (GTT3(1),LGTT(1,1,3)),   ALMGL031
  D (G4(1),LG(1,1,4)), (GT4(1),LGT(1,1,4)), (GTT4(1),LGTT(1,1,4)),   ALMGL032
  E (G5(1),LG(1,1,5)), (GT5(1),LGT(1,1,5)), (GTT5(1),LGTT(1,1,5)),   ALMGL033
  F (G6(1),LG(1,1,6)), (GT6(1),LGT(1,1,6)), (GTT6(1),LGTT(1,1,6)),   ALMGL034
  G (G7(1),LG(1,1,7)), (GT7(1),LGT(1,1,7)), (GTT7(1),LGTT(1,1,7))    ALMGL035
*****  THE FOLLOWING DATA CARDS CONTAIN THE FIELD COEFFICIENTS        ALMGL036
*****  FOR THE FOLLOWING SEVEN MODELS:                                ALMGL037
*****   G1,GT1: HENDRICKS + CAIN       99-TERM  GSFC  9/65  EPOCH 1960.ALMGL038
*****   G2,GT2,GTT2: CAIN ET. AL.     120-TERM  GSFC 12/66  EPOCH 1960.ALMGL039
*****   G3,GT3: CAIN + LANGEL         143-TERM  POGO 10/68  EPOCH 1960.ALMGL040
*****   G4,GT4: CAIN + SWEENEY        120-TERM  POGO  8/69  EPOCH 1960.ALMGL041
*****   G5,GT5: IGRF 1965.0            80-TERM        10/68  EPOCH 1965.ALMGL042
*****   G6,GT6: LEATON MALIN + EVANS 1965        80-TERM   EPOCH 1965.ALMGL043
*****             FOR MODEL 6 (LME 1965) SET RKM = 6371.2 + ALTITUDE   ALMGL044
*****   G7,GT7: HURWITZ US COAST + GEODETIC S.  168-TERM   EPOCH 1970.ALMGL045
   DATA G1 / 10, -304249,-15361,13009,9576,-2277,498,709,48,99,3*0,   ALMGL046
  A 57748,-21615,30002,-19870,8028,3595,607,-572,67,29,3*0,-19498,   ALMGL047
  B 2043,15853,12904,5026,2313,45,56,-88,74,3*0,-4310,2308,-1300,8712ALMGL048
  C ,-3940,-312,-2417,75,-138,-156,3*0,1520,-2684,29,-2505,2714,     ALMGL049
  D -1573,-12,-244,-33,114,3*0,86,1212,-1160,-1104,799,-652,5,-15,71,ALMGL050
  E 111,3*0,-119,1028,609,-272,-124,-116,-1091,141,-56,10,3*0,-540,  ALMGL051
  F -244,-91,22,276,-211,-201,58,117,4*0,69,-122,58,-170,26,236,-25, ALMGL052
  G -160,64,16,3*0,-220,156,51,-35,-18,96,121,2,-25,15,42*0 /        ALMGL053

   DATA GT1 / 100, 2059,-2907,266,-86,255,-70,6*0,-394,602,121,-1003,ALMGL054
  H 194,-8,99,6*0,-1369,-1578,-70,163,-117,153,85,6*0,649,293,-924,  ALMGL055
  I -130,-54,-42,211,6*0,-177,-154,318,-548,-417,-72,157,6*0,304,288,ALMGL056
  J -186,125,80,164,-9,6*0,-139,12,153,-73,-6,45,6,84*0/             ALMGL057

   DATA GTT1 /1,168*0/                                               ALMGL058
    DATA((G2(J,I),J=1,13),I=1,6)/ 10, -304012,-15401,13071,9493,
 *-2335,492,724,85,104,-29,
  A 2*0,57782,-21638,29979,-19889,8035,3557,575,-537,65,58,-9,       ALMGL060
  B 2*0,-19320,2029,15903,12768,5029,2284,-8,79,-93,75,-22,2*0,-4254,ALMGL061
  C 2278,-1338,8812,-3977,-288,-2383,156,-96,-151,8,2*0,1603,-2743,  ALMGL062
  D 23,-2466,2605,-1579,-15,-243,-61,121,-28,2*0,51,1178,-1148,-1089,ALMGL063
  E 824,-622,-29,-36,55,47,64,2*0/

   DATA((G2(J,I),J=1,13),I=7,13) /-121,1044,566,-234,-148,-133,-1089,
  F 155,-81,2,47,2*0,-537,-274,-81,70,243,-225,-214,36,130,16,-2,2*0,ALMGL065
  G 54,-117,42,-153,46,219,-7,-171,74,9,18,2*0,-224,138,63,-30,-19,  ALMGL066
  H 90,115,1,-15,2,20,2*0,-1,45,-10,26,-44,-13,-36,40,10,-20,11,28*0/ALMGL067

    DATA((GT2(J,I),J=1,13),I=1,6)/100,1403,-2329,-93,145,
 *161,-42,-57, 35,-10,-1,2*0,-371,
  I 876,-9,-1062,90,60,82,-34,50,-13,-13,2*0,-1431,-1662,-456,231,   ALMGL069
```

```
J -175,334,82,-144,170,-120,88,2*0,520,253,-698,-589,66,-4,235,-90, ALMGL070
K -11,8,-18,2*0,-219,-14,188,-652,-301,-60,83,3,34,-8,17,2*0,224,  ALMGL071
L 159,-261,50,-12,176,1,-60,-7,-39,-2,2*0/

  DATA((GT2(J,I),J=1,13),I=7,13)/5,9,255,-119,33,84,23,-17,
M  43,-36,5,2*0,-96,1,43,75,-33,49,90,-64,-15,47,17,2*0,-50,-21,3, ALMGL073
N -79,5,10,-30,-43,-42,37,16,2*0,66,54,3,35,-3,-1,45,-5,75,-46,31, ALMGL074
O 2*0,-61,-64,2,5,-63,-7,7,-3,-2,-45,-23,28*0/                     ALMGL075

 DATA((GTT2(J,I),J=1,13),I=1,6)/1000,
*-62,-154,-123,1,45,-6,-14,6,-5,-3,2*0,-43,114,-18,
P-27,-44,1,15,-6,8,-1,-3,2*0,54,-16,-253,28,17,75,10,-34,39,-27,20, ALMGL077
Q 2*0,95,-7,79,-183,7,8,50,-4,-8,5,-8,2*0,4,56,-35,-47,-97,15,-11, ALMGL078
R -6,15,-7,7,2*0,-46,7,-7,1,-24,56,26,-27,-2,-6,1,2*0/

 DATA((GTT2(J,I),J=1,13),I=7,13)/20,-11,15,
S -29,29,-10,23,-1,5,-9,1,2*0,-14,16,14,5,-8,16,11,-4,-8,6,1,2*0,  ALMGL080
T -15,-12,5,-11,0,-3,-9,-3,-7,5,5,2*0,22,7,-2,9,6,-1,9,-4,19,-9,4, ALMGL081
U 2*0,-12,-14,1,1,-11,-1,1,-1,1,-6,-2,28*0/                        ALMGL082

  DATA(( G3(J,I),J=1,13),I=1,6)/10,
*-304650,-15414,13258,9591,-2343,491,759,74,110,-26,
A 23,0,57910,-21633,29763,-19837,8196,3577,545,-524,60,66,-20,-18, ALMGL084
B 0,-19772,1506,16075,13169,4864,2339,48,80,-81,18,10,-21,0,-4453, ALMGL085
C 2334,-949,8420,-3724,-210,-2491,100,-92,-125,-55,55,0,1354,-2667,ALMGL086
D 207,-2415,2262,-1471,17,-367,-8,158,-7,-15,0,169,1133,-1287,-1151ALMGL087
E ,1303,-452,-37,-83,91,17,75,24,0/

  DATA(( G3(J,I),J=1,13),I=7,13)/-96,1064,568,-272,-149,-43,-916,
F 66,-114,26,78,-35,0,-579,-250,-8,63,95,-117,-376,-227,79,87,17,  ALMGL089
G -13,0,101,-130,115,-164,55,223,-49,-262,351,51,-53,25,0,-204,144,ALMGL090
H 6,-15,14,34,148,24,-9,-24,13,-12,0,11,9,-3,75,-23,14,-5,43,80,   ALMGL091
I -137,-27,127,0,-8,44,-1,-39,-6,18,-32,8,-59,-17,105,50,14*0/     ALMGL092

  DATA((GT3(J,I),J=1,13),I=1,6)/100,
*2542,-2390,-559,-62,272,-61,-89,61,-24,-1,3,0,-466,
J 988,350,-1152,-251,48,106,-21,-12,30,-9,11,0,-707,-1070,-214,-441ALMGL094
K ,-122,317,62,-108,87,4,12,5,0,848,68,-1489,287,-296,-246,396,70, ALMGL095
L -33,4,19,-30,0,345,-39,-87,-652,86,-89,-94,107,-14,-40,-20,1,0,5,ALMGL096
M 300,32,311,-635,-315,149,96,-85,-28,-2,-34,0/

  DATA((GT3(J,I),J=1,13),I=7,13)/-26,-48,258,-80,50,
N 82,-167,101,99,-57,-43,48,0,-87,-46,-102,25,188,-243,232,523,81, ALMGL098
O -132,-33,52,0,-15,-10,-122,-26,15,-37,29,91,-498,-14,103,-19,0,  ALMGL099
P -38,16,67,-14,-83,130,-33,-38,99,50,22,-3,0,21,5,54,-26,-30,-3,  ALMGL100
Q -39,-2,-104,79,46,-165,0,35,-26,-17,17,18,-50,23,-34,37,22,-155, ALMGL101
R -40,14*0/                                                        ALMGL102

 DATA GTT3 /1,168*0/                                               ALMGL103
  DATA(( G4(J,I),J=1,13),I=1,6)/10,
*-304708,-15425,13334,9647,-2375,448,793,99,96,-17,
A 2*0,57571,-21702,29893,-19826,8108,3566,594,-516,32,93,-22,2*0,  ALMGL105
B -19793,2661,15559,12922,5068,2498,-37,-3,-56,31,13,2*0,-4249,    ALMGL106
C 2417,-1740,8336,-3978,-143,-2324,89,-165,-120,16,2*0,1344,-3037, ALMGL107
D 194,-2764,2247,-1497,96,-335,-33,153,-22,2*0,51,1080,-1073,-1083,ALMGL108
E 1171,-757,20,-33,50,7,94,2*0/

  DATA(( G4(J,I),J=1,13),I=7,13)/-76,1181,583,-181,-270,1,-831,100,
F -120,8,87,2*0,-544,-212,-87,55,151,-236,-278,39,102,4,3,2*0,98,  ALMGL110
G -162,99,-189,106,206,-2,-207,187,62,-24,2*0,-254,128,31,-25,-21, ALMGL111
H 73,127,47,7,-38,-1,2*0,29,35,-7,66,-50,10,-28,21,42,-88,53,28*0/ ALMGL112

  DATA((GT4(J,I),J=1,13),I=1,6)/100,
```

```
*2682,-2366,-724,-157,359,12,-160,19,17,-3,2*0,225,
I 1003,150,-1142,-118,58,38,-26,27,-8,-8,2*0,-684,-2832,792,84,     ALMGL114
J -536,-27,235,72,33,-46,17,2*0,449,-96,177,327,102,-326,128,86,83,ALMGL115
K -9,-87,2*0,369,564,-109,-205,834,-108,-277,84,42,-37,-12,2*0,234,ALMGL116
L 401,-424,63,-503,504,8,-57,0,-3,-33,2*0/

  DATA((GT4(J,I),J=1,13),I=7,13)/-65,-238,249,-170,234,
M -259,-130,101,49,-48,-33,2*0,-168,-114,58,123,94,40,60,-140,73,  ALMGL118
N 54,-21,2*0,1,39,-106,-9,-49,56,-67,-8,-148,-13,27,2*0,48,42,17,  ALMGL119
O -41,-22,21,1,-113,16,33,49,2*0,-14,-37,51,-2,4,-19,7,40,-53,31,  ALMGL120
P -75,28*0/                                                        ALMGL121

 DATA GTT4 /1,168*0/                                               ALMGL122
 DATA G5 / 1, -30339,-1654,1297,958,-223,47,71,10,4*0,5758,-2123,  ALMGL123
A 2994,-2036,805,357,60,-54,9,4*0,-2006,130,1567,1289,492,246,4,0, ALMGL124
B -3,4*0,-403,242,-176,843,-392,-26,-229,12,-12,4*0,149,-280,8,-265ALMGL125
C ,256,-161,3,-25,-4,4*0,16,125,-123,-107,77,-51,-4,-9,7,4*0,-14,  ALMGL126
D 106,68,-32,-10,-13,-112,13,-5,4*0,-57,-27,-8,9,23,-19,-17,-2,12, ALMGL127
E 4*0,3,-13,5,-17,4,22,-3,-16,6,56*0/                              ALMGL128

 DATA GT5 / 1^, 153,-244,2,-7,19,-1,-5,1,4*0,-23,87,3,-108,2,11,-3,ALMGL129
F -3,4,4*0,-118,-167,-16,7,-30,29,11,-7,6,4*0,42,7,-77,-38,-1,6,19,ALMGL130
G -5,5*0,-1,10,29,-42,-21,0,-4,3,5*0,23,17,-24,8,-3,13,-4,0,-1,4*0,ALMGL131
H-9,-4,20,-11,1,9,-2,-2,3,4*0,-11,3,4,2,4,2,3,-6,-3,4*0,1,-2,-3,-2,ALMGL132
I -3,-4,-3,-3,-5,56*0/                                             ALMGL133

 DATA GTT5 /1,168*0/                                               ALMGL134
 DATA G6 / 1, -30375,-1648,1164,930,-179,42,77,11,4*0,5769,-2087,  ALMGL135
A 2954,-2033,811,357,55,-56,23,4*0,-1995,116,1579,1299,490,248,12, ALMGL136
B 8,-6,4*0,-309,230,-141,880,-402,-20,-239,5,-17,4*0,142,-276,5,   ALMGL137
C -264,262,-11,16,-35,5,4*0,30,135,-123,-100,84,-64,8,-16,20,4*0,  ALMGL138
D -18,101,60,-32,-27,-12,-110,9,-1,4*0,-47,-35,-9,2,27,-17,-24,2,  ALMGL139
E 12,4*0,5,-7,3,-20,8,26,10,-12,7,56*0/                            ALMGL140

 DATA GT6 / 10, 155,-266,0,6,8,7*0,6,83,-13,-95,10,4,-5,6*0,-114,  ALMGL141
F -182,13,-19,-22,16,18,6*0,32,16,-85,-6,2,-3,14,6*0,30,-7,27,-27, ALMGL142
G -30,-11,6,6*0,19,23,-18,14,5,17,2,6*0,-22,2,9,-21,-1,-2,-22,84*0/ALMGL143

 DATA GTT6 /1,168*0/                                               ALMGL144
  DATA(( G7(J,I),J=1,13),I=1,6)/10,
*-302059,-17917,12899,9475,-2145,460,734,121,107,-39,16,
A -457446,-20664,29971,-20708,8009,3595,651,-546,77,57,-26,-31,30,ALMGL146
B -20582,430,16086,12760,4579,2490,95,46,-32,23,7,-36,5,-3699,2456,ALMGL147
C -1880,8334,-3960,-290,-2188,175,-124,-110,-19,37,-3,1617,-2758,  ALMGL148
D 185,-2788,2436,-1669,20,-210,-44,131,-15,-3,-13,157,1420,-1310,  ALMGL149
E -911,808,-582,-22,-32,45,33,74,-6,4/

  DATA(( G7(J,I),J=1,13),I=7,13)/-171,1146,625,-323,-78,38,
F -1125,143,34,2,46,-8,-14,-666,-265,-34,81,209,-240,-186,41,125,  ALMGL151
G 15,6,1,-12,121,-160,22,-176,46,189,-46,-187,94,9,-8,2,-12,-174,  ALMGL152
H 163,14,-27,-32,80,137,-4,-14,-4,22,-24,-1,27,19,0,35,-45,22,-31, ALMGL153
I 56,-1,-63,14,4,10,-2,26,-26,-9,21,-1,18,-14,-28,-17,-14,6,-4,-3, ALMGL154
J 4,9,-1,-10,26,-32,13,-6,-19,7,19,12/                             ALMGL155

 DATA GT7/10,231,-244,-19,-7,12,-7,0,3,4*0,-46,112,-1,-90,-6,7,6,  ALMGL156
K -3,3,4*0,-104,-166,40,-20,-36,12,14,3,4,4*0,72,21,-52,-54,-11,0, ALMGL157
L 17,6,1,4*0,22,-5,14,-24,-23,-15,6,3,-1,4*0,1,25,-14,9,1,11,-3,2, ALMGL158
M -3,4*0,-5,11,2,-3,7,22,-5,1,9,4*0,-17,-3,7,1,-2,-3,-2,-1,-2,4*0, ALMGL159
N 2,-6,-3,-4,1,-2,-2,-1,6,56*0/                                    ALMGL160

 DATA GTT7 /1,168*0/                                               ALMGL161
    DATA RAD/57.29578/
*****  NON-SUBSCRIPTED, FIXED-INDEX VERSION BEGINS HERE (NO DO-LOOPS)ALMGL163
```

```
C  *****  BEGIN PROGRAM                                                    ALMGL164
C  *****  INITIALIZE * ONCE ONLY, FIRST TIME SUBROUTINE IS CALLED          ALMGL166
      IF (MODEL.LE.7)GO TO 330
      CALL      DERMAG(MODEL,TM,RKM,ST,CT,SPH,CPH,BR,BT,BP,B,
     1SHMIT,G,NMAX,MODOLD,TMOLD)
      GO TO 11
  330 IF(SHMIT(1,1).EQ.-1.)   GO TO 8                                       ALMGL165
      SHMIT(1,1)=-1.                                                        ALMGL167
      DO 2 N=2,13                                                           ALMGL168
      SHMIT(N,1) = (2*N-3) * SHMIT(N-1,1) / (N-1)                           ALMGL169
      JJ=2                                                                  ALMGL170
      DO 2 M=2,N                                                            ALMGL171
      SHMIT(N,M) = SHMIT(N,M-1) * SQRT(FLOAT((N-M+1)*JJ)/(N+M-2))           ALMGL172
      SHMIT(M-1,N)=SHMIT(N,M)                                               ALMGL173
    2 JJ = 1                                                                ALMGL174
      DO 7 K=1,7                                                            ALMGL175
      F1=LG(1,1,K)                                                          ALMGL176
      F2=LGT(1,1,K)                                                         ALMGL177
      F3=LGTT(1,1,K)                                                        ALMGL178
      NMAX=NMX(K)                                                           ALMGL179
      L = 0                                                                 ALMGL180
      DO 3 I=1,3                                                            ALMGL181
    3 ISUM(K,I) = 0                                                         ALMGL182
      DO 4 N=1,NMAX                                                         ALMGL183
      DO 4 M=1,NMAX                                                         ALMGL184
      L = L+1                                                               ALMGL185
      ISUM(K,1)=ISUM(K,1)+L*LG(N,M,K)                                       ALMGL186
      ISUM(K,2)=ISUM(K,2)+L*LGT(N,M,K)                                      ALMGL187
    4 ISUM(K,3)=ISUM(K,3)+L*LGTT(N,M,K)                                     ALMGL188
      DO 6 I=1,3                                                            ALMGL189
      IF(ISUM(K,I).EQ.LSUM(K,I))  GO TO 6                                   ALMGL190
C  *****  ERROR IN DATA CARDS - NOTE WRITE AND STOP STATEMENTS              ALMGL191
      WRITE(6,5) K,I,LSUM(K,I),ISUM(K,I)                                    ALMGL192
    5 FORMAT(///29H DATA WRONG IN ALLMAG--MODEL ,I2,3X,2HI=,I1,3X,          ALMGL193
     A17HPRECALCULATED SUM,I10,3X,17HTHIS MACHINE GETS,I10)                 ALMGL194
      STOP                                                                  ALMGL195
    6 CONTINUE                                                              ALMGL196
      DO 7 N=1,NMAX                                                         ALMGL197
      DO 7 M=1,NMAX                                                         ALMGL198
      GG(N,M,K)=LG(N,M,K)*SHMIT(N,M)/F1                                     ALMGL199
      GGT(N,M,K)=LGT(N,M,K)*SHMIT(N,M)/F2                                   ALMGL200
    7 GGTT(N,M,K)=LGTT(N,M,K)*SHMIT(N,M)/F3                                 ALMGL201
    8 IF((MODEL.EQ.MODOLD).AND.(TM.EQ.TMOLD))  GO TO 11                     ALMGL202
C  *****  NOTE WRITE STATEMENT - NEW MODEL OR NEW TIME                      ALMGL203
      IF(MODEL.LT.1.OR.MODEL.GT.7) STOP                                     ALMGL204
      IF(MODEL.EQ.1) WRITE(6,21) TM                                         ALMGL205
      IF(MODEL.EQ.2) WRITE(6,22) TM                                         ALMGL206
      IF(MODEL.EQ.3) WRITE(6,23) TM                                         ALMGL207
      IF(MODEL.EQ.4) WRITE(6,24) TM                                         ALMGL208
      IF(MODEL.EQ.5) WRITE(6,25) TM                                         ALMGL209
      IF(MODEL.EQ.6) WRITE(6,26) TM                                         ALMGL210
      IF(MODEL.EQ.7) WRITE(6,27) TM                                         ALMGL211
   21 FORMAT(1HO,20X,41HMODEL 1 HENDRICKS+CAIN GSFC 9/65 FOR TM =F9.3//)    ALMGL212
   22 FORMAT(1HO,20X,41HMODEL 2 (CAIN ET AL GSFC 12/66)  FOR TM =F9.3//)    ALMGL213
   23 FORMAT(1HO,20X,41HMODEL 3 (CAIN+LANGEL POGO 10/68) FOR TM =F9.3//)    ALMGL214
   24 FORMAT(1HO,20X,41HMODEL 4 (CAIN+SWEENEY POGO 8/69) FOR TM =F9.3//)    ALMGL215
   25 FORMAT(1HO,20X,41HMODEL 5    (IGRF 1965.0)         FOR TM =F9.3//)    ALMGL216
   26 FORMAT(1HO,20X,41HMODEL 6 LEATON MALIN EVANS 1965  FOR TM =F9.3//)    ALMGL217
   27 FORMAT(1HO,20X,41HMODEL 7  (HURWITZ USC+GS 1970)   FOR TM =F9.3//)    ALMGL218

      MODOLD=MODEL                                                          ALMGL219
      TMOLD=TM                                                              ALMGL220
      NMAX=NMX(MODEL)                                                       ALMGL221
```

```
      T=TM-TO(MODEL)                                                    ALMGL222
      DO 10 N=1,NMAX                                                    ALMGL223

      DO 10 M=1,NMAX                                                    ALMGL224
   10 G(N,M)=GG(N,M,MODEL)+T*(GGT(N,M,MODEL)+GGTT(N,M,MODEL)*T)         ALMGL225
      WLONG = -RAD*ATAN(G(1,2)/G(2,2))                                  ALMGL//2
      COLAT = RAD*ATAN(SQRT(G(1,2)**2+G(2,2)**2)/G(2,1))                ALMGL//3
      PRINT 19, WLONG,COLAT                                             ALMGL//4
   19 FORMAT("0GEOGRAPHIC COORDINATES OF BOREAL MAGNETIC DIPOLE POLE:   ALMGL//5
     $WEST LONGITUDE =",F9.3,",GEOC. COLATITUDE =",F7.3/)               ALMGL//6
C*****  CALCULATION USUALLY BEGINS HERE                                 ALMGL226
   11 P21=CT                                                            ALMGL227
      P22=ST                                                            ALMGL228
      AR=6371.2/RKM                                                     ALMGL229
      SP2=SPH                                                           ALMGL230
      CP2=CPH                                                           ALMGL231
      DP21=-P22                                                         ALMGL232
      DP22=P21                                                          ALMGL233
      AOR=AR*AR*AR                                                      ALMGL234
      C2=G(2,2)*CP2+G(1,2)*SP2                                          ALMGL235
      BR=-(AOR+AOR)*(G(2,1)*P21+C2*P22)                                 ALMGL236
      BT=AOR*(G(2,1)*DP21+C2*DP22)                                      ALMGL237
      BP=AOR*(G(1,2)*CP2-G(2,2)*SP2)*P22                                ALMGL238
      IF (NMAX.LE. 2) GO TO 1                                           ALMGL239
C                                                          N= 3         ALMGL240
      SP3=(SP2+SP2)*CP2                                                 ALMGL241
      CP3=(CP2+SP2)*(CP2-SP2)                                           ALMGL242
      P31=P21*P21-0.333333333                                           ALMGL243
      P32=P21*P22                                                       ALMGL244
      P33=P22*P22                                                       ALMGL245
      DP31=-P32-P32                                                     ALMGL246
      DP32=P21*P21-P33                                                  ALMGL247
      DP33=-DP31                                                        ALMGL248
      AOR=AOR*AR                                                        ALMGL249
      C2=G(3,2)*CP2+G(1,3)*SP2                                          ALMGL250
      C3=G(3,3)*CP3+G(2,3)*SP3                                          ALMGL251
      BR=BR-3.0*AOR*(G(3,1)*P31+C2*P32+C3*P33)                          ALMGL252
      BT=BT+AOR*(G(3,1)*DP31+C2*DP32+C3*DP33)                           ALMGL253
      BP=BP-AOR*((G(3,2)*SP2-G(1,3)*CP2)*P32+2.0*(G(3,3)*SP3-G(2,3)*CP3)ALMGL254
     1*P33)                                                             ALMGL255
      IF (NMAX.LE. 3) GO TO 1                                           ALMGL256
C                                                          N= 4         ALMGL257
      SP4=SP2*CP3+CP2*SP3                                               ALMGL258
      CP4=CP2*CP3-SP2*SP3                                               ALMGL259
      P41=P21*P31-0.26666666*P21                                        ALMGL260
      DP41=P21*DP31+DP21*P31-0.26666666*DP21                            ALMGL261
      P42=P21*P32-0.20000000*P22                                        ALMGL262
      DP42=P21*DP32+DP21*P32-0.20000000*DP22                            ALMGL263
      P43=P21*P33                                                       ALMGL264
      DP43=P21*DP33+DP21*P33                                            ALMGL265
      P44=P22*P33                                                       ALMGL266
      DP44=3.0*P43                                                      ALMGL267
      AOR=AOR*AR                                                        ALMGL268
      C2=G(4,2)*CP2+G(1,4)*SP2                                          ALMGL269
      C3=G(4,3)*CP3+G(2,4)*SP3                                          ALMGL270
      C4=G(4,4)*CP4+G(3,4)*SP4                                          ALMGL271
      BR=BR-4.0*AOR*(G(4,1)*P41+C2*P42+C3*P43+C4*P44)                   ALMGL272
      BT=BT+AOR*(G(4,1)*DP41+C2*DP42+C3*DP43+C4*DP44)                   ALMGL273
      BP=BP-AOR*((G(4,2)*SP2-G(1,4)*CP2)*P42+2.0*(G(4,3)*SP3-G(2,4)*CP3)ALMGL274
     1*P43+3.0*(G(4,4)*SP4-G(3,4)*CP4)*P44)                             ALMGL275
      IF (NMAX.LE. 4) GO TO 1                                           ALMGL276
C                                                          N= 5         ALMGL277
```

```
      SP5=(SP3+SP3)*CP3                                                 ALMGL278
      CP5=(CP3+SP3)*(CP3-SP3)                                           ALMGL279
      P51=P21*P41-0.25714285*P31                                        ALMGL280
      DP51=P21*DP41+DP21*P41-0.25714285*DP31                            ALMGL281
      P52=P21*P42-0.22857142*P32                                        ALMGL282
      DP52=P21*DP42+DP21*P42-0.22857142*DP32                            ALMGL283
      P53=P21*P43-0.14285714*P33                                        ALMGL284
      DP53=P21*DP43+DP21*P43-0.14285714*DP33                            ALMGL285
      P54=P21*P44                                                       ALMGL286
      DP54=P21*DP44+DP21*P44                                            ALMGL287
      P55=P22*P44                                                       ALMGL288
      DP55=4.0*P54                                                      ALMGL289
      AOR=AOR*AR                                                        ALMGL290
      C2=G(5,2)*CP2+G(1,5)*SP2                                          ALMGL291
      C3=G(5,3)*CP3+G(2,5)*SP3                                          ALMGL292
      C4=G(5,4)*CP4+G(3,5)*SP4                                          ALMGL293
      C5=G(5,5)*CP5+G(4,5)*SP5                                          ALMGL294
      BR=BR-5.0*AOR*(G(5,1)*P51+C2*P52+C3*P53+C4*P54+C5*P55)            ALMGL295
      BT=BT+AOR*(G(5,1)*DP51+C2*DP52+C3*DP53+C4*DP54+C5*DP55)           ALMGL296
      BP=BP-AOR*((G(5,2)*SP2-G(1,5)*CP2)*P52+2.0*(G(5,3)*SP3-G(2,5)*CP3)ALMGL297
     1*P53+3.0*(G(5,4)*SP4-G(3,5)*CP4)*P54+4.0*(G(5,5)*SP5-G(4,5)*CP5)*PALMGL298
     255)                                                               ALMGL299
      IF (NMAX.LE. 5) GO TO 1                                           ALMGL300
                                                        N= 6            ALMGL301
      SP6=SP2*CP5+CP2*SP5                                               ALMGL302
      CP6=CP2*CP5-SP2*SP5                                               ALMGL303
      P61=P21*P51-0.25396825*P41                                        ALMGL304
      DP61=P21*DP51+DP21*P51-0.25396825*DP41                            ALMGL305
      P62=P21*P52-0.23809523*P42                                        ALMGL306
      DP62=P21*DP52+DP21*P52-0.23809523*DP42                            ALMGL307
      P63=P21*P53-0.19047619*P43                                        ALMGL308
      DP63=P21*DP53+DP21*P53-0.19047619*DP43                            ALMGL309
      P64=P21*P54-0.11111111*P44                                        ALMGL310
      DP64=P21*DP54+DP21*P54-0.11111111*DP44                            ALMGL311
      P65=P21*P55                                                       ALMGL312
      DP65=P21*DP55+DP21*P55                                            ALMGL313
      P66=P22*P55                                                       ALMGL314
      DP66=5.0*P65                                                      ALMGL315
      AOR=AOR*AR                                                        ALMGL316
      C2=G(6,2)*CP2+G(1,6)*SP2                                          ALMGL317
      C3=G(6,3)*CP3+G(2,6)*SP3                                          ALMGL318
      C4=G(6,4)*CP4+G(3,6)*SP4                                          ALMGL319
      C5=G(6,5)*CP5+G(4,6)*SP5                                          ALMGL320
      C6=G(6,6)*CP6+G(5,6)*SP6                                          ALMGL321
      BR=BR-6.0*AOR*(G(6,1)*P61+C2*P62+C3*P63+C4*P64+C5*P65+C6*P66)     ALMGL322
      BT=BT+AOR*(G(6,1)*DP61+C2*DP62+C3*DP63+C4*DP64+C5*DP65+C6*DP66)   ALMGL323
      BP=BP-AOR*((G(6,2)*SP2-G(1,6)*CP2)*P62+2.0*(G(6,3)*SP3-G(2,6)*CP3)ALMGL324
     1*P63+3.0*(G(6,4)*SP4-G(3,6)*CP4)*P64+4.0*(G(6,5)*SP5-G(4,6)*CP5)*PALMGL325
     265+5.0*(G(6,6)*SP6-G(5,6)*CP6)*P66)                               ALMGL326
      IF (NMAX.LE. 6) GO TO 1                                           ALMGL327
                                                        N= 7            ALMGL328
      SP7=(SP4+SP4)*CP4                                                 ALMGL329
      CP7=(CP4+SP4)*(CP4-SP4)                                           ALMGL330
      P71=P21*P61-0.25252525*P51                                        ALMGL331
      DP71=P21*DP61+DP21*P61-0.25252525*DP51                            ALMGL332
      P72=P21*P62-0.24242424*P52                                        ALMGL333
      DP72=P21*DP62+DP21*P62-0.24242424*DP52                            ALMGL334
      P73=P21*P63-0.21212121*P53                                        ALMGL335
      DP73=P21*DP63+DP21*P63-0.21212121*DP53                            ALMGL336
      P74=P21*P64-0.16161616*P54                                        ALMGL337
      DP74=P21*DP64+DP21*P64-0.16161616*DP54                            ALMGL338
      P75=P21*P65-0.09090909*P55                                        ALMGL339
      DP75=P21*DP65+DP21*P65-0.09090909*DP55                            ALMGL340
```

```
      P76=P21*P66                                                       ALMGL341
      DP76=P21*DP66+DP21*P66                                            ALMGL342
      P77=P22*P66                                                       ALMGL343
      DP77=6.0*P76                                                      ALMGL344
      AOR=AOR*AR                                                        ALMGL345
      C2=G(7,2)*CP2+G(1,7)*SP2                                          ALMGL346
      C3=G(7,3)*CP3+G(2,7)*SP3                                          ALMGL347
      C4=G(7,4)*CP4+G(3,7)*SP4                                          ALMGL348
      C5=G(7,5)*CP5+G(4,7)*SP5                                          ALMGL349
      C6=G(7,6)*CP6+G(5,7)*SP6                                          ALMGL350
      C7=G(7,7)*CP7+G(6,7)*SP7                                          ALMGL351
      BR=BR-7.0*AOR*(G(7,1)*P71+C2*P72+C3*P73+C4*P74+C5*P75+C6*P76+C7*P7ALMGL352
     17)                                                                ALMGL353
      BT=BT+AOR*(G(7,1)*DP71+C2*DP72+C3*DP73+C4*DP74+C5*DP75+C6*DP76+C7*ALMGL354
     1DP77)                                                             ALMGL355
      BP=BP-AOR*((G(7,2)*SP2-G(1,7)*CP2)*P72+2.0*(G(7,3)*SP3-G(2,7)*CP3)ALMGL356
     1*P73+3.0*(G(7,4)*SP4-G(3,7)*CP4)*P74+4.0*(G(7,5)*SP5-G(4,7)*CP5)*PALMGL357
     275+5.0*(G(7,6)*SP6-G(5,7)*CP6)*P76+6.0*(G(7,7)*SP7-G(6,7)*CP7)*P77ALMGL358
     3)                                                                 ALMGL359
      IF (NMAX.LE. 7) GO TO 1                                           ALMGL360
C                                                        N= 8           ALMGL361
      SP8=SP2*CP7+CP2*SP7                                               ALMGL362
      CP8=CP2*CP7-SP2*SP7                                               ALMGL363
      P81=P21*P71-0.25174825*P61                                        ALMGL364
      DP81=P21*DP71+DP21*P71-0.25174825*DP61                            ALMGL365
      P82=P21*P72-0.24475524*P62                                        ALMGL366
      DP82=P21*DP72+DP21*P72-0.24475524*DP62                            ALMGL367
      P83=P21*P73-0.22377622*P63                                        ALMGL368
      DP83=P21*DP73+DP21*P73-0.22377622*DP63                            ALMGL369
      P84=P21*P74-0.18881118*P64                                        ALMGL370
      DP84=P21*DP74+DP21*P74-0.18881118*DP64                            ALMGL371
      P85=P21*P75-0.13986013*P65                                        ALMGL372
      DP85=P21*DP75+DP21*P75-0.13986013*DP65                            ALMGL373
      P86=P21*P76-0.07692307*P66                                        ALMGL374
      DP86=P21*DP76+DP21*P76-0.07692307*DP66                            ALMGL375
      P87=P21*P77                                                       ALMGL376
      DP87=P21*DP77+DP21*P77                                            ALMGL377
      P88=P22*P77                                                       ALMGL378
      DP88=7.0*P87                                                      ALMGL379
      AOR=AOR*AR                                                        ALMGL380
      C2=G(8,2)*CP2+G(1,8)*SP2                                          ALMGL381
      C3=G(8,3)*CP3+G(2,8)*SP3                                          ALMGL382
      C4=G(8,4)*CP4+G(3,8)*SP4                                          ALMGL383
      C5=G(8,5)*CP5+G(4,8)*SP5                                          ALMGL384
      C6=G(8,6)*CP6+G(5,8)*SP6                                          ALMGL385
      C7=G(8,7)*CP7+G(6,8)*SP7                                          ALMGL386
      C8=G(8,8)*CP8+G(7,8)*SP8                                          ALMGL387
      BR=BR-8.0*AOR*(G(8,1)*P81+C2*P82+C3*P83+C4*P84+C5*P85+C6*P86+C7*P8ALMGL388
     17+C8*P88)                                                         ALMGL389
      BT=BT+AOR*(G(8,1)*DP81+C2*DP82+C3*DP83+C4*DP84+C5*DP85+C6*DP86+C7*ALMGL390
     1DP87+C8*DP88)                                                     ALMGL391
      BP=BP-AOR*((G(8,2)*SP2-G(1,8)*CP2)*P82+2.0*(G(8,3)*SP3-G(2,8)*CP3)ALMGL392
     1*P83+3.0*(G(8,4)*SP4-G(3,8)*CP4)*P84+4.0*(G(8,5)*SP5-G(4,8)*CP5)*PALMGL393
     285+5.0*(G(8,6)*SP6-G(5,8)*CP6)*P86+6.0*(G(8,7)*SP7-G(6,8)*CP7)*P87ALMGL394
     3+7.0*(G(8,8)*SP8-G(7,8)*CP8)*P88)                                 ALMGL395
      IF (NMAX.LE. 8) GO TO 1                                           ALMGL396
C                                                        N= 9           ALMGL397
      DP91=P21*DP81+DP21*P81-0.25128205*DP71                            ALMGL401
      P92=P21*P82-0.24615384*P72                                        ALMGL402
      P91=P21*P81-0.25128205*P71                                        ALMGL400
      CP9=(CP5+SP5)*(CP5-SP5)                                           ALMGL399
      SP9=(SP5+SP5)*CP5                                                 ALMGL398
      DP92=P21*DP82+DP21*P82-0.24615384*DP72                            ALMGL403
```

```
      P93=P21*P83-0.23076923*P73                                        ALMGL404
      DP93=P21*DP83+DP21*P83-0.23076923*DP73                            ALMGL405
      P94=P21*P84-0.20512820*P74                                        ALMGL406
      DP94=P21*DP84+DP21*P84-0.20512820*DP74                            ALMGL407
      P95=P21*P85-0.16923076*P75                                        ALMGL408
      DP95=P21*DP85+DP21*P85-0.16923076*DP75                            ALMGL409
      P96=P21*P86-0.12307692*P76                                        ALMGL410
      DP96=P21*DP86+DP21*P86-0.12307692*DP76                            ALMGL411
      P97=P21*P87-0.06666666*P77                                        ALMGL412
      DP97=P21*DP87+DP21*P87-0.06666666*DP77                            ALMGL413
      P98=P21*P88                                                       ALMGL414
      DP98=P21*DP88+DP21*P88                                            ALMGL415
      P99=P22*P88                                                       ALMGL416
      DP99=8.0*P98                                                      ALMGL417
      AOR=AOR*AR                                                        ALMGL418
      C2=G(9,2)*CP2+G(1,9)*SP2                                          ALMGL419
      C3=G(9,3)*CP3+G(2,9)*SP3                                          ALMGL420
      C4=G(9,4)*CP4+G(3,9)*SP4                                          ALMGL421
      C5=G(9,5)*CP5+G(4,9)*SP5                                          ALMGL422
      C6=G(9,6)*CP6+G(5,9)*SP6                                          ALMGL423
      C7=G(9,7)*CP7+G(6,9)*SP7                                          ALMGL424
      C8=G(9,8)*CP8+G(7,9)*SP8                                          ALMGL425
      C9=G(9,9)*CP9+G(8,9)*SP9                                          ALMGL426
      BR=BR-9.0*AOR*(G(9,1)*P91+C2*P92+C3*P93+C4*P94+C5*P95+C6*P96+C7*P9ALMGL427
     17+C8*P98+C9*P99)                                                  ALMGL428
      BT=BT+AOR*(G(9,1)*DP91+C2*DP92+C3*DP93+C4*DP94+C5*DP95+C6*DP96+C7*ALMGL429
     1DP97+C8*DP98+C9*DP99)                                             ALMGL430
      BP=BP-AOR*((G(9,2)*SP2-G(1,9)*CP2)*P92+2.0*(G(9,3)*SP3-G(2,9)*CP3)ALMGL431
     1*P93+3.0*(G(9,4)*SP4-G(3,9)*CP4)*P94+4.0*(G(9,5)*SP5-G(4,9)*CP5)*PALMGL432
     295+5.0*(G(9,6)*SP6-G(5,9)*CP6)*P96+6.0*(G(9,7)*SP7-G(6,9)*CP7)*P97ALMGL433
     3+7.0*(G(9,8)*SP8-G(7,9)*CP8)*P98+8.0*(G(9,9)*SP9-G(8,9)*CP9)*P99) ALMGL434
      IF (NMAX.LE. 9) GO TO 1                                           ALMGL435
C                                                     N=10              ALMGL436
      SP10=SP2*CP9+CP2*SP9                                              ALMGL437
      CP10=CP2*CP9-SP2*SP9                                              ALMGL438
      P101=P21*P91-0.25098039*P81                                       ALMGL439
      DP101=P21*DP91+DP21*P91-0.25098039*DP81                           ALMGL440
      P102=P21*P92-0.24705882*P82                                       ALMGL441
      DP102=P21*DP92+DP21*P92-0.24705882*DP82                           ALMGL442
      P103=P21*P93-0.23529411*P83                                       ALMGL443
      DP103=P21*DP93+DP21*P93-0.23529411*DP83                           ALMGL444
      P104=P21*P94-0.21568627*P84                                       ALMGL445
      DP104=P21*DP94+DP21*P94-0.21568627*DP84                           ALMGL446
      P105=P21*P95-0.18823529*P85                                       ALMGL447
      DP105=P21*DP95+DP21*P95-0.18823529*DP85                           ALMGL448
      P106=P21*P96-0.15294117*P86                                       ALMGL449
      DP106=P21*DP96+DP21*P96-0.15294117*DP86                           ALMGL450
      P107=P21*P97-0.10980392*P87                                       ALMGL451
      DP107=P21*DP97+DP21*P97-0.10980392*DP87                           ALMGL452
      P108=P21*P98-0.05882352*P88                                       ALMGL453
      DP108=P21*DP98+DP21*P98-0.05882352*DP88                           ALMGL454
      P109=P21*P99                                                      ALMGL455
      DP109=P21*DP99+DP21*P99                                           ALMGL456
      P1010=P22*P99                                                     ALMGL457
      DP1010=9.0*P109                                                   ALMGL458
      AOR=AOR*AR                                                        ALMGL459
      C2=G(10,2)*CP2+G(1,10)*SP2                                        ALMGL460
      C3=G(10,3)*CP3+G(2,10)*SP3                                        ALMGL461
      C4=G(10,4)*CP4+G(3,10)*SP4                                        ALMGL462
      C5=G(10,5)*CP5+G(4,10)*SP5                                        ALMGL463
      C6=G(10,6)*CP6+G(5,10)*SP6                                        ALMGL464
      C7=G(10,7)*CP7+G(6,10)*SP7                                        ALMGL465
      C8=G(10,8)*CP8+G(7,10)*SP8                                        ALMGL466
```

```
      C9=G(10,9)*CP9+G(8,10)*SP9                                        ALMGL467
      C10=G(10,10)*CP10+G(9,10)*SP10                                    ALMGL468

      BR=BR-10.0*AOR*(G(10,1)*P101+C2*P102+C3*P103+C4*P104+C5*P105+C6*P1ALMGL469
     1106+C7*P107+C8*P108+C9*P109+C10*P1010)                            ALMGL470
      BT=BT+AOR*(G(10,1)*DP101+C2*DP102+C3*DP103+C4*DP104+C5*DP105+C6*DPALMGL471
     1106+C7*DP107+C8*DP108+C9*DP109+C10*DP1010)                        ALMGL472
      BP=BP-AOR*((G(10,2)*SP2-G(1,10)*CP2)*P102+2.0*(G(10,3)*SP3-G(2,10)ALMGL473
     1*CP3)*P103+3.0*(G(10,4)*SP4-G(3,10)*CP4)*P104+4.0*(G(10,5)*SP5-G(4ALMGL474
     2,10)*CP5)*P105+5.0*(G(10,6)*SP6-G(5,10)*CP6)*P106+6.0*(G(10,7)*SP7ALMGL475
     3-G(6,10)*CP7)*P107+7.0*(G(10,8)*SP8-G(7,10)*CP8)*P108+8.0*(G(10,9)ALMGL476
     4*SP9-G(8,10)*CP9)*P109+9.0*(G(10,10)*SP10-G(9,10)*CP10)*P1010)    ALMGL477
      IF (NMAX.LE.10) GO TO 1                                           ALMGL478
C                                                        N=11           ALMGL479
      SP11=(SP6+SP5)*CP6                                                ALMGL480
      CP11=(CP6+SP5)*(CP6-SP6)                                          ALMGL481
      P111=P21*P101-0.25077399*P91                                      ALMGL482
      DP111=P21*DP101+DP21*P101-0.25077399*DP91                         ALMGL483
      P112=P21*P102-0.24767801*P92                                      ALMGL484
      DP112=P21*DP102+DP21*P102-0.24767801*DP92                         ALMGL485
      P113=P21*P103-0.23839009*P93                                      ALMGL486
      DP113=P21*DP103+DP21*P103-0.23839009*DP93                         ALMGL487
      P114=P21*P104-0.22291021*P94                                      ALMGL488
      DP114=P21*DP104+DP21*P104-0.22291021*DP94                         ALMGL489
      P115=P21*P105-0.20123839*P95                                      ALMGL490
      DP115=P21*DP105+DP21*P105-0.20123839*DP95                         ALMGL491
      P116=P21*P106-0.17337461*P96                                      ALMGL492
      DP116=P21*DP106+DP21*P106-0.17337461*DP96                         ALMGL493
      P117=P21*P107-0.13931888*P97                                      ALMGL494
      DP117=P21*DP107+DP21*P107-0.13931888*DP97                         ALMGL495
      P118=P21*P108-0.09907120*P98                                      ALMGL496
      DP118=P21*DP108+DP21*P108-0.09907120*DP98                         ALMGL497
      P119=P21*P109-0.05263157*P99                                      ALMGL498
      DP119=P21*DP109+DP21*P109-0.05263157*DP99                         ALMGL499
      P1110=P21*P1010                                                   ALMGL500
      DP1110=P21*DP1010+DP21*P1010                                      ALMGL501
      P1111=P22*P1010                                                   ALMGL502
      DP1111=10.0*P1110                                                 ALMGL503
      AOR=AOR*AP                                                        ALMGL504
      C2=G(11,2)*CP2+G(1,11)*SP2                                        ALMGL505
      C3=G(11,3)*CP3+G(2,11)*SP3                                        ALMGL506
      C4=G(11,4)*CP4+G(3,11)*SP4                                        ALMGL507
      C5=G(11,5)*CP5+G(4,11)*SP5                                        ALMGL508
      C6=G(11,6)*CP6+G(5,11)*SP6                                        ALMGL509
      C7=G(11,7)*CP7+G(6,11)*SP7                                        ALMGL510
      C8=G(11,8)*CP8+G(7,11)*SP8                                        ALMGL511
      C9=G(11,9)*CP9+G(8,11)*SP9                                        ALMGL512
      C10=G(11,10)*CP10+G(9,11)*SP10                                    ALMGL513
      C11=G(11,11)*CP11+G(10,11)*SP11                                   ALMGL514
      BR=BR-11.0*AOR*(G(11,1)*P111+C2*P112+C3*P113+C4*P114+C5*P115+C6*P1ALMGL515
     1116+C7*P117+C8*P118+C9*P119+C10*P1110+C11*P1111)                  ALMGL516
      BT=BT+AOR*(G(11,1)*DP111+C2*DP112+C3*DP113+C4*DP114+C5*DP115+C6*DPALMGL517
     1116+C7*DP117+C8*DP118+C9*DP119+C10*DP1110+C11*DP1111)             ALMGL518
      BP=BP-AOR*((G(11,2)*SP2-G(1,11)*CP2)*P112+2.0*(G(11,3)*SP3-G(2,11)ALMGL519
     1*CP3)*P113+3.0*(G(11,4)*SP4-G(3,11)*CP4)*P114+4.0*(G(11,5)*SP5-G(4ALMGL520
     2,11)*CP5)*P115+5.0*(G(11,6)*SP6-G(5,11)*CP6)*P116+6.0*(G(11,7)*SP7ALMGL521
     3-G(6,11)*CP7)*P117+7.0*(G(11,8)*SP8-G(7,11)*CP8)*P118+8.0*(G(11,9)ALMGL522
     4*SP9-G(8,11)*CP9)*P119+9.0*(G(11,10)*SP10-G(9,11)*CP10)*P1110+10.0ALMGL523
     5*(G(11,11)*SP11-G(10,11)*CP11)*P1111)                             ALMGL524
      IF (NMAX.LE.11) GO TO 1                                           ALMGL525
C                                                        N=12           ALMGL526
      SP12=SP2*CP11+CP2*SP11                                            ALMGL527
```

```
      CP12=CP2*CP11-SP2*SP11                                                    ALMGL528
      P121=P21*P111-0.25062656*P101                                             ALMGL529
      DP121=P21*DP111+DP21*P111-0.25062656*DP101                                ALMGL530
      P122=P21*P112-0.24812030*P102                                             ALMGL531
      DP122=P21*DP112+DP21*P112-0.24812030*DP102                                ALMGL532
      P123=P21*P113-0.24060150*P103                                             ALMGL533
      DP123=P21*DP113+DP21*P113-0.24060150*DP103                                ALMGL534
      P124=P21*P114-0.22807017*P104                                             ALMGL535
      DP124=P21*DP114+DP21*P114-0.22807017*DP104                                ALMGL536
      P125=P21*P115-0.21052631*P105                                             ALMGL537
      DP125=P21*DP115+DP21*P115-0.21052631*DP105                                ALMGL538
      P126=P21*P116-0.18796992*P106                                             ALMGL539
      DP126=P21*DP116+DP21*P116-0.18796992*DP106                                ALMGL540
      P127=P21*P117-0.16040100*P107                                             ALMGL541
      DP127=P21*DP117+DP21*P117-0.16040100*DP107                                ALMGL542
      P128=P21*P118-0.12781954*P108                                             ALMGL543
      DP128=P21*DP118+DP21*P118-0.12781954*DP108                                ALMGL544
      P129=P21*P119-0.09022556*P109                                             ALMGL545
      DP129=P21*DP119+DP21*P119-0.09022556*DP109                                ALMGL546
      P1210=P21*P1110-0.04761904*P1010                                          ALMGL547
      DP1210=P21*DP1110+DP21*P1110-0.04761904*DP1010                            ALMGL548
      P1211=P21*P1111                                                           ALMGL549
      DP1211=P21*DP1111+DP21*P1111                                              ALMGL550
      P1212=P22*P1111                                                           ALMGL551
      DP1212=11.0*P1211                                                         ALMGL552
      AOR=AOR*AR                                                                ALMGL553
      C2=G(12,2)*CP2+G(1,12)*SP2                                                ALMGL554
      C3=G(12,3)*CP3+G(2,12)*SP3                                                ALMGL555
      C4=G(12,4)*CP4+G(3,12)*SP4                                                ALMGL556
      C5=G(12,5)*CP5+G(4,12)*SP5                                                ALMGL557
      C6=G(12,6)*CP6+G(5,12)*SP6                                                ALMGL558
      C7=G(12,7)*CP7+G(6,12)*SP7                                                ALMGL559
      C8=G(12,8)*CP8+G(7,12)*SP8                                                ALMGL560
      C9=G(12,9)*CP9+G(8,12)*SP9                                                ALMGL561
      C10=G(12,10)*CP10+G(9,12)*SP10                                            ALMGL562
      C11=G(12,11)*CP11+G(10,12)*SP11                                           ALMGL563
      C12=G(12,12)*CP12+G(11,12)*SP12                                           ALMGL564
      BR=BR-12.0*AOR*(G(12,1)*P121+C2*P122+C3*P123+C4*P124+C5*P125+C6*P1ALMGL565
     126+C7*P127+C8*P128+C9*P129+C10*P1210+C11*P1211+C12*P1212)                 ALMGL566
      BT=BT+AOR*(G(12,1)*DP121+C2*DP122+C3*DP123+C4*DP124+C5*DP125+C6*DPALMGL567
     1126+C7*DP127+C8*DP128+C9*DP129+C10*DP1210+C11*DP1211+C12*DP1212)          ALMGL568
      BP=BP-AOR*((G(12,2)*SP2-G(1,12)*CP2)*P122+2.0*(G(12,3)*SP3-G(2,12)ALMGL569
     1*CP3)*P123+3.0*(G(12,4)*SP4-G(3,12)*CP4)*P124+4.0*(G(12,5)*SP5-G(4ALMGL570
     2,12)*CP5)*P125+5.0*(G(12,6)*SP6-G(5,12)*CP6)*P126+6.0*(G(12,7)*SP7ALMGL571
     3-G(6,12)*CP7)*P127+7.0*(G(12,8)*SP8-G(7,12)*CP8)*P128+8.0*(G(12,9)ALMGL572
     4*SP9-G(8,12)*CP9)*P129+9.0*(G(12,10)*SP10-G(9,12)*CP10)*P1210+10.0ALMGL573
     5*(G(12,11)*SP11-G(10,12)*CP11)*P1211+11.0*(G(12,12)*SP12-G(11,12)*ALMGL574
     6CP12)*P1212)                                                              ALMGL575
      IF (NMAX.LE.12) GO TO 1                                                   ALMGL576
    1 BR = BR / 100000.                                                         ALMGL632
      BT = BT / 100000.                                                         ALMGL633
      BP = BP / ST / 100000.                                                    ALMGL634
      B =  SQRT(BR*BR+BT*BT+BP*BP )                                             ALMGL635
      RETURN                                                                    ALMGL636
      END                                                                       ALMGL637
```

```
      SUBROUTINE DEKMAG(MODEL,TM,RKM,ST,CT,SPH,CPH,BR,BT,BP,B,
     1SHMIT,G,NMAX,MODOLD,TMOLD)
C ****  THIS VERSION READS IN COEFFICIENTS AS DATA CARDS.  SEE BELOW.    DEKMG004
C ****  GEOCENTRIC VERSION OF GEOMAGNETIC FIELD ROUTINE                  DEKMG006
C ****  SINGLE PRECISION DECK FOR IBM 360 MACHINES (EBCDIC, 029 PUNCH)   DEKMG008
C ****  SHORT DECK' USES SUBSCRIPTED VARIABLES AND DO LOOPS              DEKMG010
C ****  EXECUTION TIME PER CALL 3 TIMES GREATER THAN LONG DECK           DEKMG012
C ****  PROGRAM DESIGNED AND TESTED BY E G STASSINOPOULOS AND G D MEAD,  DEKMG014
C ****  CODE 641, NASA GODDARD SPACE FLT CTR, GREENBELT, MD 20771        DEKMG016
C  *****  INPUT: MODEL     CHOICE OF 7 MODELS                           DEKMG018
C  *****         TM        TIME IN YEARS FOR DESIRED FIELD              DEKMG020
C  *****         RKM       GEOCENTRIC DISTANCE IN KILOMETERS            DEKMG022
C  *****         ST,CT     SIN + COS OF GEOCENTRIC COLATITUDE           DEKMG024
C  *****         SPH,CPH   SIN + COS OF EAST LONGITUDE                  DEKMG026
C  ***** OUTPUT: BR,BT,BP  GEOCENTRIC FIELD COMPONENTS IN GAUSS         DEKMG028
C  *****         B         FIELD MAGNITUDE IN GAUSS                     DEKMG030
C  *****  NOTE: FOR GREATEST EFFICIENCY, COMPLETE ALL CALCULATIONS WITH DEKMG032
C              ONE MODEL AND ONE TIME BEFORE CHANGING MODELS OR TIME.   DEKMG034
C  *****  FOR DOUBLE PRECISION ADD THE FOLLOWING CARD                   DEKMG036
C     IMPLICIT REAL*8(A-H,O-Z)                                          DEKMG038
C  *****  SEE END OF DECK FOR ONE MORE CHANGE                           DEKMG040
      DIMENSION CONST(13,13),FN(13),FM(13)                             DEKMG050
      DIMENSION P(13,13),DP(13,13),SP(13),CP(13)                       DEKMG052
      DIMENSION TO(7),NMX(7),G(13,13)                                  DEKMG042
      REAL*8 LABEL(9,7)
      REAL*4     GG(13,13,7),GGT(13,13,7),GGTT(13,13,7),SHMIT(13,13)   DEKMG046
      DATA P(1,1),CP(1),DP(1,1),SP(1) / 2*1.,2*0. /                    DEKMG054
C  *****  BEGIN PROGRAM                                                 DEKMG056
       MODEL = MODEL-7
      IF(SHMIT(1,1).EQ.-1.)   GO TO 8                                  DEKMG058
C  *****  INITIALIZE * ONCE ONLY, FIRST TIME SUBROUTINE IS CALLED       DEKMG060
      SHMIT(1,1)=-1.                                                   DEKMG062
      DO 18 N=1,13                                                     DEKMG064
      FN(N)=N                                                          DEKMG066
      DO 18 M=1,13                                                     DEKMG068
      FM(M)=M-1                                                        DEKMG070
      CONST(N,M) = FLOAT((N-2)**2-(M-1)**2) / ((2*N-3)*(2*N-5))        DEKMG072
      DO 18 K=1,7                                                      DEKMG074
      GG(N,M,K) = 0.                                                   DEKMG076
      GGT(N,M,K) = 0.                                                  DEKMG078
   18 GGTT(N,M,K) = 0.                                                 DEKMG080
      DO 2 N=2,13                                                      DEKMG082
      SHMIT(N,1) = (2*N-3) * SHMIT(N-1,1) / (N-1)                      DEKMG084
      JJ=2                                                             DEKMG086
      DO 2 M=2,N                                                       DEKMG088
      SHMIT(N,M) = SHMIT(N,M-1) * SQRT(FLOAT((N-M+1)*JJ)/(N+M-2))      DEKMG090
      SHMIT(M-1,N)=SHMIT(N,M)                                          DEKMG092
    2 JJ = 1                                                           DEKMG094
C COEFFICIENTS ARE READ IN WHEN DEKMAG IS CALLED THE FIRST TIME        DEKMG096
C SET UP INPUT DECK AS FOLLOWS:                                        DEKMG098
C CARD 1. NMODLS,NPRINT (2I5).  NMODLS = NO. OF MODLS TO BE READ IN    DEKMG100
C DECK A: FIRST MODEL IN STANDARD GAIN FORMAT.                         DEKMG102
C DECK B: SECOND MODEL, ETC.                                           DEKMG104
C FIRST CARD IN EACH DECK CONTAINS EPOCH (COLS 4-9) AND LABEL (10-73).  DEKMG106
C LAST CARD IN EACH MODEL DECK CONTAINS ZERO OR BLANK IN COLS 1-3.      DEKMG108
      READ(5,4) NMODLS,NPRINT                                          DEKMG110
    4 FORMAT(2I5)                                                      DEKMG112
      IF(NMODLS.GT.7) NMODLS = 7                                       DEKMG114
      DO 3 K=1,NMODLS                                                  DEKMG116
      READ(5,20) TO(K),(LABEL(I,K),I=1,9)                              DEKMG118
   20 FORMAT(3X,F6.1,9A6)                                              DEKMG120
      WRITE(6,21) K,(LABEL(I,K),I=1,9)                                 DEKMG122
```

```
 21 FORMAT("0 MODEL NUMBER"I3,5X,9A6)                                   DEKMG124
    MAXN=0                                                              DEKMG126
  5 READ (5,6) N,M,GNM,HNM,GTNM,HTNM,GTTNM,HTTNM                        DEKMG128
  6 FORMAT (2I3,6F11.4)                                                 DEKMG130
    IF (N.LE.0) GOTO7                                                   DEKMG132
    IF(NPRINT.EQ.1) WRITE(6,6)N,M,GNM,HNM,GTNM,HTNM,GTTNM,HTTNM         DEKMG134
    MAXN=(MAX0(N,MAXN))                                                 DEKMG136
    GG(N,M,K) = GNM                                                     DEKMG138
    GGT(N,M,K) = GTNM                                                   DEKMG140
    GGTT(N,M,K) = GTTNM                                                 DEKMG142
    IF (M.EQ.1) GOTO5                                                   DEKMG144
    GG(M-1,N,K) = HNM                                                   DEKMG146
    GGT(M-1,N,K) = HTNM                                                 DEKMG148
    GGTT(M-1,N,K) = HTTNM                                               DEKMG150
    GO TO 5                                                             DEKMG152
  7 CONTINUE                                                            DEKMG154
    WRITE(6,100)
100 FORMAT(1H0,9X,46HGEOCENTRIC COORDINATES    GEODETIC COORDINATES,      018
   1 10X,1HB,14X,1HL,/,11X,18HLAT    LONG    ALT,7X,11HLAT    LONG,      020
   2 4X,3HLAT,/,10X,19H(DEGR) (DEGR)  (KM),6X,19H(DEGR) (DEGR)  (KM),     022
   3 9X,7H(GAUSS),6X,13H(EARTH RADII),6X,9HELEVATION)
    IF(NPRINT.EQ.0) WRITE(6,22) GG(2,1,K)                               DEKMG156
 22 FORMAT("  G(2,1) ="F9.1)                                            DEKMG158
    NMX(K) = MAXN                                                       DEKMG160
    TO(K) = TZ                                                          DEKMG162
    DO 3 N=1,MAXN                                                       DEKMG164
    DO 3 M=1,MAXN                                                       DEKMG166
    GG(N,M,K) = GG(N,M,K) * SHMIT(N,M)                                  DEKMG168
    GGT(N,M,K) = GGT(N,M,K) * SHMIT(N,M)                                DEKMG170
  3 GGTT(N,M,K) = GGTT(N,M,K) * SHMIT(N,M)                              DEKMG172
  8 IF((MODEL.EQ.MODOLD).AND.(TM.EQ.TMOLD)) RETURN
C *****  NOTE WRITE STATEMENT - NEW MODEL OR NEW TIME                   DEKMG176
    PRINT 9,   MODEL,(LABEL(I,MODEL),I=1,9),TM
  9 FORMAT("0 MODEL USED IS NUMBER",I2,2X,9A6,"  FOR TM =",F9.3/)       DEKMG180
    IF(MODEL.LT.1.OR.MODEL.GT.NMODLS) STOP                              DEKMG182
    MODOLD=MODEL                                                        DEKMG184
    TMOLD=TM                                                            DEKMG186
    NMAX=NMX(MODEL)                                                     DEKMG188
    T=TM-TO(MODEL)                                                      DEKMG190
    DO 10 N=1,NMAX                                                      DEKMG192
    DO 10 M=1,NMAX                                                      DEKMG194
 10 G(N,M)=GG(N,M,MODEL)+T*(GGT(N,M,MODEL)+GGTT(N,M,MODEL)*T)           DEKMG196
     MODEL=7+MODEL
      RETURN
       END
```

REFERENCES

Akasofu, S. -I. and S. Chapman	1961	J. geophys. Res. 66, 1321.
Akasofu, S. -I.	1963	J. geophys. Res. 68, 1667.
Akasofu, S. -I.	1964	Planet. Space Sci. 12, 273.
Akasofu, S. -I.	1968	*Polar and Magnetospheric Substorms*. Springer-Verlag.
Akasofu, S. -I.	1969	*Polar and Magnetospheric Substorms*. D. Reidel Publ. Co. Dordrecht, Holland.
Akasofu, S. -I.	1974	Planet. Space Sci. 22, 885.
Akasofu, S. -I.	1974	Space Sci. Rev. 16, 617.
Akasofu, S. -I.	1975	Planet. Space Sci. 23, 817.
Alven, H.	1950	Cosmical Electrodynamics, Oxford Uni. Press.
Angerami, J.J. and D.L. Carpenter	1966	J. geophys. Res. 71, 711.
Arnoldy, R.L.	1970	J. geophys. Res. 75, 228.
Atkinson, G.	1971	in Proceedings of the advanced study Institute of Magnetosphere-Ionosphere interactions, 1971. Oslo Univ. Press.
Aubry, M.P. and R.L. McPherron	1971	J. geophys. Res. 76, 4381.
Axford, W.I.	1967	Space Sci. Rev. 7, 149.
Axford, W.I.	1969	Rev. Geophys. Space Phys. 7, 421.
Axford, W.I.	1970	in *Particles and Fields in the Magnetosphere*, Ed. B.M. McCormac, D. Reidel.
Axford, W.I. and C.O. Hines	1961	Can. J. Phys. 39, 1433.
Bame, S.J., J.R. Ashbridge, H.E. Felthauser, E.W. Hones and I.B. Strong	1967	J. geophys. Res. 72, 113.
Barraclough, D.R., J.M. Harwood, B.R. Leaton and S.R.C. Malin	1975	J. geophys. Res. 43, 645.
Bernard, L.C.	1973	J. atmos. terr. Phys. 35, 871.
Block,L.P.	1973	*Cosmical Geophysics*. Ed. A. Egeland, Ø. Holter, A. Omholt. Universitetsforlaget.

Bond, F.R. and I.L. Thomas	1971	Aust. J. Phys. 24, 97.
Brice, N.M.	1964	Tech. Rep. No. 3412-6, Stanford Uni., August.
Bryant, D.A., G.M. Courtier and G. Bennett	1971	J. atmos. terr. Phys. 33, 859.
Bryant, D.A., M.J. Smith and G.M. Courtier	1975	Planet. Space Sci. 23, 867.
Buchau, J., G.J. Gasmann and C.P. Pike	1972	Ann. Geophys. 28, 443.
Burch, J.L.	1968	J. geophys. Res. 73, 3585.
Burrows, J.R. and I.B. McDiarmid	1972	in *Critical Problems of Magnetospheric Physics*. IUCSTP Secretariat.
Burton, E.T. and E.M. Boardman	1933	Proc. IRE 21, 1476.
Carpenter, D.L.	1959	Stanford Electronics Labs. Tech. Report number 5.
Carpenter, D.L.	1963	J. geophys. Res. 68, 1675.
Carpenter, D.L.	1966	J. geophys. Res. 71, 693.
Carpenter, D.L.	1970	J. geophys. Res. 75, 3837.
Carpenter, D.L. and C.G. Park	1973	Rev. Geophys. Space Phys. 11, 133.
Chappell, C.R.	1972	Rev. Geophys. Space Phys. 10, 951.
Chappell, C.R.	1974	J. geophys. Res. 79, 1861.
Chase, L.M.	1969	J. geophys. Res. 74, 348.
Chen, A.J. and R.A. Wolf	1972	Planet. Space Sci. 20, 483.
Christense, A.B. and R. Karas	1970	J. geophys. Res. 75, 4266.
Corcuff, Y.	1974	Physics of the Plasmapause Symposium, Trieste.
Cresswel,, G.R. and Davis T.N.	1966	J. geophys. Res. 71, 3155.
Cresswell, G.R.	1972	J. atmos. terr, Phys. 34, 549.
Davidson, G.T.	1965	J. geophys. Res. 70, 1061.
Davis, T.N.	1966	Space Sci. Rev. 6, 222.
Deehr, C.S., J.D.Winningham, F. Yasuhara and S. -I. Akasofu	1976	J. geophys. Res. 81, 5527.
Dowden, R.L.	1961	J. geophys. Res. 66, 1587.

Dowden, R.L.	1962	J. geophys. Res. 67, 1745.
Dowden, R.L. and G. McK. Allock	1971	J. atmos. terr. phys. 33, 1125.
Dungey, J.W.	1963	Planet. Space Sci. 11, 591.
Duthie, D.D. and M.W.J. Scourfield	1977	J. atmos. terr. Phys. 39, 1429.
Eastwood, J.W.	1973	Rep. RCS4, Dep. of Comput. Sci., Univ. of Reading.
Eather, R.H.	1967	Rev. Geophys. 5, 207.
Eather, R.H. and S.B. Mende	1971	J. geophys. Res. 7, 1746.
Eather, R.H.	1973	Rev. Geophys. Space Phys. 11, 155.
Eather, R.H.	1975	Rev. Geophys. Space Phys. 13, 925.
Egeland, A. and A. Omholt	1967	in *Aurora and Airglow.* Ed. B.M. McCormack, D. Reinhold.
Ellis, G.R.	1957	J. atmos. terr. Phys. 10, 302.
Ellis, G.R.	1959	Planet. Space Sci. 1, 253.
Evans, D.S.	1966	Rep. X-611-66-376.
Evans, D.S.	1967	J. geophys. Res. 72, 4281.
Falthammar, C.G.	1973	*Cosmical Geophysics.* Ed. A. Egeland, Ø. Holter, A. Omholt. Universitetsforlaget.
Feldstein, Y.I.	1963	Geomagn. Aeron. 3, 183.
Feldstein, Y.I.	1964	Tellus 16, 252.
Feldstein, Y.I. and G.V. Starkov	1967	Planet. Space Sci. 15, 209.
Frank, I.M. and I.G. Tamm	1937	Akad. Nauk. USSR. 14, 109-000.
Frank, I.M.	1939	'Zh. fis. USSR', J. Phys. 1, 439-000.
Frank, L.A.	1967	J. geophys. Res. 72, 3753.
Frank, L.A.	1971	J. geophys. Res. 76, 2265.
Frank, L.A.	1971	J. geophys. Res. 76, 5202.
Frank, L.A.	1975	Rev. Geophys. Space Phys. 13, 974.
Frank, L.A. and K.L. Ackerson	1971	J. geophys. Res. 76, 3612.
Frank, L.A. and K.L. Ackerson	1972	J. geophys. Res. 77, 4116.

Fukunishi, H.	1975	J. geophys. Res. 80, 553.
Gallet, R.M.	1959	Proc. IRE 47, 211.
Gendrin, R.	1960	C.r.hebd. Seanc. Acad. Sci. Paris 251, 1122.
Gringauz, K.I.	1963	Planet. Space Sci. 11, 281.
Gurnett, D.A.	1966	J. geophys. Res. 71, 5699.
Gurnett, D.A. and L.A. Frank	1972	J. geophys. Res. 77, 172.
Gurnett, D.A. and L.A. Frank	1973	J. geophys. Res. 78, 145.
Hallinan, T.J. and T.N. Davis	1970	Planet. Space Sci. 18, 1735.
Hansen, S.F.	1963	J. geophys. Res. 68, 5925.
Harang, L. and A. Omholt	1960	Geophys. Publ. 22 (2).
Harang, L. and R. Larsen	1965	J. atmos. terr. Phys. 27, 481.
Harang, L.	1968	J. atmos. terr. Phys. 30, 1143.
Hartz, T.R. and N.M. Brice	1967	Planet. Space Sci. 15, 301.
Hartz, T.R.	1971	*Particle Precipitation pattems in the radiating atmosphere.* Ed. McCormac, van Nostrand Reinhold, NY p222.
Hayakawa, M., Y. Tanaka and J. Ohtsu	1975	J. atmos. terr. Phys. 37, 517.
Helliwell, R.A.	1965	*Whistlers and related ionospheric phenomena.* Stanford Univ. Press.
Helliwell, R.A., J.H. Crary, J.H. Pope and R.L. Smith	1956	J. geophys. Res. 61, 139.
Heppner, J.P.	1972	*Critical problems of magnetospheric physics.* IUCSTP Secretariat.
Hill, T.W.	1974	Rev. Geophys. Space Phys. 12, 379.
Hill, T.W. and A.J. Dessler	1971	Planet. Space Sci. 19, 1275.
Hirasawa, T. and T. Nagata	1972	JARE Sci. Rept. A, No. 10, 1.
Ho, D. and L.C. Bernard	1973	J. atmos. terr. Phys. 35, 881.
Hoffman, R.A.	1969	J. geophys. Res. 74, 2425.
Hoffman, R.A. and T. Laaspere	1972	J. geophys. Res. 77, 640.
Hoffman, R.A. and J.L. Burch	1973	J. geophys. Res. 78, 2867.
Hones, E.W., J.R. Ashbridge, S.J. Bame and I.B. Strong	1967	J. geophys. Res. 72, 5879.

Hones, E.W., J.R. Ashbridge, S.J. Bame and S. Singer	1971	J. geophys. Res. 76, 63.
Hughes, A.R.W.	1970	Ph.D. Thesis, Dept. of Physics, Univ. of Sheffield, Sheffield.
Hunten, D.M.	1955	J. atmos. terr. Phys. 7, 141.
Innes, W.F.	1973	M.Sc. Thesis, Dept. of Physics, Calgary, Alberta.
James, H.G., Johansen, O.E. and A. Omholt	1973	J. geophys. Res. 78, 4578.
Johansen, R.G. and R.D. Sharp	1966	Planet. Space Sci. 14, 207.
Johansen, R.G. and R.D. Sharp	1969	*Atmospheric Emissions*. Ed. McCormac, van Nostrand Reinhold, N.Y.
Johnstone, A.D. and T.N. Davis	1974	J. geophys. Res. 79, 1416.
Jorgensen, T.S. and Unstrup.	1962	Jonos faer dalaboratariet Danmarks Tekniske Hojskole, Rapport No. 13.
Jorgensen, T.S.	1964	J. atmos. terr. Phys. 26, 626.
Jorgensen, T.S.	1966	J. geophys. Res. 71, 1367.
Jorgensen, T.S.	1968	J. geophys. Res. 73, 1055.
Kavanagh, L.D., J.W. Freeman and A.J. Chen	1968	J. geophys. Res. 73, 5511.
Kennel, C.F. and H.E. Petschek	1966	J. geophys. Res. 71, 1.
Kimura, I.	1967	Planet. Space Sci. 15, 1427.
Knox, C.F.	1964	Proc. Phys. Soc. London, 83, 783.
Kokubun, S., K. Makita and T. Hirasawa	1972	Rept. Jonos. Space Res. Japan 26, 138.
Kolomenskii, A.A.	1956	Akad. Nauk. USSR. 106, 982-000.
Laaspere, T., W.C. Johnson and L.C. Semprebon	1971	J. geophys. Res. 76, 4477.
Laaspere, T. and R.A. Hoffman	1976	J. geophys. Res. 81, 524.
Lassen, K.	1974	J. geophys. Res. 79, 3857.
Liemohn, H.B. and F.L. Scarf	1962	J. geophys. Res. 67, 1785.
Liemohn, H.B.	1965	Radio Sci. 69D, 741.

Lim, T.L. and T. Laaspere	1972	J. geophys. Res. 77, 4145.
Linscott, G.R.	1975	M.Sc. Thesis, Univ. of Natal, Durban.
Linscott, G.R. and M.W.J. Scourfield	1975	Planet. Space Sci. 24, 299. (in press)
Lui, A.T.Y.	1975	J. geophys. Res. (in press)
Lui, A.T.Y. and C.D. Anger	1973	Planet. Space Sci. 21, 799.
Lui, A.T.Y., C.D. Anger and S. -I. Akasofu	1975	J. geophys. Res. 80, 3603.
Lui, A.T.Y, E.W. Hones, D. Venkatesan, S. -I. Akasofu and S.J. Bame	1975	J. geophys. Res. 80, 929.
Mackenzie, J.F.	1963	Phil. Trans. Roy. Soc. London, 255, 585.
Mansfield, D.V.N.	1967	Astrophys. j. 147, 672.
Maggs, J.E. and T.N. Davis	1968	Planet. Space Sci. 16, 205.
Martin, L.H., R.A. Helliwell and K.R. Marks	1960	Nature 187, 751.
Mathur, A., M.J. Rycroft and J.L. Sagredo	1972	Nature, 237, 508.
Meng, C. -I. and J.D. Mihalov	1972	J. geophys. Res. 77, 1739.
Michel, F.C. and A.J. Dessler	1965	J. geophys. Res. 70, 4305.
Morfill, G. and J.J. Quenby	1971	Planet. Space Sci. 19, 1541.
Morozumi, H.M.	1963	Trans. Am. geophys. Un. 44, 798.
Morozumi, H.M.	1965	Rept. Ionos. Space Res. Japan 19, 286.
Morozumi, H.M. and R.A. Helliwell	1966	Sci. Rep. 2 SU-SEL -66-124 p16, Stanford Univ., California.
Mosier, S.R. and D.A. Gurnett	1972	J. geophys. Res. 77, 1137.
Nishida, A.	1966	J. geophys. Res. 71, 5669.
Oguti, T.	1975	J. atmos. terr. Phys. 37, 761.
Omholt, A. and H. Pettersen	1967	Planet. Space Sci. 15, 347.
Omholt, A., G.J. Kvifte and H. Pettersen	1969	Proc. of the NATO Advanced Institute of Aurora and Airglow 1968 (in press).
Omholt, A.	1971	*The Optical Aurora*. Springer-Verlag.

Ondoh, T.	1965	J. Radio Res. Lab. 12, 197.
Park, C.G.	1972	Stanford Electronics Labs. Tech. Report 3454-1.
Parker, E.N.	1958	Astophys. J. 128, 644.
Paulikas, G.A.	1974	Rev. Geophys. Space Phys. 12, 117.
Paulson, K.V. and G.G. Shepherd	1966	Can. J. Phys. 44, 921.
Pike, C.P. and J.A. Whalen	1974	J. geophys. Res. 79, 985.
Rabe, E. and M.W.J. Scourfield	1977	Planet. Space Sci. 25, 303.
Rich, F.J., D.L. Reasoner and W.J. Burke	1973	J. geophys. Res. 78, 8097.
Roederer, J.G.	1974	Science 183, 37.
Rosenbauer, H., H. Grunwaldt, M.D. Montgomery, G. Paschmann and N. Schkopke	1975	J. geophys. Res. 80, 2723.
Rosenberg, J.J.	1968	Planet. Space Sci. 16, 1419.
Russell, C.T.	1972	*Critical Problems of Magnetospheric Physics*. IUCSTP Secretariat.
Russell, C.T.	1975	Rev. Geophys. Space Phys. 13, 952.
Russell, C.T. and Thorne	1970	Cosmic Electrodynamics 1, 67.
Rycroft, M.J.	1972	Radio Sci. 7, 811.
Rycroft, M.J. and A. Mathur	1973	J. atmos. terr. Phys. 35, 2177.
Sagredo, J.L. and K. Bullough	1972	Planet. Space Sci. 20, 731.
Sandford, B.P.	1964	J. atmos. terr. Phys. 26, 749.
Sandford, B.P.	1968	J. atmos. terr. Phys. 30, 1921.
Scourfield, M.W.J.	1967	M.Sc. Thesis, Univ. of Calgary.
Scourfield, M.W.J. and N.R. Parsons	1969	Planet. Space Sci. 17, 1141.
Scourfield, M.W.J. and N.R. Parsons	1969	Planet. Space Sci. 19, 437.
Scourfield, M.W.J. and G.R. Linscott	1974	S.A.J. Antarctic Res. 4, 31.
Shepherd, G.G. and E.V. Pemberton	1968	Radio Sci. 3, 350.
Singh,R.N. and R.P. Singh	1969	Ann. Geophys. 25, 629.
Singh,R.P.	1972	Planet. Space Sci. 20, 2073.

Siren, J.C.	1975	J. geophys. Res. 80, 93.
Smith, R.L.	1961	J. geophys. Res. 66, 3699.
Snyder, A.L. and S. -I. Akasofue	1974	Planet. Space Sci. 22, 1511.
Snyder, A.L., S. -I. Akasofu and T.N. Davis	1974	J. geophys. Res. 79, 1393.
Spreiter, J.R. and B.K. Briggs	1962	J. geophys. Res. 67, 3779.
Srivastava, R.N.	1974	Planet. Space Sci. 22, 1545.
Storey, L.R.O.	1953	Phil. Trans. Roy. Soc., London, A, 246, 113.
Sturrock	1962	J. Res. Nat. Bur. Stand. 660, 153.
Swift, D.W. and R. Kan	1975	J. geophys. Res. 80, 985.
Swift, D.W. and R.N. Srivastava	1974	Rept. DAH (04-69-C-0054) Geophys. Inst. Uni. Alaska, Fairbanks.
Tanaka, Y.	1972	Proc. Res. Inst. Atmos. Nagoya Uni. 19, 63.
Taylor, W.W.L.	1973	Ph.D. Thesis Univ. Iowa, Iowa City.
Taylor, W.W.L. and S.D. Shawhan	1974	J. geophys. Res. 79, 105.
Vallance Jones, A.	1974	*Aurora*. D. Reidel.
Van Allen, J.A., J.F. Fennell and N.F. Ness	1971	J. geophys. Res. 76, 4262.
Vasyliunas, V.M.	1968	J. geophys. Res. 73, 2839.
Vasyliunas, V.M.	1970	in *Polar Ionosphere and Magnetospheric Processes*. Ed. B. Skovli, Gordon and Breach.
Walker, A.D.M. and K.F. Deane	1974	S.A.J. Antarctic Res. 4, 27.
Wentworth, R.C., W.M. McDonald and S.F. Singer	1959	Phys. Fluids 2, 499.
Winningham, J.D., F. Yasuhara, S. -I. Akasofu and W.J. Heikkila	1975	J. geophys. Res. 80, 3148.
Woods, A.C.	1974	M.Sc. Thesis, Univ. of Natal.
Woods, A.C., M.W.J. Scourfield and N.D. Clarence	1974	Planet. Space Sci. 22, 1139.